Investigation of Processing Polyurethane via Reactive Extrusion 3D Printing

by

Yuyang Wu

A doctoral thesis submitted to

The Graduate School of The University of Nottingham

in partial fulfilment of the requirements for the awards of

Doctor of Philosophy

Department of Mechanical, Materials, and Manufacturing Engineering

Jan 2023

Acknowledgements

I would like to pay my greatest gratitude to my supervisors/mentors: Prof. Derek Irvine, Prof. Ricky Wildman, Prof Chris Tuck, Dr Zuoxin Zhou who relentlessly offered their support and advice from the day one since I began the PhD journey. The invaluable lesson of being independent and stay open minded is valuable for my both professional career and personal development.

I would also like to thank my colleagues at the Centre of Additive Manufacturing (CfAM), the big CfAM family: Dr Feiran Wang, Dr Kaiyang Wang, Dr Alice Konta, Ling Yong, Marica Malencia, Dr Xuesong Lu. It was truly a pleasure to enjoy so many great conversations about life and work and share such an awesome journey with you. I am grateful to be in such a talent pool and learn something new from you all on the daily basis.

Lastly, thank you to my beloved family: my father (Hong Wu), mother (Qin Tang), my grandparents and rest of family members, my dearest loved one (Yujia Ren) who endlessly support me whenever I am on the top or low. As we always said to each other "Home is always your safe heaven, regardless of how high you fly or how further being away". It was a tough pandemic period for us all to be through. I love you all and without your love and support, I will not become who I am today to reach this chapter of my life.

Abstract

Additive manufacturing (AM, also known as 3D Printing) describes a range of technologies that build structures layer by layer to translate a 3D computer aided design parts into functional solid objects for different customised applications. Polyurethane (PU) is a polymer with versatile applications used as foams, coatings, adhesives, and biomedical devices, due to the easily tuneable rubbery/rigid nature. To push a broader industrial application of AM functional polymeric parts, such as polyurethane (PU), research in the academia field explored the desirable PU functionalities through a range of AM technologies.

Reactive Extrusion 3D Printing (REX) is one of the AM technologies pursued to realise the potential of AM PU functional parts. REX is a newly invented manufacturing route¹, whereby two feeds comprising reactive functional groups are mixed in-situ during the process and extruded to construct 3D structures. At its early stage, the few research conducted in the REX field focused on demonstrating the capability of printing isotropic and functional graded parts through in-situ tailoring of the reaction and targeted on fabricating large-scale structure with fast deposition speed.

There is a clear gap in the AM PU via REX, to systematically understand the processing of PU via REX process. Therefore, this PhD project started by establishing a workflow: progressing from screening the printability of PU feedstocks through a printing optimisation for these feedstocks, to achieve good resolution / reproducibility by investigating the filament quality produced. It highlighted that transitional ink rheology as the key characterisation tools for the formulation printability analysis, and optimum flowrate to be the key parameter to evaluate during process optimisation.

In REX, the mixing efficiency and reaction kinetics are highly synergistic. Furthermore, both are greatly influenced by the rheology of the two feeds, the effects of which are relatively

unexplored. To understand the impact of feed rheology on the print quality, three mixing modes differed by distinct rheological properties of the isocyanates and polyol dual feeds were designed and investigated by leveraging PU reaction. This was achieved through incorporating different amount of fumed silica into feeds as rheology modifier. It demonstrated the properties of 3D printed PU can be tuneable by adjusting the rheological relationship between the isocyanates and polyol feeds. Both viscosity ratio and elasticity ratio of the feeds influenced the mixing efficiency, the reaction kinetics, and the quality of the printed structures. The isocyanates and polyol feeds demonstrating great differences in viscosity and elasticity reacted more rapidly due to less restriction in diffusion of feed materials during mixing. Consequently, a high level of cross-linking was achieved within the printed PU structure, resulting in better thermal properties and improved stiffness than the other two mixing modes investigated. It showed feed rheology shall be optimised to find the best combination of MMs, with prominent printing performance.

To further explore the effect of filler on the process and enhance the cross-linking network of such PU systems, two types of functional silica nanoparticles (FSP) were developed (SiO₂-NH₂ and SiO₂-NH₂/CH₃) and served as reactive filler to afford hybrid reinforcing effect in the matrix through physical entanglements and intramolecular bonding. This study has successfully demonstrated such dual-network reinforcing effect with SiO₂-NH₂/CH₃ reinforced PU system, showed faster reaction kinetics, higher glass transition temperature, better thermal stability, and enhanced increments in storage modulus than the SiO₂-NH₂ reinforced system. Furthermore, SiO₂-NH₂/CH₃ reinforced PU system exhibited comparable thermo-mechanical properties, with commercial fumed silica particles (SiO₂-PDMS) filled PU system. The improvement in FSP reinforcing efficiency was attained by improving the dispersion of SiO₂-NH₂/CH₃ in matrix and the formation of additional urea bonds in the structure. Without the alkyl groups on the particle surface, SiO₂-NH₂ reinforced PU composite exhibited significantly

inferior printing performance, as the results of SiO₂-NH₂ aggregation. It hindered the widely formation of PU reaction and further inhibited the cross-linking networks.

These findings offer guidance on further developing reactive formulations in material extrusion AM, enabling a greater variety of chemistries with tuneable functions to be 3D printed in the future. It also offers guidance on developing FSPs with additional functionality and 3D printing of multi-functional nanoparticle reinforced composite systems. It has shown that the concept of introducing dual-network particle reinforcing filler to strengthen the REX matrix materials, opens a new route for developing advanced nanoparticle reinforcement composite systems via AM.

Table of Contents

Acknow	vledg	ementsii
Abstrac	t	iii
Table of	f Cor	ntentsvi
Table of	f Abł	previationsix
List of I	Figur	esxii
List of 7	Table	esxxi
1 Int	rodu	ction1
1.1	Bac	ekground1
1.2	Ain	n of Research5
1.3	Res	search Methodology6
1.3	3.1	Statement of Novelty
1.4	Strı	acture of Thesis
1.4	4.1	Thesis chapters8
2 Lit	teratu	re Review11
2.1	Intr	roduction11
2.2	Pol	yurethane Backgrounds
2.2	2.1	Chemistry
2.2	2.2	Conventional Process and Applications
2.3	Ada	ditive Manufacturing Polyurethane 22.

	2.3.1	Route 1: Pre-synthesised PU Feed	22
	2.3.2	Route 2: <i>In-situ</i> Reactive 3D Printing	38
	2.4 Rea	active Extrusion 3D Printing Polyurethane	45
	2.4.1	Commercial examples	49
	2.5 Sili	ca Nanoparticles (SiO ₂) as reinforcing filler	50
	2.5.1	SiO ₂ Reinforced Composite via AM	50
	2.5.2	Functional SiO ₂ reinforced composite	54
	2.6 Gap	os in research	59
3	Materia	ls and Methods	60
	3.1 Me	thods	60
	3.1.1	Feed Formulation and Preparation	61
	3.1.2	Printability Analysis	75
	3.1.3	Reactive Extrusion 3D Printing (REX)	80
	3.1.4	Printing Characterisations	83
4	Investig	gation the Workflow for Printability Screening and Printing Optimisation of Fa	ast
C	uring Polyu	urethane Formulations via Reactive Extrusion 3D Printing	86
	4.1 Res	sults	88
	4.1.1	Printability Analysis	88
	4.1.2	Process Optimisation	98
	4.2 Dis	cussion1	20
	4.2.1	Printability Analysis1	20
	4.2.2	Process Optimisation	22

Table of Contents

	4.2	3	Porous structure	124
	4.3	Cor	nclusion	125
5	Inv	estig	gation the Effects of Feed Rheology on the Three Types of Mixin	g Modes and
Pri	inted	Poly	urethane Properties	126
	5.1	Res	sults	126
	5.2	Dis	cussion	140
	5.3	Cor	nclusion	144
6	Inv	estig	gation the Reinforcing Effect from Amine-based Functional Silica	Nanoparticles
on	the P	rinte	ed Polyurethane Crosslink Network	145
	6.1	Res	sults	147
	6.2	Dis	cussion	168
	6.3	Cor	nclusion	172
7	Co	nclus	sion and Future Work	173
	7.1	Cor	nclusion	173
	7.2	Fut	ure Work	175
	7.2	.1	Functional Parts with Fully Dense Structure	175
	7.2	2	Expanded Feed Processing Windows for Material Extrusion (Lov	wer Rheology
	Fee	ed Fo	ormulations)	175
	7.2	3	Parts with Functional Gradient Properties	176
	7.2	.4	Scale-Up REX Printer	176
	7.2	5	Expanding the Applications of FSPs to Other AM Processes	177
R	Do	feren		178

Table of Abbreviations

Process

AM Additive Manufacturing
CAD Computer Aided Design

DIW Direct Ink Writing

DLP Digital Light Processing

DoD Drop on Demand

FDM Fused Deposition Modelling
FFF Fused Filament Fabrication

SLA Stereolithography

SLS Selective Laser Sintering

MMs (MM1, MM2, MM3) Mixing Modes (Mixing modes 1, 2 and 3)

REX Reactive Extrusion 3D Printing

Chemicals

PU Polyurethane

PUA Poly (urethane acrylate)

PDMS Poly (dimethyl siloxane)

PMMA poly (methyl methacrylate)

PEG-PPG-PEG poly (ethylene glycol)-block-poly (propylene glycol)-

block-poly (ethylene glycol)

PMDI Poly [(phenyl isocyanate)-co-formaldehyde]

PPG Poly (propylene glycol)
PTES n-propyltriethoxysilane

TPU Thermoplastic Polyurethane

TEOS Tetraethyl orthosilicate
SiO₂ or Si-NP Silica Nanoparticles

SiO₂-NH₂ Amine functional silica nanoparticles

SiO₂-NH₂/CH₃ Amine/alkyl Functional Silica Nanoparticles

SiO₂-PDMS or FS Fumed silica, surface coated with PDMS

AUD Aliphatic Urethane Diacrylate
APTS or APTES 3-aminopropyl triethoxysilane

Table of Abbreviations

1,4 - BD 1,4 - Butanediol

CNTs Carbon nanotubes

DBTDL Dibutyltin dilaurate

EAA Epoxy Aliphatic Acrylate

EtOH Ethanol

FSP Functional Silica Nanoparticles

IPDI Isophorone diisocyanate

N3900 Desmodur® N3900, is a multi-functional

polyisocyanate crosslinker

NH₄OH Ammonia

NCO Isocyanate

HDI Hexamethylene diisocyanate

OH Alcohol (diol/polyol)

Devices

TEM Transmission electron microscopy

DAC Dual Axial Centrifugal

FTIR Fourier-transform infrared spectroscopy

TGA Thermogravimetry Analysis

DSC Differential scanning calorimetry

DMA Dynamic Mechanical Analysis

·

SEM Scanning Electron Microscope

Dimensionless number/pre-defined parameters/terms

Oh Ohnesorge number

We Weber number

Re Reynolds number

FGM Functional graded materials

Ratio between print speed and extrusion speed

Q_f REX Extrusion flowrate

 $R(W_b)$ The block width ratio

 $R(W_L)$ The line width ratio

 $\Delta T/\Delta t$ Rate of reaction exotherm

D_I Infill distance, i.e. the travel distance between in-plane

adjacent filaments

DTG Differential thermogravimetric

DTG (I)_{max} Lower peak temperature in the DTG thermogram

DTG (II)_{max} Higher peak temperature in the DTG thermogram

 $\mathbf{W}_{_{\mathrm{L}}}$ Line Width

 W_{b1}, W_{b2} The width of the block

FIGURE 1- 1. WORKFLOW SHOWING THE PROCESS OF RESEARCH
FIGURE 2- 1. LITERATURE REVIEW WORKFLOW STRUCTURE
FIGURE 2- 2. GENERAL POLYURETHANE REACTION MECHANISM
FIGURE 2- 3. COMMON ADDITION REACTIONS BETWEEN ISOCYANATES AND COMPOUNDS WITH REACTIVE HYDROGEN. A) ALCOHOL. B)
THIOL. C) AMINE. D) WATER. FIGURE TAKEN FROM DELEBECQ ⁴³ , REPRODUCED WITH PERMISSION OF RIGHTS HOLDER 13
FIGURE 2- 4. SCHEMATIC OF POLYURETHANE STRUCTURE. A) STRUCTURE OF SOFT AND HARD SEGMENTS IN THE POLYURETHANE
CHAINS. FIGURE TAKEN FROM DE AVILA BOCKORNY ⁴⁴ , REPRODUCED WITH PERMISSION OF RIGHTS HOLDER. B) SCHEMATIC OF
CHEMICAL LINKAGE WITHIN THE SOFT SEGMENTS, HARD SEGMENTS, AND HYDROGEN BONDS IN THE POLYURETHANE
STRUCTURE; SCHEMATIC OF AGGREGATED HARD SEGMENTS
FIGURE 2- 5. INTERFACIAL MIXING OBSERVED UPON CONTACTING A POLYETHER DIAMINE (D2000) AND 4,4' DIPHENYLMETHANE
DIISOCYANATE (MDI), 40X MAGNIFICATION. INTERFACE A) UPON REACTANT CONTACT. B) 0.2S FROM CONTACT. C) 0.8S
FROM CONTACT. FIGURE TAKEN FROM MACHUGA ⁵⁵ , REPRODUCED WITH PERMISSION OF RIGHTS HOLDER17
FIGURE 2- 6. GROWTH OF INTERFACIAL ZONE OVER TIME AT VARYING DBTDL CATALYST CONCENTRATION IN POLYETHER DIOL AND
MDI SYSTEM. FIGURE TAKEN FROM MACHUGA ⁵⁵ , REPRODUCED WITH PERMISSION OF RIGHTS HOLDER
FIGURE 2-7. INTERFACIAL POLYMERIZATION AT 25°C AND TIME: 30s FOR (A) TOP PHASE, 25%, 1,4 BD + 75 % PPO +0.1 WT. %,
CATALYST; BOTTOM PHASE, DI-ISOCYANATE MDI. (B) TOP PHASE, 50%, 1,4 BD + 50 % PPO +0.1 WT. %, CATALYST;
BOTTOM PHASE, DI-ISOCYANATE MDI. FIGURE TAKEN FROM FIELDS ⁵³ , REPRODUCED WITH PERMISSION OF RIGHTS HOLDER. 18
FIGURE 2-8. SCHEMATIC OF TWO STEP POLYMERISATION PROCESS FOR POLYURETHANE PRODUCTION. FIGURE TAKEN FROM LAN ⁵⁹ ,
REPRODUCED WITH PERMISSION OF RIGHTS HOLDER
Figure 2- 9. Systematic method for evaluating the powders for SLS system. Figure taken from Yuan ⁶³ , reproduced
WITH PERMISSION OF RIGHTS HOLDER.
FIGURE 2- 10. DSC SCAN OF THE TPU POWDERS UPON HEATING AND COOLING FROM -50 °C TO 200 °C AT THE RATE OF 10 °C/MIN.
FIGURE TAKEN FROM YUAN ¹⁰ , REPRODUCED WITH PERMISSION OF RIGHTS HOLDER
FIGURE 2- 11. DSC THERMOGRAM SHOWING THE "SLS SINTERING WINDOW" WITHIN REGION BETWEEN MELTING AND
CRYSTALLISATION. FIGURE TAKEN FROM SCHMID ⁶³ . REPRODUCED WITH PERMISSION OF RIGHTS HOLDER

FIGURE 2- 12. SCHEMATIC OF THE STRUCTURE FORMED IN THE SLS-PROCESSED TPU/CNTS COMPOSITES. FIGURE TAKEN FROM LI ^O	,
REPRODUCED WITH PERMISSION OF RIGHTS HOLDER.	26
FIGURE 2-13. POWDER COALESCENCE ON A HOT STAGE: A) PA12 POWDER AND B-D) TPU/CNTS POWDER WITH DIFFERENT CNTS	;
CONTENTS: B) 0 wt\% , c) 0.2 wt\% , d) 0.5 wt\% . Figure taken from Li^{61} , reproduced with Permission of Rights	
HOLDER	27
FIGURE 2- 14. SCHEMATIC OF FDM PROCESS OF (A) A RIGID FILAMENT. FALLING OF FILAMENT BETWEEN THE GAP OF DRIVE GEARS	
and hot end, due to (B) filament misalignment (C) filament kinking or buckling. Figure taken from Kim^{70} ,	
REPRODUCED WITH PERMISSION OF RIGHTS HOLDER	30
FIGURE 2- 15. EXAMPLES OF PRINTING WITH DIFFERENT OVERHANG ANGLES (A) 60 DEGREE (B) 45 DEGREE (C) 30 DEGREE. FIGURE	:
TAKEN FROM KIM ⁷⁰ , REPRODUCED WITH PERMISSION OF RIGHTS HOLDER	31
FIGURE 2- 16. SCHEMATIC OF INTERFACIAL DIFFUSION BETWEEN TWO ADJACENT FDM DEPOSITED BEADS AT LAYER HEIGHT FROM	
0.2 mm, 0.3 mm and 0.4 mm. The inner diameter of the nozzle d $^{\sim}0.4$ mm. Figure taken from ${\rm Lin}^{71}$, reproduced	
WITH PERMISSION OF RIGHTS HOLDER.	32
FIGURE 2- 17. (A) CHEMICAL STRUCTURE OF THE SYNTHESISED SUPRAMOLECULAR POLYURETHANE (SPU). (B) SCHEMATIC OF HOT	
MELT EXTRUSION PROCESS OF SPU/PEG/PARACETAMOL FORMULATION FOR DRUG-RELEASE IMPLANT APPLICATION. (C AND	
D) SIDE AND END VIEW OF THE PRINTED BAR STRUCTURE FROM THE SPU/PEG/PARACETAMOL FORMULATION. FIGURE TAKE	N
FROM SALIMI ⁷ , REPRODUCED WITH PERMISSION OF RIGHTS HOLDER	33
FIGURE 2-18. SCHEMATIC OF TWO TYPES OF STEREOLITHOGRAPHY SYSTEMS. LEFT (SLA): A BOTTOM-UP SYSTEM WITH SCANNING	
LASER. RIGHT (DLP): A TOP-DOWN SETUP WITH DIGITAL LIGHT PROJECTION. FIGURE TAKEN FROM MELCHELS ⁶³ , REPRODUCE)
WITH PERMISSION OF RIGHTS HOLDER.	35
FIGURE 2- 19. SCHEMATIC OF INKJET 3D PRINTING PROCESS STEPS: (A) INK EJECTION, (B) INK DEPOSITION, (C) INK COALESCENCE, ((D)
LAYER ADDITION. FIGURE TAKEN FROM STURGESS ⁷⁹ , REPRODUCED WITH PERMISSION OF RIGHTS HOLDER	39
FIGURE 2- 20. PRINTABLE INK REGION FOR INKJET PRINTING PROCESS BASED ON THE REYNOLDS NUMBER AND WEBER NUMBER FOR	
INK JETTABILITY EVALUATION. FIGURE TAKEN FROM DERBY ⁸¹ , REPRODUCED WITH PERMISSION OF RIGHTS HOLDER	40
FIGURE 2-21. MICROSCOPIC IMAGES OF INK DEPINNING AND COALESCENCE ISSUES, THE DESIGNED PRINTING PATTERN FOR THIS JOB	i
WAS A SQUARE. FIGURE TAKEN FROM STURGESS ²⁰ , REPRODUCED WITH PERMISSION OF RIGHTS HOLDER	41
FIGURE 2- 22. SCHEMATIC OF TWO INKJET PRINTING STRATEGIES: LAYER STRATEGY AND DOT STRATEGY. FOR LAYER STRATEGY:	
COMPLETE FILMS WERE PRINTED WITH ONE REACTANT INK FOLLOWED BY ANOTHER INK IN THE SUBSEQUENT LAYER. FOR THE	

DOT STRATEGY, HIGHER DROPLET SPACING WAS EMPLOYED TO ENSURE DROPLETS DO NOT COALESCE. FIGURE TAKEN FROM
Schuster ⁸² , reproduced with permission of rights holder
FIGURE 2- 23. SCHEMATIC OF DROPLET MIXING MODULE, WHICH ALLOWING FOR MICRO-REACTIVE INKJET PRINTING. FIGURE TAKEN
FROM ŚLIWIAK ⁸⁴ , REPRODUCED WITH PERMISSION OF RIGHTS HOLDER
FIGURE 2- 24. SCHEMATIC OF A) THERMOSET REACTIVE EXTRUSION PROCESS B) LARGE SCALE REACTIVE EXTRUSION PRINTER
DEVELOPED BY MAGNUM VENUS PRODUCTS AT OAK RIDGE NATIONAL LAB. FIGURE TAKEN FROM ROMBERG ⁸⁶ , REPRODUCED
WITH PERMISSION OF RIGHTS HOLDER
FIGURE 2- 25. A) SCHEMATIC OF A HONEYCOMB STRUCTURE WITH GRADIENT INFILL PATTERN. B) ACTUAL HONEYCOMB PRINTS USING
VINYL ESTER MATERIALS. FIGURE TAKEN FROM LINDAHL ⁸⁶ , REPRODUCED WITH PERMISSION OF RIGHTS HOLDER
FIGURE 2- 26. A) SCHEMATIC OF A BENCHTOP REX SYSTEM. B) DEMO PRINTS OF A LONGHORN LOGO FROM THE CUSTOM-BUILT REX
SYSTEM. FIGURE TAKEN FROM UITZ ⁸⁷ , REPRODUCED WITH PERMISSION OF RIGHTS HOLDER
FIGURE 2- 27. A) THE WORKFLOW OF FABRICATING BOTH 2D AND 3D FUNCTIONAL GRADIENT STRUCTURE WITH A REX SYSTEM WITH
ACTIVE MIXER, COUPLED WITH GREY SCALE MODELLING. FIGURE TAKEN FROM REN ¹⁴ , REPRODUCED WITH PERMISSION OF
RIGHTS HOLDER
FIGURE 2- 28. RHEOLOGICAL BEHAVIOUR OF DIFFERENT FILLERS (SILICA CARBIDE (SIC), FUMED SILICA (FS), NANOCLAY (NC)) ON THE
EPOXY FILLED DIW INKS. (A) VISCOSITY VS SHEAR RATE. (B) MODULI VS OSCILLATORY SHEAR STRESS. FIGURE TAKEN FROM
HMEIDAT ⁹⁶ , REPRODUCED WITH PERMISSION OF RIGHTS HOLDER
FIGURE 2- 29. SCHEMATIC OF INTERFACIAL NETWORK BETWEEN THE FUNCTIONAL SI NPS: (a) SNP, (b) SNP-NH2, (c) SNP-EP, AND
(D) SNP-C and the amine cured epoxy system. Figure taken from Guo ²⁵ , reproduced with permission of rights
HOLDER
FIGURE 2- 30. SCHEMATIC STRUCTURE OF THE DGEBA (BLACK COLOUR)/IPD (BLUE COLOUR)/AMINE FUNCTIONALIZED SI NPS
(ORANGE AND GREEN COLOUR). FIGURE TAKEN FROM BEHNIAFAR ³⁸ , REPRODUCED WITH PERMISSION OF RIGHTS HOLDER 5.
Figure 2.4 The survival area of Paul (/annual area of paul //annual //annual area of paul //annual area of paul //annual area of pau
FIGURE 3- 1.THE CHEMICAL STRUCTURE OF POLY [(PHENYL ISOCYANATE)-CO-FORMALDEHYDE]. THE MOLECULAR WEIGHT USED IN
This project was Average M_N =340, 400
FIGURE 3- 2. THE CHEMICAL STRUCTURE OF ISOPHORONE DIISOCYANATE
FIGURE 3- 3. THE CHEMICAL STRUCTURE OF DESMODUR® N3900.
FIGURE 3- 4. THE CHEMICAL STRUCTURE OF HEXAMETHYLENE DISOCYANATE

FIGURE 3-5. THE CHEMICAL STRUCTURE OF POLY (ETHYLENE GLYCOL)-BLOCK-POLY (PROPYLENE GLYCOL)-BLOCK-POLY (ETHYLENE	
GLYCOL). THE MOLECULAR WEIGHT USED IN THIS PROJECT WAS AVERAGE $M_N = 1900$	63
FIGURE 3- 6. THE CHEMICAL STRUCTURE OF 1,4-BUTANEDIOL.	64
FIGURE 3- 7. THE CHEMICAL STRUCTURE OF FUMED SILICA (FS)	64
Figure 3- 8. The chemical structure of Dibutyltin dilaurate (DBTDL).	65
FIGURE 3- 9. THE CHEMICAL STRUCTURE OF TETRAETHYL ORTHOSILICATE (TEOS)	69
Figure 3- 10. The chemical structure of Ethanol (EtOH).	69
FIGURE 3- 11. THE CHEMICAL STRUCTURE OF AMMONIA (NH40H).	70
FIGURE 3- 12. THE CHEMICAL STRUCTURE OF (3-AMINOPROPYL)TRIETHOXYSILANE (APTES).	70
FIGURE 3- 13. THE CHEMICAL STRUCTURE OF N-PROPYLTRIETHOXYSILANE (PTES).	70
FIGURE 3- 14. THE CHEMICAL STRUCTURE OF AMINE FUNCTIONAL SILICA NANOPARTICLES.	71
FIGURE 3- 15. THE CHEMICAL STRUCTURE OF AMINE/ALKYL FUNCTIONAL SILICA NANOPARTICLES.	71
FIGURE 3- 16. SYNTHESIS ROUTE FOR AMINE FSP: SIO ₂ -NH ₂ AND AMINE/ALKYL FSP: SIO ₂ -NH ₂ /CH ₃	71
FIGURE 3- 17. DAC MIXER WORKING PRINCIPLES. A) DAC MIXING CHAMBER. B) SCHEMATIC OF DUAL AXIAL MIXING INSIDE CHAM	1BER.
c) DAC mixing principles: rotation and revolution. Images from online brochure.	74
FIGURE 3- 18. SCHEMATIC OF REX WORKFLOW.	75
FIGURE 3- 19. KINEXUS PRO+ RHEOMETER (MALVERN INSTRUMENTS, NOW BRANDED AS NETZSCH). IMAGES FROM ONLINE	
BROCHURE	76
FIGURE 3- 20. A) SCHEMATIC DIAGRAM OF REX DOSING UNIT AND STATIC MIXER. B) REX SYSTEM SET UP. C) STATIC MIXER AT CLO	OSER
LOOK	80
FIGURE 3- 21. THE PREEFLOW ROTATOR/STATOR ASSEMBLY. IMAGES FROM ONLINE BROCHURE	81
FIGURE 3- 22. PREEFLOW ECO-CONTROL EC200-DUO. IMAGES FROM ONLINE BROCHURE.	81
FIGURE 3- 23. SCREENSHOT OF THE CURA LUZLBOT EDITION 3.6.20.	82
FIGURE 4- 1. RHEOLOGICAL PROPERTIES OF THE FEEDS. A) NCO FEEDS, B) OH FEEDS SHOWING STORAGE MODULUS AND LOSS	
MODULUS AS A FUNCTION OF FREQUENCY.	88
Figure 4- 2. Rheological properties of investigated NCO feeds showing a) Storage modulus as a function of	
EDECLIENCY B) LOSS MODILILIS AS A FUNCTION OF EDECLIENCY	Q۵

FIGURE 4- 3. TRANSITIONAL RHEOLOGY PROPERTIES FOR PU BLANK FORMULATIONS USING DIFFERENT ISOCYANATES SHOWING A)
STORAGE MODULUS VERSUS TIME COMPARISON BETWEEN PU BLANK FORMULATIONS, B) PMDI MN340 BLANK
FORMULATIONS, C) HDI BLANK FORMULATIONS, D) PMDI MN340 BLANK FORMULATIONS, E) N3900 BLANK FORMULATIONS,
f) IPDI BLANK FORMULATIONS
FIGURE 4- 4. TRANSITIONAL RHEOLOGY PROPERTIES FOR PMDI MN340 FORMULATIONS USING DIFFERENT LEVEL CATALYST. A)
Storage modulus (G') versus time comparison between formulations using different level of catalyst.
DYNAMIC MODULI AND TAN DELTA FOR B) PMDI MN340_1 WT. % DBTDL FORMULATION. C) PMDI MN340_0.5 WT. %
DBTDL FORMULATION. d) PMDI Mn340_1.5 wt. % DBTDL FORMULATION
FIGURE 4- 5. REACTION CONVERSION AND FT-IR SPECTRA OF INVESTIGATED PU FORMULATIONS. A) REACTION CONVERSION FOR
INVESTIGATED PU FORMULATIONS. FT-IR SPECTRA FOR ISOCYANATES, PRINTED PU FORMULATIONS AT 1MIN, 5MIN, 10MIN
AND 15MIN FOR B) HDI FORMULATION. C) PMDI MN340 FORMULATION. D) PMDI MN400 FORMULATION. E) N3900
formulation. f) IPDI formulation
FIGURE 4- 6. REACTION CONVERSION AND FT-IR SPECTRA OF PMDI MN340 FORMULATIONS WITH DIFFERENT CATALYST LEVEL. A)
REACTION CONVERSION COMPARISON BETWEEN PMDI Mn340 FORMULATIONS. B) AMPLIFIED SPECTRA OF NCO REGION FOR
PMDI Mn340 Formulations at 1 min. FT-IR spectra of PMDI Mn340 Formulations with c) 0.5 wt. % DBTDL
AND D) 1.5 WT. % DBTDL
FIGURE 4-7. AVERAGE SINGLE FILAMENT SIZES OF PMDI MN340_1 WT. % DBTDL FORMULATION PRINTING USING DIFFERENT
RATIO BETWEEN PRINT SPEED AND EXTRUSION SPEED
FIGURE 4- 8. SINGLE FILAMENT SIZE OF PMDI MN340 FORMULATION USING RATIO (R=0.5, 0.75, 1.0 AND 1.25 FOR GROUP
IMAGES A, B, C, AND D RESPECTIVELY) BETWEEN PRINT SPEED AND EXTRUSION SPEED. FIVE MEASUREMENTS AT EACH RATIO.
100
FIGURE 4- 9. FEATURE BLOCK ANALYSIS OF WOODPILE PRINTING USING PMDI MN340_1 wt. % DBTDL FORMULATION WITH
different flowrate (Q_f) . A) Woodpile design pattern. B) Woodpile design top view and schematic of block
FEATURE (W_{B1} and W_{B2} = the width of the block; W_L = Line width; D_I = Infill distance, i.e., the travel distance
BETWEEN IN-PLANE ADJACENT FILAMENTS). C) FEATURE ANALYSIS OF BLOCK WIDTH RATIO ($R(W_B) = W_{B1}/W_{B2}$) AND LINE
WIDTH RATIO (R(W_L) = W_{L1}/W_{L2}) of printings with different Q_F . D) Feature analysis of X-axis (D_{11}) and Y-axis (D_{12})
INFILL DISTANCE OF PRINTINGS WITH DIFFERENT $Q_{\scriptscriptstyle F}$.
FIGURE 4- 10. WOODPILE FEATURE BLOCK SIZE MEASUREMENTS FOR W_{B1} and W_{B2} . OF PMDI Mn340 formulation using
DIECEDENT EXTRIBICION ELONOPATES (O.). FINE MEASUREMENTS WERE TAVEN AT EACH ELONOPATE: A1 A2 A4 A5 EOR O

=1ML/MIN; B1, B2, B3, B4, B5 FOR Q_F =2ML/MIN AND C1, C2, C3, C4, C5 FOR Q_F = 3 ML/MIN. (W_{B1} AND W_{B2} : THE WIDTH
OF THE BLOCK)
FIGURE 4- 11. WOODPILE FEATURE BLOCK SIZE MEASUREMENTS FOR W_{L1} OF PMDI Mn340 FORMULATION USIN DIFFERENT
EXTRUSION FLOWRATE (Q_F). FIVE MEASUREMENTS WERE TAKEN AT EACH FLOWRATE: A1, A2, A3, A4, A5 FOR Q_F =1ML/MIN;
B1, B2, B3, B4, B5 FOR $Q_F = 2ML/MIN$ AND C1, C2, C3, C4, C5 FOR $Q_F = 3$ ML/MIN. (W _{L1} : LINE WIDTH AT X DIRECTION) 105
FIGURE 4- 12. WOODPILE FEATURE BLOCK SIZE MEASUREMENTS FOR W_{L2} OF PMDI Mn340 FORMULATION USING DIFFERENT
EXTRUSION FLOWRATE (Q_F). FIVE MEASUREMENTS WERE TAKEN AT EACH FLOWRATE: A1, A2, A3, A4, A5 FOR Q_F = 1ML/MIN;
B1, B2, B3, B4, B5 FOR $Q_F = 2ML/MIN$ AND C1, C2, C3, C4, C5 FOR $Q_F = 3$ ML/MIN. (W_{L2} : LINE WIDTH AT Y DIRECTION) 107
FIGURE 4- 13. REACTION EXOTHERM OF PMDI MN340 FORMULATION WITH 1 WT. % DBTDL AT EXTRUSION FLOWRATE (\mathbf{Qf} =1, 2
AND 3 ML/MIN)
FIGURE 4- 14. SIDE VIEW OF THE WOODPILE PRINTS OF PMDI MN340_1 WT. % DBTDL FORMULATION, USING DIFFERENT LAYER
HEIGHT (H): (A1,B1); (A2, B2); (A3, B3); (A4, B4) FOR H=0.5; 0.75; 1; 1.25 MM RESPECTIVELY. SCHEMATIC OF FLOW AT
C1) LOWER LAYER HEIGHT AND C2) OPTIMUM LAYER HEIGHT
FIGURE 4- 15. SEM IMAGES AND IMAGE THRESHOLD OF PMDI MN340_1 WT. % DBTDL FORMULATION PRINTED WOODPILE FOUR
LAYER STRUCTURES CROSS-SECTION. SEM IMAGES OF SAMPLE CROSS-SECTION FOR M1) FIRST AND THIRD LAYER MACRO VIEW.
A1) THIRD LAYER VIEW. A3) FIRST LAYER VIEW. M2) SECOND AND FOURTH LAYER MACRO VIEW. A3) FOURTH LAYER VIEW. A4)
SECOND LAYER VIEW. IMAGE THRESHOLD CREATED USING IMAGEJ OF SAMPLE CROSS-SECTION FOR B1) THIRD LAYER. B2) FIRST
LAYER. B3) FOURTH LAYER. B4) SECOND LAYER
FIGURE 4- 16. AVERAGE POROSITY FOR PRINTING STRUCTURES USING PMDI MN340_1 wt. % DBTDL FORMULATION FOR. A)
DIFFERENT LAYER POROSITY FOR FOUR LAYER WOODPILE STRUCTURES. B) FIRST LAYER POROSITY OF SINGLE FILAMENT, TWO
LAYER WOODPILE AND FOUR LAYER WOODPILE
FIGURE 4- 17. SEM IMAGES AND IMAGE THRESHOLD OF PMDI MN340_1 WT. % DBTDL FORMULATION PRINTED STRUCTURES
CROSS-SECTION. SEM IMAGES OF SAMPLE CROSS-SECTION FOR A1) SINGLE FILAMENT. A2) FIRST LAYER OF A TWO LAYER
WOODPILE PRINT. A3) FIRST LAYER OF A FOUR LAYER WOODPILE PRINT. IMAGE THRESHOLD CREATED USING IMAGEJ OF SAMPLE
CROSS-SECTION FOR B1) SINGLE FILAMENT. B2) FIRST LAYER OF A TWO LAYER WOODPILE PRINT. B3) FIRST LAYER OF A FOUR
LAYER WOODPILE PRINT. SCALE BAR = 1MM
FIGURE 4- 18. SEM IMAGES OF PRINTED WOODPILE STRUCTURE CROSS-SECTION FROM PMDI Mn340 FORMULATION WITH
CATALYST LEVEL: A1) 1 WT % DRTDL A2) 0.5 WT % DRTDL A3) 0 WT % DRTDL 115

FIGURE 4- 19. MICROSCOPIC IMAGES OF OH AND NCO INKS AFTER DIFFERENT DUAL CENTRIFUGAL MIXING (DAC) TIME PRIOR TO
LOADING TO THE REX SYSTEM
FIGURE 4- 20. MICROSCOPIC IMAGES OF OH INKS. A1) BEFORE LOADING TO THE REX SYSTEM. A2) AFTER LOADING AND REST IN THE
REX SYSTEM. NCO INKS. B1) BEFORE LOADING TO THE REX SYSTEM. B2) AFTER LOADING AND REST IN THE REX SYSTEM 11
FIGURE 4- 21. REACTION EXOTHERM OF PMDI MN340 FORMULATION WITH DIFFERENT CATALYST LEVEL: 0 WT. %, 0.5 WT. % AND
1wт. % DBTDL
FIGURE 5- 1. RHEOLOGICAL COMPARISONS BETWEEN MM1, MM2 AND MM 3. A) A SCHEMATIC OF MIXING PROCESS IN THE STATION.
MIXER FOR ALL MIXING MODES. B) A PLOT OF VISCOSITY AS A FUNCTION OF SHEAR RATE FOR ALL THE MIXING MODES. C) A PLO
OF THE VISCOSITY RATIO (OH: NCO), ELASTICITY RATIO (OH:NCO) AND PARTICLE CONTENT LOADINGS THAT RESULT IN THE
THREE MIXING MODES. D) A PLOT OF G $^\prime$ AS A FUNCTION OF FREQUENCY FOR ALL MIXING MODES
FIGURE 5- 2. RHEOLOGICAL PROPERTIES OF THE FEEDS. VISCOSITY AS A FUNCTION OF SHEAR RATE FOR A) NCO FEEDS, B) OH FEEDS.
STORAGE MODULUS AND LOSS MODULUS AS A FUNCTION OF FREQUENCY C) NCO FEEDS, D) OH FEEDS
FIGURE 5- 3. OSCILLATORY RHEOLOGY DATA OF INVESTIGATED FEEDS. A) ISOCYANATES FEEDS AND B) POLYOL FEEDS
FIGURE 5- 4. FT-IR SPECTRA OF SAMPLES AFTER PRINTING AT 1 MIN (DASH LINE) AND 10 MIN (SOLID LINE) FROM THREE MIXING
MODES, SCHEMATIC OF HYDROGEN BONDS WITHIN THE PU STRUCTURE. A) FT-IR SPECTRA OF PMDI M _N 340, PU SAMPLES
PRINTED FROM MM1, MM2 AND MM3. AMPLIFIED SPECTRA OF B) FREE AND HYDROGEN BONDED CARBONYL PEAKS (C=O)
13
Figure 5- 5. FT-IR spectra of PMDI M_N 340, PU samples printed from MM1, MM2 and MM3. A) Amplified spectra of
ISOCYANATE PEAK (-NCO). B) SCHEMATIC OF HARD SEGMENT, SOFT SEGMENT AND HYDROGEN BOND WITHIN THE PRINTED P
STRUCTURE AND AGGREGATED HYDROGEN BONDED URETHANE CARBONYL GROUP (C=O)
FIGURE 5- 6. A) TGA MASS LOSS AND B) DIFFERENTIAL THERMOGRAVIMETRIC (DTG) ANALYSIS THERMOGRAMS OF PU SAMPLES
PRINTED FROM THREE MIXING MODES
FIGURE 5- 7. DSC CURVES OF PU SAMPLES PRINTED FROM THREE MIXING MODES
FIGURE 5- 8. REACTION EXOTHERM FOR PU SAMPLES PRINTED FROM MMS
FIGURE 5- 9. DMA TEMPERATURE SCAN OF PU SAMPLES FROM THREE MIXING MODES. A) STORAGE MODULUS. B) TAN DELTA 13
FIGURE 5- 10. WOODPILE FEATURE BLOCKS PRINTED USING INVESTIGATED PU FORMULATION MM1. A) DESIGN PATTERN. B) FRONT
VIEW AND C) TOP-VIEW OF THE PRINTED STRUCTURE. D) MICROSCOPIC IMAGES OF THE PRINTED STRUCTURE

Figure 5- 11.Woodpile feature block size measurements. A-1, A-2, A-3: Three separate measurements of W_{B1} and W_{B2} .
B-1, B-2 AND B-3: THREE SEPARATE MEASUREMENTS OF W_L . (W_{B1} AND W_{B2} : THE WIDTH OF THE BLOCK; W_L : LINE WIDTH; D_l :
Infill distance)
FIGURE 5- 12. SCHEMATIC OF BLOCK FEATURE (W_{B1} and W_{B2} = the width of the block; W_L - Line width; D_I = Infill distance,
I.E. THE TRAVEL DISTANCE BETWEEN IN-PLANE ADJACENT FILAMENTS)
FIGURE 6- 1. SCHEMATIC DIAGRAM OF HOW ISOCYANATE AND POLYOL WERE PROCESSED USING REX 3D PRINTING TO FORM PU. THE
CHEMICAL STRUCTURE OF ISOCYANATES AND POLYOL USED IN THE STUDY AND GENERAL PU REACTION SCHEME ARE PRESENTED
THE COVALENT BONDING FORMED BETWEEN THE FSP AND THE PU NETWORK IS ILLUSTRATED
FIGURE 6- 2. PARTICLE CHARACTERISATIONS. A) TGA THERMOGRAMS AND B) FT-IR SPECTRA OF SILICA PARTICLES (SIO ₂ , SIO ₂ -NH ₂
AND THREE VARIANTS OF SIO ₂ -NH ₂ /CH ₃)
FIGURE 6-3. FULL FT-IR SPECTRA OF SIO ₂ AND SYNTHESISED SIO ₂ -NH ₂ /CH ₃ (01, 02 AND 03)
FIGURE 6- 4. FT-IR SPECTRA OF PARTICLES (SIO ₂ , SIO ₂ -NH ₂ AND SIO ₂ -NH ₂ /CH ₃). A) N-H AND B) C-H REGION OF SIO ₂ VS SIO ₂ -
$NH_2\text{VS}SIO_2-NH_2/CH_3.C)N-H\text{AND}D)C-H\text{REGION}\text{OF}SIO_2\text{VS}SIO_2-NH_2/CH_3-01\text{VS}SIO_2-NH_2/CH_3-02\text{VS}SIO_2-NH_2/CH_2/CH_2/CH_2/CH_2/CH_2/CH_2/CH_2/C$
NH ₂ /CH ₃ -03
FIGURE 6-5. TEM IMAGES OF THE DIFFERENT SILICA NANOPARTICLES. A) SIO ₂ -PDMS, B) SIO ₂ -NH ₂ AND C) SIO ₂ -NH ₂ /CH ₃ -O3.
152
FIGURE 6- 6. OPTICAL MICROSCOPY IMAGES OF OH FEEDS WITH DIFFERENT SILICA NANOPARTICLES. A) SIO ₂ -PDMS, B) SIO ₂ -NH ₂
AND C) SIO ₂ -NH ₂ /CH ₃ -03
FIGURE 6-7. TEM IMAGES OF DIFFERENT AMINE/ALKYL FSPS. A) SIO ₂ -NH ₂ /CH ₃ -01. B) SIO ₂ -NH ₂ /CH ₃ -02. C) SIO ₂ -NH ₂ /CH ₃ -
03
FIGURE 6-8. MICROSCOPIC IMAGES OF OH INKS USING DIFFERENT AMINE/ALKYL FSPS. A) SIO ₂ -NH ₂ /CH ₃ -O1. B) SIO ₂ -NH ₂ /CH ₃ -
02. c) SiO ₂ -NH ₂ /CH ₃ -03
FIGURE 6- 9. RHEOLOGICAL PROPERTIES OF THE OH FEEDS WITH THREE DIFFERENT SILICA PARTICLES (SIO ₂ -PDMS, SIO ₂ -NH ₂ AND
SiO_2 -NH ₂ /CH ₃ -O3). A) Viscosity as a function of shear rate, B) Storage modulus and loss modulus as a
FUNCTION OF FREQUENCY

FIGURE 6- 10. RHEOLOGICAL COMPARISONS BETWEEN THREE INVESTIGATED FORMULATIONS IN TERMS OF MIXING MODES (MMs). A)
A PLOT OF VISCOSITY AS A FUNCTION OF SHEAR RATE FOR ALL FORMULATIONS. B) A PLOT OF ${\sf G}^{\prime}$ AS A FUNCTION OF
FREQUENCY FOR ALL MIXING MODES
FIGURE 6- 11. RHEOLOGICAL PROPERTIES OF THE OH FEEDS WITH FUNCTIONAL SILICA PARTICLES (THREE VERSIONS OF SIO ₂ -
NH_2/CH_3). A) VISCOSITY AS A FUNCTION OF SHEAR RATE. B) STORAGE MODULUS AND LOSS MODULUS AS A FUNCTION OF
FREQUENCY
FIGURE 6- 12. OSCILLATORY RHEOLOGY DATA OF -OH FEEDS. A) OH FEEDS WITH FSP (THREE VERSION OF SIO ₂ -NH ₂ /CH ₃), B) -OH
FEEDS WITH THREE DIFFERENT SILICA PARTICLES (SIO ₂ -PDMS, SIO ₂ -NH ₂ AND SIO ₂ -NH ₂ /CH ₃ -O3)
FIGURE 6-13. FTIR SPECTRA OF PMDI MN340, PU SAMPLES USING THREE DIFFERENT SILICA PARTICLES (SIO2-PDMS, SIO2-NH2
AND SIO2-NH2/CH3-03) AFTER PRINTING AT 1 MINUTE (DASH LINE) AND 10 MINUTES (SOLID LINE)
FIGURE 6- 14. FT-IR SPECTRUM OF PMDI MN340 AND POLYURETHANE SAMPLES PRINTED FROM FORMULATIONS WITH (SIO ₂ -
PDMS, SIO ₂ -NH ₂ AND SIO ₂ -NH ₂ /CH ₃). A) C=O CARBONYL REGION. AMPLIFIED C=O REGION FOR SAMPLES PRINTED FROM
B) SIO ₂ -PDMS. c) SIO ₂ -NH ₂ . D) SIO ₂ -NH ₂ /CH ₃
FIGURE 6- 15. FT-IR SPECTRUM OF PMDI Mn340 and polyurethane samples printed from formulations with (SiO_2 -
PDMS, SIO ₂ -NH ₂ AND SIO ₂ -NH ₂ /CH ₃). A) H-BONDED N-H STRETCHING. B) AMIDE III PEAK (C-N STRETCHING AND N-H
BENDING)
FIGURE 6- 16. A) TGA CURVES AND B) DIFFERENTIAL THERMOGRAVIMETRIC (DTG) ANALYSIS CURVES OF PU SAMPLES PRINTED USING
THREE DIFFERENT SILICA PARTICLES (SIO ₂ -PDMS, SIO ₂ -NH ₂ AND SIO ₂ -NH ₂ /CH ₃ -O3)
FIGURE 6- 17. DSC CURVES OF PU SAMPLES PRINTED USING THREE DIFFERENT SILICA PARTICLES (SIO ₂ -PDMS, SIO ₂ -NH ₂ AND SIO ₂ -
NH ₂ /CH ₃ -03)
FIGURE 6- 18. DMA TEMPERATURE SCAN OF PU SAMPLES USING THREE DIFFERENT SILICA PARTICLES (SIO ₂ -PDMS, SIO ₂ -NH ₂ AND
S ₁ O ₂ -NH ₂ /CH ₃ -03)
FIGURE 6- 19. SINGLE FILAMENT PROFILE UNDER MICROSCOPE. A) SIO ₂ -PDMS, B) SIO ₂ -NH ₂ AND C) SIO ₂ -NH ₂ /CH ₃ -O3167

List of Tables

Table 3- 1. Mass composition of feed formulations use in printability analysis.	65
Table 3-2. Mass composition of PMDI Mn340 formulation with 0.5 wt. % and 1.5 wt. % DBTDL for printability	
ANALYSIS.	66
Table 3-3. Mass composition of PMDI Mn340 formulation for process optimisation.	66
TABLE 3-4. MASS COMPOSITION OF FEED FORMULATIONS FOR THREE MIXING MODES (MM1, MM2 AND MM3)	67
TABLE 3-5. MASS COMPOSITION OF FEED FORMULATIONS USING DIFFERENT SILICA NANOPARTICLES.	68
Table 3-6. The quantities of silica coupling agents used in the synthetic procedures to produce the functionalised	D
SiNPs	72
Table 3- 7. Printing parameters used for bar samples/woodpile feature samples	83
Table 4- 1. Storage modulus data of the formulations obtained from transitional rheology test	92
Table 4-2. Storage modulus data of the PMDI Mn340 formulations with 0.5 wt. %, 1 wt. % and 1.5 wt. % DBTD	DL,
OBTAINED FROM TRANSITIONAL RHEOLOGY TEST.	94
Table 4-3. Reaction kinetics of investigated formulations.	96
Table 4-4. The woodpile feature block calculated percentage deviation of width block ratio $R(W_B)$ and line block	K
RATIO R(W _L) FOR PMDI MN340_1 WT. % DBTDL FORMULATIONS PRINTING USING DIFFERENT FLOWRATE	108
Table 4-5. The woodpile feature block calculated percentage deviation of X-axis (D_{11}) and Y-axis (D_{12}) infill distant	NCE
FOR PMDI Mn340_1 wt. % DBTDL FORMULATIONS PRINTING USING DIFFERENT FLOWRATE.	109
Table 4- 6. Reaction exotherm of PMDI Mn340 formulation with 1 wt. % DBTDL at extrusion flowrate ($f Qf$ =1, 2	<u>.</u>
AND 3 ML/MIN)	110
Table 4-7. Reaction exotherm for PMDI Mn340 formulation printed using different catalyst level. T_1 and T_2 are	THE
SAMPLE TEMPERATURE AT T1 AND T2 RESPECTIVELY, WHEREAS T1 AND T2 ARE THE STARTING POINT WHEN THE TEMPERATUR	RE
INCREASED AND THE TIME WHEN PEAK TEMPERATURE WAS REACHED, RESPECTIVELY. THE DOTTED LINE DEFINED THE RANGE	Ē
BETWEEN T ₁ AND T ₂	119
TABLE 5-1 VIELD STRESS OF THE INKS ORTAINED FROM OSCILLATORY RHEOLOGY TEST	131

List of Tables

TABLE 5- 2. REACTION CONVERSION OF POLYURETHANE SAMPLES PRINTED UTILISING MM1, MM2 AND MM3 AT 1 MIN AND 10
MIN
Table 5- 3. Thermal properties of PU samples printed from MM1, MM2 and MM3. T _{5%} : Temperature at 5% weight
LOSS OBTAINED FROM TGA MASS LOSS THERMOGRAM. DTG (I) $_{\text{MAX}}$ and DTG(II) $_{\text{MAX}}$: Lower and higher peak temperature
IN THE DTG THEROMOGRAM, RESPECTIVELY
Table 5- 4. Reaction exotherm for PU samples printed from MMs. T_1 and T_2 are the sample temperature at T_1 and T_2
RESPECTIVELY, WHEREAS T ₁ AND T ₂ ARE THE STARTING POINT WHEN THE TEMPERATURE INCREASED AND THE TIME WHEN PEAK
TEMPERATURE WAS REACHED, RESPECTIVELY. THE DOTTED LINE DEFINED THE RANGE BETWEEN T_1 AND T_2
Table 5- 5. Block feature size measurements. 140
TABLE 5- 6. THE WOODPILE FEATURE BLOCK CALCULATED PERCENTAGE DEVIATION OF THE FEATURE
TABLE 6- 1. WEIGHT LOSS DATA OF SIO ₂ , SIO ₂ -NH ₂ AND SIO ₂ -NH ₂ /CH ₃ OBTAINED FROM TGA
TABLE 6- 2. SUMMARY OF THE RESULTS OF THE ELEMENTARY ANALYSIS OF SIO ₂ -NH ₂ /CH ₃ PARTICLES
TABLE 6-3. VISCOSITY RATIO (OH: NCO) AND STORAGE MODULUS RATIO (OH: NCO) COMPARISON BETWEEN THE THREE
INVESTIGATED FORMULATIONS
TABLE 6- 4. YIELD STRESS OF THE INKS OBTAINED FROM OSCILLATORY RHEOLOGY TEST
TABLE 6- 5. REACTION CONVERSION OF PU SAMPLES USING THREE DIFFERENT SILICA PARTICLES (SIO ₂ -PDMS, SIO ₂ -NH ₂ AND SIO ₂ -
NH_2/CH_3 -03) at 1 minute and 10 minutes.
Table 6- 6. Peak data obtained from Perkin Elmer Spectrum for isocyanate and reference peak at different reaction
TIMES
TABLE 6- 7. DTG ANALYSIS CURVES OF PU SAMPLES PRINTED USING THREE DIFFERENT SILICA PARTICLES (SIO ₂ -PDMS, SIO ₂ -NH ₂
AND SIO ₂ -NH ₂ /CH ₃ -03). T _{5%} : Temperature at 5% weight loss obtained from TGA graph. DTG (I)max and DTG
(II)MAX: LOWER AND HIGHER PEAK TEMPERATURE IN THE DTG CURVE, RESPECTIVELY

CHAPTER ONE

1 Introduction

1.1 Background

Additive manufacturing (AM), also known as 3D printing, is a broad descriptor for a range of techniques that build structures layer by layer *via* translation from 3D computer-aided design (CAD) models. AM techniques have great benefits in fabricating complex, personalised and multi-functional structures in comparison with conventional manufacturing methods. Meanwhile, polyurethane (PU) polymers are one of the most versatile materials currently in commercial use. This is because they combine domains of the rubbery nature, due to the presence of an elastomeric segment within the polymers molecular structure, with rigid plasticity domains imparted by the "hard" di-isocyanate segment^{2,3}. Additionally, their mechanical properties can be tuned by modifying the chemical structure of both the hard and soft segments to meet specific application needs. Consequently, they are applied in a great number of applications in different end-use fields, such as; foams ⁴, coatings ⁵, adhesives ⁶, and biomedical devices ⁷.

There is an increasing demand in many application areas for greater levels of customisation/personalisation of products, and AM has shown great potential to enable increased flexibility in the fabrication of PU products. To date, the use of PU materials in AM has centred on the application of commercially available synthesised powders, filaments or resins as feedstocks for various AM techniques, such as vat photopolymerisation, powder bed fusion, and material extrusion ^{8–11}. For example, thermoplastic PU powders were processed using powder bed

fusion to fabricate a very specifically designed soft auxetic lattice structure for use in energy absorption and mechanical damping applications, which was demonstrated to withstand a wide range of compression strain ¹⁰. Also, thermoplastic PU filaments were used to print a flexible cellular structure containing a density gradient for repeated energy absorption *via* material extrusion AM ^{11,12}. Additionally, biomedical PU implants with tuneable drug release rates have also been fabricated *via* direct ink writing from a thermo-responsive supramolecular PU that had been pre-synthesised ⁷. Thus, using pre-synthesised PU feedstock for fabrication has an advantage in the ease to processing. However, it also limits the capability of selectively tailoring the material properties that can be offered by *in situ* chemical reaction of PU.

An alternative approach to existing techniques for processing PU is reactive AM, whereby an *in situ* reaction takes place during the process of forming the 3D structure ¹³. As an evolving AM technology, reactive 3D printing has gained great attention for producing devices *via* an in-line mixer using two-component curing PU ¹⁴⁻¹⁶, or reactive silicone formulations ^{17,18}. Meanwhile, reactive ink jetting has also be employed to fabricate PU or poly(dimethyl siloxane) (PDMS) *via in-situ* reaction without "pre-mixing" of the ink components prior to printing ^{19,20}. For example, a micro-sized PU structure was successfully printed by jetting inks from two separate print heads such that they successively mixed after jetting. One ink consisted of isophorone diisocyanate, and the other comprised polypropylene glycol, a catalyst, and a cross-linking agent. This reactive material jetting approach also demonstrated the capabilities of producing PU structure containing a mechanical gradient by adjusting the stoichiometric ratio of reactants during processing ¹⁹. However, due to the nature of material jetting processes, the use of solvent was typically necessary for successful material jetting, to improve the printability of the inks i.e. to lower their viscosity. This was problematic as solvent evaporation could result in structural shrinkage ^{13,19}. Thus, there is significant restriction on the number and

type of materials that can be used based on the viscosity and surface tension constraints this process places on the inks ²¹.

Reactive extrusion (REX) offers advantages over reactive jetting process, as it enables both a broader material selection and the capability of printing relatively large structures. REX is a relatively recently AM route, in which reactive materials are mixed and start to react and/or crosslink upon deposition in an ambient environment ¹. This printing process has been reported to deliver; (a) improved interlayer adhesion through the creation of *in-situ* crosslinking between layers, (b) reduced thermal distortion during printing and (c) offered the potential for high printing speed by capitalising on fast reaction kinetics ²². Furthermore, a product's material properties can be tailored using REX by varying the ratio of the reactive feeds. For example, a printed reactive formulation has been reported to show a higher work-to-failure in contrast to an analogous casted sample from the same formulation ²². Due to the nature of in situ polymerisation, the success of REX was driven by the achieving a good balance between the ink rheology properties and the reaction kinetics of the ink components. However, whilst the feed rheology is recognised as one of the crucial parameters for REX processes determining mixing homogeneity and degree of reaction the link between these properties and the final material properties, the link between these properties has not been systematically investigated to date ^{22,23}. Thus, to achieve the desirable material properties, feed with appropriate rheological characteristics need to be identified and the methods for successfully applying them developed. This can be attained by incorporation of nanoparticles as rheology filler.

Nanoparticles have been widely employed as reinforcing fillers in polymer composite systems. There have been a number of reports of nanoparticles, such as silica, carbon nanotubes, clays, silicon carbide (SiC), being introduced to polymeric systems to enhance the flow, processability and material thermo-mechanical properties ^{24–29}. Silica nanocomposite systems

have received considerable attention, owing to their: (a) ease of synthesis and functionalisation and (b) high specific surface area which provides a larger interface between the particle and the matrix ³⁰.

Consequently, these reported benefits of including silica nanoparticles (SiO₂) as reinforcing fillers have led to their applications in additive manufacturing (AM) of nanocomposites. For example, the inclusion of SiO₂ into vat photopolymerisation resins for stereolithography (SLA) 3D printing processing was reported to increase the curing rate and improve the product tensile / compressive strength ^{31–33}. Similarly, when dispersed uniformly in Nylon-12 powders via a dissolution-precipitation process, SiO₂ were shown to successfully reinforce composite images generated by SLA 3DP ³⁴ with improved tensile strength, impact strength and thermal stability. SiO₂ have also been introduced in material extrusion AM processing to act as rheology modifiers, to tailor the ink viscoelastic properties and printability ^{15,23,35}. The advantages of SiO₂ reinforced composites have been attributed to physical interactions/entanglements being established between the particles and the particles/matrix. There are also potential benefits offered by SiO₂ that act as a reactive filler, such that covalent bonds with the polymer matrix are established in the composite. These covalent linkages should augment the typical physical interactions, such as hydrogen bonding, that are responsible for the matrix to filler interactions within the current systems.

This concept of utilising SiO₂ as reactive fillers to promote the reinforcement performance has been investigated in silica/epoxy and silica/polyurethane (PU) composites via traditional synthetic routes ^{25,36}. In such systems, organo-functional groups were grafted onto the SiO₂ surface through the use of silane coupling agents, e.g. 3-aminopropyltriethoxysilane and/or 3-

glycidyloxypropyltrimethoxysilane, to create functional silica nanoparticles (FSP). These FSPs were subsequently loaded into the polymer matrix as reactive fillers, to strengthen the particle/matrix interface interactions via covalent bonding ^{25,37}. Amine FSPs have been used as a co-hardener with the multiple amine groups on the particle surface reacting with epoxy or isocyanate polymer matrices to form the desired covalent particle-matrix bonds and thus provide enhanced mechanical properties ^{38,39}. However, whilst there are clear benefits observed in polymer composite system reinforced by FSPs, to date the implementation of FSPs as reactive fillers in AM produced nanocomposites has yet to be reported.

In this project, the utilisation of reactive FSPs in reinforcing polyurethane system printed via REX was reported. Two types of amine based FSPs were synthesised to show their potential as reactive fillers which could enhance polyurethane material properties through a hybrid reinforcing effect combining both physical and covalent crosslink network. Both the amine FSPs (SiO₂-NH₂ and SiO₂-NH₂/CH₃) and the commercial fumed silica (SiO₂-PDMS) parties were then incorporated into 3D printing PU composites via REX. The effect of different functional groups on the dispersion of particles in matrix, feed rheology properties and thermomechanical properties of printed PU are described and the concept of utilising FSPs as reactive fillers to strengthen AM nanocomposites was demonstrated.

1.2 Aim of Research

The aim of this project is to systematically study processing polyurethane (PU) *via* the reactive extrusion 3D Printing (REX) system.

The following objectives were outlined for this project:

- Develop the understanding of the REX system
 - Standardise a workflow for reactive formulation screening and printing process optimisaitons
 - A fast-curing PU formulation is printed and identified as optimal REX formulation
- Understand the effect of non-reactive rheological filler in REX system
 - Correlation between the dual-feed rheology on the mixing, and product properties from REX system is shown
- Understand the effect of reactive filler in REX system
 - Reinforcing the PU matrix with dual network (both particle entanglements and covalent bonding) when reactive filler is applied

1.3 Research Methodology

PU formulations with different isocyanate feeds, catalyst level were explored. Feed rheology and reaction kinetics were identified as the key characterisations required for printability screening. A fast-curing PU formulation was screened out as optimal REX formulation. The fast-curing PU was applied for the printing process optimisation. This helped to produce the first standard workflow for printability analysis and process optimisation of REX system.

Once the standard workflow was established, following work investigated the effect of non-reactive rheological filler on the REX system. Three PU formulations with same dual feed materials, presenting distinctive rheological properties were printed and characterised. The effect of the non-reactive rheological filler on the feed rheology, reaction kinetics, mixing, and printing products' thermo-mechanical properties were highlighted. A correlation between the dual feed rheology to the proposed mixing modes, and final part properties was addressed.

With these understanding of the importance of feed rheology properties in the REX system, subsequent studies uncovered the effect of reactive rheological filler on the REX system. Here, two types of functional silica nanoparticles (FSPs) were synthesised in-house and applied as reactive rheological filler in AM PU *via* REX system. The differences between the non-reactive filler (fumed silica) and the reactive filler (FSPs) in the REX system was outlined, by characterising the reaction kinetics, thermo-mechanical properties of the AM PU products. The concept of reactive filler in reinforcing PU network with hybrid network was demonstrated in the chemical characterisation.

1.3.1 Statement of Novelty

This research demonstrates novelty in the following areas:

- 1. Established a formulation printability screening methodology for REX system
- 2. Established a standard workflow for REX printing process optimisation
- 3. Printed and characterised fast curing PU formulations using REX system
- 4. Proposed and investigated three mixing modes (MMs) between the isocyanate and polyol feeds in AM PU *via* REX system
- 5. Demonstrated the effect of different feed rheological properties on the AM product properties *via* REX system
- 6. Synthesised two functional silica nanoparticles (FSP): Amine-functionalised silica nanoparticles and Amine/alkyl functionalised silica nanoparticles
- 7. Demonstrated the use of FSPs as reactive filler in AM PU via REX system
- 8. Demonstrated the concept of use of FSPs in reinforcing the AM products through dual network (both physical entanglements and intramolecular bonding)

1.4 Structure of Thesis

The thesis presented the fundamental study of REX system and is structured into three results chapters: Printability Analysis and Process Optimisation, Effect of Dual-feed Rheology on AM PU, FSP as Reactive Fillers on AM dual-network PU.

The workflow of the research is shown in Figure 1- 1. The research started by establishing a baseline understanding on how to screen fast curing PU formulations and optimised the printing quality for REX system. Then, three distinct mixing modes during the AM PU *via* REX were created. The dependence of the feed rheology on the AM PU qualities were highlighted. Finally, FSPs were manufactured in-house and used as reactive filler in AM PU *via* REX. The concept of reactive filler to provide dual reinforcing network was demonstrated.

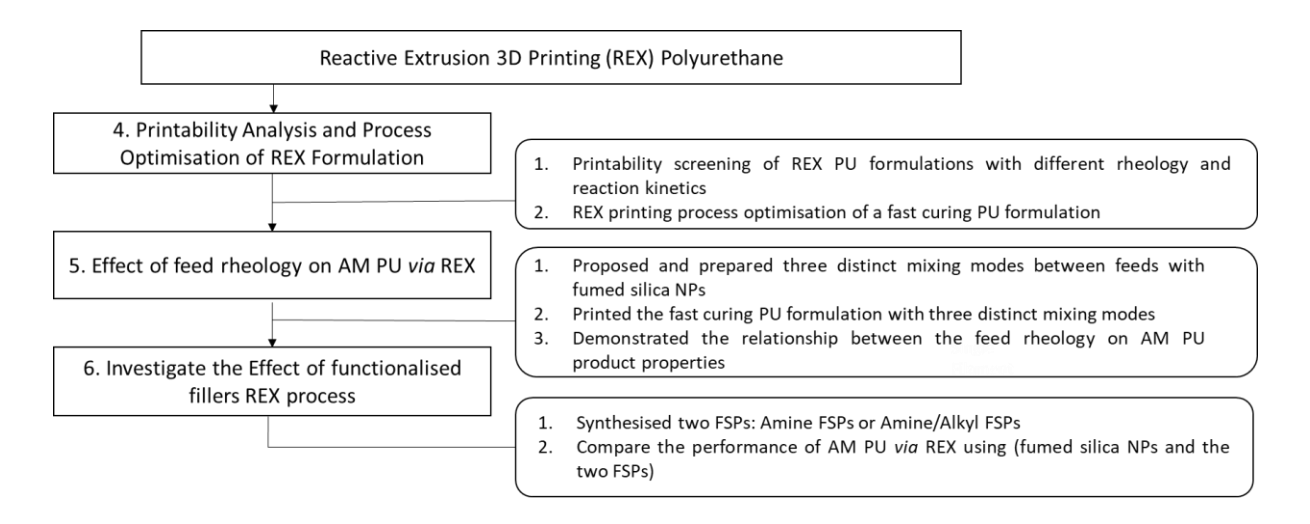


Figure 1-1. Workflow showing the process of research.

1.4.1 Thesis chapters

A description of the content of each chapter in the thesis is discussed below:

Chapter 2: Literature Review starts with a review of the relevant PU chemistry studies and conventional manufacturing techniques. The literatures of producing PU via AM are reviewed and are split into two main routes: staring from pre-synthesised PU feed or in-situ reactive 3D Printing. The relevant studies of in-situ reactive 3D Printing of PU are then reviewed in detail,

fall into two categories: reactive ink-jetting and reactive extrusion. Finally, the review of applications of silica NP and FSP as reinforcing filler in material matrix are presented.

Chapter 3: Materials and Methods shows all the materials and formulation investigated in the research. The methodology part details all the steps involving in the study, from feed preparation/FSP synthesis and characterisations, printability analysis of feed formulations based on rheology and reaction kinetics characterisations, printing PU formulations via REX. A detailed description of the REX system is presented. Finally, characterisation of the thermomechanical properties and dimensional accuracy of printed PU products are discussed.

Chapter 4: Investigation the Workflow for Printability Screening and Printing Optimisation of Fast Curing Polyurethane Formulations via Reactive Extrusion 3D Printing presents the work related to establish a standard workflow for printability analysis and process optimisation for any reactive formulations fabricated via REX system. It established the framework for future REX explorations to follow. It highlighted the importance of transitional rheology characterisation of the feeds, as it offers insight on the printability of reactive formulations. It also identified a fast-curing PU formulation suitable for REX (i.e. Poly [(phenyl isocyanate)-co-formaldehyde] (PMDI Mn340)). PMDI Mn340 formulation was subsequently used for both Chapter 5 and Chapter 6 study.

Chapter 5: Investigation the Effects of Feed Rheology on the Three Types of Mixing Modes and Printed Polyurethane Properties demonstrates a systematic understanding between the feed rheological properties and final product properties printed via REX system. This was gained through programmably design, print, and characterise the three PMDI Mn340 formulations with distinct rheological properties. A strong correlation between feed rheological properties to the proposed mixing modes, and the final product properties is presented.

Chapter 6: Investigation the Reinforcing Effect from Amine-based Functional Silica Nanoparticles on the Printed Polyurethane Crosslink Network presents the concept of using FSPs as reactive fillers in AM PU via REX system. The reinforcing effect of Si NPs in the PU matrix is compared between using non-reactive fumed silica, and the two types of in-house synthesised FSPs (i.e., Amine or amine/alkyl functionalised FSPs). The dual reinforcing network is attained when FSPs are used. The effect of alkyl functional groups on the silica particles surface to improve the particle dispersion in the matrix is highlighted.

Chapter 7: Conclusions and Future Work summarise the main findings of this research and discuss the novelty of these findings from the projects. It also highlights areas where this project has not been able to fully explore and propose the way it can be carried out.

CHAPTER TWO

2 Literature Review

2.1 Introduction

The project is to fundamentally understand the reactive extrusion 3D printing (REX) process in producing cross-linked polyurethane (PU).

The literatures were reviewed in the creation of PU, by the means of conventional route and *via* additive manufacturing (AM) technologies. The review specifically focuses on the process benefits offered by *in-situ* reactive AM. Thus, the advantages of REX over other AM technologies can be highlighted. The workflow structure for the literature review is shown in Figure 2-1.

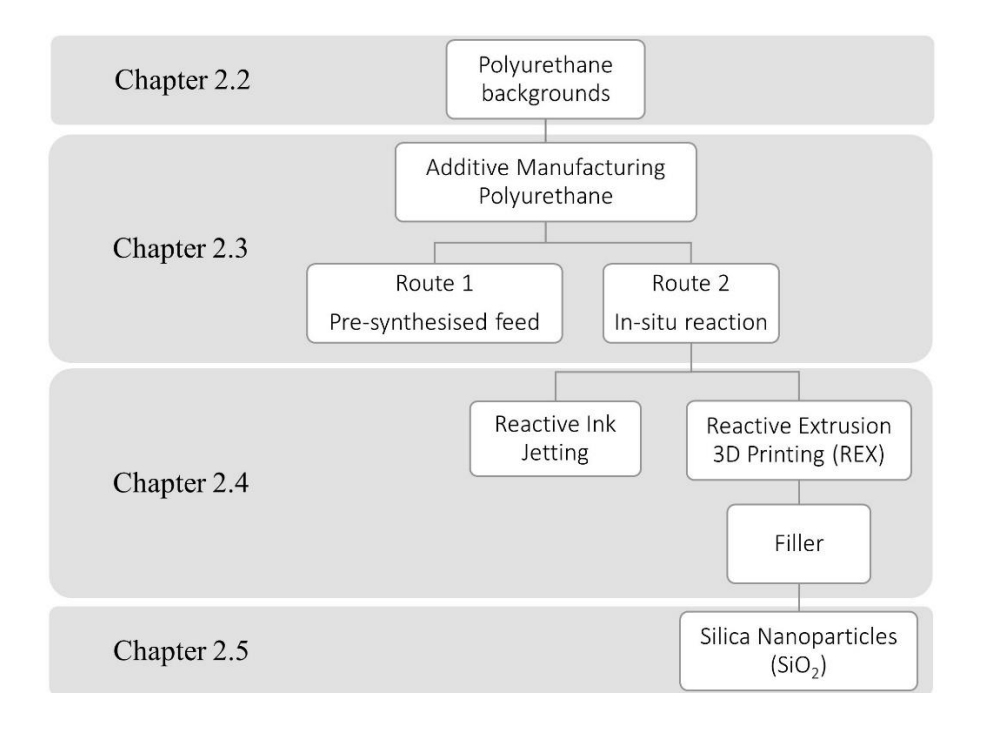


Figure 2-1. Literature review workflow structure.

The review comprises four sections: (1) polyurethane backgrounds; (2) additive manufacturing polyurethane; (3) reactive extrusion 3D printing polyurethane and (4) Silica nanoparticles as

reinforcing filler. In the first section, the backgrounds associated with PU manufacturing are briefly discussed, including chemistry and conventional process employed. Next, PU fabrication *via* AM technologies are categorised into two routes (i.e. route 1: start from presynthesised PU feedstock; route 2: leverage the *in-situ* reaction). The available literatures associated with each route are reviewed in detail, to highlight the advantages of route 2: *In-situ* reactive AM. Afterwards, all the existing studies in discussing AM PU *via* REX are discussed. Focus was devoted in revealing the effect of fillers in AM PU *via* REX. Finally, studies showing silica nanoparticles as reinforcing filler are reviewed, to highlight the potential of it being leveraged as reactive filler to create the dual-reinforcing network in the PU system. The gaps remained in the current research will be reviewed.

2.2 Polyurethane Backgrounds

Polyurethane (PU) is a class of polymer which has the urethane bond (–NHCOO–) in the chain. It is one of the most versatile group of polymer, which can be thermoset or thermoplastic depending on the chemistries used for synthesis. With both the elasticity of rubber and durability, toughness of metal, they could be applied to a range of industries, such as automobile, construction and biomedical.

PU was firstly discovered by Dr Otto Bayer in 1937, he pioneered the polyaddition reaction between the polyisocyanate and polyol to synthesis PU ⁴⁰. It was first developed as a substitute for rubber. Early formulation studies were carried out to synthesis PU for specific application. For instance, PUs were used as chemical resistant coating for wood and metal. Besides application in coatings, PUs were later found commonly used as elastomers, rigid foams and adhesives by mid 1950s. Flexible PU foams were later developed to produce furniture cushions, car interior components such as molded foam seats and cushion instrument panel. Since then, PU has become one of the most researched material in the world due to their superior properties, including hardness, strength and lightweight compared to metals ^{2 41}.

2.2.1 Chemistry

Reaction Mechanism

The poly-addition PU reaction is a step growth polymerisation. The isocyanate functional group (–N=C=O) has high reactivity as a result from the presence of two cumulated double bond ⁴². The general reaction scheme is illustrated as in **Figure 2-2**, where by nucleophilic centre of the hydroxyl group is added to the electrophilic carbon atom in the isocyanate. Because a large electrophilic character is presented to the centre carbon atom imparted by the electronegativity of nitrogen and oxygen ⁴¹.

$$R^{\frac{1}{N}} = C = O + HO - R^{2} \longrightarrow \begin{bmatrix} R^{\frac{1}{N}} - N = C - O^{-} & R^{\frac{1}{N}} - C = O \\ H - O^{\frac{1}{N}} - R^{2} & H - O^{\frac{1}{N}} - R^{2} \end{bmatrix} \longrightarrow R^{\frac{1}{N}} - C = O$$
Isocyanate alcohol

Figure 2-2. General polyurethane reaction mechanism.

Other common reactions could also happen between isocyanates and other reagents, apart from the one with hydroxyl group (-OH) as shown in Figure 2-3. The isocyanate group could react with thiol, amine to form thiourethane or urea respectively. It can also react with water to form unstable carbamic acid, and further form primary amine and carbon dioxide via decomposition. This reaction is commonly used for producing PU foams or moisture-curing coatings.

a.
$$R^{1}-N=C=O$$
 + $R^{2}-OH$ \longrightarrow $R^{1}-N$ $O-R^{2}$

b. $R^{1}-N=C=O$ + $R^{2}-SH$ \longrightarrow $R^{1}-N$ $S-R^{2}$

c. $R^{1}-N=C=O$ + R^{2} NH \longrightarrow $R^{1}-N$ $N-R^{2}$ R^{3}

d. $R^{1}-N=C=O$ + $H_{2}O$ \longrightarrow $R^{1}-N$ $O-H$ \longrightarrow $R^{1}-NH_{2}$ + CO_{2}

Figure 2- 3. Common addition reactions between isocyanates and compounds with reactive hydrogen. a) Alcohol. b)

Thiol. c) Amine. d) Water. Figure taken from Delebecq⁴³, reproduced with permission of rights holder.

PU can be either thermoplastic or thermoset, depending on the synthesis route and the formulations used. Thermoset PU is obtained when reactants have multi-functional groups (number of functional groups: f>2), and crosslinking occurs during the reaction. Thermoplastic PU is segmented block copolymer, formed by reactants have di-functional group (f=2)³. Thermoplastic PU is synthesised when chain extender added into the reaction. CEs are usually low molecular weight hydroxyl or amine groups ended compounds. They contribute the hydrogen bonding and improve the overall mechanical properties by increasing the molecular weight of PUs. Chain extenders react with di-isocyanate to form the hard segment, and the long chain alcohol forms the soft segment. These rigid hard segments and flexible soft segments are connected by covalent links, and hydrogen bonds are presented in between the hard segments (more specifically between the –NH groups and C=O groups in the urethane chain)⁴² as shown in Figure 2- 4.

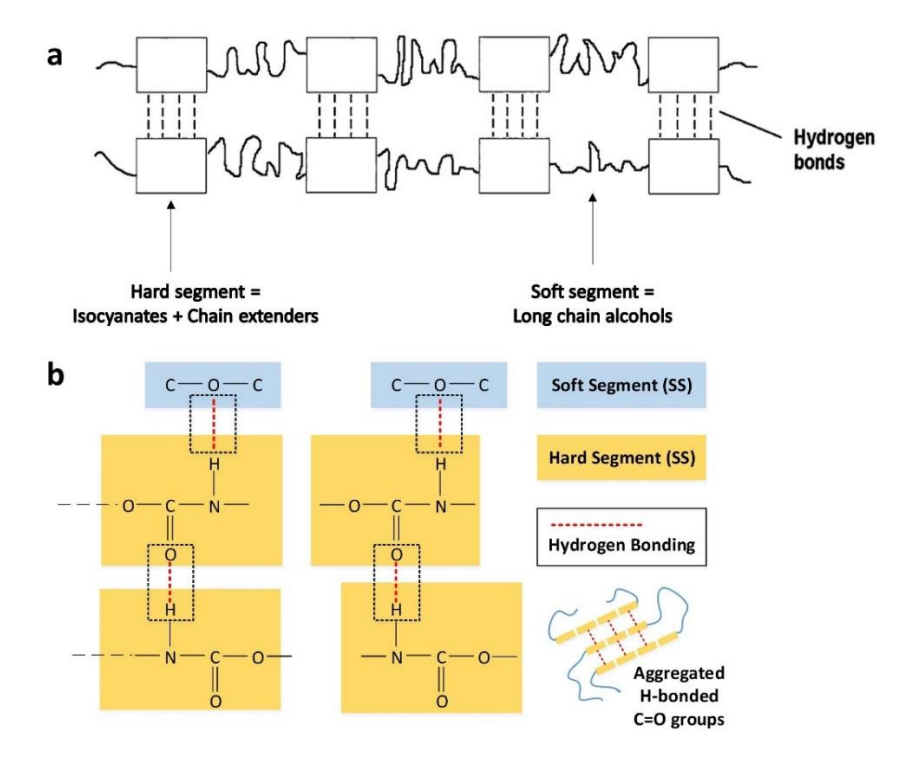


Figure 2- 4. Schematic of polyurethane structure. a) Structure of soft and hard segments in the polyurethane chains. Figure taken from de Avila Bockorny⁴⁴, reproduced with permission of rights holder. b) Schematic of chemical linkage within the soft segments, hard segments, and hydrogen bonds in the polyurethane structure; Schematic of aggregated hard segments.

The interactions between the hard segments in the polyurethane structure, owing to the hydrogen bonds and the dispersion influences of polar urethane groups, can aggregate together into a hard domain, as shown in Figure 2- 4b. As the result, phase separation in the PU morphology persists when the hard domains are mixed with the less polar soft segments⁴². The degree of the phase separation is greatly influenced by a number of factors including: (1) the types and compositions of isocyanates/alcohols used (i.e. di-functional or multi-functional reactant, the molecular weight and the chemical structure of the reactants)^{45–48}; (2) molecular weight and molecular weight distribution of the PU. The size, polarity and mobility of the soft and hard segment^{46,49} and (3) the synthesis routes employed in fabricating the PU⁵⁰.

It was reported by Tan et al. that phase separation was promoted with linear chain extender (namely pentanediol and butanediol), whilst not with branched chain extender (dipropyleneglycol or tripropyleneglycol). It was anticipated that the linear chain extenders could promote the association of hard segments into the hard domains via hydrogen bonding as depicted in Figure 2-4b. This ultimately led to cured PU samples with higher tensile shear strength. They also observed that the thermal properties i.e. glass transition temperature of the urethane prepolymer were highly dependent on the amount of chain extenders in the formulation, whereas higher amount of chain extender could enhance the glass transition temperature through greater interaction between the hard segments. The urethane prepolymer exhibited more randomly dispersed hard segments in the structure when produced using oneshot process, in contrast to a two-step pre-polymer process⁵⁰. Barikani and et al. reported that chain extender with higher molecular weight would in favour of producing thermoplastic polyurethane elastomer with larger hard segment, and better phase separation, in this case (1, 10-decane diol, 1,6- Hexane diol, 1,4 butane diol, 1,3 propane-diol and ethylene glycol were investigated)⁵¹. Chu and et al. found out that when the molecular weight of the soft segment increased from 1000 to 2000, the phase separation rate was greatly enhanced. They attributed this change of phase separation behaviour to the longer chain length of soft segment, in turn enhancing the hard segment mobility. The findings supported their hypothesis that the hard segment mobility, system viscosity and segments interactions are the decisive factors in controlling the phase separation in the system⁴⁶. Based on these studies, it can be concluded that the final synthesized PU thermos-mechanical properties (namely thermal stability, glass transitional temperature, tensile strength, elongation at break, modulus of elasticity, hardness) are essentially dependent on the micro-phase separation behaviour within the structure. This structure-property relationship highlights the importance of understanding the phase separation behaviour, to tune the material properties to meet the demand.

Reaction Kinetics

It is the typical interfacial reaction found in polyurethane reaction, due to the incompatibility of the isocyanate and alcohol feedstocks⁵². The reaction takes place at the interface between the two feedstocks. This interface has previously been investigated under optical microscopy at small scale^{53–55}. These studies deposited droplet of reactants from two sides and brought them into contact between two glass slides and characterized the interface under microscope. The results showed the interfacial mixing and reaction can be characterized into three stages: (1) an interfacial zone quickly formed when isocyanate and alcohol feeds mixed together; (2) the fast reaction could lead to the formation of viscous reaction products and growth of interfacial zone. These viscous products presented in the interfacial zone increased the resistance of the dispersive flow momentum of the reactants to other side; (3) with the decay of reaction rate owing to the barrier formed by the viscous reaction products, molecular diffusion governed the final stage of reaction, eventually lead to a completion of reaction. A typical interface growth of such system (i.e. polyurethane or polyurea) is shown in Figure 2-5, whereas the interfacial zone grew rapidly at a fraction of a second after the reaction started.

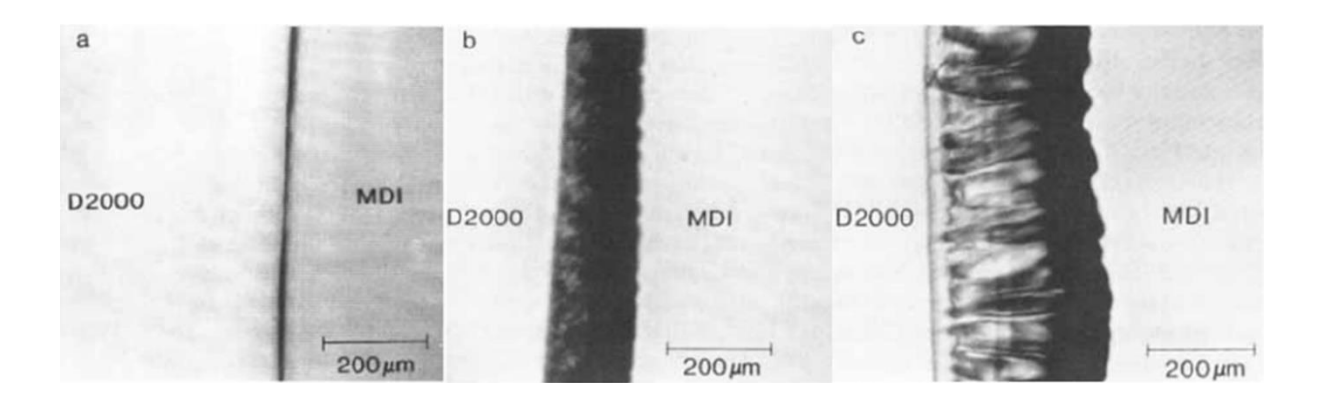


Figure 2- 5. Interfacial mixing observed upon contacting a polyether diamine (D2000) and 4,4' Diphenylmethane diisocyanate (MDI), 40X magnification. Interface a) upon reactant contact. b) 0.2s from contact. c) 0.8s from contact. Figure taken from Machuga⁵⁵, reproduced with permission of rights holder.

The size of the interfacial zone was greatly impacted by the reaction kinetics (i.e., how fast the reaction products formed in the interface, and how viscous the reactant products became). There was a correlation between the level of catalyst introduced to the system and the change of the interfacial reaction zone size over time presented in Figure 2- 6.

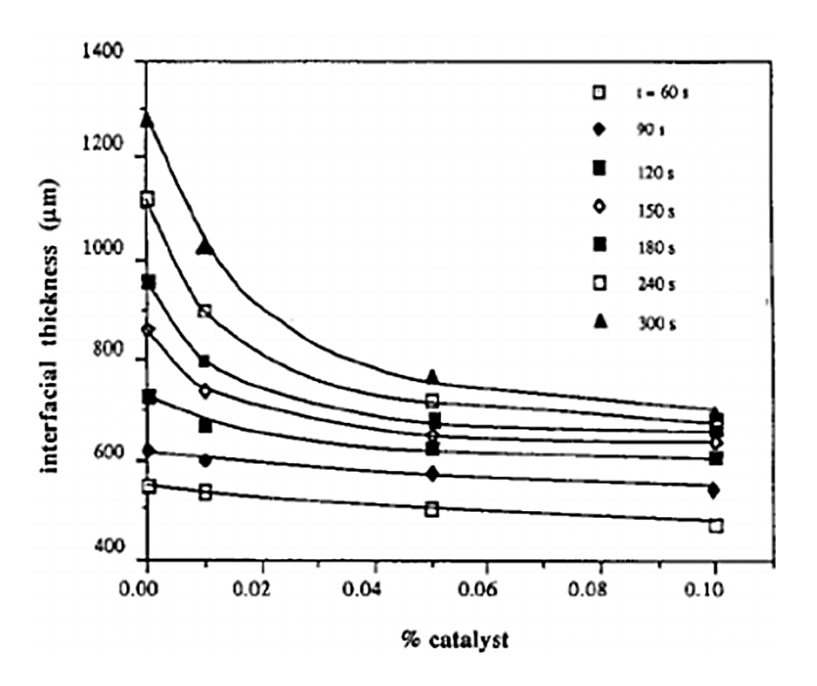


Figure 2- 6. Growth of interfacial zone over time at varying DBTDL catalyst concentration in polyether diol and MDI system. Figure taken from Machuga⁵⁵, reproduced with permission of rights holder.

It was found that the initial sizes of the interfacial reaction zone stayed relatively constant at low catalyst range (≤ 0.1 wt. %). A decay in the growth rate of interfacial reaction zone size

over time was demonstrated at higher catalyst level (0.1 wt. %). This observations indicated faster reaction kinetics hinder the growth of interfacial reaction zone, and consequently will lead to the decay in interfacial mixing intensity⁵⁵.

In addition, it was also found various interface morphology and interface stability existed depending on the reactive system (i.e., different isocyanate/alcohol system (crosslinked or linear) and reaction temperature), shown in Figure 2-7

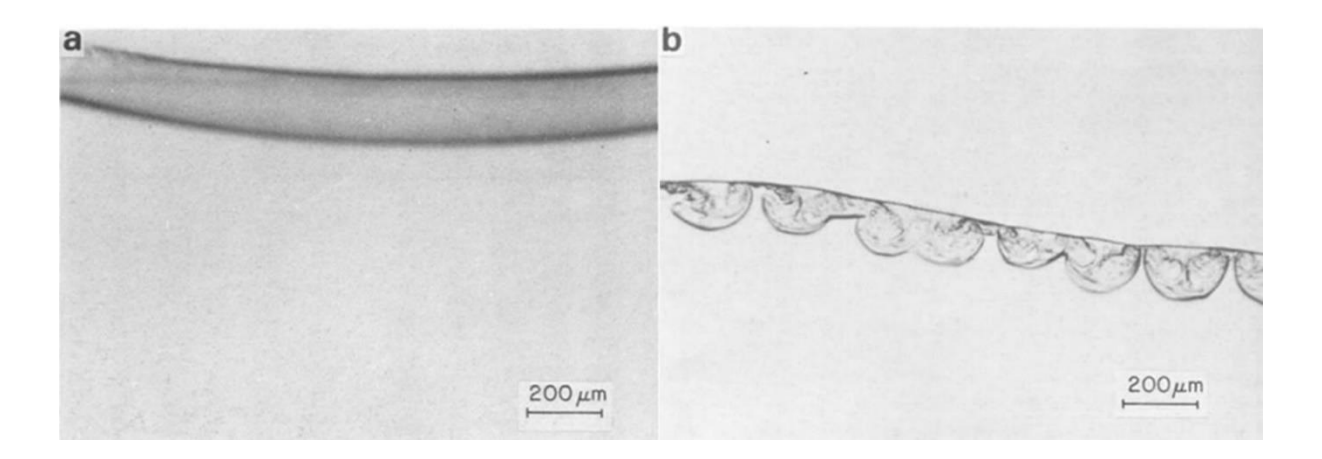


Figure 2- 7. Interfacial polymerization at 25° C and Time: 30s for (a) top phase, 25%, 1,4 BD + 75 % PPO +0.1 wt. %, catalyst; bottom phase, di-isocyanate MDI. (b) top phase, 50%, 1,4 BD + 50% PPO +0.1 wt. %, catalyst; bottom phase, di-isocyanate MDI. Figure taken from Fields⁵³, reproduced with permission of rights holder.

Instable interface was observed for the three component PU system formed by reacting disocyanate MDI with a short-chain diol (1,4 butane-diol: 1,4 BD) and long-chain diol (polypropylene oxide) at different compositions. This instability at the interface was attributed to the interfacial tension resulting from the composition gradients along the interface. It resulted in interfacial reaction zone was stretched up to $100 \ \mu m^{53}$. The results indicated the interface mixing profile is dependent on the formulation and the reaction condition.

These studies visually demonstrated the evolution of the interface for PU reactions at micron scale. They offered fundamental insight on how the reaction kinetics in the bulk system might be influenced by the interfacial reaction zone. In summary, the reaction kinetics for a specific

PU formulation are determined by the reaction condition, diffusion rate of the reactants and the interfacial parameters. The latter include the interfacial tension, thickness, and area of interfacial zone. It can be conceived that larger interfacial reaction zone would promote the reaction rate.

For reactive injection molding system equipped with impingement mixing, the reaction rate can be promoted by altering the flow condition i.e. increasing the flowrate⁵⁶. This is owing to the fact more intensified mixing can be generated with the formation of the favourable smaller dispersed droplets⁵⁴. It was found that there is a finite dispersed droplets size can be reduced down to by altering the flow condition⁵⁶. This indicated further promotion of reaction rate in overcoming diffusion limitation may need other mixing apparatus. Thus, static mixer, the passive in-line mixer consists of multiple mixing elements/stages often was equipped, either at the pre-mixing stage prior to feeding into the extruder⁵⁷ or after the impingement mixing head⁵⁶ to further mix the reactants, in improving the mixing efficiencies and accelerating the reaction rate in the system. In particular, the static mixer was effective to mitigate the adverse effect of diffusion limitation at higher catalyst level, in which case the viscous high molecular weight reaction products quickly formed⁵⁷.

2.2.2 Conventional Process and Applications

Polyurethane (PU) is a one of the most versatile polymers, combing the flexible and rubbery nature of elastomer with rigid plastic nature. It has a great number of applications in different fields, such as rigid or flexible foaming, coating, elastomers, sealant, adhesives, biomedical devices and etc³. Its mechanical properties can be tuned by modifying the chemical structure to meet the specific needs. Together with 3D printing, variety of PU products could be printed with tailored functionality, and customisation. This leads to great potentials in this field of 3D printing PU.

There are two processes been widely used in producing PU, including one-shot process and two step pre-polymer process. In the one-shot process, all the reactants including isocyanates, alcohol (diol or polyols, chain extenders) and additives are all added at once. In contrast, two step pre-polymer process is conducted as depicted in **Figure 2-8**, long chain alcohol and isocyanate are mixed to form a polyurethane pre-polymer at the first step. Then the chain extenders are added to form the final PU structure. It is conceived that the PU produced *via* the two step pre-polymer process, presenting better phase separation between hard and soft segments, well defined chain structures and narrower molecular weight distribution as discussed in section 2.2.1^{50,58}.

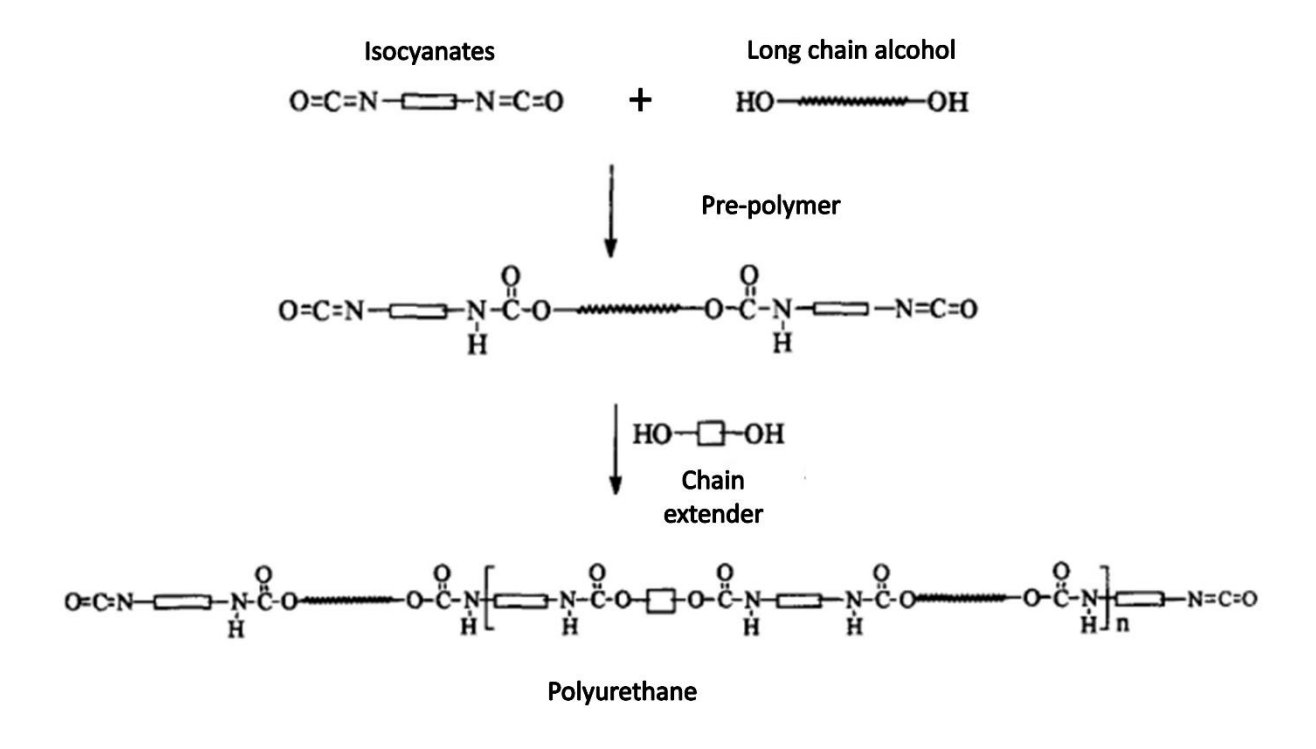


Figure 2- 8. Schematic of two step polymerisation process for polyurethane production. Figure taken from Lan⁵⁹, reproduced with permission of rights holder.

The production of pure PU products is conducted in an inert environment, namely nitrogen or argon environment. This is due to the side reaction in which isocyanate can react with water to produce undesirable carbon dioxide and urea. This competing reaction shall be supressed to the minimal in the formation of pure PU products. Whilst this side reaction will become equally

important one as with the reaction between isocyanates with alcohols for PU rigid/flexible foams production. Thus, it is critical to promote the main reaction with respect to the specific PU product application. This is often accomplished by introducing the desirable additives, i.e., catalyst, filler, surfactant etc. into the formulation.

2.3 Additive Manufacturing Polyurethane

There is an increasing demand in many application areas for greater levels of customisation/personalisation of products, and AM has shown great potential to enable increased flexibility in the fabrication of PU products. To date, the use of PU materials in AM has centred on the application of commercially available synthesised powders, filaments or resins as feedstocks for various AM techniques, such as vat photopolymerisation, powder bed fusion, and material extrusion ^{8–11}. An alternative approach to existing techniques for processing PU is reactive AM, whereby an *in situ* reaction takes place during the process of forming the 3D structure ¹³.

2.3.1 Route 1: Pre-synthesised PU Feed

PU Powder

Here, PU is printed via powder bed fusion, which is one of the seven AM processes being classified in the International Organization for Standardization (ISO)/American Society for Testing and Materials (ASTM) 52900:2015 standard, here more specifically via selective laser sintering (SLS). SLS is an AM technology firstly developed by Carl Deckard at University of Texas back in 1986⁶⁰. In SLS, laser beam is illuminated selectively onto the powder bed, and powders get heated and fused together. Once finishing printing a layer, another layer of powder is spread on top of the previous layer by a roller and get sintered based on the design. The nonfused powders then serve as the supporting material during the printing process. 3D structure is built by following this procedures repeatably⁸.

There have been a few attempts in demonstrating the thermoplastic polyurethane (TPU) parts printed via SLS^{10,61,62}. A 3D soft auxetic PU lattice structure, which could withstand a wide range of compression strains for energy absorption and mechanical damping applications was produced via SLS, by carefully evaluating the suitability of commercially available thermoplastic polyurethane powders (DESMOSINT X92 from BASF Germany) and

optimising the printing process parameters¹⁰. They have also proposed a systematic way for evaluating the suitability of powders, based on intrinsic properties (Chemical/Thermal/Rheological properties) and extrinsic properties (Flow/Optical properties) for SLS process as shown in Figure 2-9.

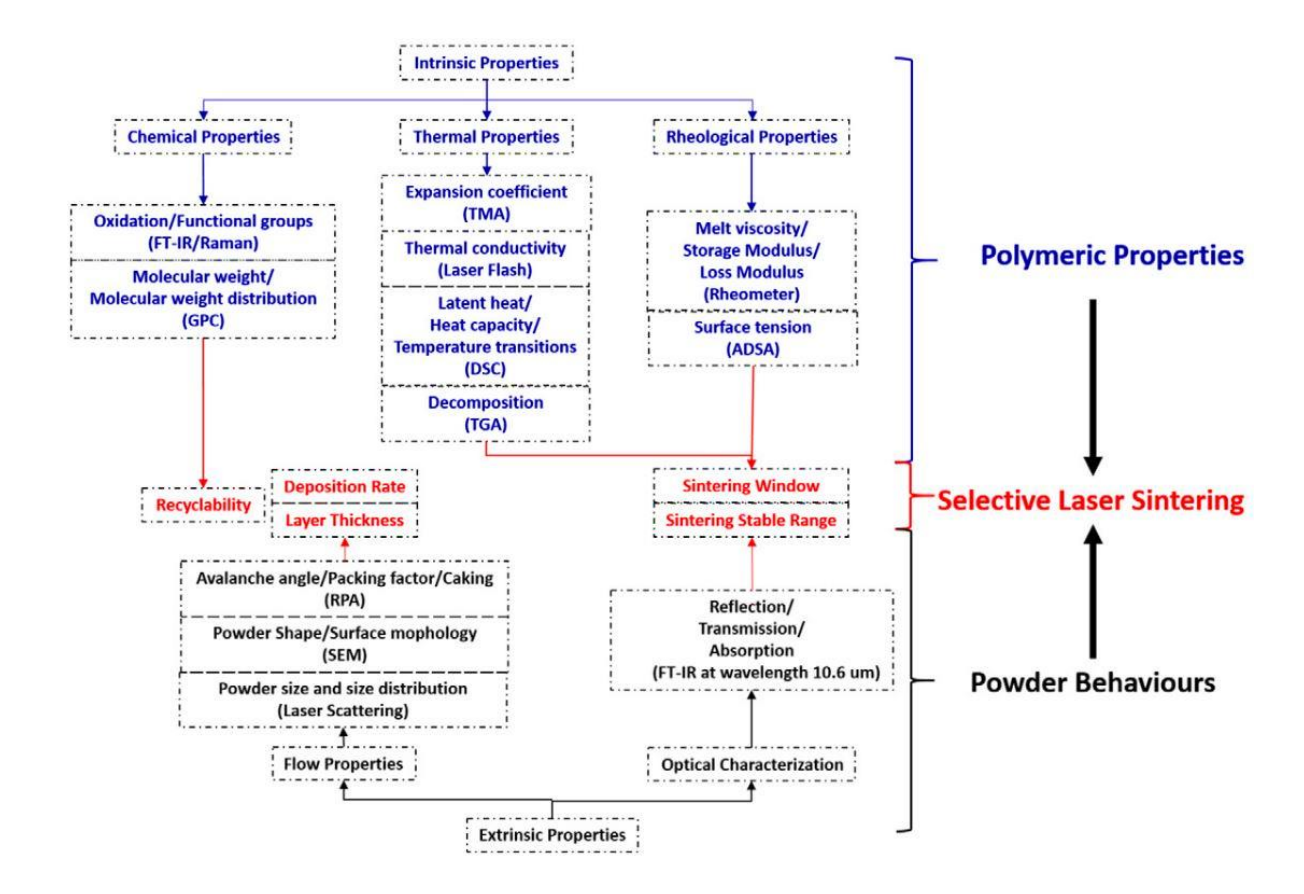


Figure 2-9. Systematic method for evaluating the powders for SLS system. Figure taken from Yuan⁶³, reproduced with permission of rights holder.

It is challenging in general to fulfil all the powder properties requirement to be a perfect candidate for SLS process. An example of such challenges is thermal properties of the TPU powder used in this study shown in

Figure 2- 10, compared with an ideal example for SLS process, where a preferable broader sintering window and narrow melting region shown in Figure 2- 11.

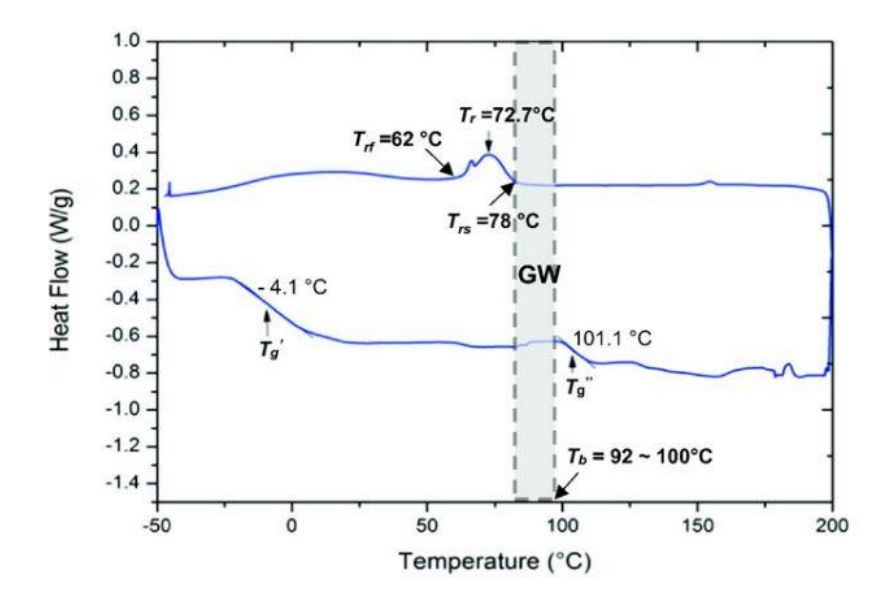


Figure 2- 10. DSC scan of the TPU powders upon heating and cooling from -50 $^{\circ}$ C to 200 $^{\circ}$ C at the rate of 10 $^{\circ}$ C/min. Figure taken from Yuan¹⁰, reproduced with permission of rights holder.

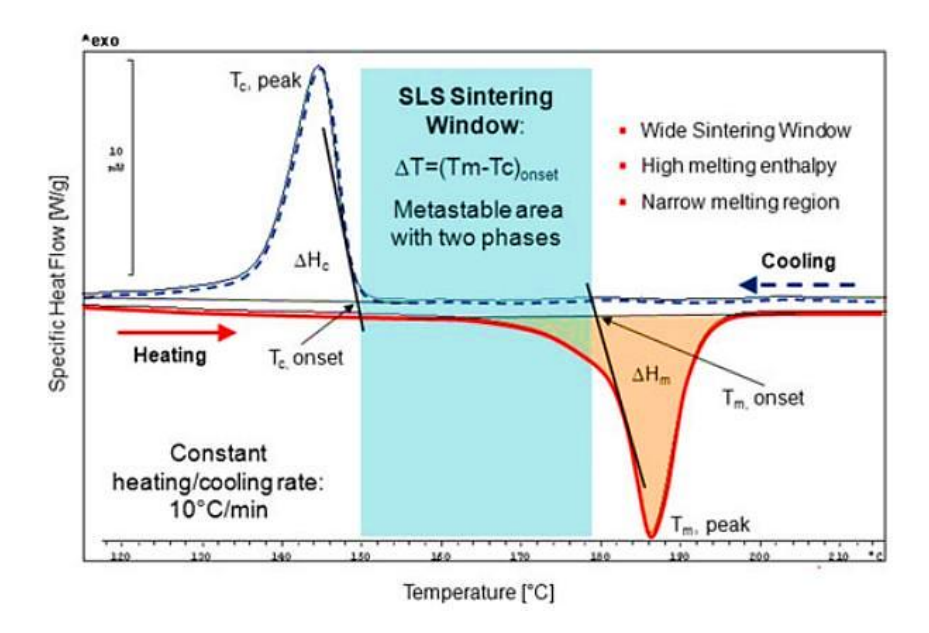


Figure 2- 11. DSC thermogram showing the "SLS sintering window" within region between melting and crystallisation. Figure taken from Schmid⁶³, reproduced with permission of rights holder.

Due to the amorphous structure, the glass transitional temperature of the TPU was shown, but not the melting temperature. Additional melt rheology test was required to detect the onset melting temperature, which is the transitional point of storage and loss modulus when subjecting to heating. The stable sintering region also knowns as the optimum temperature for laser sintering, which is defined by the temperature region between the offset of melting and onset of decomposition⁶⁴. The TPU presented a narrower stable sintering window ranged from 171°C to 242°C, in contract to commercially available polyamides PA12 (PA2200 from EOS GmbH, Munich, Germany) which is from 198°C to 360°C ⁶⁵. Due to the narrower laser optimum operating window, more careful control of the laser powder input would be needed to print TPU vis SLS. It was found that cross-section of the sintered TPU parts showed different level of porosity, when subjected to different laser power/scanning speed. It was challenging to print fully dense parts, due to the poor penetration of laser in the mid of closely packed and weakly conductive TPU powders ¹⁰.

The porosity issue was also reported by Verbelen⁶², where they investigated the correlation between material properties to the sintering behaviour of four different grades of TPU powders (Luvosint TPU X92A-1, and three other ester-based TPU with distinct hardness: TPU-SA95, TPU-SA85, TPU-SA70). The porosity led to significantly inferior mechanical properties (tensile strength and elongation at break) than the compression molded counterparts⁶². Also, the broad melting peaks and the narrow sintering windows for all four TPUs were also discussed in this study. The full coalescence of the TPU powders were hard to achieved at the short time when the laser was applied⁶².

To further realise the potential of parts printed via SLS, nanofillers were introduced into the SLS powder to prepare a composite powder. This approach was firstly demonstrated in AM

CNT-coated polyamide 12 (CNTs/PA12) powders, whereby introducing the CNTs as nanoreinforcer. An extended stable sintering region was extended and enhancement in tensile strength, elongation at break and toughness were all attained in the printed CNTs/PA12 composite, in compared with PA12 samples⁶⁵.

Following the same approach, a flexible thermoplastic polyurethane (TPU) conductor was fabricated via SLS, by wrapping the commercial TPU powders (LUVOSINT X92A-1) with multi-wall carbon nanotubes (CNTs). This application harnessed the porosity embedded in the TPU powder network and let the CNTs to fill into the voids between the TPU powders as shown in Figure 2- 12. The CNTs formed a conductive segregated network at the TPUs powder boundary.

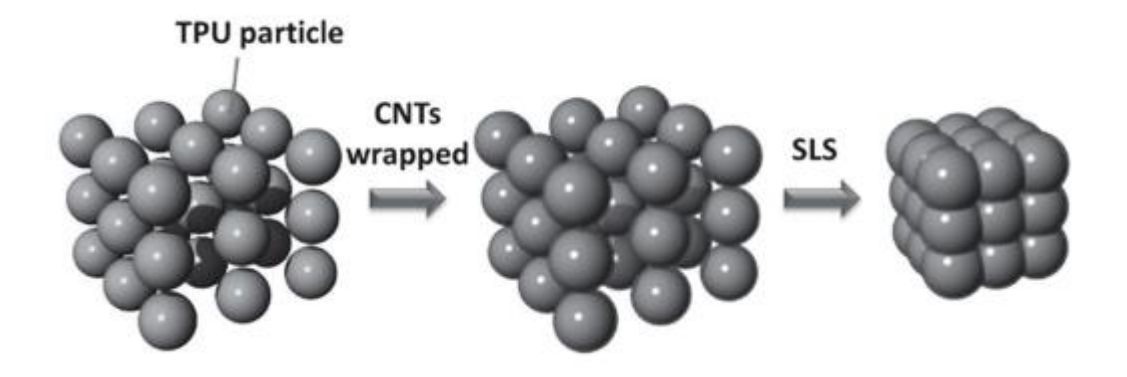


Figure 2- 12. Schematic of the structure formed in the SLS-processed TPU/CNTs composites. Figure taken from Li⁶¹, reproduced with permission of rights holder.

This was demonstrated by the coalescence study of the melt powders. Commercial PA12 powder melted quickly and achieved a full coalescence as shown in Figure 2-13 a). In contrast, slow and insufficient coalescence was presented in the TPU/CNTs powders. The poor coalescence of the powder proved to be beneficial for the CNTs powder to stay segregated as presented in Figure 2-13 c) and d). Together with the superior electrical conductivity provided by CNTs and complex geometric design freedom presented by SLS, the printed TPU/CNTs conductor outperformed the injection moulded sample with seven orders of magnitude higher in electrical conductivity. The electrical resistance of the conductor remains nearly unchanged after repeatably bending for 1000 cycles⁶¹.

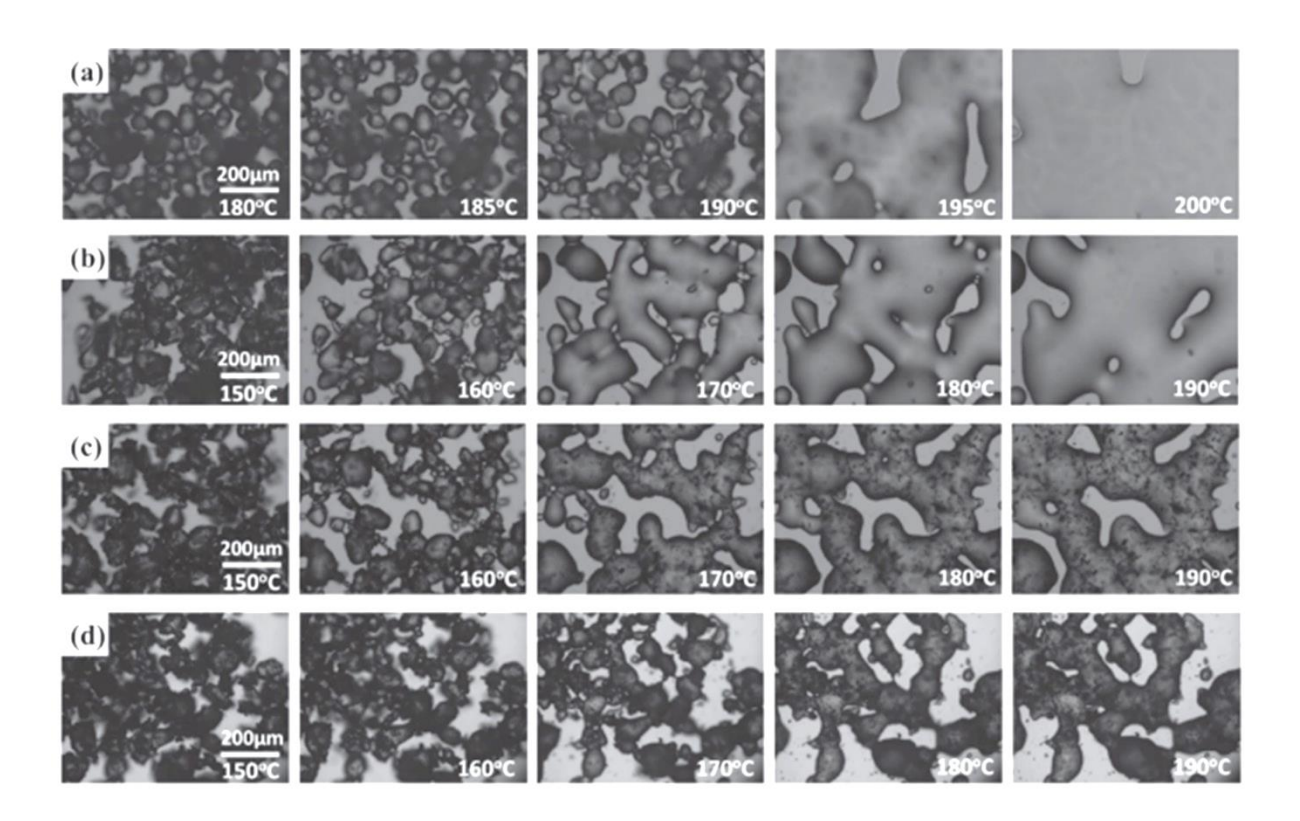


Figure 2- 13. Powder coalescence on a hot stage: a) PA12 powder and b-d) TPU/CNTs powder with different CNTs contents: b) 0 wt%, c) 0.2 wt%, d) 0.5 wt%. Figure taken from Li⁶¹, reproduced with permission of rights holder.

Summary of 3D printing PU from PU powder

There is great potential with AM TPU via SLS, and specifically nanofiller (CNTs⁶¹, single wall CNTs⁶⁶, graphene nanoplatelets⁶⁷) reinforced TPU network has drawn great attention due to the synergetic benefits offered by the nanofillers: (1) stayed segregated between the unfilled TPU powder boundaries; (2) excellent electric conductivity. However, Pure TPU SLS printing remains challenging.

One of the main constraints of SLS PU is the limited powder options available. There are rigorous selection criteria for the powders suitable for SLS. It is preferable to have a regular powder morphology and narrower power size distribution, to ensure the good flowability of the powders and can be uniformly deposited on the print bed. In order to achieve a better coalescence of adjacent powders, it is favourable to employ less viscous powders in the SLS process, since there is no additional compacting as in traditional injection moulding⁶⁸. The processing window for SLS process is governed by the onset temperature of crystallisation and melting. In the case of dual segmented TPU owing to the amorphous phase is often presented in the structure, the thermal properties of the polymer are more complex than the semicrystalline polyamide with clear onset temperature¹⁰. Hence, it adds extra complexity to determine the processing window for TPU. The broad melting range which can often led to slow and insufficient coalescence of the powders. Consequently, fully dense TPU parts are challenging to be printed via SLS, due to the powder coalescence issues. As the nature of sintering process, thermal gradient is often introduced into the structure, in the vertical built direction. Residual stress tends to induce at the interface between the sintering layer and the previous built layer. Warpage, curling or breakage will occur as the result of relaxation of the residual stress, which could deteriorate the built structure⁸.

PU Filament/Inks

The journey of AM PU via material extrusion, starts from (1) either extrusion of a filament type of PU feedstock via fused deposition modelling (FDM), also known as fused filament fabrication (FFF); (2) or extrusion of PU liquid inks with specific viscoelastic properties via direct ink writing (DIW) or hot melt extrusion. FDM or FFF is now a well-known low-cost AM process, with the applications centred on rapid prototyping as a result of inferior surface finish and mechanical properties compared with other AM process⁶⁹. In FDM or FFF, a TPU filament passes through a spool and into the extruder (heated nozzle). The filament was heated to the molten state and then deposited layer by layer onto the printing platform based on the design profile.

A great example of printing functional PU parts via FDM/FFF was demonstrated, here A flexible PU cellular structure with density gradient for repeated energy absorption application was 3D printed via FDM, using commercially available Ninja-Flex thermoplastic polyurethane filaments ^{11,12}. The customised design and printed repeated hexagonal honeycomb structure exhibited a maximum energy absorbing efficiency of 0.36, which shows comparable performance to that of closed cell polyurethane foams fabricated via traditional process¹².

With the same Ninja-Flex TPU filaments, A TPU bladder was AM via FDM, and used for composite manufacturing. Despite the success in fabricating such bladder, it was reported that difficulties involved in different stages of the FDM process: filament feeding, filament printing. The rigid filament which can be well aligned and easily fed from the driving gear to the entrance of the extruder hot end, shown in Figure 2- 14 (A). In contrast, the flexible TPU filament was more susceptible to fall into the gap between the gear and the hot end entrance, due to low elastic modulus, illustrated in Figure 2- 14 (B) and (C).

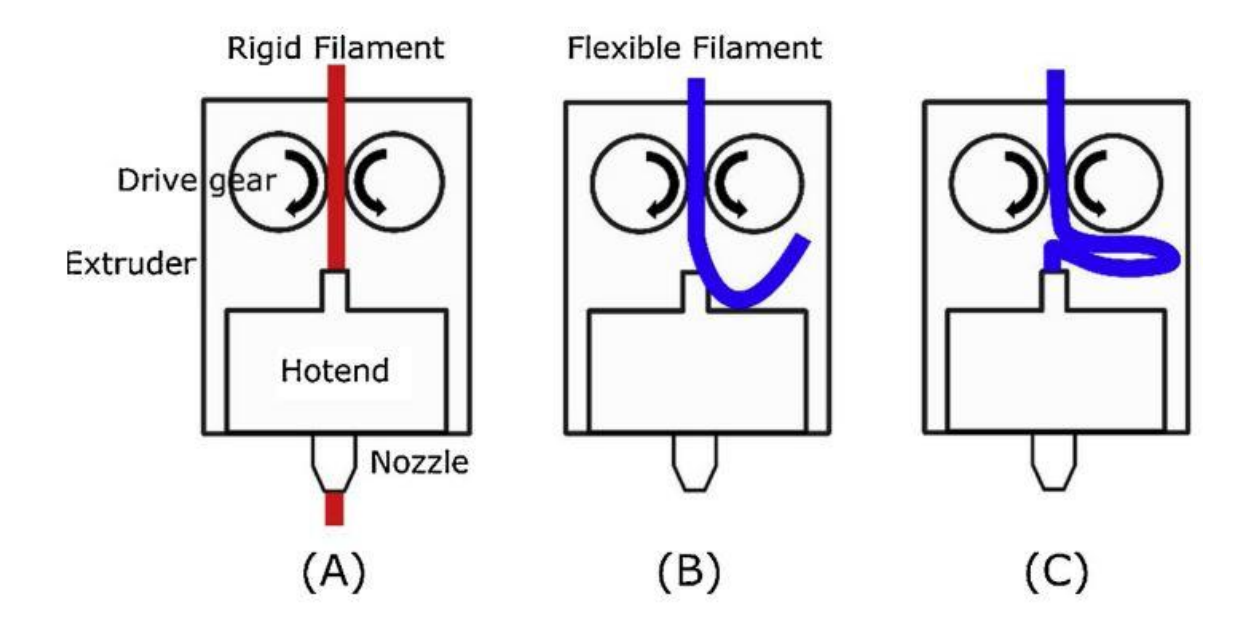


Figure 2- 14. Schematic of FDM process of (A) a rigid filament. Falling of filament between the gap of drive gears and hot end, due to (B) filament misalignment (C) filament kinking or buckling. Figure taken from Kim^{70} , reproduced with permission of rights holder.

These filament feeding issues were attributed to the mismatching of the gear feeding rate and the nozzle extrusion rate. The filament slippage in the feeding system was also caused by the filament diameter reduction when subject to continuous tension from the spool to the filament feeding system. To overcome these filament feeding issues, a lower printing speed and unwinding of the filament from the spool before printing would be favoured⁷⁰. Overhang issue was presented in the filament printing stage, shown in Figure 2- 15. Significant material sagging shown when printing with 60-degree overhang angle, due to the insufficient interlayer adhesion and lack of support from the bottom layers.

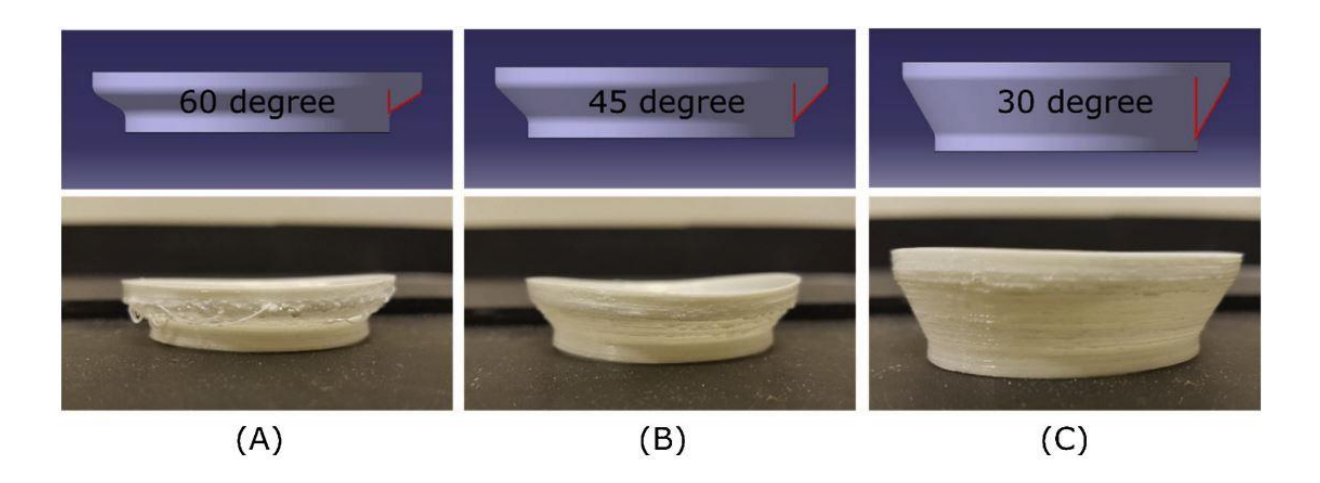


Figure 2- 15. Examples of printing with different overhang angles (A) 60 degree (B) 45 degree (c) 30 degree. Figure taken from Kim⁷⁰, reproduced with permission of rights holder.

There are a few other factors during the filament printing stage needs to be carefully investigated, as discussed by Lin⁷¹. These includes die swelling effect, filament beads to beads interface and most critically layer height. The die swelling effect is known when the pressure driven TPU filament extruded out from the nozzle, which can consequently affect the printing dimensional accuracy, surface roughness and mechanical properties. It was found in this study that increasing the melting temperature can be favoured in reducing the die swell effect. This study highlighted the importance of layer height on governing the geometry of printed TPU beads. It was reported that when the layer heigh was set to be lower than that of the nozzle diameter, a squeezing effect will be incurred to promote the interfacial diffusion between the

adjacent beads, shown in Figure 2- 16. This resulted in the improvement in interfacial bonding strength, and hence enhanced mechanical properties of the printed TPU parts⁷¹. It needs be bear in mind the prolonged printing time will be associated when the layer height is reduced.

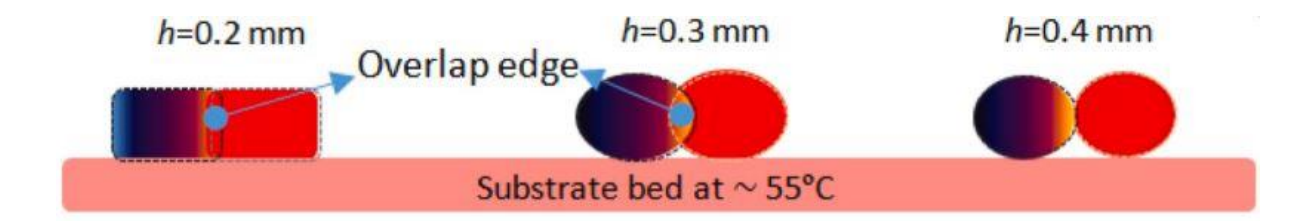


Figure 2- 16. Schematic of interfacial diffusion between two adjacent FDM deposited beads at layer height from 0.2mm, 0.3mm and 0.4mm. The inner diameter of the nozzle d \sim 0.4 mm. Figure taken from Lin⁷¹, reproduced with permission of rights holder.

Under the spectrum of material extrusion, DIW or hot melt extrusion of the TPU is achieved by extrusion of the TPU feeds with tailored viscoelastic properties. TPU feeds are loaded into the print head and heated to a viscoelastic liquid state. Then pressure-driven process will ensure the materials extruded from the print head nozzles, cool and solidifies on the print bed in a layer-to-layer fashion.

A great example of this was shown in fabricating a biomedical PU implant with tunable drug release rate via hot melt extrusion shown in Figure 2- 17, by exploiting the excellent extrudability of the pre-synthesised thermo-responsive supramolecular PU⁷. As reported by the article, the pre-synthesised self-assembly supramolecular PU requires a dedicate design of hydrogen bonding motifs (highlighted in red colour in Figure 2- 17 (A)) to the end of the PU chains. This enables a self-supporting, stiff, and flexible structure quicky formed upon cooling, makes it an excellent candidate for the hot melt extrusion process. Despite the great potential of applying such PU formulation for tailored drug implant application, sophisticated chemical synthesis and formulation design is needed to ensure the PU formulations has the right thermorheological properties to be processed.

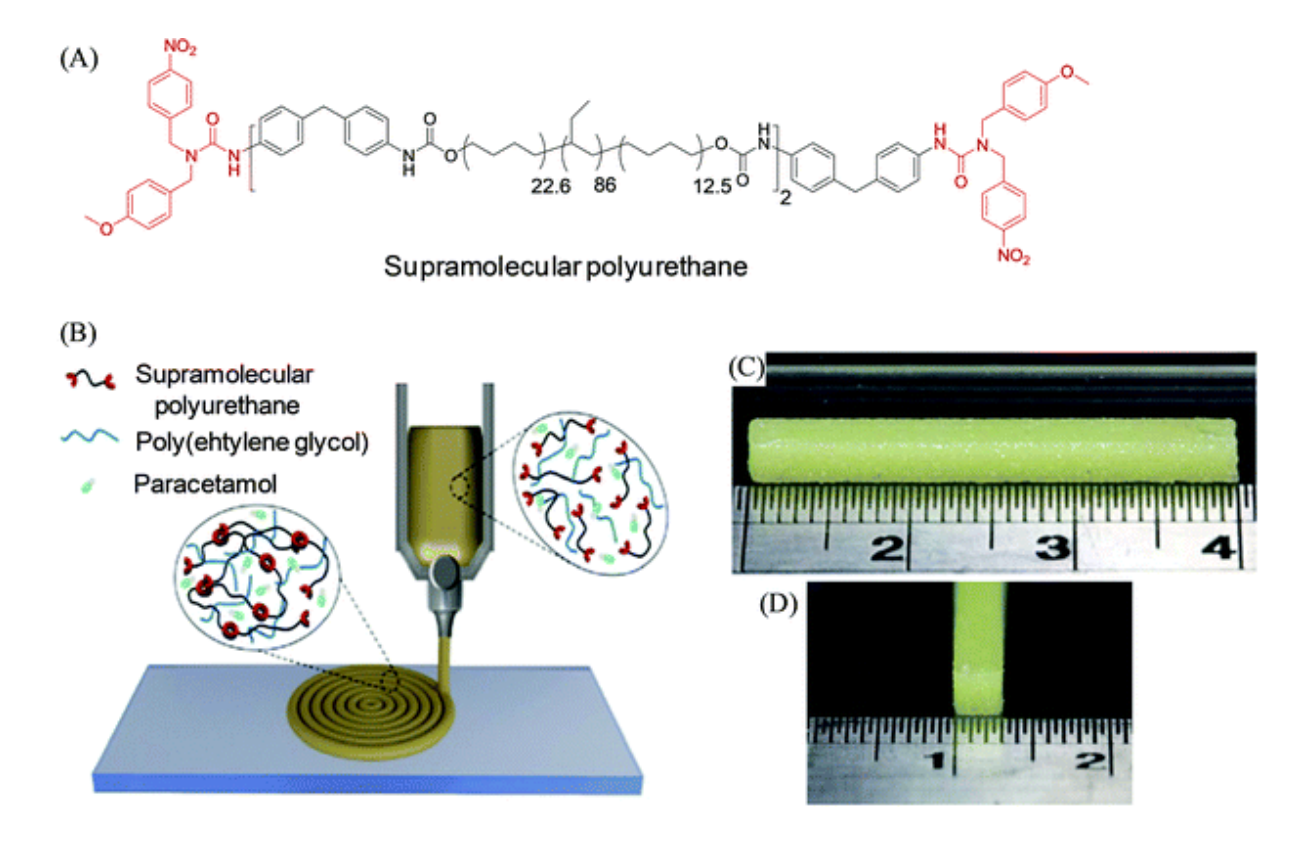


Figure 2-17. (A) Chemical structure of the synthesised supramolecular polyurethane (SPU). (B) Schematic of hot melt extrusion process of SPU/PEG/paracetamol formulation for drug-release implant application. (C and D) Side and end view of the printed bar structure from the SPU/PEG/paracetamol formulation. Figure taken from Salimi⁷, reproduced with permission of rights holder.

Summary of 3D printing PU from PU Filaments/Inks

PU fabrication via FDM/FFF draws the great interest due to the low cost and ease of operation. However, challenges remained in the flexible TPU filament feeding between the drive gear and the entrance of the hot end of the FDM extruder, namely filament misalignment, filament buckling and kinking. To address these issues, nanofiller (e.g. multi wall CNTs) can be introduced to the prepare a TPU composite filament with enhancing modulus, consequently minimising the filament buckling⁷². In addition, during the filament printing, the overhang angles can be printed without any support materials are considerably lower than other AM process (e.g., SLS), which hinder the wider application of PU fabrication via FDM/FFF. The sophisticated formulation design involved for the PU feed inks processed via hot melt extrusion, limited the application of such process.

PU Resin

In this approach, PU is created via vat photo-polymerisation, by spatially illuminate the light to the resin in the vat. Either Laser beams or digital light projectors are applied as light source to solidify the photo-curable resin in a layer-by-layer approach as shown in Figure 2- 18 Left and Right respectively. In stereolithography (SLA), the laser beam moves point to point to selectively cure the designed pattern. Whereas in digital light processing (DLP), light is projected via a digital mirror device and created the two-dimensional pattern on the transparent plate. A complete layer is cured at one time in DLP, which improves the printing speed compared with the point-to-point curing approach in SLA. Additionally, the top-down approach has been increasingly implemented in the stereolithography as in Figure 2- 18 Right. The main benefit of this over the bottom-up approach, oxygen inhibition is constrained with illuminated layer not exposed to atmosphere shown in Figure 2- 18 Left⁶³.

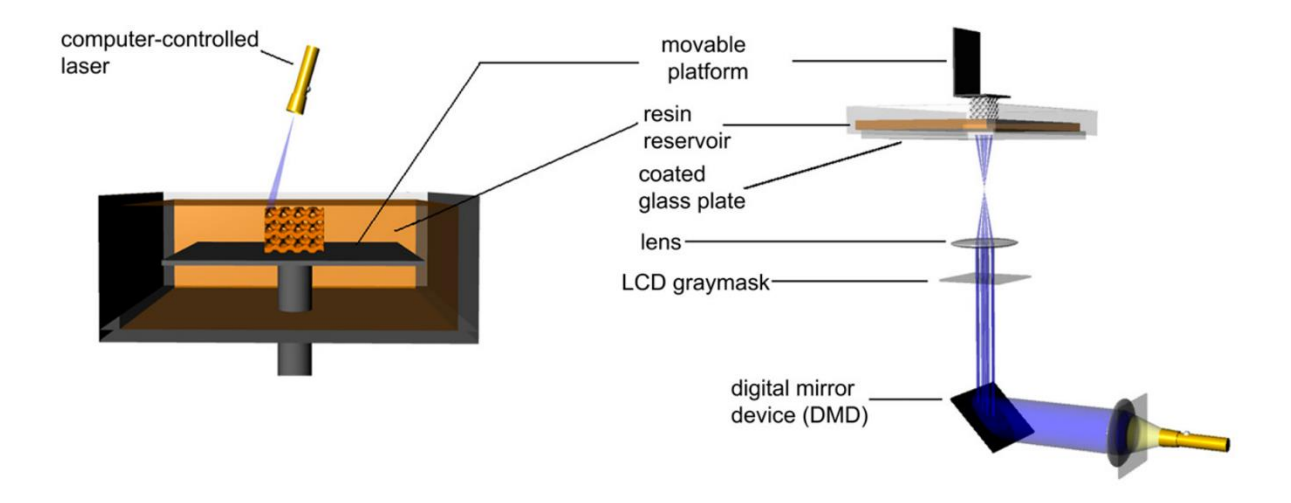


Figure 2- 18. Schematic of two types of stereolithography systems. Left (SLA): a bottom-up system with scanning laser. Right (DLP): a top-down setup with digital light projection. Figure taken from Melchels⁶³, reproduced with permission of rights holder.

Transparent PU elastomers combining shape recovery ability, superior compressibility and durability were printed via DLP, using three different synthesised poly (urethane acrylate) (PUA) oligomers together with diluent isobornyl acrylate. The three PUAs (PPPGA,

PPTMGA, and PPCLA) were synthesized based on poly(propylene glycol) (PPG), poly-(tetrahydrofuran) (PTMG) and polycaprolactone diol PCL polyols, respectively. Among the three PUA resins, PPTMGA outperformed the other two resins and exhibited excellent mechanical properties with tensile strength 15.7 MPa and elongation break at 414.3%. Additionally, it yielded high transparency and stayed in form without fracture after 100 cycles compressions at 80% strain. A piezoelectric strain sensor was then fabricated by dip-coating the surface of the PUA elastomer into conductive hydrogel, which can be applied as wearable sensors. It shall be noted that the viscosity of a photocurable resin shall be lower than 10 Pa s. This set up a strict bar for a PU formulation design perspective, it requires introduction of reactive diluents to tailor the viscosity of the prepared PU formulation⁷³.

A PU elastomer exhibited tensile strength of 3.7 MPa and high elasticity of an elongation at break of 195% was printed via SLA, using the synthesised PUA resin without introducing diluent. The printed elastomer also showed excellent cell adhesion and proliferation, with cell viability over 97% in in-vitro cytotoxicity test, therefore proven to be ideal candidates used for biomedical applications⁹.

A highly stretchable and UV curable PU elastomer with stretchability up to 1100% and elongation at break five times higher than it of commercial UV curable elastomers (such as Carbon EPU40, Stratasys Tango Plus, Formlab Flexible) was printed via DLP. The PU elastomer resin was prepared by mixing epoxy aliphatic acrylate (EAA), a difunctional cross-linker comprising aliphatic urethane diacrylate (AUD) and isobornyl acrylate as diluent. The mechanical properties can be tuned by adjusting the mixing ratio between EAA and AUD, where a higher loading of EAA showed reduced crosslinking density, lower level of hydrogen bonding in the system, hence a poorer stretchability and stiffness. Despite the significant improvement in PU elastomer mechanical properties compared with commercial ones, this

printing process required a specific customer designed heating resin to lower the viscosity for achieving successful printing⁷⁴.

Summary of 3D printing PU from PU resin

Overall, PU printed from pre-synthesised PUA resins yielded superior elasticity, compressibility, and durability.

From the studies undertaken in this field, there are stronger demands for new resins development. Photo-curing 3D printing is constrained by the limited available resins. The majority of the available resins are multi-functional monomers with low molecular weight, and highly crosslinked network⁶³. Most of the reins are normally glassy, brittle, and rigid. Only few available resins possessed flexible and elastomeric nature. These resins consist of macromers with low glass transition temperature and relatively high molecular weight. As the result, the viscosity of the resin is typically quite high and requires modification with the introduction of non-reactive diluent, to reduce the viscosity of the resin⁶³. With the presence of diluent in the resin, the printed structure can be fragile and is prone to shrinkage due to the internal stress⁷⁵.

Summary of Route 1

Thus, AM PU using pre-synthesised feedstock has advantages such as the ease to processing without support demonstrated by SLS process, rapid prototyping opportunity presented by FDM/FFF process, and superior printing resolution offered by SLA/DLP process. However, it also limits the capability of selectively tailoring the material properties that can be offered by *in situ* chemical reaction of PU.

2.3.2 Route 2: *In-situ* Reactive 3D Printing

An alternative approach to existing techniques for processing PU is reactive AM, whereby an in situ reaction takes place during the process of forming the 3D structure ¹³. As an evolving AM technology, reactive 3D printing has gained great attention for producing devices via an in-line mixer using two-component curing PU ^{14–16}, or reactive silicone formulations ^{17,18}. Meanwhile, reactive ink jetting has also be employed to fabricate PU or poly(dimethyl siloxane) (PDMS) via in-situ reaction without "pre-mixing" of the ink components prior to printing ^{19,20}.

Reactive ink-jet 3D printing

Reactive ink-jet 3D printing by its name is based on material jetting technology, depositing two reactive inks to form a solid part relied on the chemical reaction, instead of solidifying a photocurable inks based on UV curing^{76,77}. Ink-jet printing is a well-established 2D printing technology for decades with application in graphics industries, and recently being adopted to inkjet printing functional polymers. Inkjet printing can operate either in continuous mode or drop on demand (DoD) mode, DoD printing is the one used in the AM field as the inks were ejected when required²¹. Two ejection mechanism exists for the DoD inkjet printing: thermal and piezoelectric. Initially thermal inkjet dominated the field due to low cost of production. In thermal inkjet, a heater was used to vaporise a bubble. The extra pressure exerted by the bubble cause a change in volume in the ink reservoir and push the ink out from the inkjet head. The drawback associated with the thermal inkjet head is the potential ink material degradation when subject to thermal cycles⁷⁸. Instead, piezoelectric inkjet head became the mainstream in the field, as it widens the ink material choices and with no risk of ink thermal degradation. The principle for the piezoelectric inkjet is based on the deformation of the piezoelectric material, to cause a volume change and induces the droplet ejection from the printheads^{21,78}. For the

inkjet 3D printing, the ink follows four process steps in the journey: ink ejection, ink deposition, ink coalescence and layer addition as depicted in Figure 2- 19.

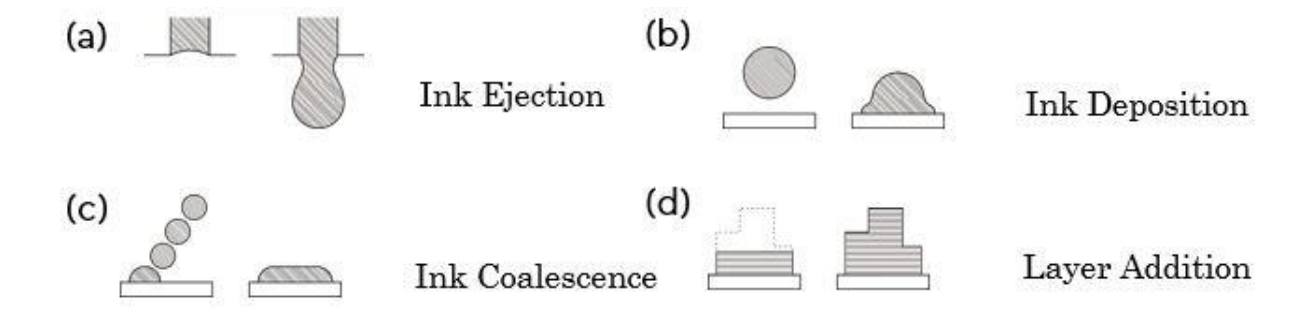


Figure 2- 19. Schematic of inkjet 3D printing process steps: (a) Ink Ejection, (b) Ink Deposition, (c) Ink Coalescence, (d) Layer Addition. Figure taken from Sturgess⁷⁹, reproduced with permission of rights holder.

The ink material properties are the most critical ones influencing the four steps mentioned above, and consequently the inkjet printing performances. The ink needs to be within a jet-table or printable range, which was determined based on ink viscosity and surface tension. It was widely acknowledged that there is a dimensionless number originally proposed by Ohnesorge⁸⁰, as shown in the equation below. It is related to other two dimensionless number, the Weber number (We) and Reynolds number (Re). Oh number is the ratio of viscous forces to the surface tension and inertial forces. Researchers have reported that Oh needs to be in a range: $0.1 < Oh < 1^{81}$.

$$Oh = \frac{\mu}{\sqrt{\rho \sigma L}} = \frac{\sqrt{We}}{Re}$$

If the ink is outside of the printable range, undesirable droplet formation could occur as shown in Figure 2- 20. There is a narrow jettable material windows for the ink-jet printing process. This strict ink printability assessment is also applicable for the reactive inkjet 3D printing ^{19,20,82}.

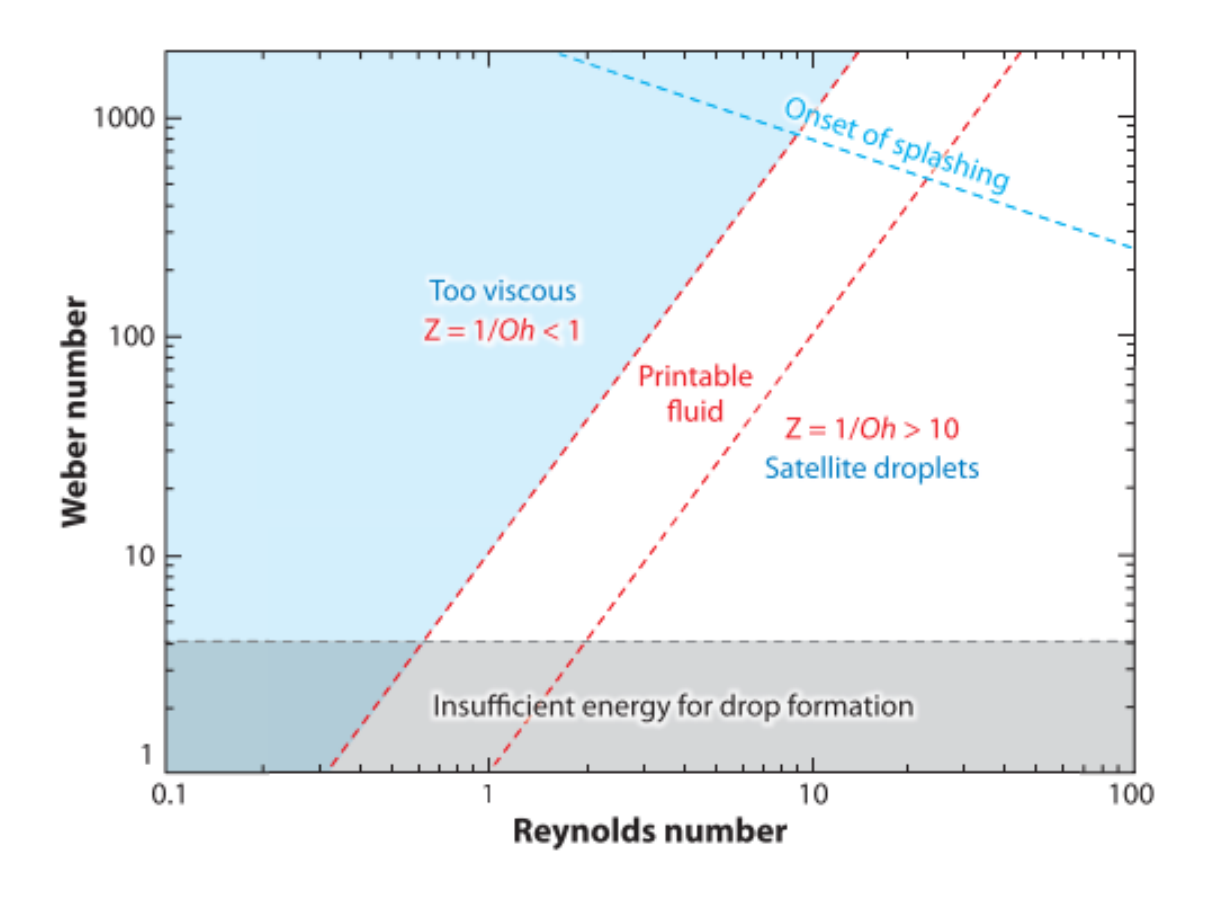


Figure 2- 20. Printable ink region for inkjet printing process based on the Reynolds number and Weber number for ink jettability evaluation. Figure taken from Derby⁸¹, reproduced with permission of rights holder.

When the ink is jettable, there are subsequent challenges involved in fabricating a successful reactive inkjet 3D printing structure. Unlike inkjet of a single ink formulation with comparatively faster curing, reactive inkjet printing of two reactant inks would require longer time before curing, as the mixing of the two inks involved. To ensure a good resolution of reactive inkjet printing, there is a demand for the layer stability after two inks were deposited. If the interaction between ink-substrate found to be weak, and together with the prolonged printing times, uncontrolled depinning and coalescence shown in Figure 2- 21, would occur impeding the printing resolution^{20,82}.

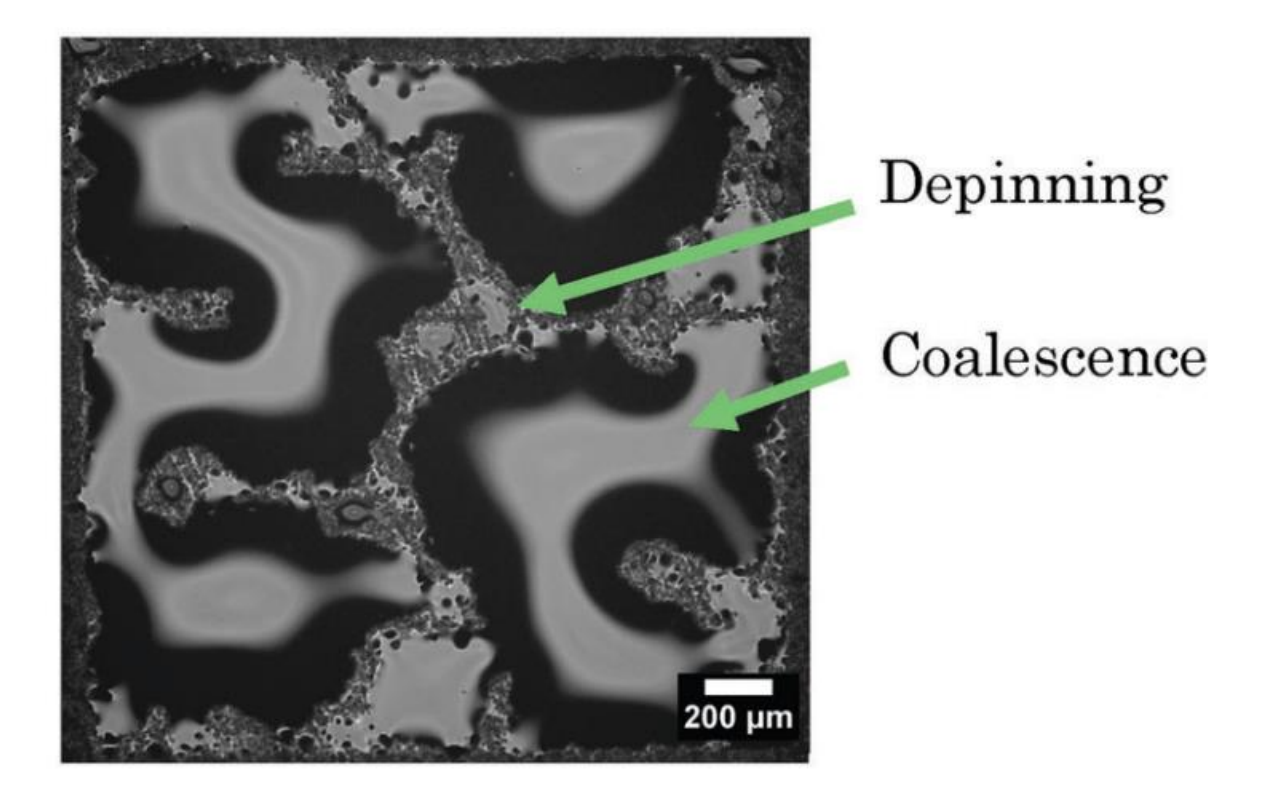


Figure 2- 21. Microscopic images of ink depinning and coalescence issues, the designed printing pattern for this job was a square. Figure taken from Sturgess²⁰, reproduced with permission of rights holder.

This coalescence issues were reported to be resolved by implementing a strategy called "substrate microstructuring"²⁰, or the dot strategy depicted in Figure 2- 22. This strategy was intended to have a larger droplet spacing than the layer strategy, to ensure a film can be formed according to the design. However, the droplet spacing needs carefully tuned to print a stable film, due to the different wetting behaviour of the ink to the substrate, coupled with different ink mixing behaviours⁸².

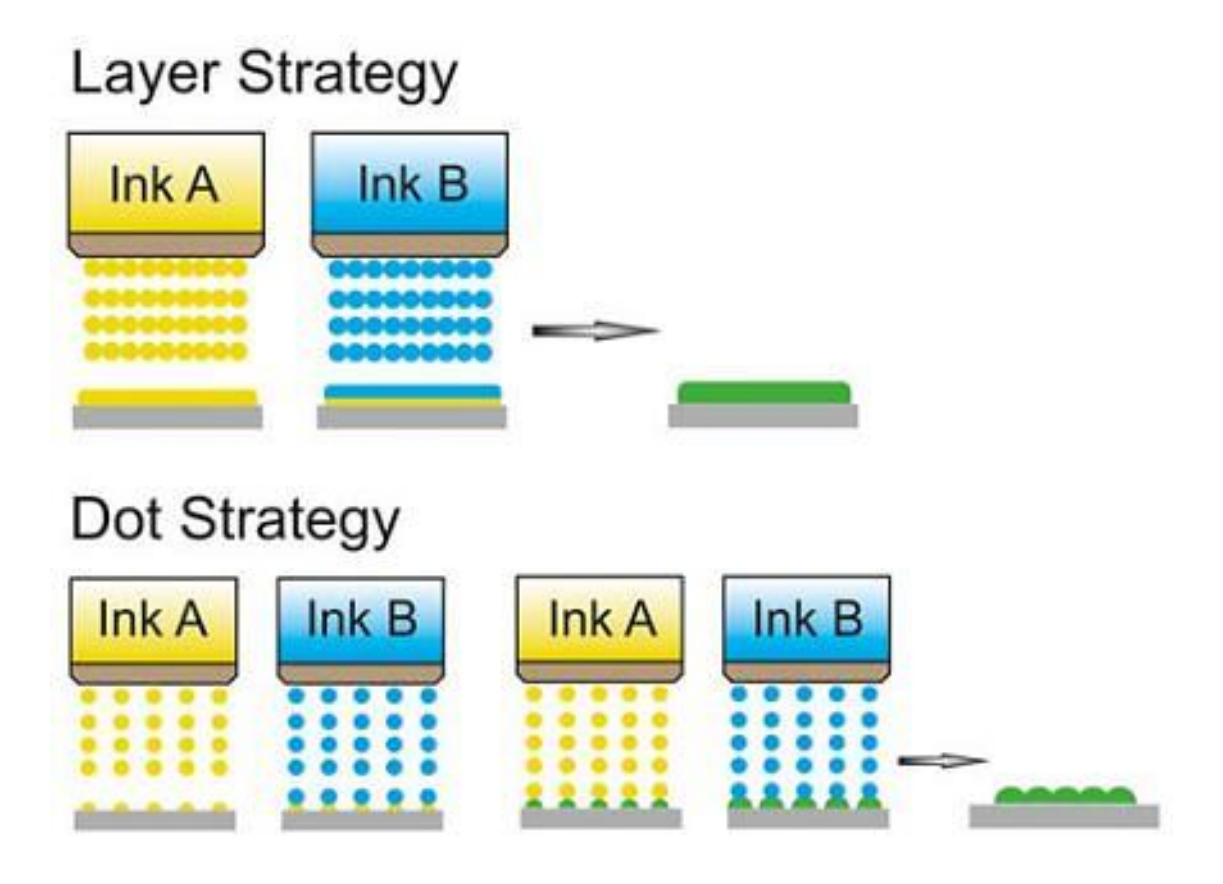


Figure 2- 22. Schematic of two inkjet printing strategies: Layer strategy and Dot strategy. For layer strategy: complete films were printed with one reactant ink followed by another ink in the subsequent layer. For the dot strategy, higher droplet spacing was employed to ensure droplets do not coalesce. Figure taken from Schuster⁸², reproduced with permission of rights holder.

Lately, a new reactive inkjet printing approach was developed, called "Micro-reactive inkjet printing". It is a specific strategy to allow in-flight mixing of two reactive ink droplets^{83–85}, illustrated in Figure 2- 23. The benefit of this approach is allowing the reaction/curing starts in flight, to mitigate the abovementioned ink wetting/coalescence issues. Different highly reactive formulations, ranging from hydrogel precursor with crosslinker⁸³, glutaraldehyde-aminosilicone⁸⁴ and aliphatic polyurea⁸⁵ were printed and demonstrated the feasibility and promise of this new developed in-situ reactive printing process. However, as the diffusion and the uniform mixing between two reactive droplet inks in flight govern the reaction, and consequently influence the homogeneity of the printing. It is a process requires dedicate tuning of the ejection based on different ink properties to ensure the correct diffusion/mixing achieved.

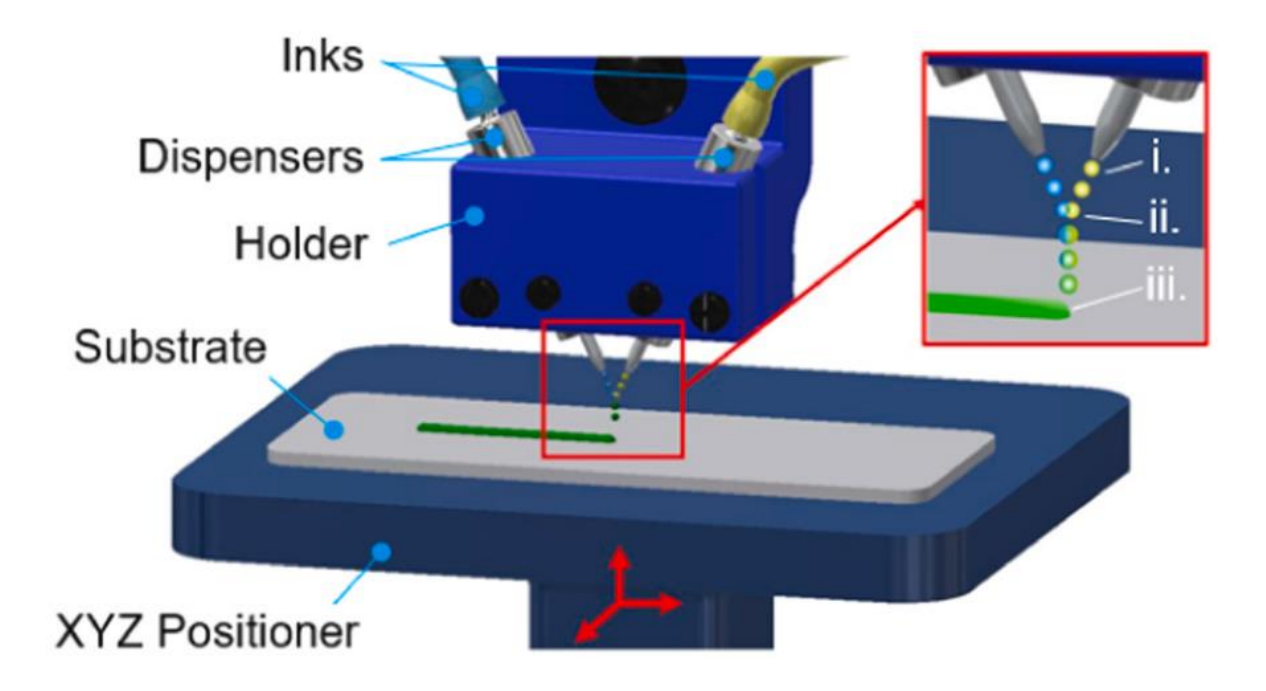


Figure 2- 23. Schematic of droplet mixing module, which allowing for micro-reactive inkjet printing. Figure taken from Śliwiak⁸⁴, reproduced with permission of rights holder.

Müller¹⁹ reported a micro-sized PU structure successfully printed by jetting inks from two separate print heads such that they successively mixed after jetting. One ink consisted of isophorone diisocyanate, and the other comprised polypropylene glycol, a catalyst, and a cross-linking agent. This reactive material jetting approach also demonstrated the capabilities of

producing PU structure containing a mechanical gradient by adjusting the stoichiometric ratio of reactants during processing. However, due to the nature of material jetting processes, the use of solvent was typically necessary for successful material jetting, to improve the printability of the inks i.e., to lower their viscosity. This was problematic as solvent evaporation could result in structural shrinkage ^{13,19}. Thus, there is significant restriction on the number and type of materials that can be used based on the viscosity and surface tension constraints this process places on the inks ²¹.

Summary of Route 2

This reactive ink-jetting approach demonstrated the capabilities of producing PU gradient structures. However, solvent needed to be added to improve the printability of the inks, which could be problematic if solvent residue remains in the printed PU samples. The post-processing process of evaporating the solvent could resulted in shrinkage of the printed structure ^{13,19}. As the nature of ink-jetting process, there's a narrow window in terms of suitable material options, considering the viscosity and surface tension constraints of the inks ²¹. Besides, the ink wetting/coalescence issues were challenging for reactive ink-jetting. Micro-reactive inkjet opened the new ways of reactive ink mixing with in-flight coalescence, whilst facing the same limited ink formulations. In contrast, reactive extrusion 3D printing (REX) offers the advantages over reactive jetting process, with broader spectrum of available materials, faster print speed and still provides locally tunable material properties.

2.4 Reactive Extrusion 3D Printing Polyurethane

REX is a new invented material extrusion process, where two feeds comprising reactive functional groups are mixed and extruded onto the print bed. In-situ chemical reaction bonds the layers through crosslinking at ambient condition. The invention claimed that REX is applicable for reactive formulations such as: polyurethane (isocyanates with hydroxyl) or polyurea (isocyanate with primary or secondary amines)¹. An example of a such system is shown in Figure 2- 24.

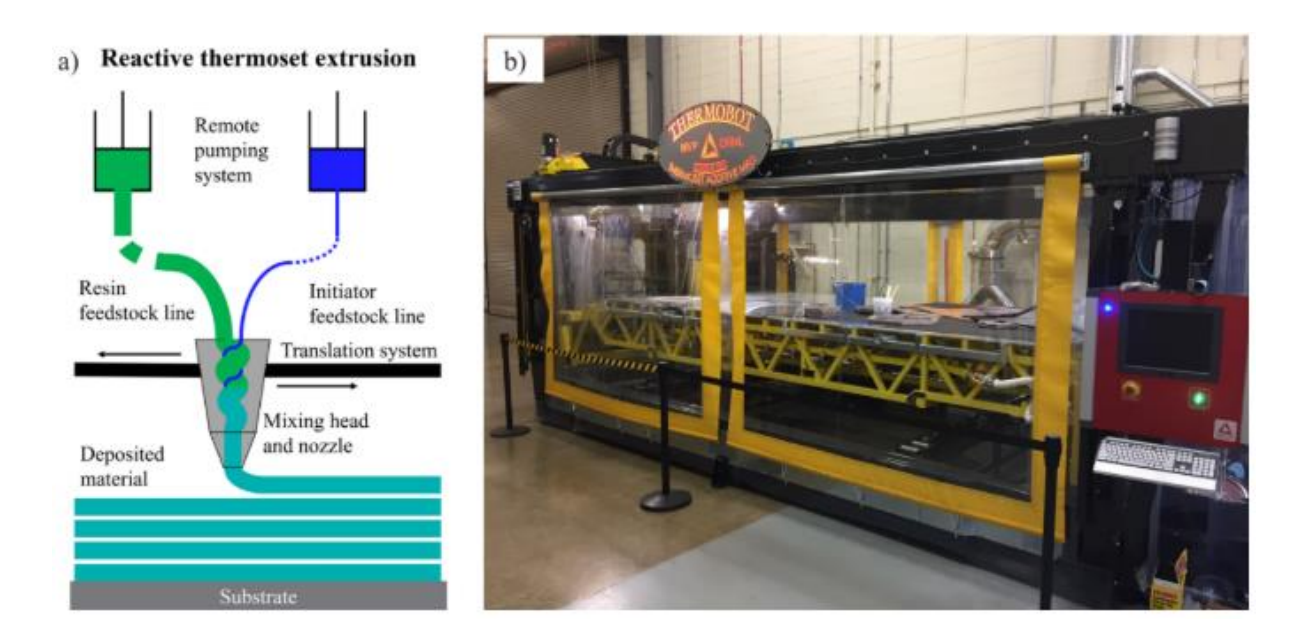


Figure 2- 24. Schematic of a) thermoset reactive extrusion process b) large scale reactive extrusion printer developed by Magnum Venus Products at Oak Ridge National Lab. Figure taken from Romberg⁸⁶, reproduced with permission of rights holder.

This printing process improves the layer adhesion through the in-situ crosslinking between layers, minimises the thermal distortion during printing and offers high printing speed capitalising on the fast reaction kinetics^{22,87}. This in-situ mixing through either passive mixer^{16,88,89}/active mixer⁹⁰ have been reported in other material extrusion process (e.g., direct ink writing 3D printing (DIW) functional parts). In these studies, the primary benefits claimed of applying in-situ mixing are (1) performing multi-material AM¹⁵ and (2) allowing fabricating a functional gradient structure by selectively mixing a soft and hard materials through the

mixer^{16,88,89}. In these DIW process, the rheology of the inks needs to be tuned with addition of rheology filler (e.g. fumed silica), coupled with additional UV curing to offer a robust printing structure fidelity^{16,89}. The focus of this review centre on studies conducted through in-situ mixing and reaction without any external energy sources (e.g., heat or UV light).

The first proof of concept study was completed by depositing two reactants (proprietary thermoset formulation) separately from two reservoirs into a lightweight mixing dosing system, and let the cross-linking happened between layers upon deposition. As the result, the strength of the parts was improved with the inter-layer covalent bonding. This presented the printed reactive formulation significantly outperformed the other thermoplastic materials (ABS, nylon) used in this study, with higher work-to-failure in Z-direction. The work of Rios²² reported the reactive formulation developed gel strength between 2 to 60s after mixing. With this fast-curing speed, the deposited layer can develop sufficient strength to sustain the weight of the subsequent printed layers, to afford the structure integrity. A printability map was proposed through empirical screening of different proprietary formulations. They suggested that successful REX formulations need to meet following criteria: (1) The initial ratio between loss modulus (G'') and storage modulus (G') should be less than 1.5; (2) The initial G' should be greater than 2000 Pa; (3) G' and G'' should be more than 1 MPa and 0.6 MPa after 6 min²². Despite the undisclosed information related to the formulation, this study showed the great potential from REX process, especially in improving the anisotropy issues. It also highlighted the importance of tailor the rheology of the reactive precursors and the reaction kinetics, for the success of REX printing.

To demonstrate the capabilities of REX in a large-scale, a group of researchers from Oak Ridge National Lab, United States together with Magnum Venus Products, developed a system capable of printing volume up to 4.88m x 2.44m x 1.02m in height length, width, height respectively. In this study, A polyester and vinyl ester base resin was investigated, together with peroxide catalyst. Rheology modifiers were also adopted to tune the rheology of the formulation. A big honeycomb structure with gradient infill as shown in Figure 2- 25, was fabricated to show the potential of application of such airfoil geometry used in wind turbine blade structure⁸⁶.

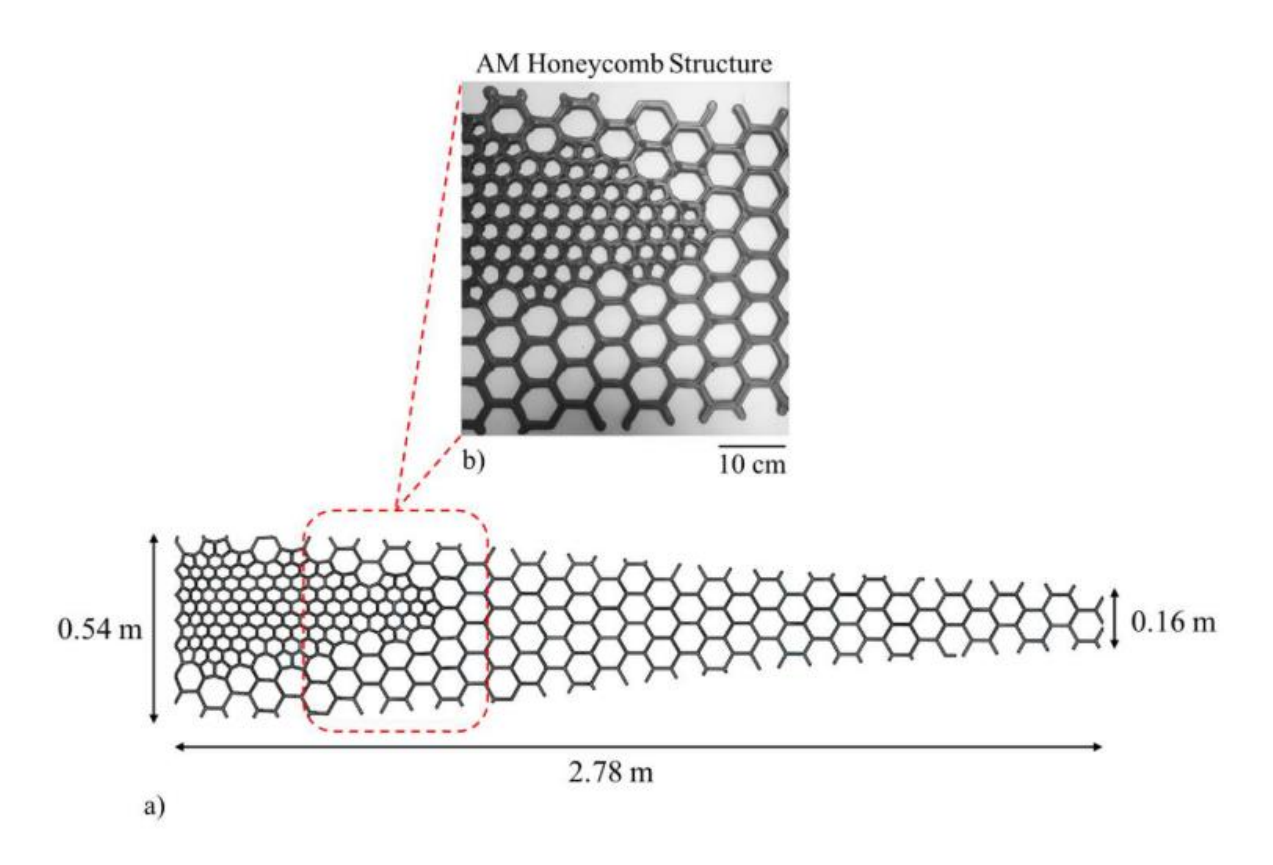


Figure 2- 25. a) Schematic of a honeycomb structure with gradient infill pattern. b) Actual honeycomb prints using vinyl ester materials. Figure taken from Lindahl⁸⁶, reproduced with permission of rights holder.

Romberg⁹¹ conducted a study using the same large REX printer, a proprietary highly exothermic reactive thermoset formulations were used to print a thin-wall structures. They reported tuning the viscoelastic properties of the feeds and print parameters could mitigate the potential yielding failure of the printing caused by bead instability.

Uitz⁸⁷ reported the use of a commercial EPON811 epoxy resin mixed with EPIKURE 3271 curing agent in a 4:1 volume ratio through the custom-built benchtop REX system, as shown in Figure 2- 26. This epoxy resin was reported to a rapid gel time of 1 min. However, due to the low viscosity of EPON811, the rheology of the resin still needs to be tailored with a thickening agent, fumed silica to afford the structure integrity when printing multiple layers without collapsing or sagging. Various level of fumed silica loadings was compared from 0% to 9% by weight, and it was found that structure with vertical edges were failed to be attained with filler loading below 2.5%. Increasing the filler loading to 3.5% helped to keep the structure integrity in the vertical edge. Higher level of filler loading would be beneficial of retaining overhangs, in the meantime the prepared mixture feed needs de-gassing to prevent the potential micro defects in the final print caused by entrained gas. The focus of the this centred on mechanical properties characterisation of the REX printed as a function of orientation. They reported that the tensile modulus and ultimate strength are isotropic, but elongation at break and toughness still depend on the orientation. The attribute the isotropic mechanical properties to the interlayer crosslinking ⁸⁷.

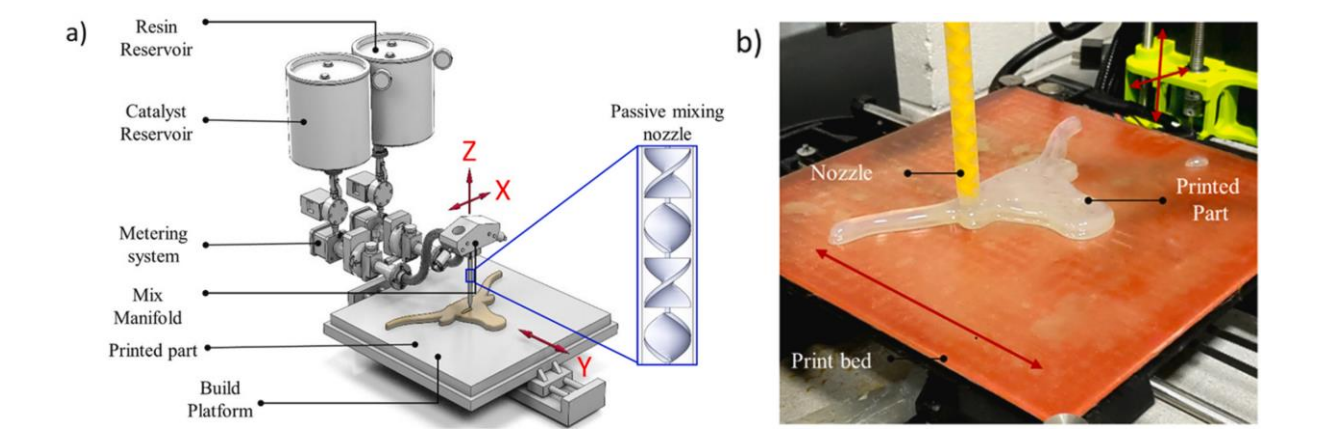


Figure 2- 26. a) Schematic of a benchtop REX system. b) Demo prints of a longhorn logo from the custom-built REX system. Figure taken from Uitz⁸⁷, reproduced with permission of rights holder.

Ren¹⁴ performed the mixing through an active mixer, other than the abovementioned REX system with passive mixer. A non-linear mechanical gradient PU structure was produced via a custom-built REX coupled with functional modelling of material properties¹⁴. The functional graded PU structure was fabricated through tuning the content fraction of an undisclosed third component along with the isocyanates (4,4 Diphenyimethane diisocyanate), and polyether polyol, which described by the authors as the additive to modify the hardness and modulus of the PU print parts. Nevertheless, the success of printing PU parts with various mechanical gradient, requires the loading of fumed silica as rheology modifier¹⁴.

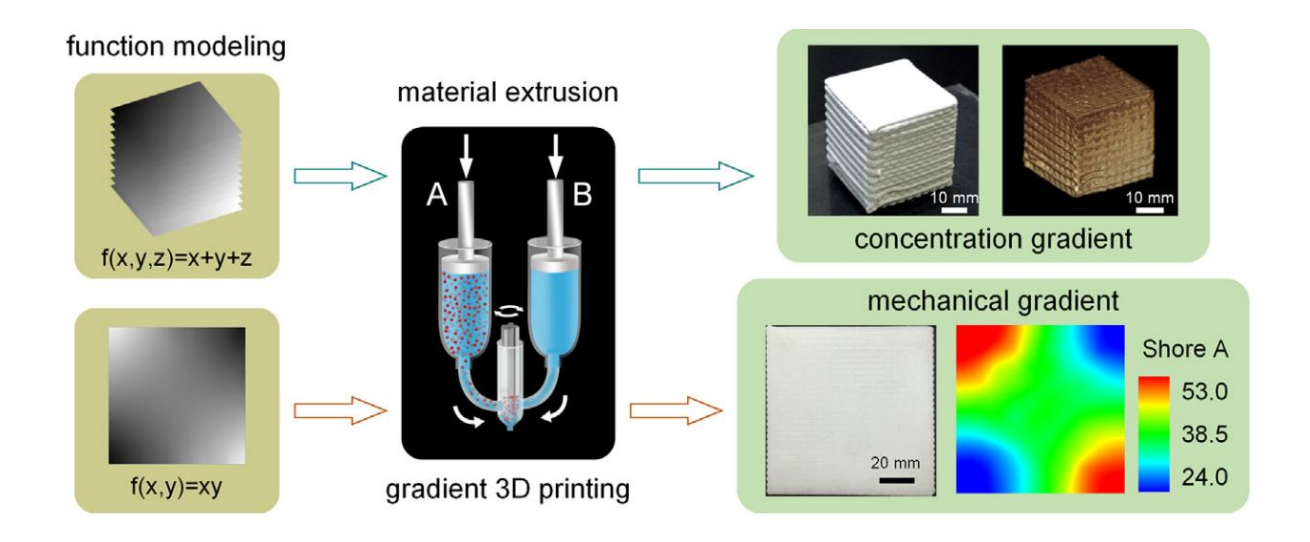


Figure 2- 27. a) The workflow of fabricating both 2D and 3D functional gradient structure with a REX system with active mixer, coupled with grey scale modelling. Figure taken from Ren¹⁴, reproduced with permission of rights holder.

2.4.1 Commercial examples

In summary, REX holds the promise to address the anisotropic issues seen in other AM process²². It offered the fast-printing speed⁸⁷ and capability to print large scale thermoset structures⁸⁶. Chromatic 3D Materials has pushed for more industry applications from their proprietary polyurethane formulations⁹², based on the REX system. As one of the commercial examples, they managed to produce rubber track pads directly onto metal plates for tractors with the same durability and abrasion resistance as the original parts. Besides, they delivered rubber grommets to help a supplier in automotive industry, avoiding production shut-down due

to a supply chain shortage. Without the need for post-processing (e.g., de-powdering, blasting seen in powder bed fusion process; or support removal in VAT Photopolymerisation), REX system can deliver more readily available industry grade elastomers to customers. It saves the capital investment and maintenance cost for the post-processing equipment other AM technologies need to embed with.

Despite the commercial success proven by Chromatic 3D Materials, All the academic paper highlighted the needs of incorporation of rheology modifier to tune the printability of the reactive feeds, along with reaction kinetics. However, the systematic study of REX process is clearly missing in terms of printability screening of new PU formulations, the effect of rheology filler (such as fumed silica) on the REX process.

2.5 Silica Nanoparticles (SiO₂) as reinforcing filler

Silica nanoparticles (Si NPs or SiO₂) have widely been investigated and used as reinforcing fillers in polymer composite system. They were introduced to the system to enhance the flowability, processability and other material functionality, such as thermo-mechanical property. The silica nanocomposite system has received considerable attention, owing to the ease of synthesis and functionalisation, high specific surface area providing larger interface between the particle and the matrix.

The review will focus on the applications of SiO₂ as reinforcing filler in AM field, primarily focused on two processes: vat photopolymerisation and material extrusion. The surface functionalisation of SiO₂, and its applications as reinforcing filler will be discussed.

2.5.1 SiO₂ Reinforced Composite via AM

The introduction of SiO_2 into photo-curable resins for SLA process was reported to increase the curing rate and improve the product tensile / compressive strength $^{31-33}$. It was great of interest to incorporate SiO_2 into vat photopolymerisation due to their reinforcing effect in

mechanical properties, and their ability for being a rheology modifier in the photo-curing resin⁹³.

The success of vat photopolymerisation depends on the viscosity and the refractive index of the resin, whereas the viscosity can influence the flowability of the resin and the refractive index can determine if the UV lights are absorbed or scattered in the desirable ways. An incomplete curing of the resins can happen when the viscosity and refractive index are not in the accepted range. To ensure the correct resin viscosity and refractive index, the SiO₂ introduced to the resin as reinforcing agent needs to equip with the right morphology. The effect of the morphology of the reinforcing agent on the reinforcing effect was presented, by introducing silica (SiO₂), attapulgite (ATP), and organic montmorillonite (OMMT), corresponding to sphere (0D), rod like (1D) and sheets (2D) respectively into the stereolithography resin. It was reported that the curing speed was improved for the SiO₂ filled resin, but not in the other two counterparts. It was also found SiO₂ filled resin demonstrated the best reinforcing effect in the tensile strength. This was attributed to the nanoparticle morphology, that the SiO₂ reinforced resin can allow full penetration of the UV light through the resin, which in contrast is not the case for ATP and OMMT reinforced resin. The refraction/reflection of the UV light was more prominent in the latter two cases. The sphere morphology of silica nanoparticle was shown to be the best resin reinforcing agent³². These effect of nanoparticle morphology on the printing quality was also demonstrated by Subramanian⁹³, when printing a blend of commercial photopolymer resins and three types of silica nanoparticles (fumed silica (fractal structures), precipitated silicas (sponge-like structures) and colloidal silica (discrete particles)) via digital light projection (DLP). It was reported that both the harness and elasticity were improved with addition of silica nanoparticles, and with incorporation of 10 wt.% fumed or precipitated silica, the hardness and tensile strength was enhanced by 58 and 141% respectively⁹³.

Dizon³³ reported the impact of silica nanoparticles loadings on the rheology and thermomechanical properties of printed poly (ethylene glycol) diacrylate (PEGDA)/ SiO₂ via SLA was investigated. The results showed the highest reinforcing effect in terms of the tensile strength, was demonstrated in 1 wt.% loading. Higher silica nanoparticles loading led to inferior printed properties, owing to the aggregation of silica nanoparticles. The homogeneity in the nanoparticle dispersion in the polymer matrix is a key factor determine the reinforcing effect, especially at higher loadings³³.

Si NPs were mixed with poly (methyl methacrylate) (PMMA) beads to produced SiO₂ reinforced filaments *via* a single-screw extruder. The composite filaments were then 3D printed via FDM. With the addition of SiO₂, the composite showed enhancement in glass transition temperature, young's modulus, elongation at break and ultimate tensile strength (UTS) compared with bare PMMA system. The increment in material properties were attributed to the H-bonding between PMMA and hydroxyl groups on the SiO₂ surface. These interfacial interactions between particles and polymer matrix reduced the chain mobility and hence led the stress transfer from the polymer matrix to the particles⁹⁴.

A PMMA grafted Si NP (SiO₂-PMMA) was firstly synthesised, and subsequently incorporated into the PMMA filaments as reinforcing fillers for PMMA composite printing *via* FDM. The FDM printed SiO₂-PMMA reinforced PMMA composite, exhibited a significant improvement compared with the counterparts (pure unfilled PMMA), with 65% increase in young's modulus, 116% increase in UTS. This substantial boost of mechanical properties were ascribed to the increasing number density of interfacial entanglements between SiO₂-PMMA and PMMA matrix⁹⁵.

Besides the applications in FDM, there are a great number of articles discussed the significances of SiO₂ as rheology modifiers using the DIW process^{35,96–98}, as the viscoelastic properties of the DIW ink needs to be robust enough to sustain the deposited shape before the crosslinking starts. In all cases, Si NPs served as rheology modifier to improve the printability of the inks for DIW process, by (1) enhancing the viscosity and modulus of the ink and (2) afford the inks with shear thinning and yield stress behaviour (the yield stress point is defined as the cross-over between the storage modulus and loss modulus)⁹⁶. An example of effect of Si NPs on the rheology of the DIW ink can be seen by Figure 2- 28.

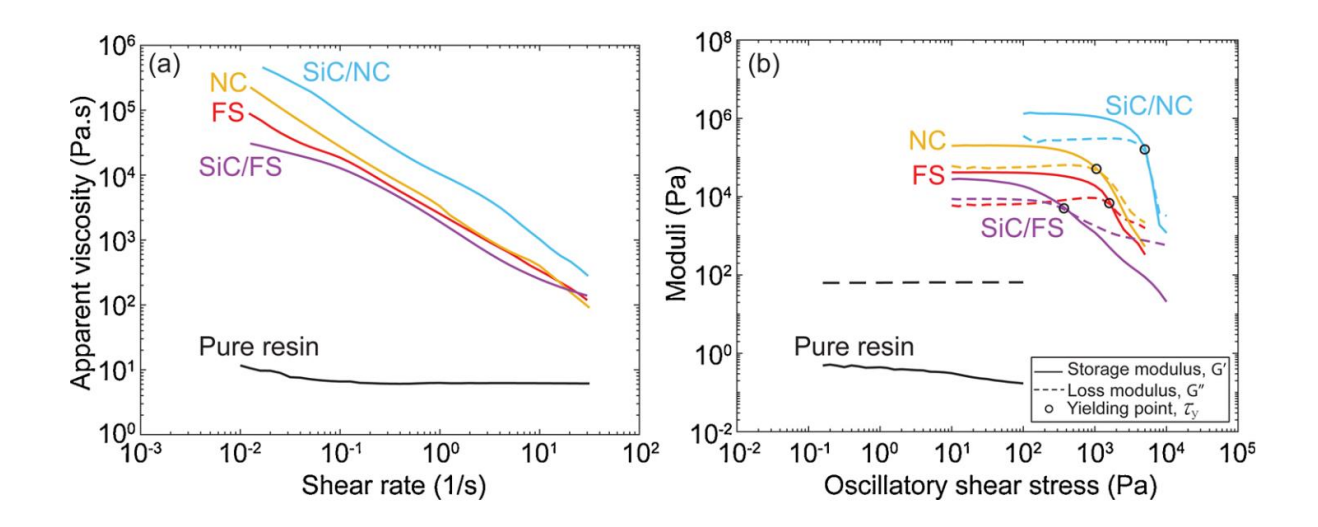


Figure 2- 28. Rheological behaviour of different fillers (Silica carbide (SiC), Fumed silica (FS), Nanoclay (NC)) on the epoxy filled DIW inks. (a) viscosity vs shear rate. (b) moduli vs oscillatory shear stress. Figure taken from Hmeidat⁹⁶, reproduced with permission of rights holder.

Summary of SiO₂ reinforced composite via AM

It can be seen from the examples that Si NPs proves to be the favourable nanofiller to be introduced in different AM process, to enhance the thermal stability and mechanical properties of the printed composite. It is important to note that, uniform dispersion of the filler in the polymer matrix is the key for the success in Si NPs reinforcing performances. This filler/matrix interaction can be influenced by the filler morphology, the amount of filler loadings, different mixing methodology (ultrasonic, heat assisted, centrifuge).

2.5.2 Functional SiO₂ reinforced composite

There are two benefits for functionalise the surface of SiO₂, to gain superior reinforcing effects: improve the dispersion of filler in the matrix and offer additional covalent bonding. (1) One of the most common problems when handling the NPs is the particle agglomeration. This also applies for Si NPs and Functional Si NPs. The non-surface treated Si NPs are hydrophilic, with the presence of the polar OH groups on the particle surface. The particles have no tendency to move towards to the non-polar and weakly polar groups, this makes the particles dispersed poorly in the polymer matrix. This leads to poor wetting at the interface between filler and matrix. Consequently it can deteriorate the strength of the composite, as the force will be distributed un-evenly at the point³⁶. (2) The advantages of Si NPs reinforced composites have been attributed to physical interactions/entanglements being established between the fillers and the fillers/matrix. Potential benefits offered by SiO₂ NPs that act as a reactive filler raised greater interest, such that covalent bonds with the polymer matrix are established in the composite. These covalent linkages should extend the typical physical interactions, such as hydrogen bonding, that are responsible for the matrix to filler interactions within the current systems^{25,38,39,99}.

Through functionalisation of the SiO₂ with different silane coupling agents (with functional groups such as amino (NH₂), alkyl chain (C), epoxide (EP)), various interfacial interaction between the filler and matrix can be attained. In one study, they compared reinforcing effect of three different functional SiO₂ (SNP-NH₂, SNP-C, SNP-EP) with an un-functionalised SiO₂ (SNP) in an epoxy formed by diglycidyl ether of Bisphenol- F type epoxy resin (DGEBF, EPON862) and diethyl toluene diamine hardener (DETDA, JER 113).

The interfacial network between the functional Si NP fillers with the matrix was illustrated by Figure 2- 29. The authors claimed the improved dispersion of SNP-NH2 and SNP-EP, resulted from the amino and epoxide groups decreased the surface energy and enhanced the compatibility between the filler the epoxy matrix. Whereas for SNP-C, the increased repulsion between the fillers due to the non-polar long alkyl chain and the polar organic matrix, diminished the compatibility between the filler and matrix, preventing the epoxy absorbed onto the filler surface. The covalent bonds formed between the amino and epoxy enhanced the viscosity and thermal stability, promoting a longer pot and shelf life of the amine-epoxy nanocomposites²⁵.

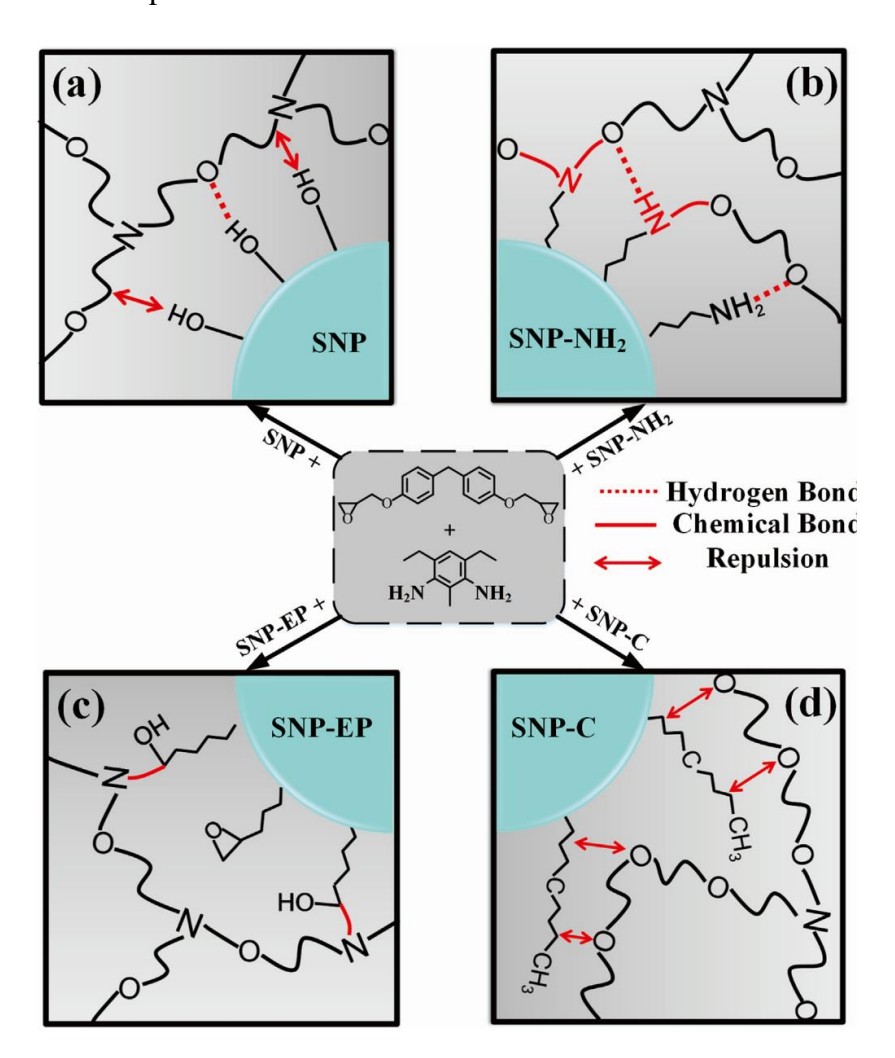


Figure 2- 29. Schematic of interfacial network between the functional Si NPs: (a) SNP, (b) SNP-NH2, (c) SNP-EP, and (d) SNP-C and the amine cured epoxy system. Figure taken from Guo²⁵, reproduced with permission of rights holder.

The inclusion of functional SiO₂ into powder-based AM, more specifically selective laser sintering (SLS) process has shown promising reinforcing effect in both thermal stability and mechanical properties of the printed products³⁴. They reported a functional nanosilica/nylon-12 composite feed with 3 wt% functional nanosilica loading, was prepared by dissolution-precipitation. The functional nanosilica was surface modified using a silane coupling agent: 3-aminopropyl triethoxysilane (APTS). The uniform dispersion of the functional Si NPs in the final printed PA12 composite parts was examined and demonstrated by the SEM. The strong interfacial interaction between the functional SiO₂ and the polymer matrix, claimed to be the key driver to afford such a reinforcing effect³⁴.

The benefits of additional covalent network in the filler/matrix network have been proved in the epoxy/amine-functionalised Si NPs filled composite system. Amine functionalised Si NPs prepared using 3-aminopropyltriethoxysilane (APTES) as coupling agent, were introduced to an epoxy system (The diglycidyl ether of bisphenol A, DGEBA) cured between the isophorone diamine (IPD) hardener.

The amine functional groups served the role as a co-hardener, to allow Si NPs to covalently incorporated into the epoxy matrix, as depicted in Figure 2- 30. This additional interconnected network was attributed to the enhancement in the thermo-mechanical properties³⁸. Rostami⁹⁹ reported similar reinforcing effect in both glass transitional temperature and mechanical performance of the synthesised composite parts, when dispersing amine functional silica NPs in PU system. They proved the urea linkage between the reaction of amine and isocyanates established in the hard segment of the PU matrix. They claimed this interaction between the amine functional and the matrix also led to better dispersion.

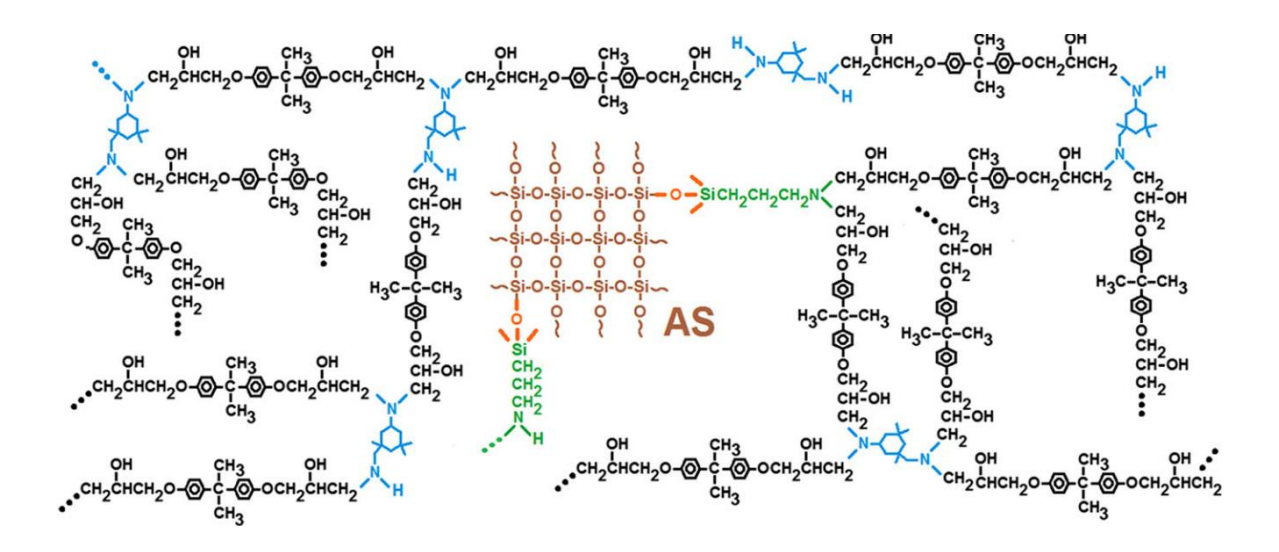


Figure 2- 30. Schematic structure of the DGEBA (black colour)/IPD (blue colour)/amine functionalized Si NPs (orange and green colour). Figure taken from Behniafar³⁸, reproduced with permission of rights holder.

Despite the great promise shown in applying the functional Si NPs as reinforcing filler in epoxy or PU network, there are no literatures reporting of introducing such concept in AM PU.

Summary of SiO₂ as reinforcing filler in AM

SiO₂ is one of the most favourable nanofiller to be incorporated in different AM process, to improve the printability, enhance the thermal stability and mechanical properties of the printed parts. The dispersion of SiO₂ to ensure the good interfacial relationship between the filler and matrix, remains to be the pivot which determining if a strong reinforcing effect can be afforded with the filler inclusion. To ensure the good interfacial properties between the SiO₂ and matrix can be attained, surface functionalisation through different silane coupling agents is recommended. Besides the benefit of improve dispersion of the Si NPs, it can also afford additional covalent bonding with the matrix network such as PU, to further enhance the composite strength. However, there is currently no such study reported to leverage this concept in AM PU.

2.6 Gaps in research

From the literature review, it demonstrates that there are a lot of interests in unlocking the potential of PU chemistry, through the customised applications offered via AM. Currently in the research of AM PU, there are two main streams. The first stream of research conducting AM PU, started from pre-synthesised PU feedstocks either in the form of filament, paste, powder or resin. This group of applications limited the opportunities to selectively tailoring the material properties via in-situ reaction, offered by the second stream.

Reactive inkjet 3D printing and REX dominate the second stream, with REX offers the wider formulation options. REX is the AM technology, which is still in an early stage with few research in the field, focusing on demonstrating the capability of the technology with superior isotropic properties, large scale, fast printing speed applications. Clearly, there is a need for systematic research looking into AM PU via REX, to understand the fundamentals especially related to the rheology effect from the filler (SiO₂) on the process.

The effect of the filler (SiO₂) in the current AM applications reveals the potentials of reinforcing benefits, such as enhancement in thermo-mechanical strength. To further exemplify the applications of such reinforcing benefits, it is reported that functionalisation of the SiO₂ surface is needed to improve the dispersion of nanoparticles in the matrix, also affording additional covalent bonding to enhance the network between the filler and matrix. Such a dual reinforcing effect has shown promises in the polymer matrix from traditional synthesis route. However, there is no literatures reporting the use of functional filler (SiO₂) in AM PU, which would need to be explored.

CHAPTER Three

3 Materials and Methods

In this chapter, the methods used throughout this research project will be presented, including *Feed formulation and preparation, Printability Analysis, Reactive Extrusion 3D Printing* (REX) and *Printing Characterisation*. The materials used in different results chapters will be revealed under the section *Feed formulation and preparation*.

3.1 Methods

The following section starts by presenting the polyurethane formulations used in chapter 4-6 and how these formulations were prepared with the materials (isocyanate, polyol, commercial additives, in-house synthesised functional silica nanoparticles (FSP)), including the synthesis methods of the FSP. Then printability evaluation of the isocyanate and hydroxyl feed will be then presented, following by a detailed description of the REX system. Finally, the characterisation methods of the printed parts are explained.

The polyurethane (PU) was synthesised using the commercially available starting materials, since the study started from evaluating the suitable formulations for the REX system. Starting with the readily available materials would reduce development time for the new feed materials, consequently higher focus can be put in fundamentally understanding the REX process.

There are three main feed materials for PU reaction, which comprise isocyanate (di-functional or multi-functional); diol (number of functional group f=2) or polyol (f>2); additives (catalyst and nano-fillers). Isocyanates with different types, such as aliphatic, aromatic, and cycloaliphatic were all picked for the formulation screening study, with the aim to find the optimum PU formulation for REX system.

In addition, to study the effect of functional filler on the REX PU, amine functionalised silica particles were developed in-house, and used as additives in the PU formulations.

3.1.1 Feed Formulation and Preparation

Feed formulation in Chapter 4 Printability and Process Analysis

The materials in Chapter 4 were selected to understand and evaluate the printability of a given polyurethane formulation for REX system.

Isocyanate

Poly [(phenyl isocyanate)-co-formaldehyde] (PMDI Mn340 and Mn400)

Figure 3- 1. The chemical structure of Poly [(phenyl isocyanate)-co-formaldehyde]. The molecular weight used in this project was Average M_n =340, 400.

The first isocyanate, Poly [(phenyl isocyanate)-co-formaldehyde], is a highly reactive, multifunctional, aromatic pre-polymer which is commonly used to producing rigid PU foams¹⁰⁰. The two PMDIs used in this study have the specific activity of 2.7 and 3.2 isocyanates/molecule for average Mn=340 and 400 respectively.

Isophorone diisocyanate (IPDI)

Figure 3-2. The chemical structure of isophorone diisocyanate.

The second isocyanate, isophorone diisocyanate (IPDI), is a di-functional cycloaliphatic monomer commonly used in producing thermoplastic PU. IPDI was used in producing light-stable PU coatings¹⁰⁰.

Desmodur® N3900

Figure 3-3. The chemical structure of Desmodur® N3900.

The third isocyanate, under the commercial brand name Desmodur® N3900, is a multifunctional polyisocyanate crosslinker used for producing thermoset PU coatings⁴¹.

Hexamethylene Diisocyanate (HDI)

Figure 3-4. The chemical structure of Hexamethylene diisocyanate.

The fourth isocyanate, Hexamethylene diisocyanate (HDI), is a linear di-functional aliphatic short chain monomer. As one of the low molecular weight isocyanate, PU produced using HDI is often hard and stiff, owning to the high concentration of urethane bond⁴¹.

Polyol

poly (ethylene glycol)-block-poly (propylene glycol)-block-poly (ethylene glycol) PEG-PPG-PEG 1900

$$H = \begin{bmatrix} O \\ X \end{bmatrix} = \begin{bmatrix} CH_3 \\ Y \end{bmatrix} = \begin{bmatrix} O \\ Z \end{bmatrix} = \begin{bmatrix} O \\ Z \end{bmatrix}$$

Figure 3- 5. The chemical structure of poly (ethylene glycol)-block-poly (propylene glycol)-block-poly (ethylene glycol). The molecular weight used in this project was Average $M_n = 1900$.

The polyol, poly (ethylene glycol)-block-poly (propylene glycol)-block-poly (ethylene glycol) (PEG-PPG-PEG 1900) is an amphiphilic block copolymer, which is sold under the trade name: Pluronic® L-35. It is characterised by the primary hydroxyl groups in the hydrophilic PEG blocks and the hydrophobic PPG blocks, whereas PEG blocks accounting for 50 wt.% in composition for PEG-PPG-PEG 1900.

This block copolymer with various block size and length, different PEG/PPG block ratio, are readily available in the market. Due to its excellent biocompatibility and it is widely used in pharmaceutical industry. It is known for the application as thermogelling system in drug delivery applications¹⁰¹. Different PEG/PPG block ratios can lead to different surface behaviours of the polymer and can subsequently affect the mixing and the phase separation of the derived PU⁵⁹. PEG-PPG-PEG 1900 was selected, based on the rheological properties and mixing behaviour when reacting with different isocyanate constituents.

1,4 Butanediol (1,4-BD)

Figure 3-6. The chemical structure of 1,4-Butanediol.

1,4 – Butanediol (1,4 – BD) is commonly used as chain extender in the PU reaction, to extend the chain length of the hard segment and improve the mechanical properties of the PU⁵⁰. Here in this study, 1,4 –BD was blended into the formulation, to ensure the correct 1:1 volumetric mixing ratio between isocyanate and hydroxyl side can be achieved, and enhance the cross-linking in the derived PU, and improve the printed PU properties.

Commercial Additives

Fumed Silica (SiO2-PDMS)

$$\begin{array}{c|c} & CH_3 \\ \end{array}$$

Figure 3-7. The chemical structure of fumed silica (FS).

Fumed silica, is a synthetic silica particles which has been surface treated, with polar groups to form an attraction network of silica chain¹⁰². It is commonly used to improve the rheology of a given polymer matrix, such as epoxy¹⁰³³⁷, PU³⁶. In this study, Polydimethylsiloxane (PDMS)-coated hydrophobic fumed silica particles (Cabosil TS720, Cabot Corporation, United States) were selected as the rheology modifier, due to its previous proof in tuning the rheology of the formulation for material extrusion 3D printing process⁹⁶¹⁰⁴.

Dibutyltin dilaurate (DBTDL)

$$CH_3$$

 $CH_2(CH_2)_9CH_3$
 $CH_3(CH_2)_9CH_2$
 $CH_3(CH_2)_9CH_3$

Figure 3-8. The chemical structure of Dibutyltin dilaurate (DBTDL).

DBTDL is the common tin-based catalyst widely used in the isocyanate/hydroxyl reaction to synthesis PU¹⁰⁵¹⁰⁶. Tin-based catalyst (DBTDL) was found more efficient in catalysing the isocyanate/hydroxyl reaction than the amine based catalyst, such as 1,4-Diazabicyclo 2.2.2 octane (DABCO)¹⁰⁷. Hence, DBTDL was used to speed up the PU reaction.

Table 3- 1 summarise the five PU formulations using different isocyanate, and the same polyol as starting materials. In addition, the catalyst level was kept at 1 wt. % for all five formulations without any fumed silica as rheology modifier.

Table 3-1. Mass composition of feed formulations use in printability analysis.

Feed	Chemicals	Functionality	Formulations (wt. %)				
			HDI	IPDI	N3900	PMDI	PMDI
						Mn340	Mn400
Isocyanate	HDI	-NCO	50.2	-	-	-	-
(NCO)	IPDI		-	50.1	-	-	-
	N3900		-	-	52.3	-	-
	PMDI Mn340		-	-	-	54.0	-
	PMDI Mn400		-	-	-	-	53.5
Polyol	PEG-PPG-PEG	-OH	25.5	32.0	35.7	29.9	29.6
(OH)							
	1,4 BD	-OH	23.3	16.9	11.0	16.1	16.0
	DBTDL	catalyst	1	1	1	1	1

Table 3- 2 shows the two formulations, using PMDI as isocyanate feedstock and same polyol as starting materials. They are differed by the amount of catalyst loadings (0.5 wt. % and 1.5 wt. %).

Table 3- 2. Mass composition of PMDI Mn340 formulation with 0.5 wt. % and 1.5 wt. % DBTDL for printability analysis.

Feed	Chemicals	Functionality	Formulations (wt. %)		
			PMDI Mn340 PMDI Mn340		
			0.5 wt. % DBTDL	1.5 wt. % DBTDL	
Isocyanate	PMDI Mn340	-NCO	53.7	53.2	
(NCO)					
Polyol	PEG-PPG-PEG	-ОН	29.7	29.4	
(OH)	1,4 BD	-OH	16.1	15.9	
	DBTDL	catalyst	0.5	1.5	

Table 3- 3 shows the formulation using PMDI Mn340 as isocyanate feedstock and the same polyol feedstock. The key characteristic for this formulation is 5 wt. % fumed silica was introduced on both isocyanate and polyol side.

Table 3-3. Mass composition of PMDI Mn340 formulation for process optimisation.

Feed	Chemicals	Functionality	Formulations (wt. %)
			PMDI Mn340 1 wt. % DBTDL
Isocyanate	PMDI Mn340	-NCO	53.3
(NCO)	Fumed silica	Rheology modifier	5.0
Polyol	PEG-PPG-PEG	-ОН	29.8
(OH)	1,4 BD	-ОН	15.9
	DBTDL	catalyst	1.0
	Fumed silica	Rheology modifier	5.0

Note: The mass composition for fumed silica in isocyanate feed and polyol feed was determined with respect to the isocyanate (PMDI) mass and total mass of polyol (PEG-PPG-PEG+1,4 BD) respectively.

Feed formulation in Chapter 5 Feed Rheology Properties and Mixing Modes

Table 3- 4 shows the three formulations (MM1, MM2 and MM3). The differences for these formulations come from the fumed silica loading in the isocyanate feedstock. All the materials used here are the same as shown in Feed formulation in Chapter 4 Printability and Process Analysis.

Table 3-4. Mass composition of feed formulations for three mixing modes (MM1, MM2 and MM3).

	Chemicals	Functionality	MM1	MM2	MM3
	Chemicais		(wt. %)	(wt. %)	(wt. %)
Isocyanate	PMDI Mn340	-NCO	53	53	53
(NCO)	Fumed Silica	rheology modifier	5	2.5	1
	PEG-PPG-PEG	-ОН	30	30	30
Polyol (OH)	1,4 BD	-ОН	16	16	16
(OII)	Fumed Silica	rheology modifier	5	5	5
	DBTDL	catalyst	1	1	1

Note: The mass composition for fumed silica in isocyanate feed and polyol feed was determined with respect to the isocyanate (PMDI) mass and total mass of polyol (PMDI+1,4 BD) respectively.

Feed formulation in Chapter 6 Functional Silica Nanoparticle as Reactive Fillers

Table 3- 5 shows the three formulations using the same mass composition for all the materials. The difference lies in the rheology modifier introduced in the polyol feed. The in-house developed functional silica nanoparticles (SiO₂-NH₂ and SiO₂-NH₂/CH₃) are mixed into the polyol feed.

Table 3-5. Mass composition of feed formulations using different silica nanoparticles.

	Chemicals	Functionality	SiO ₂ -PDMS	SiO ₂ -NH ₂	SiO ₂ -NH ₂ /CH ₃
			(wt. %)	(wt. %)	(wt. %)
Isocyanate	PMDI Mn340	-NCO	53	53	53
(NCO)	Fumed Silica	rheology modifier	1	1	1
	(SiO ₂ -PDMS)				
Polyol	PEG-PPG-PEG	-OH	30	30	30
(OH)	1,4 BD	-OH	16	16	16
	Fumed Silica	rheology modifier	5	-	-
	(SiO ₂ -PDMS)				
	SiO ₂ -NH ₂	rheology modifier	-	5	-
	SiO ₂ -NH ₂ /CH ₃	rheology modifier	-	-	5
	DBTDL	catalyst	1	1	1

Note: The mass composition for silica particles in isocyanate feed and polyol feed was determined with respect to the isocyanate (PMDI) mass and total mass of polyol (PEG-PPG-PEG+1,4 BD) respectively.

Functional Silica Nanoparticles (FSP)

Two steps were involved in synthesising FSP. First step is to hydrolysis and condensate an alkyl silicate with the presence of solvent and catalyst. Second step is to use coupling agents to functionalise the surface of the first-step produced silica particle.

Tetraethyl orthosilicate (TEOS)

Figure 3-9. The chemical structure of Tetraethyl orthosilicate (TEOS).

TEOS is the widely used alkyl silicate precursor in producing silica particles 30,108 . It hydrolysis in alcohol (e.g. methanol/ethanol) in the presence of catalyst, to form ethoxysilanols (e.g. $Si(OC_2H_5)_3OH$). Then a condensation reaction results in monodispersed silica particles with a loss of water/alcohol¹⁰⁹.

Ethanol (EtOH)

Figure 3-10. The chemical structure of Ethanol (EtOH).

Ethanol is the common alkaline solvent used in the silica particles synthesis¹⁰⁸. It was reported that stable and homogenous silica particles 7.1 ± 1.9 nm were produce in ethanol condition¹¹⁰.

Ammonia (NH₄OH)

Figure 3- 11. The chemical structure of Ammonia (NH_4OH) .

The ammonia serves as the catalyst, by promoting the hydrolysis rate of the TEOS and the condensation rate of the hydrolysed precursor in producing the silica nanoparticle^{108,110,111}.

(3-aminopropyl)triethoxysilane (APTES)

$$\begin{array}{c|c} & O & CH_3 \\ \hline H_3C & O & Si & NH_2 \end{array}$$

Figure 3-12. The chemical structure of (3-aminopropyl)triethoxysilane (APTES).

APTES is an aminosilane coupling agent, which can functionalise the silica particle surface with amine groups by silanisation^{38,112}.

n-propyltriethoxysilane (PTES)

$$CH_3$$
 O
 CH_3
 CH_3
 CH_3
 CH_3

Figure 3-13. The chemical structure of n-propyltriethoxysilane (PTES).

PTES is another coupling agent with similar structure to APTES, with the alkyl groups substituting the amine groups in the APTES.

Amine Functional Silica Nanoparticles (SiO₂-NH₂)

Figure 3- 14. The chemical structure of amine functional silica nanoparticles.

SiO₂-NH₂ is the amine FSP synthesised in-house. It was used as a co-hardener with the multiple amine groups on the particle surface reacting with epoxy or isocyanate polymer matrices to form the desired covalent particle-matrix bonds and thus provide enhanced mechanical properties³⁸³⁹.

Amine/alkyl Functional Silica Nanoparticles (SiO₂-NH₂/CH₃)

Figure 3-15. The chemical structure of Amine/alkyl Functional Silica Nanoparticles.

SiO₂-NH₂/CH₃ is the amine/alkyl FSP synthesised in-house. The key characteristic of SiO₂-NH₂/CH₃ is the alkyl chain on the particle surface could promote the hydrophobicity, reduce the particle aggregation³⁶.

The strategy taken to generate the functionalised filler particles, used in Chapter 6 is depicted in Figure 3-16.

Figure 3-16. Synthesis route for amine FSP: SiO₂-NH₂ and amine/alkyl FSP: SiO₂-NH₂/CH₃.

Synthesis of the amine functionalised SiNPs (SiO_2 - NH_2):

Tetraethyl orthosilicate (3 mL, 13.43 mmol) was added to a mixture of ammonium hydroxide (4.4 mL, 35%) and ethanol (110 mL) and left to stir at 1000 rpm at ambient temperature for 3 hours. (3-Aminopropyl)triethoxysilane (4.72 mL, 20.17 mmol) was then added slowly to the mixture and stirred for 3 h. The solvent was removed in vacuo to provide a fine white powder. The powder was then washed by ethanol (3×25 mL) and the mixture was centrifuged in order to isolate the solid. Between each wash the dispersion of particles in fresh ethanol was vortexed. The powder was then dried in a vacuum oven at 100 °C for 2 hours at 400 mbar.

Synthesis of the mixed amine/alkyl functionalised SiNPs (SiO₂-NH₂/CH₃)

Absolute ethanol (110 mL) and 4.4 mL of ammonia solution (35%) were mixed in a flask before the addition of tetraethyl orthosilicate (TEOS). The solution was stirred at room temperature for 2.5 hours. (3 Aminopropyl)triethoxysilane (APTES) and n propyltriethoxysilane (PTES) were then added slowly and simultaneously to the solution and left overnight (See Table 3- 6 for the reactant quantities). The solution was then centrifuged at 4000 rpm for 10 minutes and the solution was decanted. The particles were washed 3 more times with fresh ethanol following the same procedure. The samples were then dried in an oven at 30 °C under vacuum.

Table 3-6. The quantities of silica coupling agents used in the synthetic procedures to produce the functionalised SiNPs.

	SiO ₂ -NH ₂ /CH ₃ -01		SiO ₂ -Nl	SiO ₂ -NH ₂ /CH ₃ -02		SiO ₂ -NH ₂ /CH ₃ -03	
	(Eq)	(mL)	(Eq)	(mL)	(Eq)	(mL)	
TEOS	1	3.00 mL	1	6.00 mL	1	6.00 mL	
APTES	0.75	2.36 mL	1	6.28 mL	0.5	3.14 mL	
PTES	0.75	2.33 mL	0.5	3.01 mL	1	6.22 mL	

Materials Summary

All chemicals were used as received without further purification. The PU materials in this study were synthesised using the following polyols and poly-isocyanates reagents.

Poly((phenyl isocyanate)-co-formaldehyde) (PMDI, CAS number: 9016-87-9, Average Mn=340 and 400), Isophorone diisocyanate (IPDI, CAS number: 4098-71-9, Molecular weight = 222.3), Hexamethylene Diisocyanate (HDI, CAS number: 822-06-0, Molecular weight = 168.2), poly((ethylene glycol)-block-poly (propylene glycol)-block-poly (ethylene glycol)) (PEG-PPG-PEG, CAS number: 9003-11-6, Average Mn = 1900), 1,4 butanediol (1,4 BD, CAS number: 110-63-4, molecular weight = 90.1), were all purchased from Sigma Aldrich and were used as received without further purification.

Dibutyltin dilaurate (DBTDL, CAS number: 77-58-7, 95%), Tetraethyl orthosilicate (TEOS, CAS number: 78-10-4), (3-aminopropyl)triethoxysilane (APTES, CAS number: 919-30-2) and n propyltriethoxysilane (PTES, CAS number: 2550-02-9) were all purchased from Sigma Aldrich and were also used as received. Desmodur® N3900, molecular weight = 504.6, the polyisocyanate and Polydimethylsiloxane (PDMS)-coated hydrophobic fumed silica particles (SiO2-PDMS) (Cabosil TS720, Cabot Corporation, United States) were kindly provided by (PPG Industries, Pittsburgh, United States). All other solvents purchased from Fisher Scientific.

Particles Characterisation

After the silica nanoparticles were synthesised, the size and morphology were characterised under Transmission electron microscopy (TEM) and the surface functional groups (amine/alkyl) were characterised by elementary analysis.

Transmission electron microscopy (TEM): TEM images of the particles were obtained to study the morphological characteristic of the particles prior to mixing with the inks. TEM images

were obtained using a JEOL 2100Plus operated at 200 kV in bright field mode equipped with a LaB6 filament as the electron source. The samples were prepared using either continuous or holey carbon films with copper grid. Particles were ground in an agate mortar and pestle prior to making an ethanol suspension. The suspension was then mixed thoroughly, and one drop was pipetted on an appropriate TEM grid. After drying the grid was loaded into the TEM microscope to be imaged.

Elemental analysis: It was conducted at MEDAC LTD using combustion analysis.

Dual Axial Centrifugal (DAC) Mixing

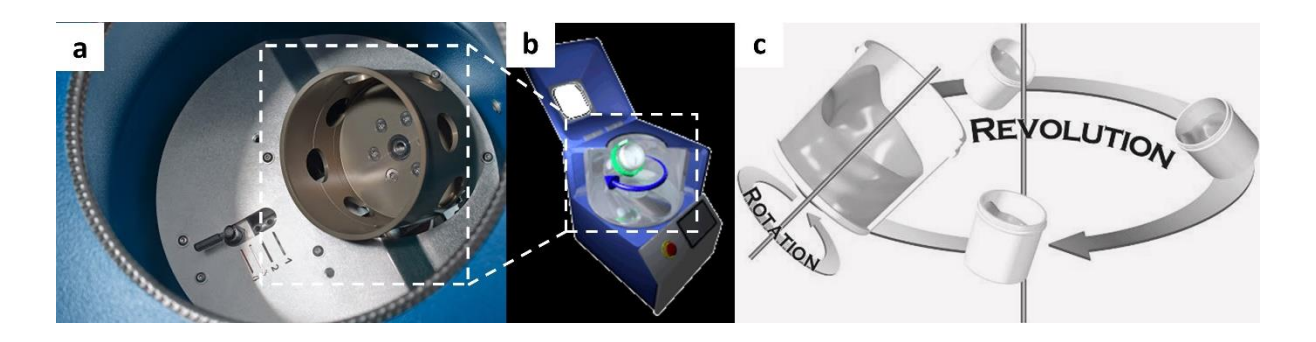


Figure 3- 17. DAC mixer working principles. a) DAC mixing chamber. b) Schematic of dual axial mixing inside chamber. c) DAC mixing principles: rotation and revolution. Images from online brochure.

Prior to being introduced to the REX apparatus, each reagent mixture was pre-mixed using a Dual Axial Centrifugal mixing unit (DAC 400 mixer, SpeedMixerTM) shown in Figure 3- 17, to prepare the separate isocyanate and polyol feedstock. Robust mixing was conducted at 2200 rpm for 20 min so homogenous mixture between the reagents and the additives was achieved. silica nanoparticles were the additive introduced to PMDI Mn340 formulation to modify the rheology and improve the printability of the feedstock ^{27,35,103,113,114}. The molar ratio between isocyanates and polyol are 1.1:1 (NCO: OH) to minimise additional reaction with both entrained and atmospheric moisture.

3.1.2 Printability Analysis

This is the first study to detail a full workflow programme, progressing from screening the printability of feedstocks through a printing optimisation for these feedstocks to achieve good resolution / reproducibility to looking at the filament quality produced for the REX system. This workflow is depicted in Figure 3- 18.

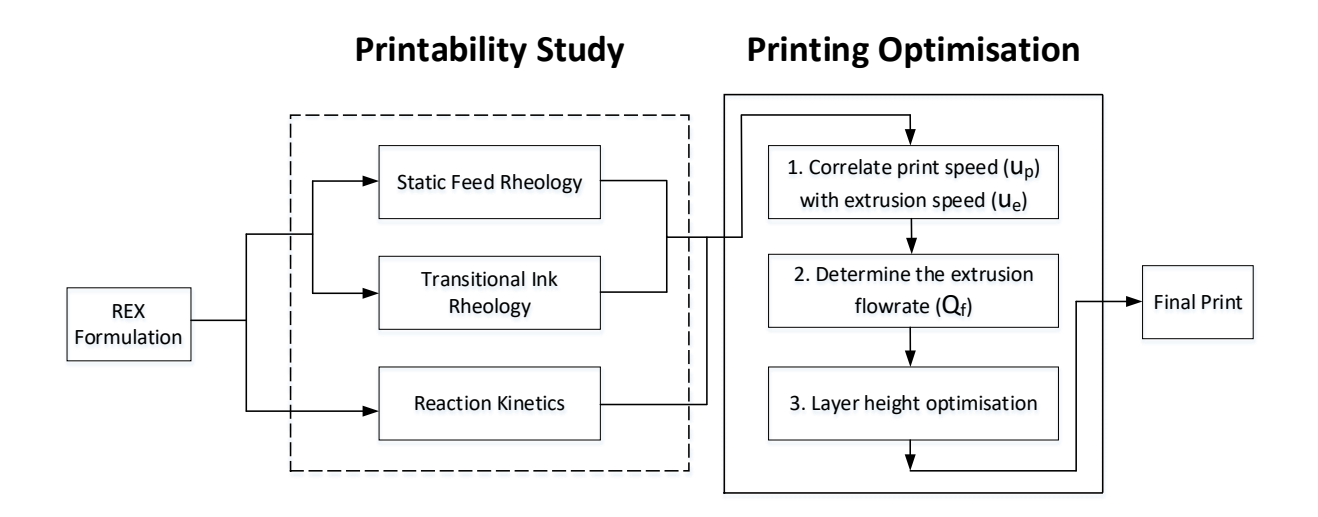


Figure 3-18. Schematic of REX workflow.

Rheology

Rheology is one of the key feed material properties to identify if the feed can be self-supportive upon extrusion. Herein, a rotational rheometer as shown in Figure 3- 19, was used to characterise the feed static and transitional feed rheology. In this rotational platform, the torque needed to shear the material is proportional to the rheological change of the loaded materials. Therefore, the system suits our needs to measure the shear viscosity and the dynamic moduli of the feed materials.



Figure 3- 19. Kinexus pro+ rheometer (Malvern Instruments, now branded as NETZSCH). Images from online brochure.

Static Ink Rheology

There are three separate tests were run to analysis the static ink rheological properties: (1) Viscosity vs shear rate; (2) Dynamic moduli (G' and G'') vs frequency; (3) Yield stress.

Static rheological properties of the NCO and OH inks were measured by the Kinexus pro+rheometer (Malvern Instruments) equipped with a 40 mm cone and plate geometry. The apparent viscosity and shear stress were recorded as a function of shear rate ranging from 1 s⁻¹ to 100 s^{-1} , at 25 °C. The shear rate range was chosen because the feed materials when mixed through static mixer will experience shear rate from 1.8 s^{-1} to 61.1 s^{-1} (tip of the nozzle), also reported from other literatures with similar 500 μ m diameter nozzle¹¹⁵.

Amplitude sweeps were performed to determine the linear viscoelastic region, automatically calculated by the software (Malvern rSpace). Subsequently, frequency sweeps were carried out to determine the viscoelastic profile of the inks at frequencies from 10 to 0.1 Hz with a fixed 1% shear strain within the pre-determined linear viscoelastic region at 25 °C. The gap between the parallel plates were set at 1 mm.

Oscillatory stress ramp tests were run to reveal the yield stress of the investigated NCO and OH inks. In this test, inks were subject to increasing shear stress from 0.01 Pa to 1000 Pa. The yield stress was determined at the cross-over point between G' and G'' data under stress-controlled oscillatory measurements ¹⁵.

In Chapter 5, two parameters were defined to compare the rheology properties between NCO and OH inks. The viscosity ratio is calculated by determining the viscosity of OH and NCO ink at the shear rate: 20 s⁻¹, which corresponding to the shear rate at the inlet of the static mixer. The elasticity ratio is determined at the frequency: 2 Hz.

Transitional Ink Rheology

Transitional rheology tests were performed to show the progression of dynamic moduli along the time, after NCO and OH inks being mixed. This was achieved by firstly loading NCO and OH inks into dual component dispense cartridges (ABM-25M1-50ml 1:1 Ratio Manual Gun, Adhesive Dispensing Ltd, UK), attached with static mixers (MBH03-16S-Mixer nozzles, Adhesive Dispensing Ltd, UK). The mixture was then deposited onto the same Kinexus protheometer (Malvern Instruments), equipped with a disposable sample plate and parallel plate spindle (25mm in diameter) (Malvern Instruments). The gap between the sample plate and spindle was set up at 0.5mm. Soon after the mixture was loaded onto the sample plate, the tests started isothermally at 25 °C, using oscillatory shear measurement (frequency at 1 Hz, 0.5% strain). Each test recorded the transitional behaviour of dynamic moduli continuously for 30 minutes. The transitional rheology tests mimicked the reaction condition in the REX system and indicated the curing kinetics of investigated formulations.

Reaction Kinetics

Fourier-transform infrared spectroscopy (FTIR): FTIR was used to investigate the conversion to PU *via* reaction between isocyanate and polyol feeds for each of the three formulations. A Frontier (Perkin Elmer) Spectrometer was used. PU samples printed from the three formulations were tested using the spectrometer immediately following extrusion from the static mixer. The spectrums were recorded from 4000 cm⁻¹ to 600 cm⁻¹, with a resolution of 4 cm⁻¹. The analysis was performed in Perkin Elmer Spectrum software, starting from normalising the designated peak in the spectrums. It followed by evaluating the normalised peak areas to determine the reaction conversion. The PU conversion was monitored by following the disappearance of the isocyanate (NCO) peak at the region from 2350 cm⁻¹ to 2100 cm⁻¹, and with a peak at 2250 cm⁻¹ 107,116,117. The reference alkane (C-H stretch) peak remains unchanged. Hence, the conversion was calculated by taking the integral of the NCO peak (from 2350 cm⁻¹ to 2100 cm⁻¹) relative to the unchanged C-H stretch peak (at around 2960 cm⁻¹) and compare to the initial isocyanate and alkane peak ratio ^{13,107}.

$$Reaction \ conversion \ = 1 - \frac{A_{NCO(t)}/A_{CH(t)}}{A_{NCO(t_0)}/A_{CH(t_0)}} \tag{E1} \label{eq:E1}$$

The reaction conversion is determined using the equation E1, by applying the peak data obtained from the Perkin Elmer Spectrum Software. $A_{NCO(t_0)}$ and $A_{NCO(t)}$ denotes the peak area of isocyanate group at the beginning of reaction and at the reaction time t respectively. $A_{CH(t_0)}$ and $A_{CH(t)}$ denotes the peak area of reference peak -CH stretching at the beginning of reaction and at the reaction time t respectively.

3.1.3 Reactive Extrusion 3D Printing (REX)

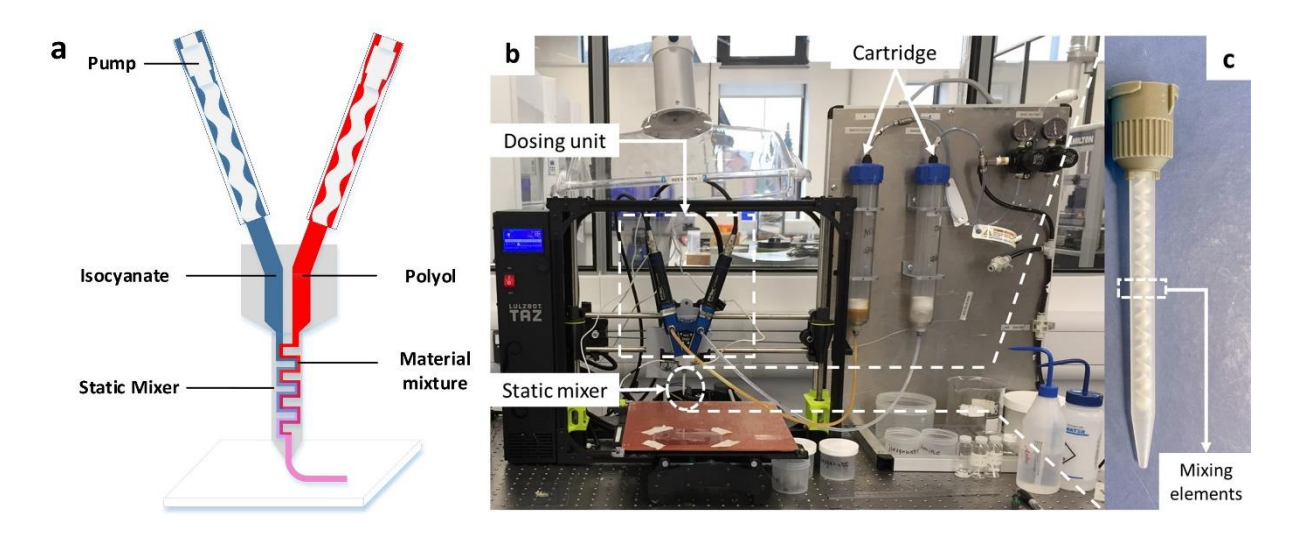


Figure 3- 20. a) Schematic diagram of REX dosing unit and static mixer. b) REX system set up. c) Static mixer at closer look.

Following inks preparation and printability analysis, the REX system was used to co-extrude isocyanate and polyol feeds to react and print PU structures. The system was modified from a LulzBot TAZ6 printer (FAME 3D, Fargo, North Dakota, USA) to integrate with a high precision volumetric dosing unit, shown in Figure 3- 20 (Preeflow eco-DUO450 two-component mixing dispenser, ViscoTec). The key characteristic of the Preeflow two-component mixing dispenser can offer the uniformly mixing ratio between the two sides and consistent dispensing accuracy in the millilitre range, irrespective of the viscosity change and ambient temperature.

This is achieved through the progressive cavity pump, with rotor/stator set up as depicted in Figure 3-21. In this set up, the fluid will have no influences from the input pressure, and a true positive displacement can be attained.

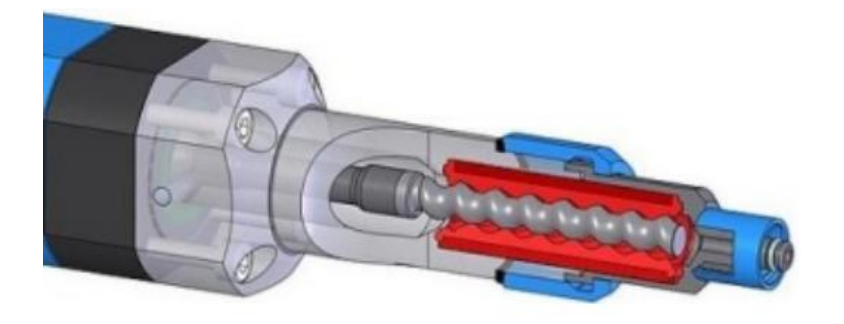


Figure 3-21. The Preeflow rotator/stator assembly. Images from online brochure.

Both isocyanate and polyol feeds were transferred into 360 ml Optimum® syringe barrels (Nordson EFD). Subsequently, a home-built feed supplying system pneumatically transported the reagent mixtures from Optimum® syringe barrels to the dosing unit by pressurised nitrogen, at 3 bars. Feeds from both sides were then driven by a screw pump inside the dosing unit. All the feed formulation as discussed in 3.1.1, were all calibrated based on the instruction manual of the Preeflow eco-Control EC200-DUO, shown in Figure 3- 22. A calibration vessel was placed under the dosing unit, where the dosing unit dispensed the set volume of the feed material. In the calibration vessel, the actual volume was read and logged into the program to complete the calibration of the feed material.



Figure 3-22. Preeflow eco-Control EC200-DUO. Images from online brochure.

Once the calibration of the new feed material was finished, the mixing ratio and the flow rate were regulated using Preeflow eco-Control EC200-DUO. The NCO and OH feeds were mixed at 1/1 (v/v), 1.1/1 (mol/mol) in the static mixer (IDMMKH03-16S, Intertronics) (outlet internal diameter (ID) =1 mm, inlet ID=3.2 mm, length (L) / diameter (D) = 23, the number of mixing elements = 16), and extruded onto the print bed.

The printing optimisation workflow (Figure 3- 18) consists of three steps, with the first two steps to were targeted to identify the best combination of print speed and extrusion speed. The latter step was employed to determine the printing parameters (suitable layer height) for optimising the printing quality. These process parameters (i.e., print speed, layer height, infill distance etc.) were set up in slicing and control software (Cura Luzlbot Edition 3.6.20), examples shown in Figure 3- 23.

To demonstrate the printability of the formulations, Woodpile structure (4 layers, 21mm x 21mm) was designed and printed. Additionally, bar samples (2 layers, 80mm x 4mm) were printed using the investigated formulations. The bar samples were later used for thermomechanical characterisations.

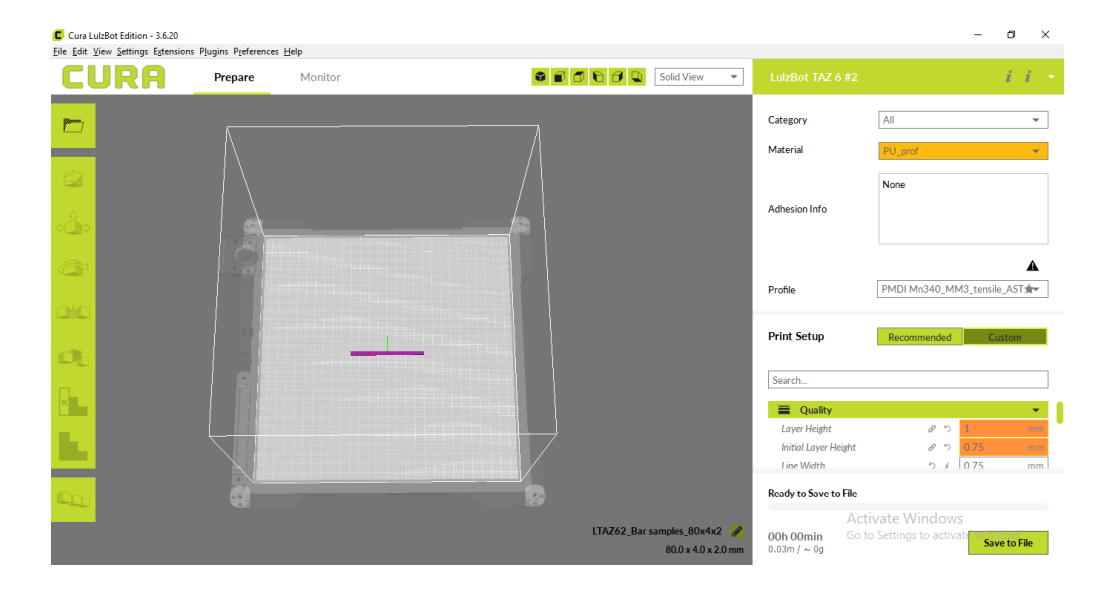


Figure 3-23. Screenshot of the Cura Luzlbot Edition 3.6.20.

The printing parameters used for both woodpile and bar samples were summarised in Table 3-7.

Table 3-7. Printing parameters used for bar samples/woodpile feature samples.

Parameters	Values (units)				
Temperature ⁱ	Ambient condition				
Extrusion flow rate	2 ml/min				
Print speed	28mm/s				
Layer height	1mm				
Infill distance (D _{I_set})	3mm				
Infill direction	[0,90]				
Infill type	Zig-zag				

i. The system temperature and the print bed temperature were all kept at ambient condition throughout all the printing.

3.1.4 Printing Characterisations

Thermogravimetric Analysis (TGA)

TGA was carried out on a Perkin Elmer Thermogravimetry Analysis 4000 apparatus to analyse the thermal stability of the printed PU samples. Specimens of approx. 10 mg were sectioned from the printed samples. They were heated from 50 °C to 800 °C at a 20 °C/min heating rate under nitrogen atmosphere.

Differential scanning calorimetry (DSC)

DSC was conducted using PerkinElmer DSC 8000 to study the phase transition temperature of the printed PU samples. Samples of approx. 10 mg were sectioned from the printed samples. The samples were heated from -50 °C to 150 °C at a 5 °C/min heating rate under nitrogen environment.

Dynamic Mechanical Analysis (DMA)

The thermomechanical properties of printed PU samples were assessed using PerkinElmer DMA 8000. Tension geometry was deployed to perform the analysis. Specimens of 10 mm

(length), 4 mm (width) and 2 mm (thickness) were sectioned from the printed samples. The specimens were subject to sinusoidal forces within linear viscoelastic regions (strain 0.001) under constant frequency (1 Hz) isothermally at 25 °C for first three minutes, and further undergone a temperature scan from 25 °C to 150 °C at 5 °C/min heat rate. The test was finished by isothermally staying at 150 °C for three minutes.

Scanning Electron Microscope (SEM)

The printed samples were sectioned using a scalpel and then mounted on double-sided conductive carbon tape and sputter coated with gold with an Agar Sputter Coater (Agar Scientific, Essex, UK). Imaging was carried out on a tilt stage. A Hitachi SEM TM3030 Tabletop microscope (Hitachi Technologies Corporation, Japan) was utilized to characterize the samples. The microscope was equipped with a Bruker Scan generator, X Flash SDD detector, MinSVE processor (Bruker Nano GmBH, Berlin, DE), Deben USB Chamberscope and Sprite HR Stage controller joystick (Deben, Suffolk, UK). The cross-section morphology of the printed PU samples was analysed under SEM.

Microscopic Imaging

Microscopic images of mixed inks and the printing profile (i.e., width of the filaments) were captured on a Nikon Reichert-Jung MEF3 optical microscope. In such, Dimensional accuracy of the printed profile in contrast to the design CAD profile was compared. In addition, the dispersion of silica nanoparticles and functional silica particles in the feed matrix (both isocyanate/polyol) was captures under microscope.

Reaction exotherm

The reaction exotherm for different mixing modes was monitored by using K-type thermocouples (RS PRO), together with Picolog data recorder. Printed sample temperatures

from three mixing modes, in Table 3- 4 shows the three formulations (MM1, MM2 and MM3). The differences for these formulations come from the fumed silica loading in the isocyanate feedstock. All the materials used here are the same as shown in Feed formulation in Chapter 4 Printability and Process Analysis.

Table 3- 4 were captured every second by the apparatus continuously for 60 seconds. The data were stored in the PicoLog6 software.

The rate of reaction exotherm is calculated according to equation E2. T_1 and T_2 are the sample temperature at t_1 and t_2 respectively, whereas t_1 and t_2 are the starting point when the temperature increased and the time when peak temperature was reached, respectively.

$$\Delta T/\Delta t = \frac{T_2 - T_1}{t_2 - t_1} \tag{E2}$$

CHAPTER FOUR

4 Investigation the Workflow for Printability Screening and Printing Optimisation of Fast Curing Polyurethane Formulations via Reactive Extrusion 3D Printing

In this chapter, PU formulations using different isocyanates feedstock (HDI, IPDI, N3900, PMDI 340, PMDI 400) and the different catalyst levels (0.5 wt.%, 1 wt.% and 1.5 wt.%) were evaluated, compared, and printed. Printing was conducted utilising Reactive Extrusion 3D printing (REX). PMDI M_n340 formulation was shown to be the best among those that were investigated, and this reagent was then used to conduct a printing optimisation study. Once printed, the samples characterisation took place to analyse the dimensional accuracy, microstructure, and reaction exotherms of the printed profiles.

Unlike traditional material extrusion AM technologies, where the printability is primarily determined by the static ink rheology properties (i.e. viscosity and viscoelastic properties)¹¹⁸. REX offers another additional degree of design of freedom, as the reaction evolves during the printing process. The in-situ reaction starts to build up the cross-linked network, which should strengthen the printing parts further throughout the process. Hence, reaction kinetics of the formulation need be evaluated along with ink rheology properties.

Thus, "ideal REX formulation", i.e., those that best utilise the benefits of this processing modality, can be characterised into two groups. The first group represents those that exhibit more prominent ink rheology properties (i.e., high viscosity, elasticity and yield stress) along with slower reaction kinetics. In contrast, comparatively lower ink rheology properties combined with faster reaction kinetics are exhibited by those inks in the second group. Both groups are anticipated to afford the required structure integrity of the printed parts during the building process. This is because the printed layers can either rely on superior rheology properties (the first group) or faster kinetics (the second group) to prevent deformation caused by the un-cured printed layers on the top, prior to the layer that is being studies is completed cured state. This is because with this type of chemistry full cure is not achieved from several days/weeks. Previous studies primarily investigated the formulations from the first group, leveraging the prominent ink rheological properties and applying additional curing stages/methods (i.e. UV or thermal curing) to assist the layer stacking process^{16,23}.

This study had the objective to investigate the second group of REX formulations, faster reaction kinetics would be the key assessing criterion to identify the target formulation by the means of transitional ink rheology, which is the progression of rheological properties after both feeds were mixed and extruded and reaction kinetics characterisations.

4.1 Results

4.1.1 Printability Analysis

Rheology

Static Feed Rheology

Static rheological properties of proposed ink formulation are good indicators to show whether the inks can be both printed and to become self-sustaining when deposited onto the print bed. Hence, the differences of static feed rheology characteristics were examined to create a map of formulations and acceptable properties. The data from comparing; (a) the change in viscosity as a function of shear rate see Figure 4-1 and (b) the change in dynamic moduli as a function of frequency collected as part of this study.

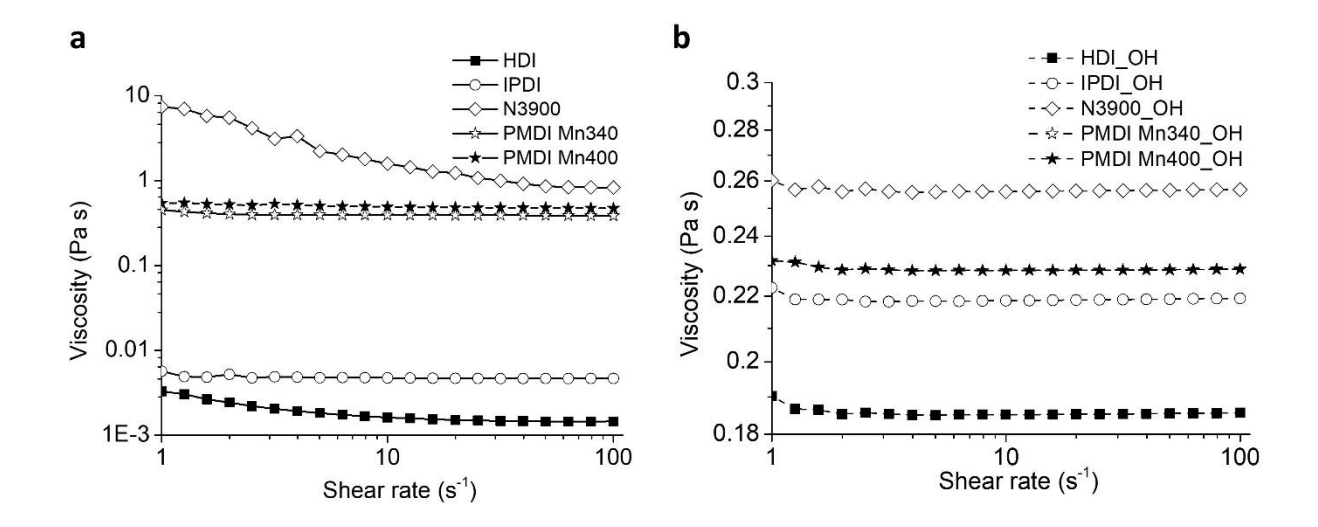


Figure 4- 1. Rheological properties of the feeds. a) NCO feeds, b) OH feeds showing storage modulus and loss modulus as a function of frequency.

Newtonian behaviour was observed with most NCO and OH feeds evaluated in this study, as they exhibited apparent viscosities that was independent of shear rate. The only exception occurred in N3900 isocyanate feeds (The polyisocyanate with three NCO functional groups in the structure and the highest molecular weight among all the isocyanate reagents investigated,

which showed a shear thinning behaviour, where the viscosity decreases when subject to higher shear rate. Furthermore, the N3900 isocyanate feeds was observed to present the highest level of viscosity followed by PMDI Mn400 and PMDI Mn340, the multi-functional aromatic isocyanate oligomers with an average reactive group (NCO) of 3.2 and 2.7 respectively; with the second and third highest molecular weight respectively. The viscosities of these three formulations were substantially higher than the remaining two isocyanate feeds (IPDI and HDI), which are the di-functional isocyanates with the two lowest molecular weight (222.3 and 168.2 respectively) in this study. In contrast, less variance was observed in viscosity values were seen in OH feeds, where these five feeds with same materials only differed in the mass compositions shown in Table 3.1. The greatest viscosity differences among the NCO feeds and OH feeds were shown more than 1000 and 1.3, for N3900/HDI and N3900_OH/HDI_OH respectively.

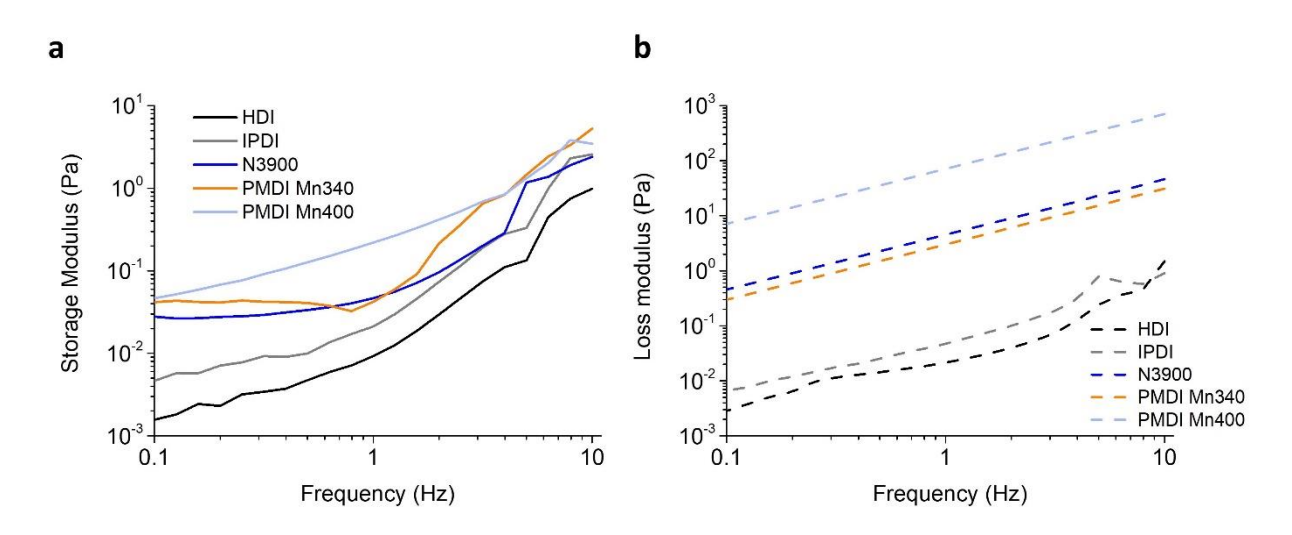


Figure 4- 2. Rheological properties of investigated NCO feeds showing a) Storage modulus as a function of frequency.
b) Loss modulus as a function of frequency.

The viscoelastic profile of isocyanate feeds was shown in Figure 4- 2. Higher storage modulus (G') values were shown in PMDI Mn400 and PMDI Mn340 NCO feed, following by N3900, IPDI and HDI NCO feeds in a descending order (Figure 4- 2a). Similar trends were presented in loss modulus (G'') values for the NCO inks (Figure 4- 2b).

Relating this data to the needs of the printing modality used in this study. Higher values of G' are desirable for material extrusion 3D printing, making layer-stacking more feasible during the printing process. Furthermore, G' was noted to dominate over G' throughout the full range of frequencies tested for all the NCO feeds, which demonstrated the all the NCO feeds displayed more liquid-like behaviour.

Transitional Ink Rheology

Transitional ink rheology defines the progression of rheological properties of both NCO and OH feeds, after mixed in the static mixer and extruded from the nozzles. Transitional ink rheology properties determine if the formulation can quickly develop a cross-linked network, which was investigated via the dynamic moduli growth profile.

To show the variation of curing kinetics between the five formulations with different isocyanates, the comparison of transitional ink rheology was examined, and the data is shown in Figure 4-3.

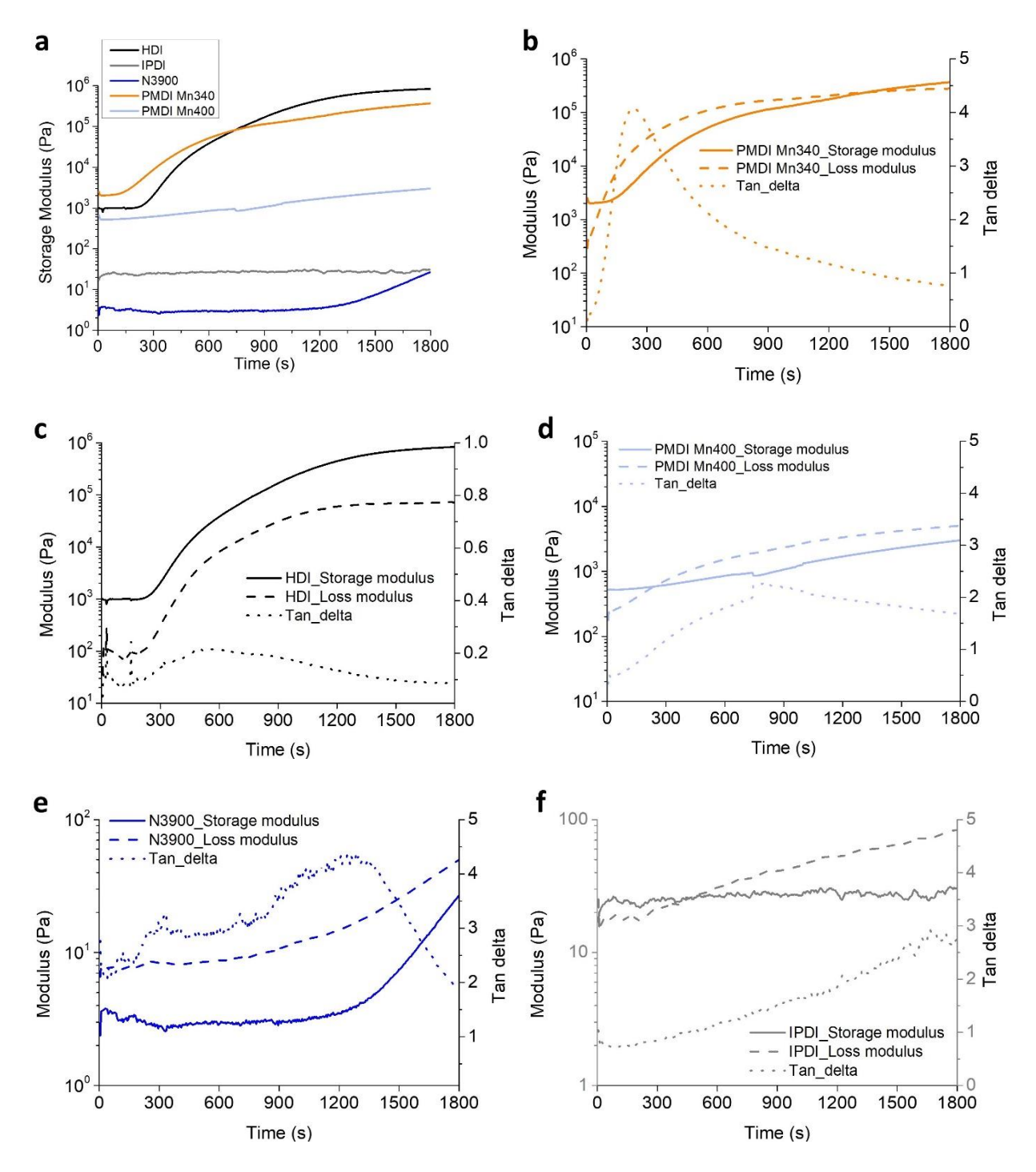


Figure 4- 3. Transitional rheology properties for PU blank formulations using different isocyanates showing a) Storage modulus versus time comparison between PU blank formulations, b) PMDI Mn340 blank formulations, c) HDI blank formulations, d) PMDI Mn340 blank formulations, e) N3900 blank formulations, f) IPDI blank formulations.

The highest initial storage modulus (G') were presented in PMDI Mn340 formulations (2013 Pa), closely followed by HDI formulations (998.4 Pa) (see Table 4- 1).

Table 4-1. Storage modulus data of the formulations obtained from transitional rheology test.

Time (min)	Storage Modulus (Pa)							
	N3900	IPDI	HDI	PMDI Mn400	PMDI Mn340			
0	2.4	17.1	998.4	519.1	2031			
1	2.8	24.3	1005	520.1	2063			
5	2.9	25.0	2074.0	617.8	8733			
10	3.6	26.5	38240.0	852.2	51690			

A significantly higher rate of storage modulus growth (dG'/dt) was presented in PMDI Mn340, and HDI formulations, in contrast to the other three formulations where the dynamic moduli values stayed stagnant. A plateau of G' was reached when the reaction progressed along the timelines used in the study. The shortest time to attain this G' plateau exhibited in PMDI Mn340 and HDI formulations (Figure 4- 3a). The PMDI Mn340 formulation started to behave as viscoelastic liquid, i.e., with higher G'' than G', after ~79 seconds. Furthermore, the PMDI Mn340 formulation presented more solid-like behaviour eventually after ~23 minutes, with G' surpassed G''. Notably, there was 25 times increase of the G' value at 10 min, from the beginning of test to the end. Furthermore, the tanδ peak denoted a transitional point, after which a greater growth of G' than G'' was observed. The sharp and narrow nature of the tanδ peak for the PMDI Mn340 formulation indicated how quickly the dynamic moduli built up as reaction progressed, when compared with the other formulations. It took only ~230 seconds to reach this tanδ peak (Figure 4- 3b). Meanwhile, the HDI formulations exhibited solid-like behaviour throughout the test and the tanδ peak was exhibited at a time ~520 seconds (Figure 4- 3c). PMDI Mn400 formulations followed the similar moduli growth trajectory as the PMDI

Mn340 formulations, showing a fast development of both G' and G''. However, longer time was needed to reach the $\tan\delta$ peak at ~795 seconds (Figure 4- 3d). N3900 formulations showed a comparatively delayed growth of moduli, whereas the $\tan\delta$ peak was found at ~1285 seconds. Furthermore, N3900 formulations behaved as visco-elastic liquid during the entire test (Figure 4- 3e). The slowest moduli growth trajectory exhibited in IPDI formulations, whereas no $\tan\delta$ peak could be found throughout the test.

To identify the optimum level of catalyst (DBTDL) that needed to be introduced into the PMDI Mn340 formulation, transitional rheology profiles of the formulation with three levels of catalysts were investigated. The comparison of data is shown in Figure 4-4.

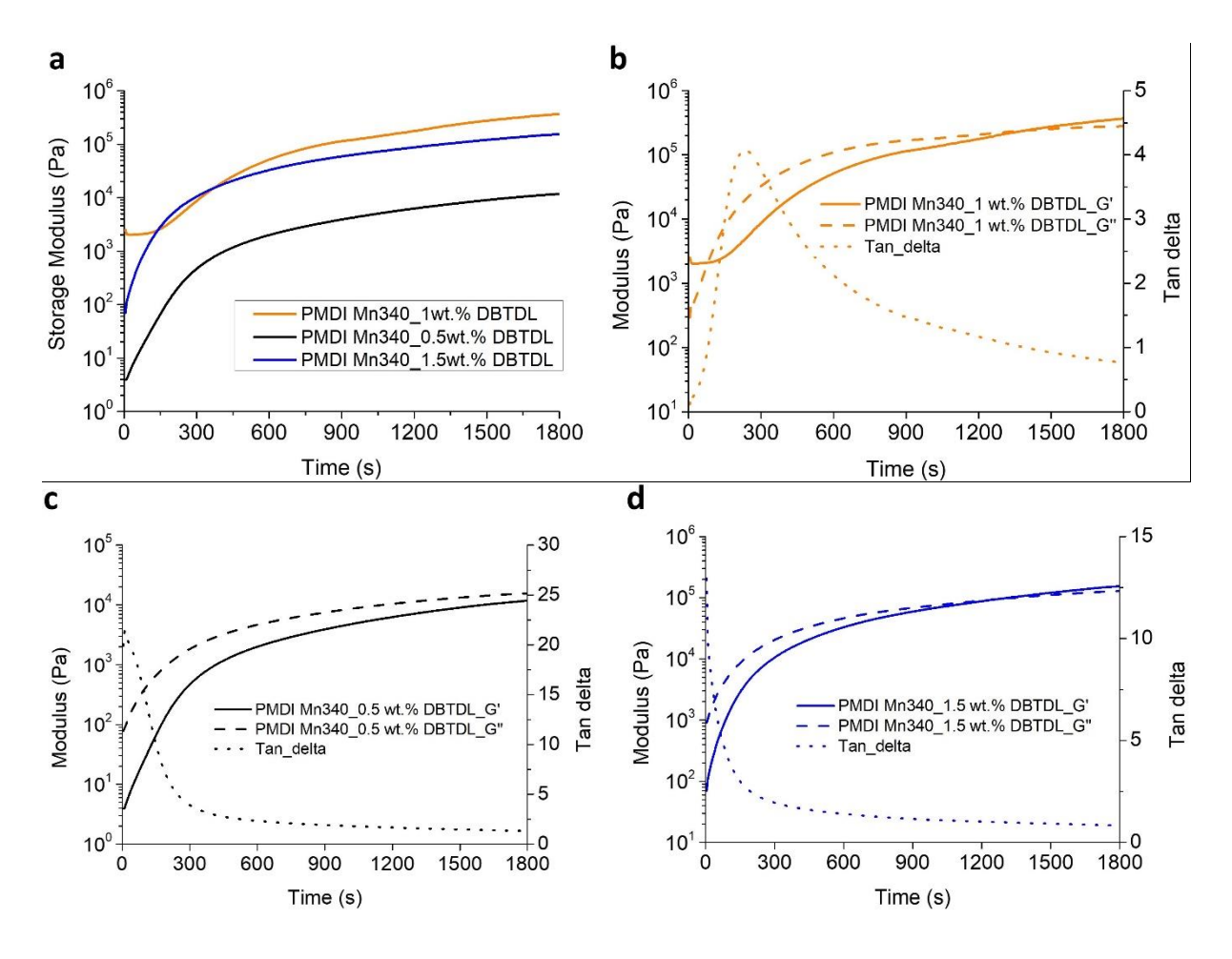


Figure 4- 4. Transitional rheology properties for PMDI Mn340 formulations using different level catalyst. a) Storage modulus (G') versus time comparison between formulations using different level of catalyst. Dynamic moduli and tan delta for b) PMDI Mn340_1 wt. % DBTDL formulation. c) PMDI Mn340_0.5 wt. % DBTDL formulation. d) PMDI Mn340_1.5 wt. % DBTDL formulation.

The initial storage modulus value for PMDI Mn340 formulations with 1 wt. % catalyst was found to be 520 and 29 times higher than the value for 0.5 wt. % and 1.5 wt. % catalysts formulation, respectively. As a result, higher storage modulus values were presented by the PMDI Mn340 formulations using 1 wt. % catalyst loading when compared with the 1.5 wt. % and 0.5 wt. % loadings throughout most of the measurements made. Furthermore, the G' value at end of the test with the 1 wt. % formulation was 31 times and 2.3 times greater than the value for 0.5 wt. % and 1.5 wt. % catalyst formulations respectively (Table 4- 2). The formulation with 0.5 wt. % catalyst displayed a more liquid-like behaviour, with G'' being dominant over G' during the test. Furthermore, a cross-over point between G' and G'' was seen in the formulation with 1.5 wt. % catalyst. This point denoted the transition from a liquid-like to more solid-like behaviour, which occurred at ~21min. The discussion of the transitional ink rheology results is detailed in 4.2.1Printability Analysis.

Table 4- 2. Storage modulus data of the PMDI Mn340 formulations with 0.5 wt. %, 1 wt. % and 1.5 wt. % DBTDL, obtained from transitional rheology test.

Time (min)	PMDI Mn340 formulation Storage Modulus (Pa)						
	0.5 wt. % DBTDL	1 wt. % DBTDL	1.5 wt. % DBTDL				
0	3.9	2031.0	70.4				
30	11800	367300	154600				

Reaction Kinetics

The reaction kinetics of the investigated formulation were another key metric to indicate how fast the cross-linking network could be built during the printing process, hence a critical parameter for printability analysis.

Therefore, the reaction kinetics of PU printed using different isocyanates formulations were monitored and compared using FT-IR spectroscopy, the data were shown in Figure 4-5.

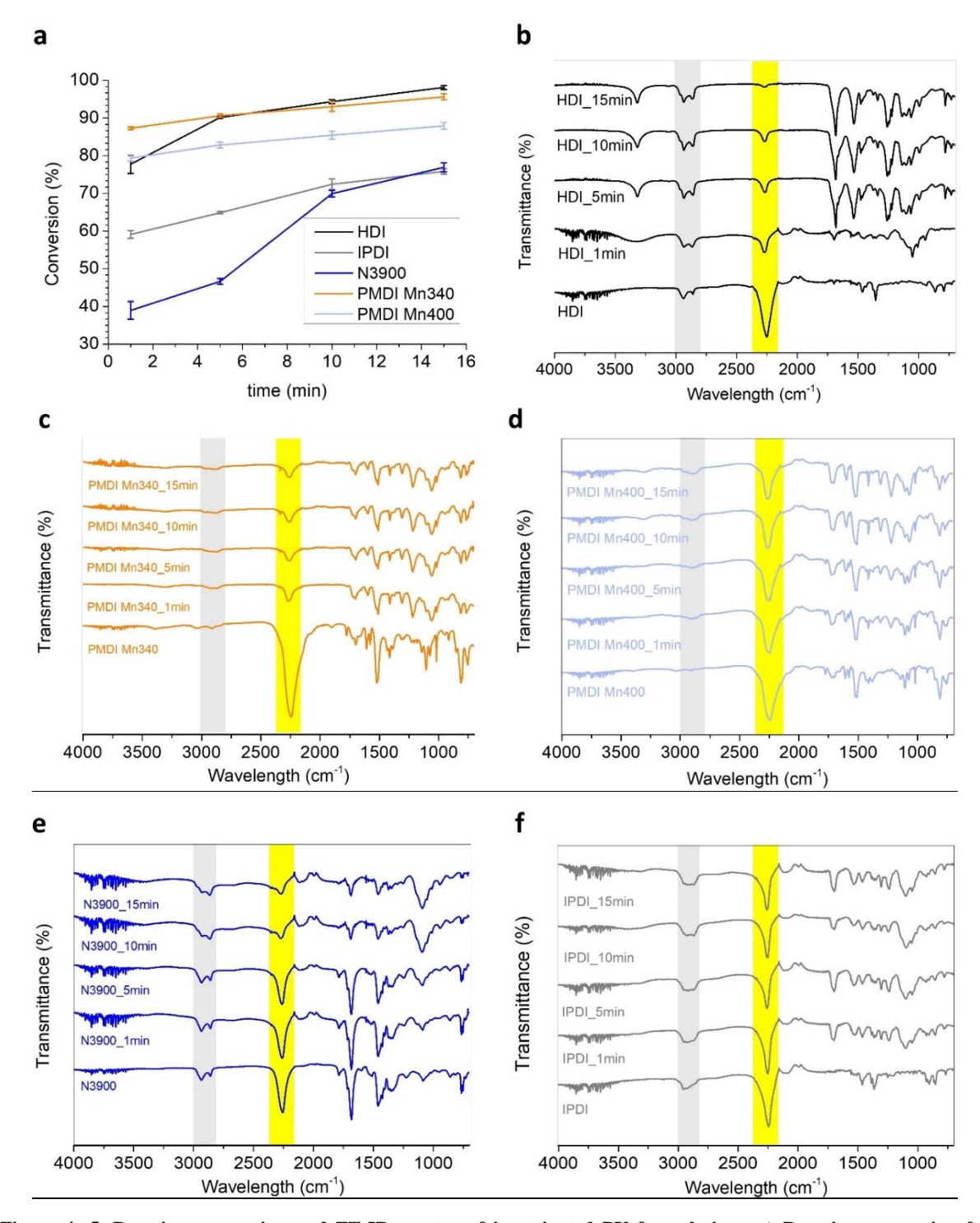


Figure 4- 5. Reaction conversion and FT-IR spectra of investigated PU formulations. a) Reaction conversion for investigated PU formulations. FT-IR spectra for isocyanates, printed PU formulations at 1min, 5min, 10min and 15min for b) HDI formulation. c) PMDI Mn340 formulation. d) PMDI Mn400 formulation. e) N3900 formulation. f) IPDI formulation.

The PU reaction progression was followed via the reduction of absorption peak at ~2250cm⁻¹ which was attributed to isocyanate peak (-NCO) ^{107,116,117}. The peaks at the region 2865-2968 cm⁻¹ were assigned to the symmetrical and non-symmetrical stretching of none C-H groups within the monomer ^{117,119}. As the reaction progressed, the intensity of -NCO peak was observed to become smaller (Figure 4- 5b, c, d, e and f) whilst the C-H peak remained unaltered throughout the reaction.

Faster reaction kinetics were exhibited in the PMDI Mn340, PMDI Mn400 and HDI formulations, relative to the IPDI and N3900 formulations (Figure 4- 5a). Furthermore, the reaction conversion after 1 min for PMDI Mn340 formulations was 7.9%, 9.5%, 28.2% and 48.3% higher than PMDI Mn400, HDI, IPDI and N3900 formulations respectively (Table 4-3. Reaction kinetics of investigated formulations.). The higher reaction conversion rate with PMDI Mn340, continued throughout the reaction period except for the HDI formulations, which surpassed the kinetics of the PMDI Mn340 formulations after 5 min.

Table 4-3. Reaction kinetics of investigated formulations.

	Reaction Kinetics (%)								
Time (min)	HDI*	IPDI*	N3900*	PMDI Mn400*	PMDI Mn340*	PMDI Mn340 0.5 %**	PMDI Mn340 1.5%**		
1	77.76±2.42	59.12±1.02	38.96±2.32	79.38±0.82	87.30±0.37	76.12±0.90	79.34±0.65		
5	90.16±0.29	64.88±0.33	46.66±0.75	82.83±0.81	90.62±0.46	80.06±0.57	83.35±1.07		
10	94.36±0.53	72.43±1.38	69.94±0.87	85.44±1.02	93.03±1.24	84.67±0.74	88.06±0.46		
15	98.14±0.53	75.85±0.74	76.92±1.18	87.92±0.93	95.63±0.78	87.86±0.64	92.70±0.82		

^{*}Formulation with 1 wt. % DBTDL as in Table 3-1.

^{**} Formulation with 0.5 wt. % and 1.5 wt. % DBTDL as in Table 3-2.

To identify the effect of the level of catalyst on the reaction speed. The reaction kinetics of PU printed using PMDI Mn340 formulations with different level of catalyst were monitored and compared, the data were shown in Figure 4-6.

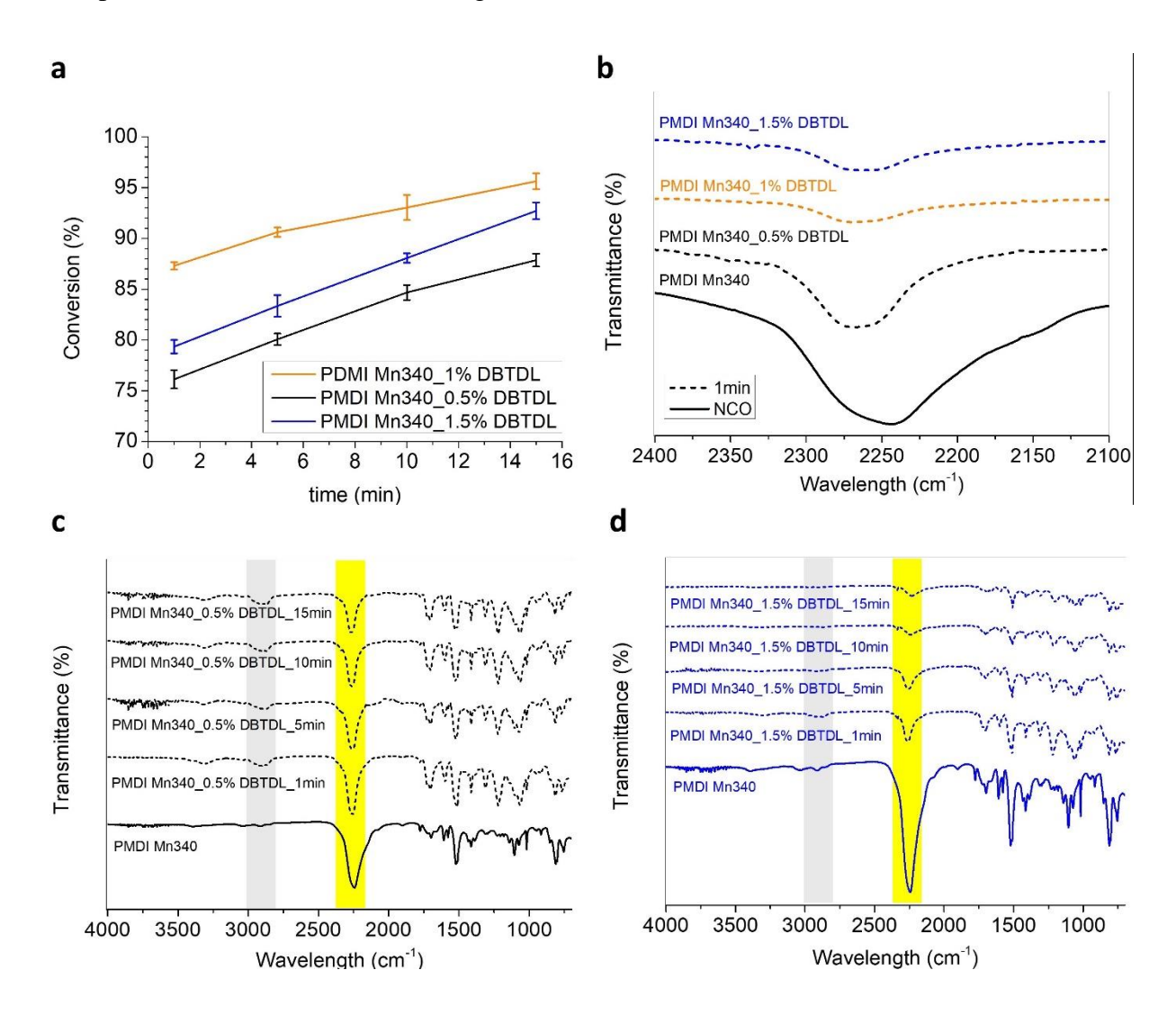


Figure 4- 6. Reaction conversion and FT-IR spectra of PMDI Mn340 formulations with different catalyst level. a) Reaction conversion comparison between PMDI Mn340 formulations. b) Amplified spectra of NCO region for PMDI Mn340 formulations at 1 min. FT-IR spectra of PMDI Mn340 formulations with c) 0.5 wt. % DBTDL and d) 1.5 wt. % DBTDL.

PMDI Mn340 formulation with 1 wt. % DBTDL afforded the fastest reaction kinetics throughout the whole test, when compared with the 0.5 wt. % and 1.5 wt. % catalyst formulations. After 1 min of reaction time, the smallest –NCO peak was exhibited in the formulation with 1 wt. % DBTDL, indicated the faster reaction rate.

4.1.2 Process Optimisation

Optimisation workflow

From the experimental programme discussed above, the PMDI Mn340 with 1 wt. % DBTDL loading was identified as good candidate for REX printing, this is because it exhibited both fast reaction speed and quick growth of dynamic moduli. Thus, this formulation was used for a subsequent optimisation study.

Step 1: Speed ratio between print speed (u_p) and extrusion speed (u_e)

The aim of this step was to correlate the print speed with the actual extrusion speed from the nozzle, the ratio between print speed and extrusion speed was varied to be 0.5, 0.75, 1 and 1.25. Additionally, this step could identify the line widths achieved by the filament under these various conditions, information which would be useful for understanding which printing parameter need to be applied to make high quality structures. The comparison between the printed single filament sizes were compared and the data was shown in Figure 4-7.

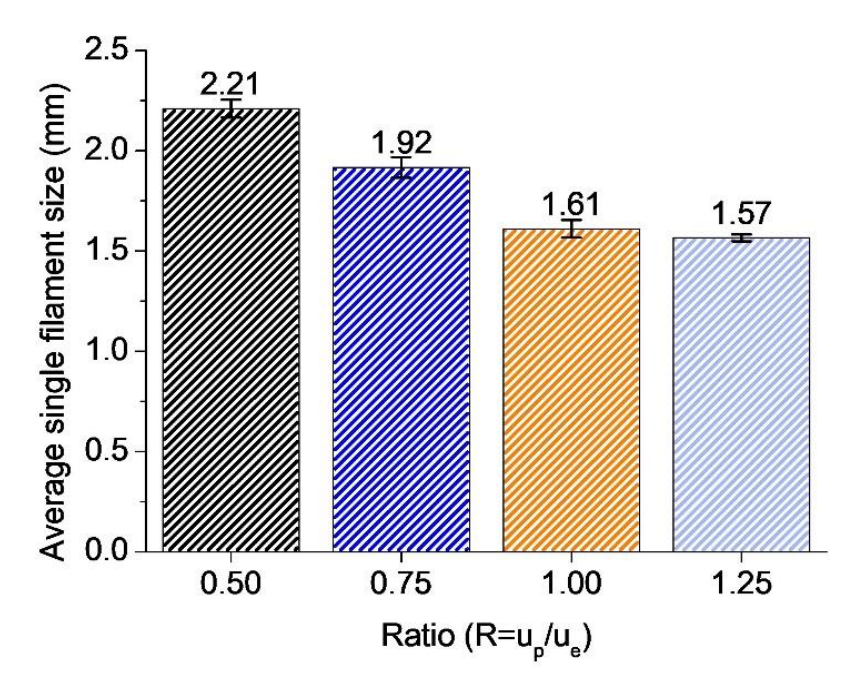
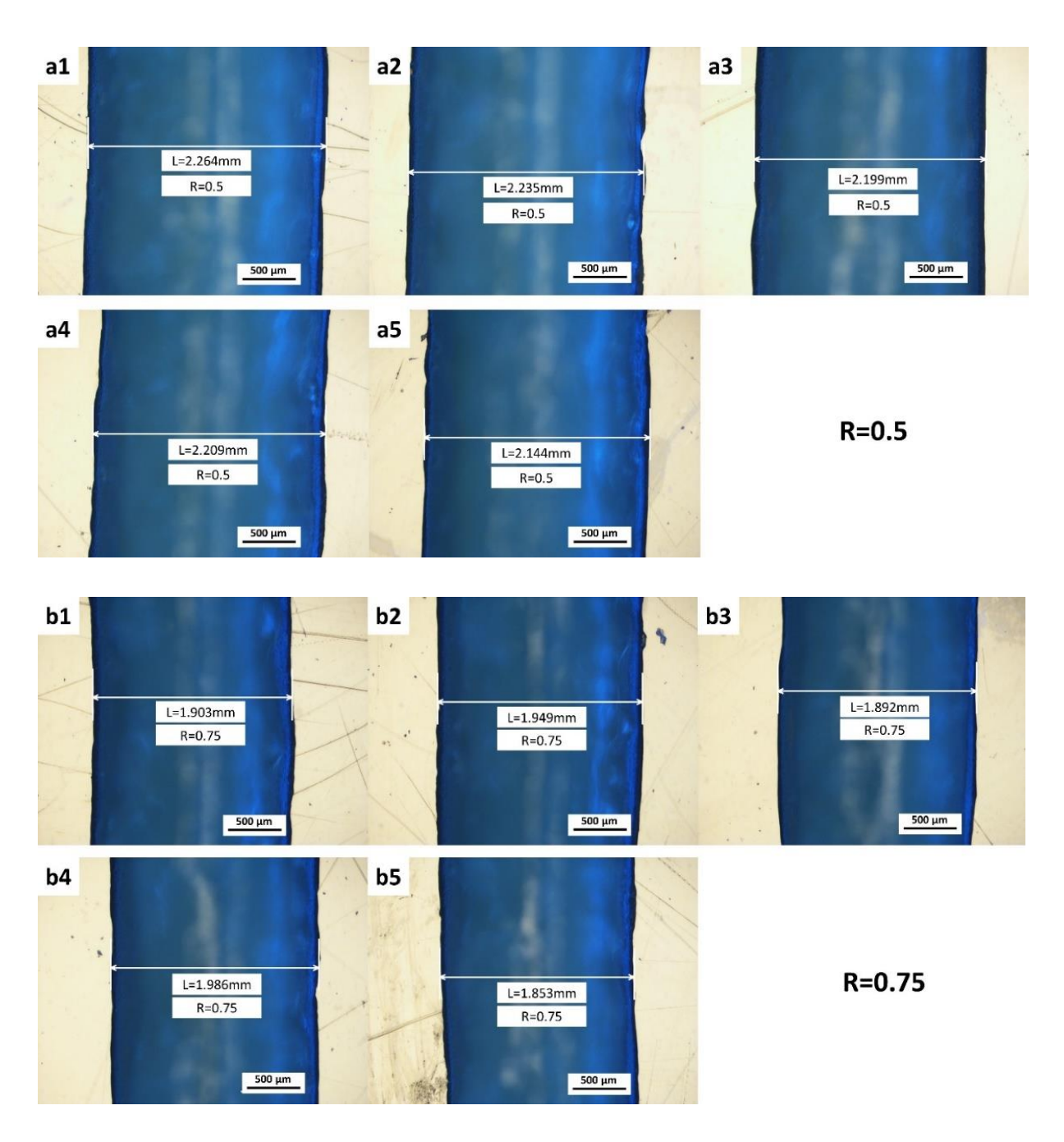


Figure 4- 7. Average single filament sizes of PMDI Mn340_1 wt. % DBTDL formulation printing using different ratio between print speed and extrusion speed.

The average single filament sizes decreased as the ratio between the print speed and extrusion speed increased from 0.5 to 1.25 (Figure 4- 8). Also, larger size deviation in the single filament prints were exhibited in the lower ratio (i.e., R=0.5 and 0.75) experiments. Both R=1 and 1.25 presented more consistent single filament size. This filament size data was later used for line width printing settings.



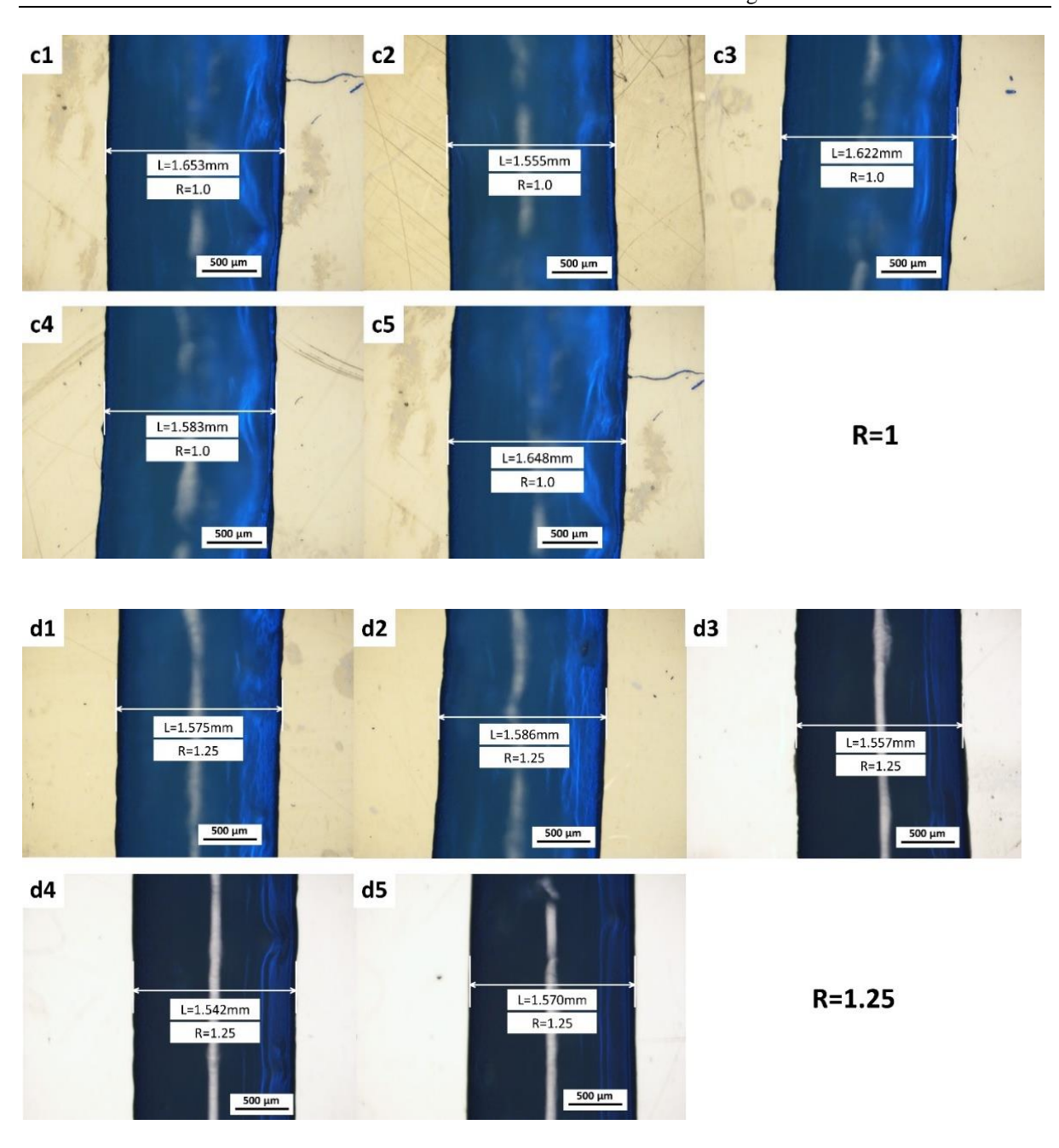


Figure 4- 8. Single filament size of PMDI Mn340 formulation using ratio (R=0.5, 0.75, 1.0 and 1.25 for group images a, b, c, and d respectively) between print speed and extrusion speed. Five measurements at each ratio.

Step 2: Find the most suitable extrusion speed

Woodpile structures, which are 3D periodic structures with spanning features (Figure 4- 9a) was widely used for printing quality evaluation ^{120–122}.

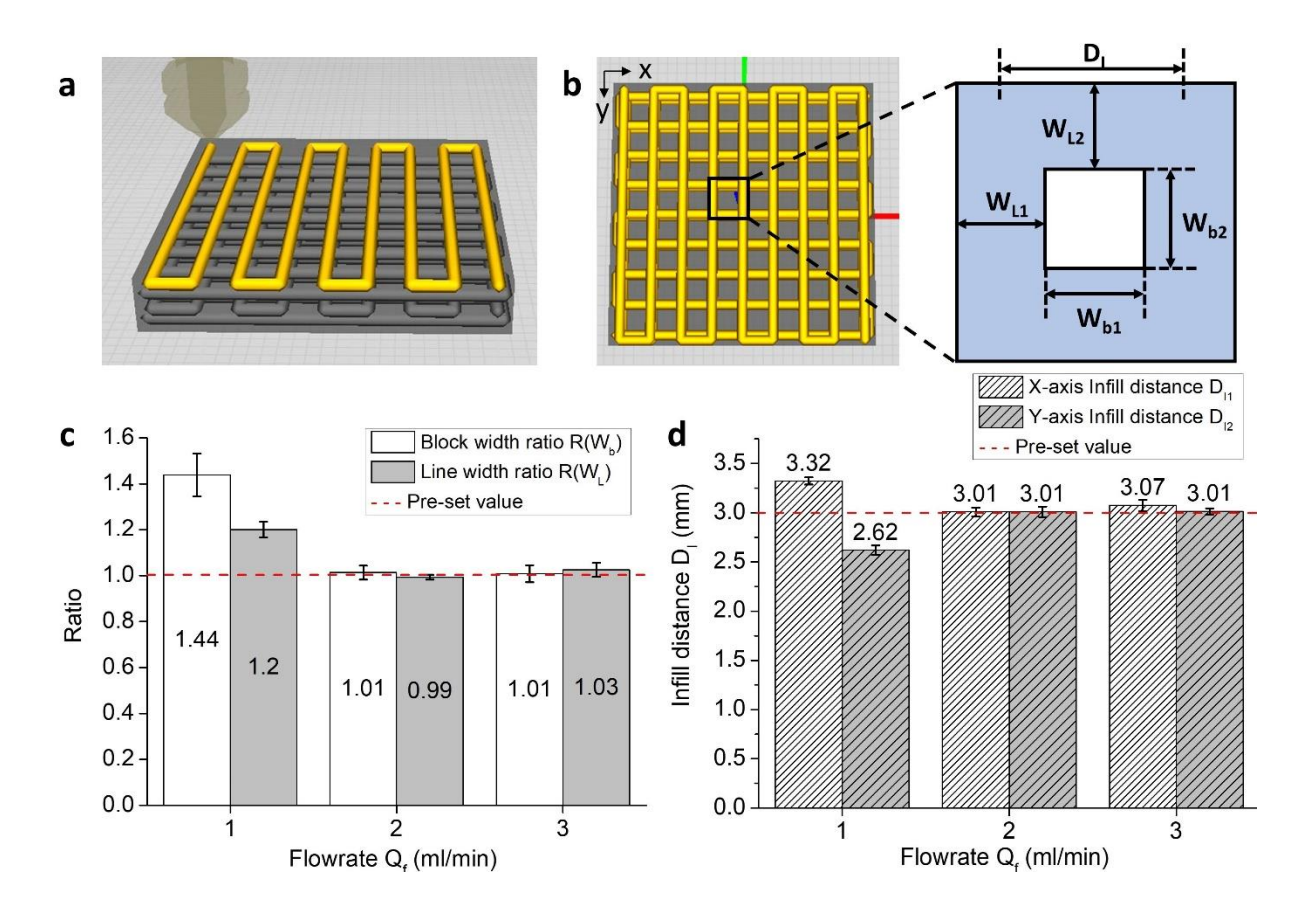
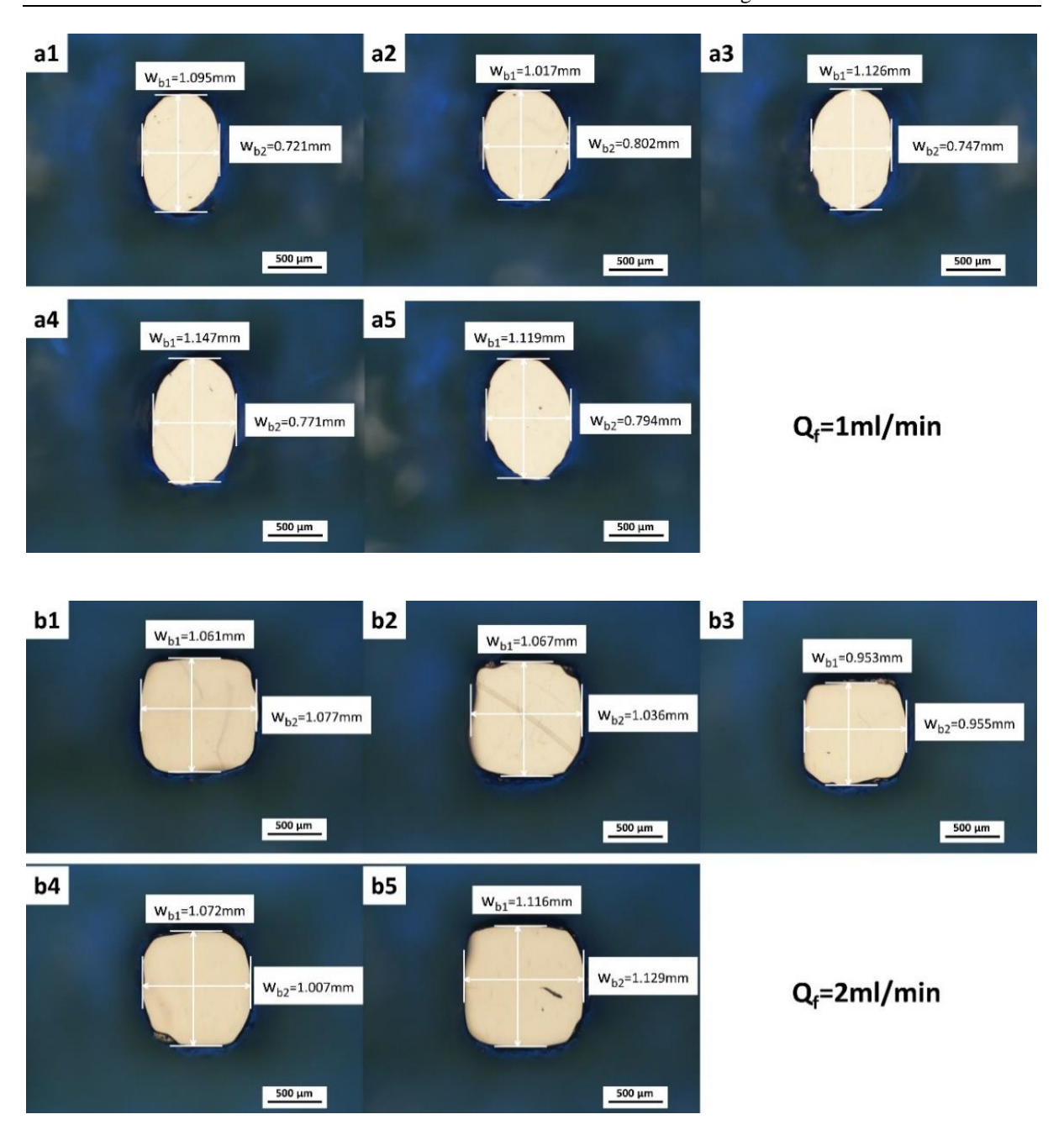


Figure 4- 9. Feature block analysis of woodpile printing using PMDI Mn340_1 wt. % DBTDL formulation with different flowrate (Q_f). a) Woodpile design pattern. b) Woodpile design top view and schematic of block feature (W_{b1} and W_{b2} = the width of the block; W_L = Line width; D_I = Infill distance, i.e., the travel distance between in-plane adjacent filaments). c) Feature analysis of block width ratio ($R(W_b) = W_{b1}/W_{b2}$) and line width ratio ($R(W_L) = W_{L1}/W_{L2}$) of printings with different Q_f . d) Feature analysis of X-axis (D_{I1}) and Y-axis (D_{I2}) infill distance of printings with different Q_f .

In these experiments, the print speed ratio (R=1) was kept consistent in printing woodpile structure using different extrusion flowrate (Q_f). The printing quality was investigated and compared based on the woodpile block features (see images of these in Figure 4- 10, Figure 4- 11 and Figure 4- 12), and the summary of the data is presented in Figure 4- 9.



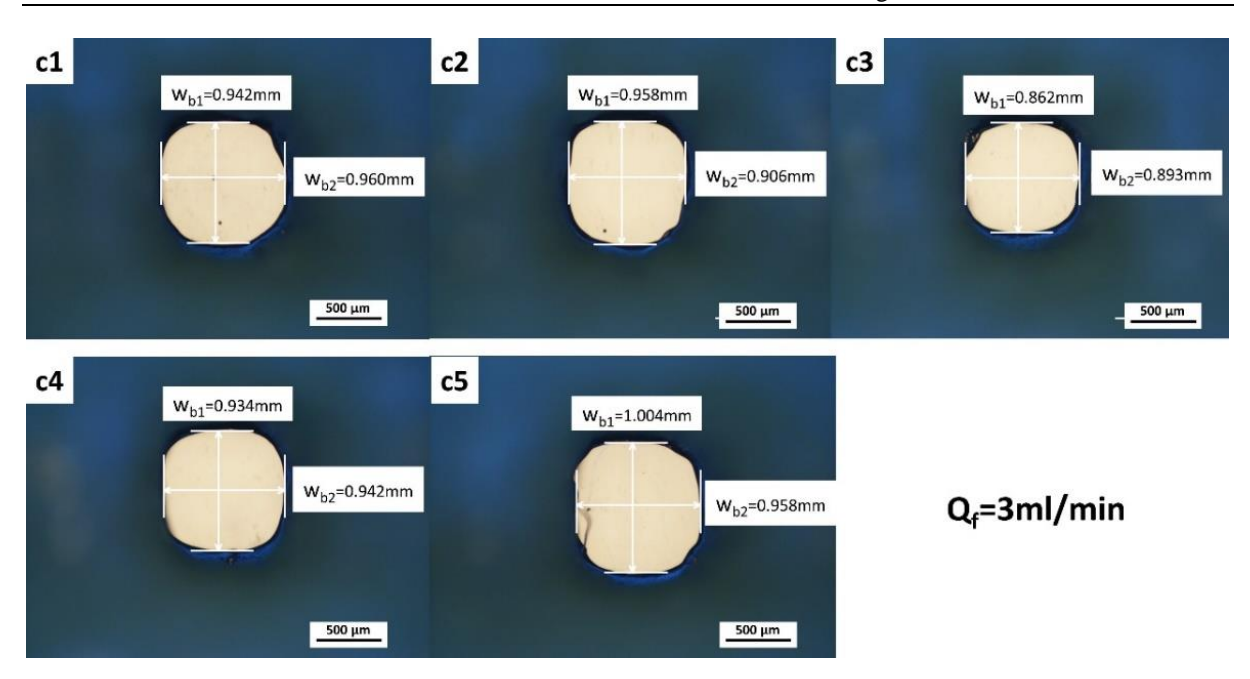
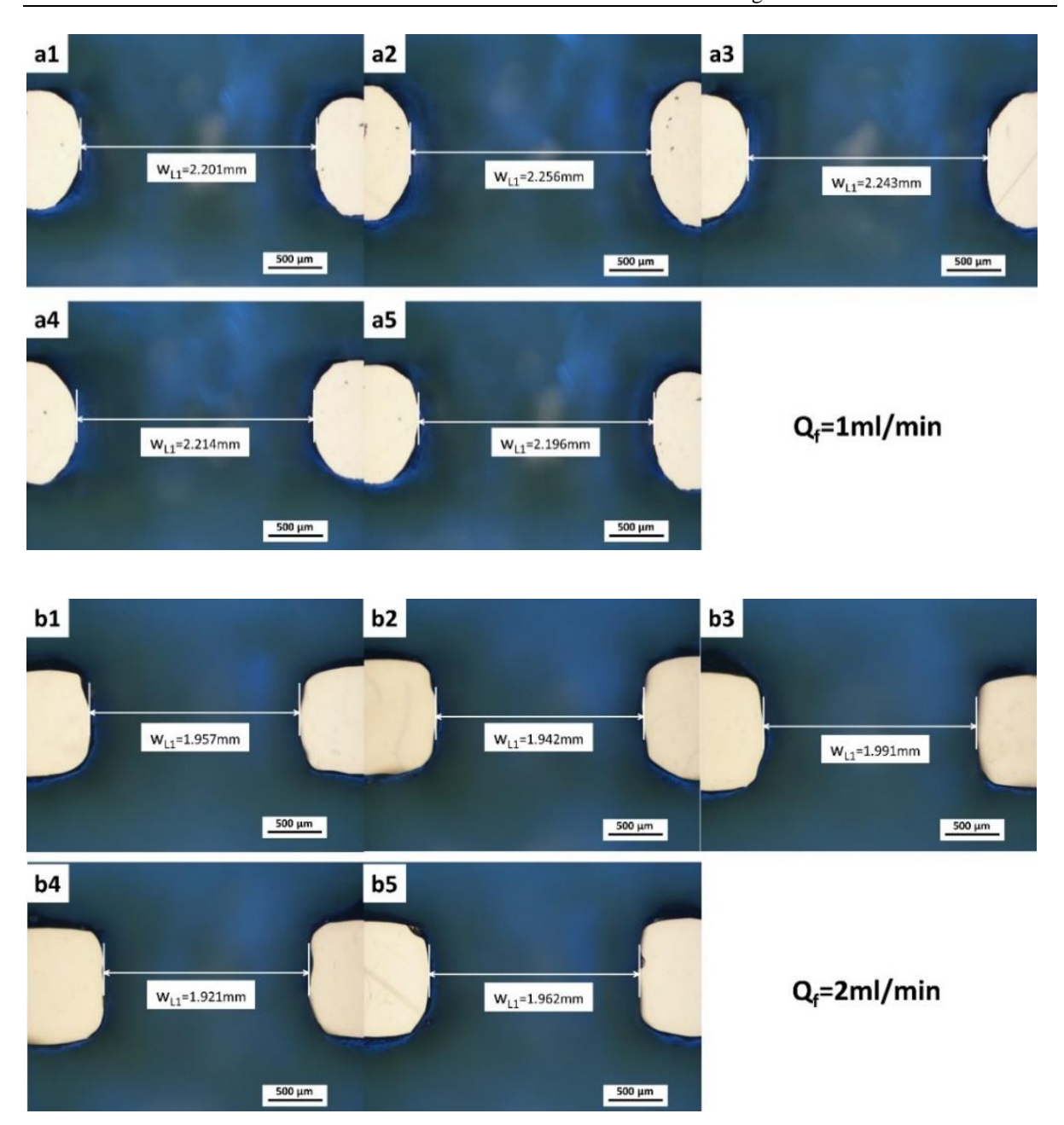


Figure 4- 10. Woodpile feature block size measurements for W_{b1} and W_{b2} .of PMDI Mn340 formulation using different extrusion flowrates (Q_f). Five measurements were taken at each flowrate: a1, a2, a3, a4, a5 for Q_f =1ml/min; b1, b2, b3, b4, b5 for Q_f =2ml/min and c1, c2, c3, c4, c5 for Q_f =3 ml/min. (W_{b1} and W_{b2} : the width of the block).



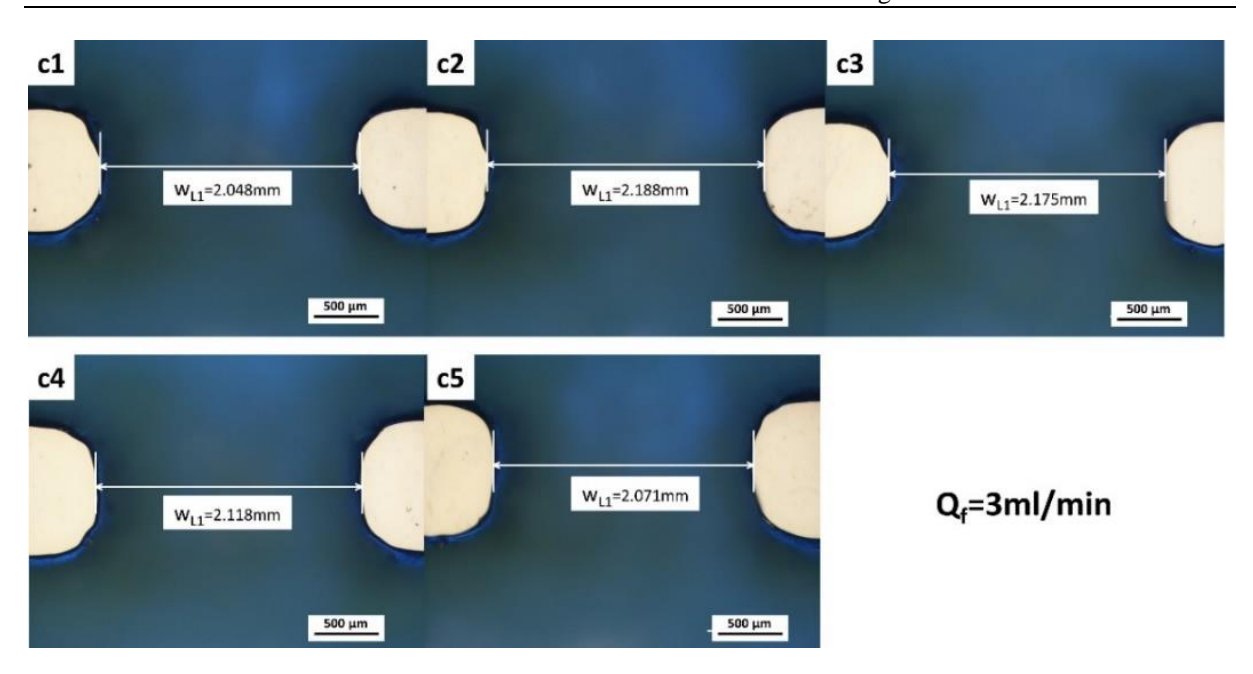
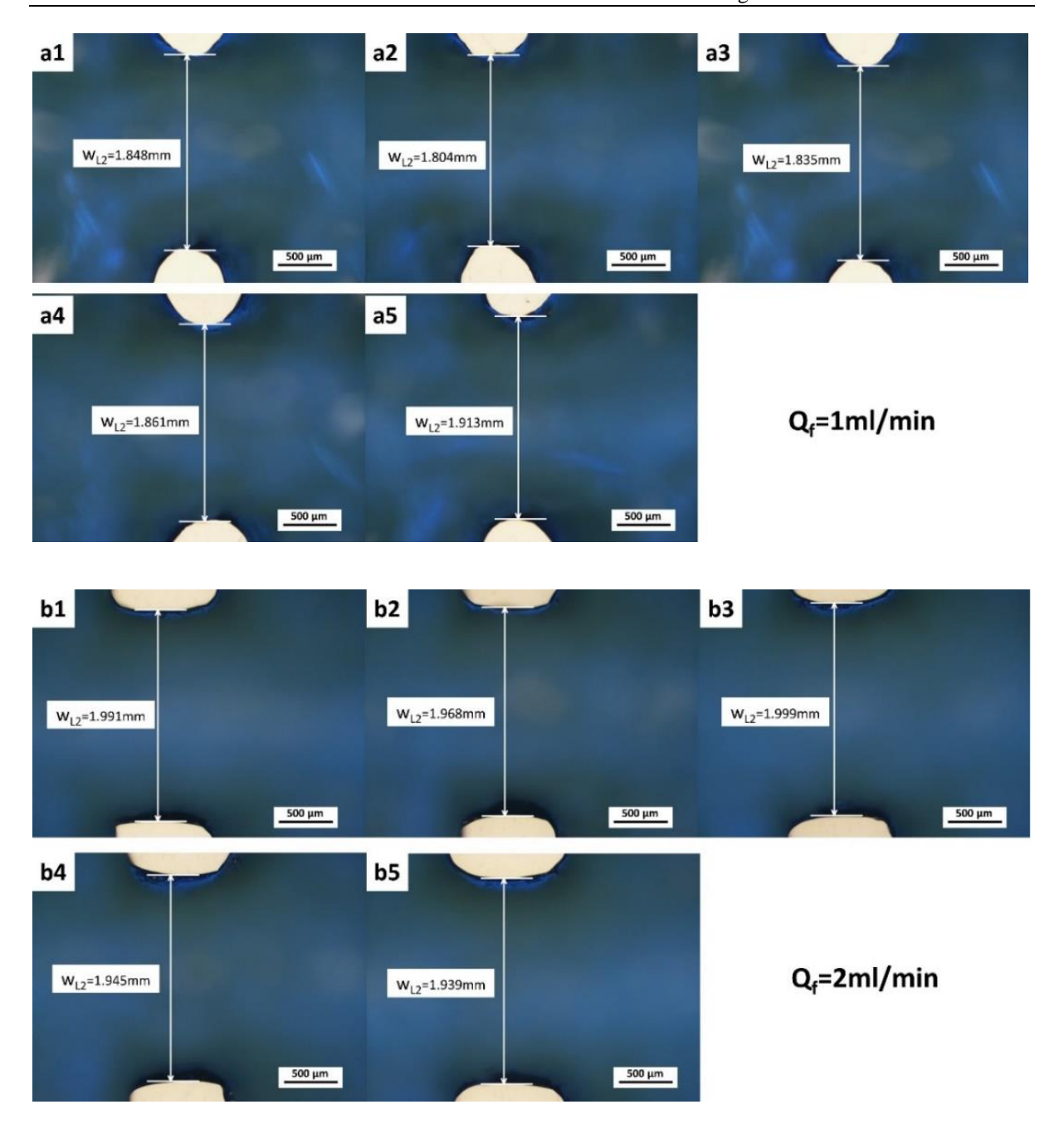


Figure 4- 11. Woodpile feature block size measurements for W_{L1} of PMDI Mn340 formulation usin different extrusion flowrate (Q_f) . Five measurements were taken at each flowrate: a1, a2, a3, a4, a5 for Q_f =1ml/min; b1, b2, b3, b4, b5 for Q_f =2ml/min and c1, c2, c3, c4, c5 for Q_f =3 ml/min. (W_{L1} : Line width at X direction).



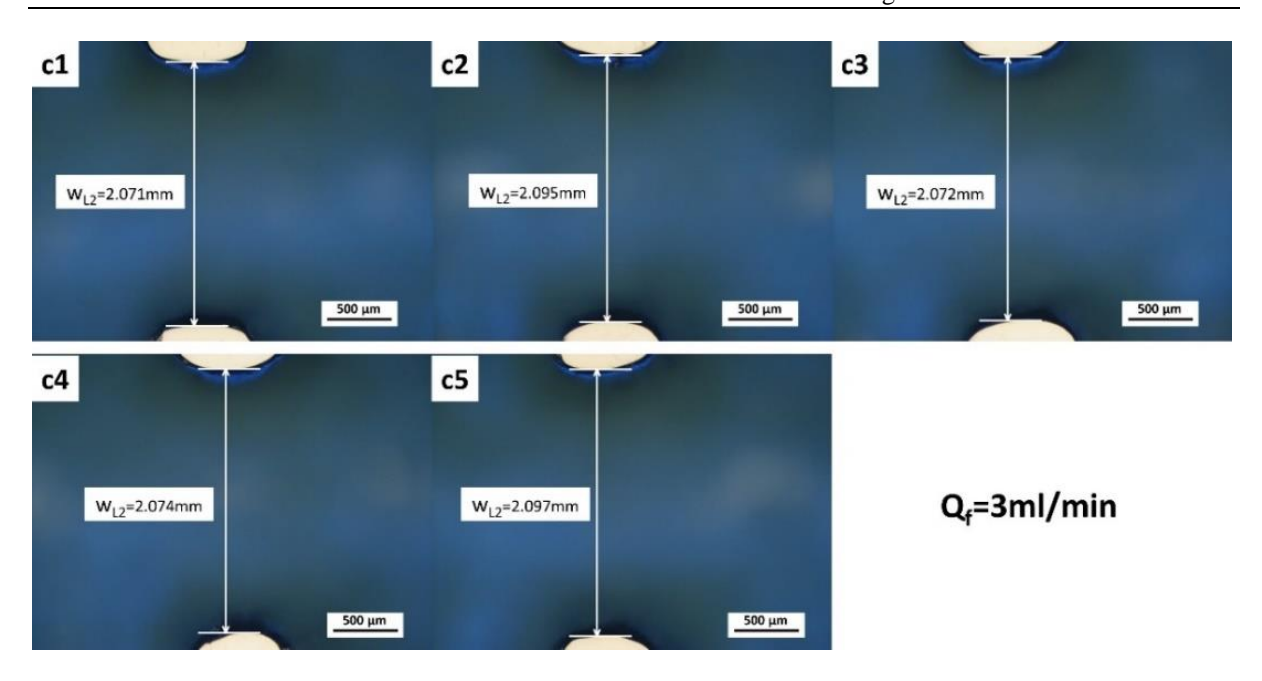


Figure 4- 12. Woodpile feature block size measurements for W_{L2} of PMDI Mn340 formulation using different extrusion flowrate (Q_f) . Five measurements were taken at each flowrate: a1, a2, a3, a4, a5 for Q_f =1ml/min; b1, b2, b3, b4, b5 for Q_f =2ml/min and c1, c2, c3, c4, c5 for Q_f =3 ml/min. $(W_{L2}$: Line width at Y direction).

The block width ratio $R(W_b)$ and line width ratio $R(W_L)$ defined the consistency of the printing quality since the block features were fabricated periodically. The average deviation of block width ratio from the pre-set value for printing of $Q_f=1$ ml/min (43.8%), was significantly higher than the two prints conducted with $Q_f=2$ ml/min (1.3%) and $Q_f=3$ ml/min (0.87%). The average deviation for line width ratio from the pre-set value was 20.0%, -0.7%, 2.5% for $Q_f=1$, 2 and 3 ml/min respectively (Table 4- 4). These results indicated printing at the flowrate ($Q_f=2$ ml/min) afforded the most consistent prints, with block and line width ratio both in closest agreement with model pre-set values.

Table 4- 4. The woodpile feature block calculated percentage deviation of width block ratio $R(W_b)$ and line block ratio $R(W_L)$ for PMDI Mn340_1 wt. % DBTDL formulations printing using different flowrate.

Flowrate	Block		Ratio	Deviation (%)			
(Q_f)	features	1st	2nd	3rd	4th	5 th	Average
(ml/min)							
1		51.87	26.81	50.74	48.77	40.93	43.82
2	$R(W_b)^{i}$	-1.49	2.99	-0.21	6.45	-1.15	1.32
3		-1.88	5.74	-3.47	-0.85	4.80	0.87
1		19.10	25.06	22.23	18.97	14.79	20.03
2	$R(W_L)^{\ ii}$	-1.71	-1.32	-0.40	-1.23	1.19	-0.70
3		-1.11	4.44	4.97	5.50	-1.24	2.51

i. $R(W_b) = W_{b1}/W_{b2}$

ii. $R(W_L) = W_{L1}/W_{L2}$

iii. Deviation =100 x $(R(W_i) - R(W_{i_set}))/R(W_{i_set})$ and i= b or L. (Note: both $R(W_{b_set})$ and $R(W_{i_set}) = 1$)

The infill distance, which is the distance between the centre position of two adjacent printed filaments (both X-axis infill D_{I1} and Y-axis infill D_{I2}) was also monitored, with respect to the model pre-set value, to further evaluate the printing quality. Printing at $Q_f=1$ ml/min gave the most inconsistent quality with average deviation of X-axis and Y-axis infill both >10%. In contrast, the average deviations of X-axis and Y-axis infill were <0.3% and <2.5% for $Q_f=2$ and 3 ml/min respectively (Table 4- 5). The results further demonstrated best printing quality was attained with printing at $Q_f=2$ ml/min.

Table 4- 5. The woodpile feature block calculated percentage deviation of X-axis ($D_{\rm II}$) and Y-axis ($D_{\rm I2}$) infill distance for PMDI Mn340_1 wt. % DBTDL formulations printing using different flowrate.

Flowrate	Block		Widtl	Deviation (%)			
(Q_f)	features	1st	Average	3rd	4th	5 th	Average
(ml/min)							
1		9.87	9.10	12.30	12.03	10.50	10.76
2	$D_{\rm I1}{}^{\rm i}$	0.60	0.30	-1.87	-0.23	2.60	0.28
3		-0.33	4.87	1.23	4.07	2.50	2.47
1		-14.37	-13.13	-13.93	-12.27	-9.77	-12.69
2	D _{I2} ii	2.27	0.13	-1.53	-1.60	2.27	0.31
3		1.03	0.03	-1.17	0.53	1.83	0.45

 $i. \hspace{0.5cm} D_{I1} = W_{L1} + W_{b1} \\$

 $ii. \quad D_{I2} = W_{L2} + W_{b2}$

iii. Width deviation: W_i Deviation=100 x $(D_i-D_{i_set})/D_{i_set}$ and i=11 or I2. (Note: both D_{I1} and $D_{I2}=1$)

Besides the characterisation on the woodpile features, the effect of different extrusion flowrate on the reaction exotherm have also been investigated. Higher flowrate were hypothesised to afford better mixing, but experimental evidence showed that this did not provide the better printing quality, when reviewing that data from the flowrate $Q_f=3$ and 2 ml/min This was attributed by the greater amount of heat released at this higher flowrate, shown in Figure 4- 13 (i.e. the peak temperature for $Q_f=3$ ml/min was 22.6% and 46.0% higher than the value for $Q_f=2$ and 1 ml/min respectively), indicating a more intensified mixing and faster reaction rate, hence a higher reaction exotherm.

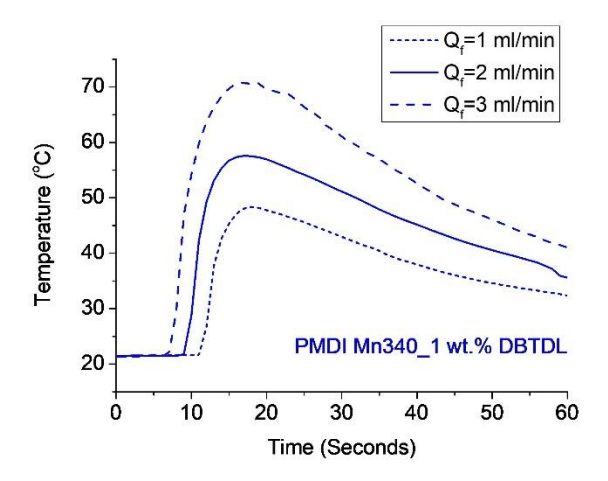


Figure 4- 13. Reaction exotherm of PMDI Mn340 formulation with 1 wt. % DBTDL at extrusion flowrate (Q_f =1, 2 and 3 ml/min).

Table 4- 6. Reaction exotherm of PMDI Mn340 formulation with 1 wt. % DBTDL at extrusion flowrate (Q_f =1, 2 and 3 ml/min).

Flowrate Q _f	T_1	T ₂	\mathbf{t}_1	t_2	$(\Delta T/\Delta t)$
(ml/min)	(°C)	(° C)	(s)	(s)	(°C/s)
1	21.62	48.38	10	18	3.3
2	21.77	57.6	9	17	4.5
3	21.66	70.62	7	16	5.4

Step 3: Layer height

The next step focused upon tuning the layer height at different parameter levels. This involved printing the same woodpile structures, to find the optimum layer height with best print quality. The quality of the print was evaluated using to the over-span features shown in Figure 4- 14.

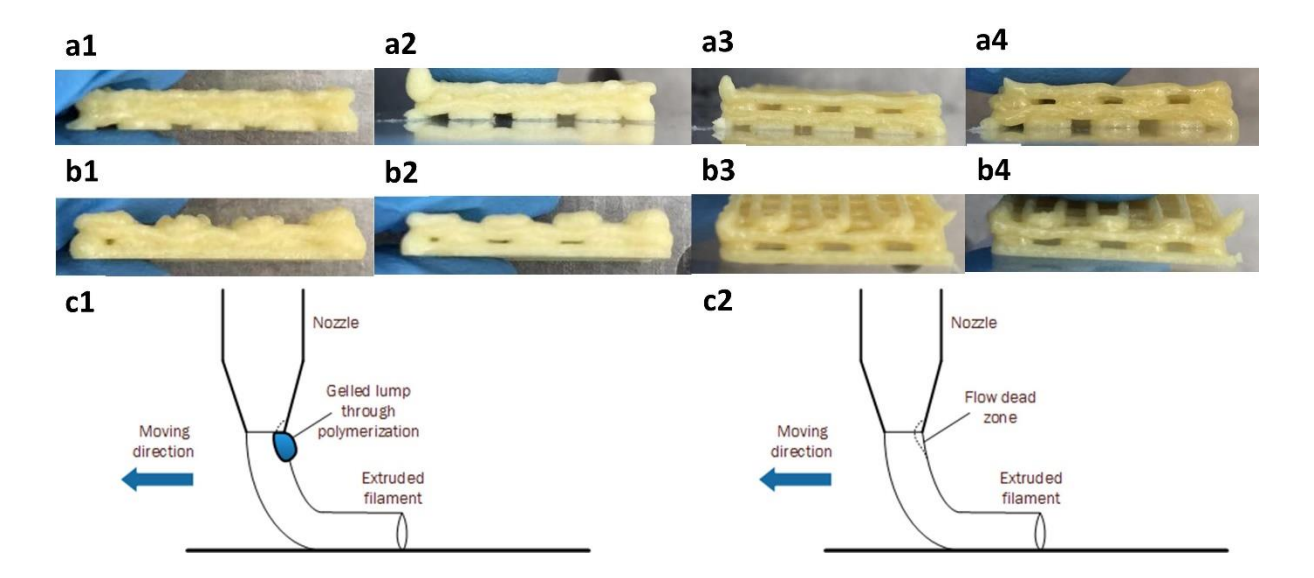


Figure 4- 14. Side view of the woodpile prints of PMDI Mn340_1 wt. % DBTDL formulation, using different layer height (h): (a1,b1); (a2, b2); (a3, b3); (a4, b4) for h=0.5; 0.75; 1; 1.25 mm respectively. Schematic of flow at c1) lower layer height and c2) optimum layer height.

The over-span on top of previous layer became more pronounced as the layer height increased from 0.5mm to 1.25mm. Printing at layer height (h=1mm), exhibited the most consistent overspans in first and third layer shown in Figure 4- 14-a3, and in second layer shown in Figure 4- 14-b3. Hence, layer height (h=1mm) was applied for printing parameters settings.

Investigation of Filament Voidage

Following printability screening and process optimisation workflow, the ability to construct prints of good quality and reproducibility had now been established. To further investigate the micro-scale level print resolution, the cross-section of the printed structures was analysed to investigate the internal structure of the filaments was conducted and the data were shown in Figure 4- 15.

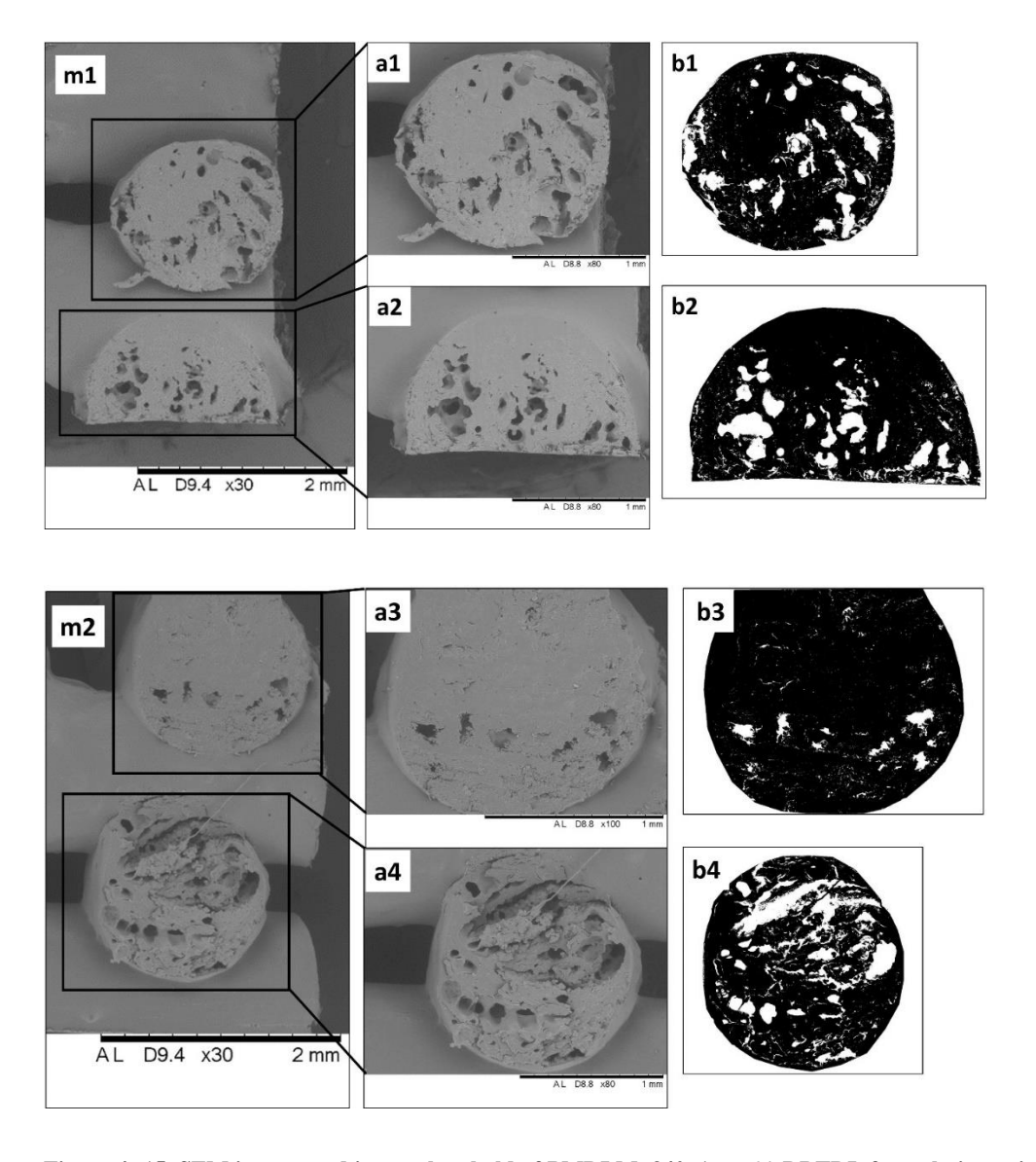


Figure 4- 15. SEM images and image threshold of PMDI Mn340_1 wt. % DBTDL formulation printed woodpile four layer structures cross-section. SEM images of sample cross-section for m1) First and third layer macro view. a1) Third layer view. a3) First layer view. m2) Second and fourth layer macro view. a3) Fourth layer view. a4) Second layer view. Image threshold created using ImageJ of sample cross-section for b1) Third layer. b2) First layer. b3) Fourth layer. b4) Second layer.

The four-layer woodpile prints showed various level of voids embedded in the different layers. The second layer presented highest level of void fraction (25.2%), which was more than five times higher than the average void level for the fourth layer. Typically, higher level of void fraction was presented in the mid layers (second and third), in compared with the first and fourth layer (Figure 4- 16a).

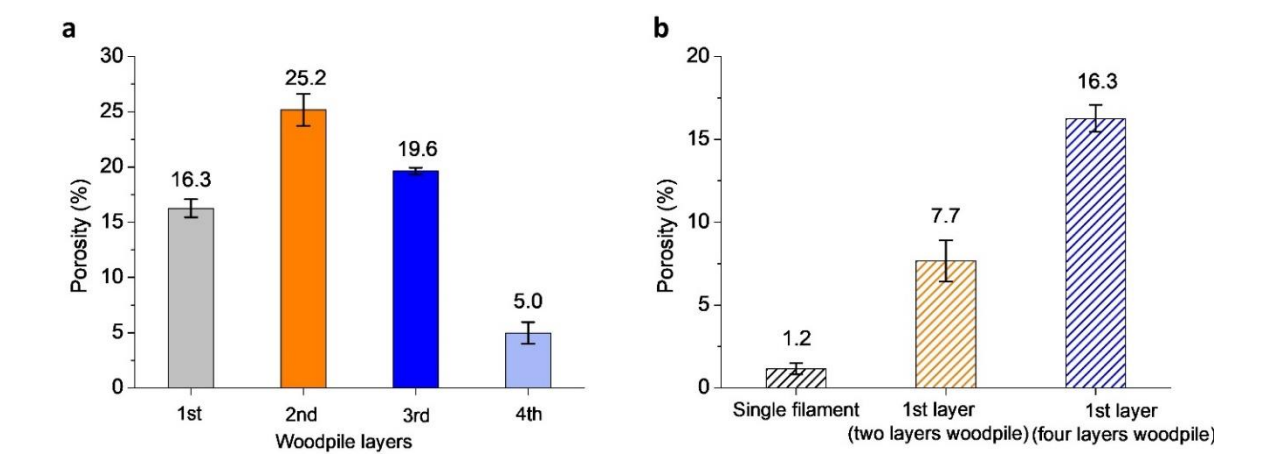


Figure 4- 16. Average porosity for printing structures using PMDI Mn340_1 wt. % DBTDL formulation for. a) Different layer porosity for four layer woodpile structures. b) First layer porosity of single filament, two layer woodpile and four layer woodpile.

The voids displayed inconsistent micro-structures among different layers in the same print. Another investigation was then conducted to identify the variance in void level within the same layer of woodpiles that contained different number of layers. The aim was to understand the effect of layer stacking on the micro-structures and the data was shown Figure 4- 17.

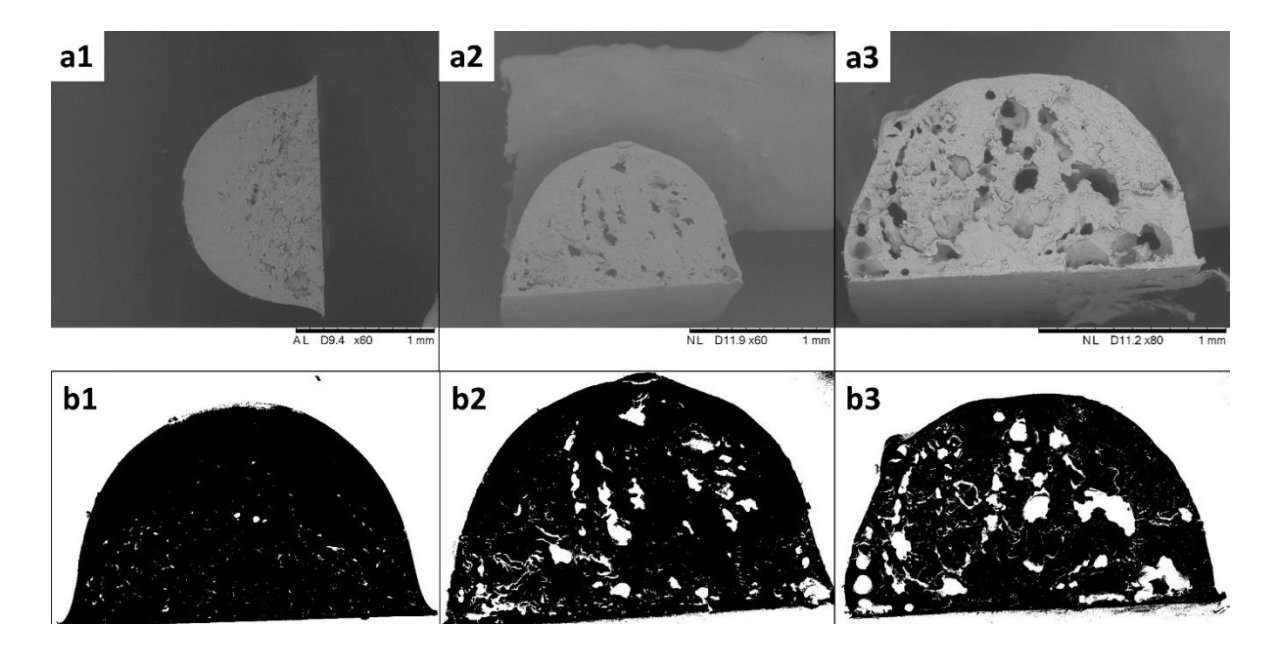


Figure 4- 17. SEM images and image threshold of PMDI Mn340_1 wt. % DBTDL formulation printed structures cross-section. SEM images of sample cross-section for a1) single filament. a2) first layer of a two layer woodpile print. a3) first layer of a four layer woodpile print. Image threshold created using ImageJ of sample cross-section for b1) single filament. b2) first layer of a two layer woodpile print. b3) first layer of a four layer woodpile print. Scale bar = 1mm.

There were higher percentages of voids exhibited in the cross-sections of samples printing when more layer were included in the stack, with four layer woodpile prints showing an average of 16.3% void fraction, which were more than two and thirteen times higher than the average void for two layer woodpile prints and single layer prints respectively (Figure 4- 16b).

To study the effect of catalyst level on the macro and micro-level print resolution, four-layer woodpile structures were printed and analysed using inks that incorporated different catalyst levels and the data is shown in Figure 4- 18.

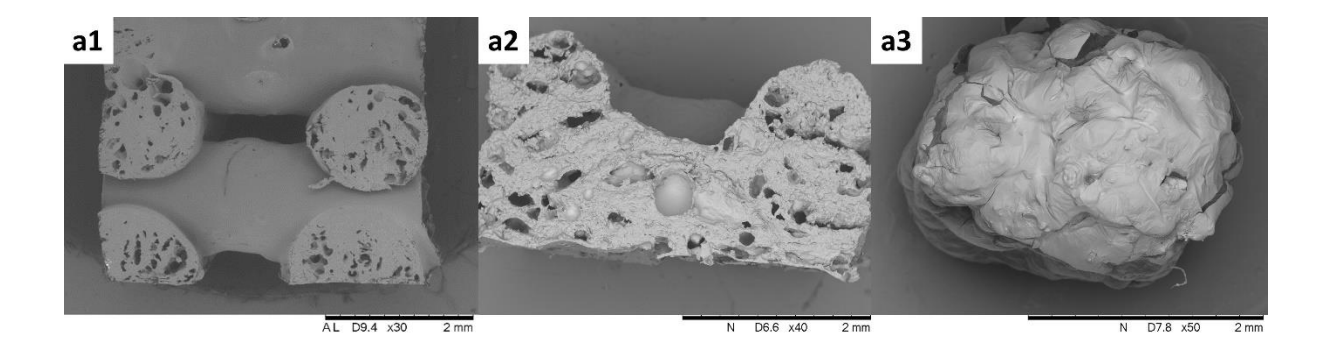


Figure 4- 18. SEM images of printed woodpile structure cross-section from PMDI Mn340 formulation with catalyst level: a1) 1 wt. % DBTDL. a2) 0.5 wt. % DBTDL. a3) 0 wt. % DBTDL.

When the catalyst level halved from 1 wt. %, highlighted as the preferred loading from the optimisation process to 0.5 wt. %, the spanning feature of the woodpile structure disappeared. Without catalyst introduced in the formulation, the upper layers of the woodpile prints sagged and merged into a single block. As the result, a dense print with no voids.

To trace the origin of the water in the system, the inks prior to printing on REX were characterised under a microscope. There were significant number of bubbles originally entrained in the viscous inks (both in the NCO and OH side), and subsequent studies showed that these could be removed by subjecting the inks to centrifugal mixing for 20 min (Figure 4-19).

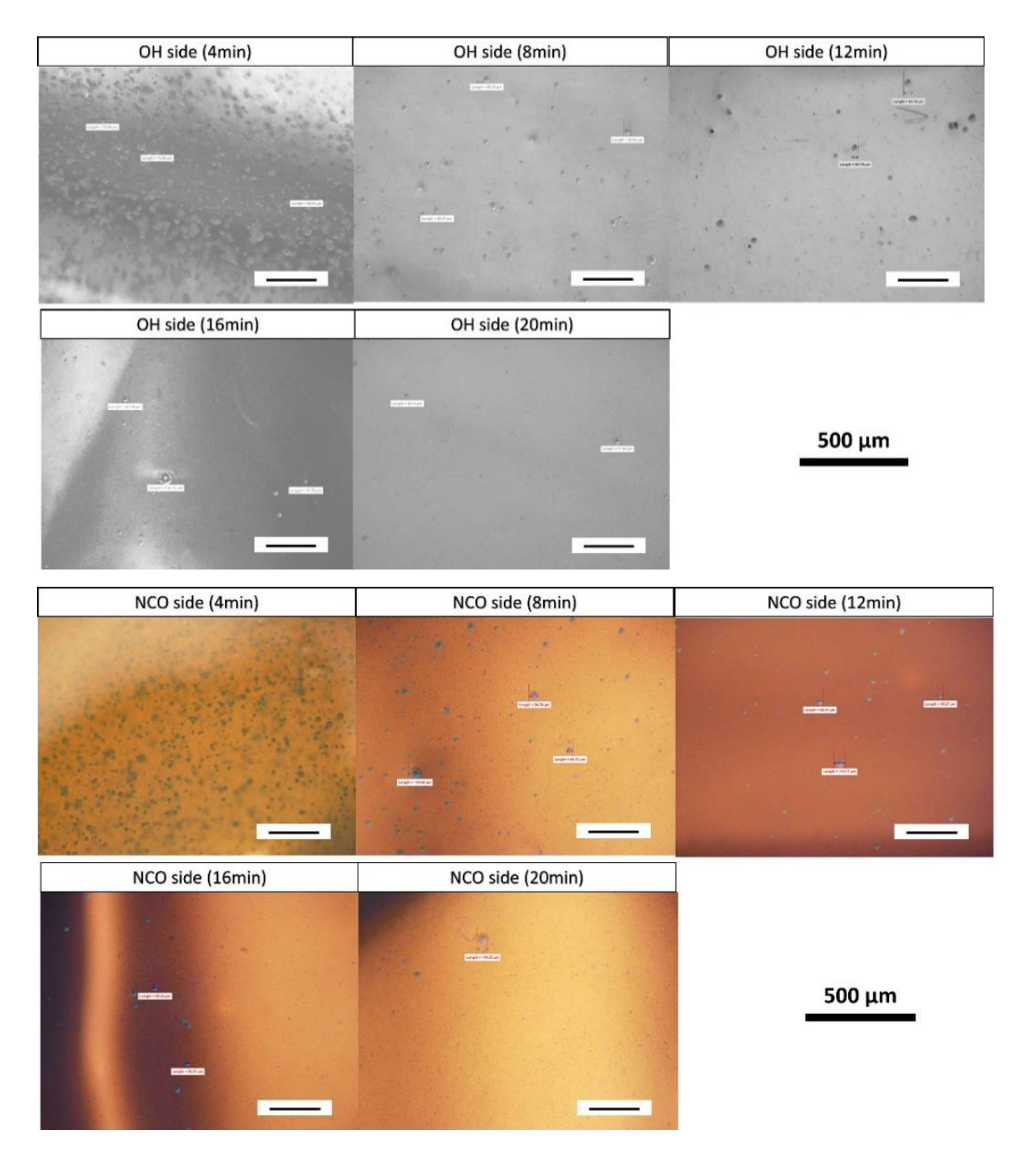


Figure 4- 19. Microscopic images of OH and NCO inks after different dual centrifugal mixing (DAC) time prior to loading to the REX system.

However, when the mixed inks were transferred into and were stored in the REX system prior to the process starting, an increased number of bubbles were noted to be present due to the action of charging the feed hoppers (Figure 4-20).

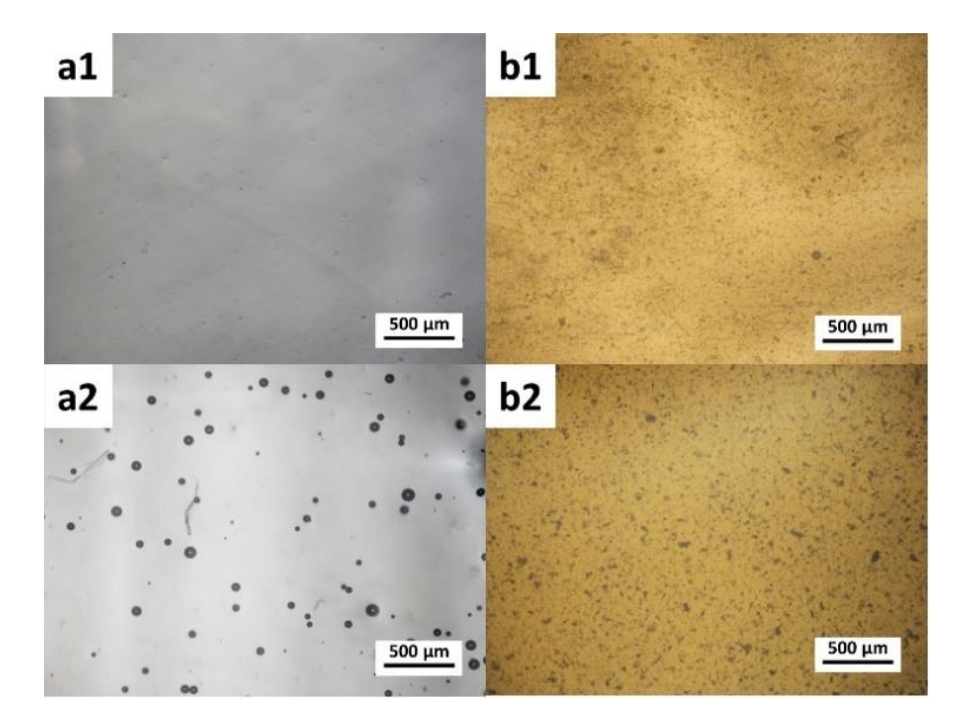


Figure 4- 20. Microscopic images of OH inks. a1) before loading to the REX system. a2) after loading and rest in the REX system. NCO inks. b1) before loading to the REX system. b2) after loading and rest in the REX system.

To understand the cause of the voids embedded in the microstructures, the reaction exotherm of the PMDI Mn340 formulation with different catalyst level was monitored and the data was shown in Figure 4- 21.

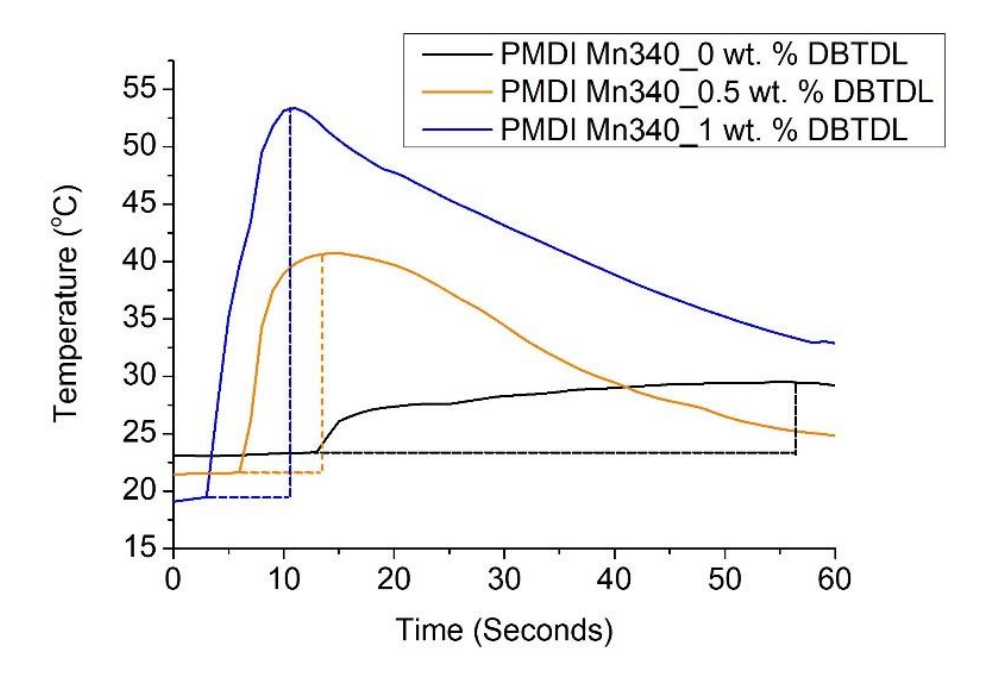


Figure 4- 21. Reaction exotherm of PMDI Mn340 formulation with different catalyst level: 0 wt. %, 0.5 wt. % and 1wt. % DBTDL.

The temperature in the printed samples was observed to rise rapidly due to the exothermic PU reaction 57 . The highest peak temperature was shown in the 1% catalyst formulation, attributed to the higher catalyst loading resulted in the fastest reaction kinetics. The rate of reaction exotherm (i.e. $\Delta T/\Delta t$), where ΔT denotes the temperature difference between the peak temperature of the PU after printed and the starting temperature when the PU was just extruded from the static mixer, for 1% catalyst formulation was 2.2 times and 32.1 times higher than the value of 0.5% and 0% catalyst formulations respectively, as shown in Table 4- 7.. This suggested there had been more intense reaction between reagents for 1% catalyst formulation, which releasing significant amount of heat over a short period of time.

Table 4- 7. Reaction exotherm for PMDI Mn340 formulation printed using different catalyst level. T_1 and T_2 are the sample temperature at t_1 and t_2 respectively, whereas t_1 and t_2 are the starting point when the temperature increased and the time when peak temperature was reached, respectively. The dotted line defined the range between t_1 and t_2 .

PMDI Mn340	T_1	T_2	$\mathbf{t_1}$	\mathbf{t}_2	$(\Delta \mathbf{T}/\Delta \mathbf{t})$
formulations	(°C)	(° C)	(s)	(s)	(°C/s)
0 wt. % DBTDL	23.11	29.58	6	55	0.1
0.5 wt. % DBTDL	21.52	40.75	5	15	1.9
1 wt. % DBTDL	19.47	53.38	3	11	4.2

4.2 Discussion

4.2.1 Printability Analysis

This study had the objective of investigating the second group of REX formulations, i.e., those that rely on faster reaction kinetics to deliver the filament fidelity. This reaction rate would be the key assessing criterion to identify the target formulation by means of monitoring the transitional ink rheology and characterising the reaction kinetics.

Transitional ink rheology measurements were shown to offer an insight on how quickly the cross-linking network was formed. There are two metric that were used for the printability evaluation in this study: (1) the transitional curve of tan $\delta = (G''/G')$ showed the growth rate of dynamic moduli, and (2) the value of tan δ defined whether the ink exhibited the viscoelastic liquid or solid dominant ink flow behaviour. In looking at the transitional curve, the presence of a tan δ peak in the curve indicated a faster transition into a region of where the increase in the storage modulus was greater than that of the loss modulus. This was attributed to a faster cross-linked network development. This is a desirable transitional ink rheology profile/property and was observed to be behaviour presented by the PMDI Mn340 formulation. The transitional ink rheology and reaction kinetics characterisation also helped to identify the optimum catalyst level. For the PMDI Mn340 formulation, 1.5 wt. % catalyst showed an inferior transitional rheology profile and reaction speed when compared with 1 wt. % catalyst loading (Table 4- 2). This can be explained by the fact that the polyurethane oligomers were formed more rapidly with higher catalyst loading, and so the viscosity quickly increases in such system. As a result the crosslinking reaction speed will be hindered due to this high viscosity, as chains have low mobility and this reactive functionalities cannot find one another 123. The inks will start to behave as favoured viscoelastic solid behaviour when $\tan \delta < 1$. Among the three catalyst loadings investigated in this study, the 1 wt. % catalyst loading showed the lowest value of tan δ . This indicated that this printed mixture has highest tendency to flow as viscoelastic solid as reaction progresses.

Additionally, the initial storage modulus of the formulation (at time $t \le 1$ min) is another key metric that was used to evaluate the printability of the formulation. This time window was chosen to correlate the maximum residence time of the flow of material within the static mixer section of the REX apparatus. The higher the value of initial storage modulus at the point when filaments are deposited onto the print platform, the better the printing fidelity. These properties were shown to be exhibited by the PMDI Mn340 formulation, in addition to the Mn340 formulation, the HDI formulation also fulfilled these evaluation metrics. However, the HDI formulations suffered from the lowest viscosity and storage modulus (i.e., the viscosity of HDI was 260 times lower than the value for PMDI Mn340 formulation at shear rate 20 s⁻¹) (Figure 4- 1). As the result, the HDI formulation would need to incorporate a significant amount of rheology modifier to tune the printability, hence it was identified as not being an ideal REX formulation.

4.2.2 Process Optimisation

Optimisation Workflow Standardise process optimisation workflow is critically needed for a good reproducible print to be fabricated via REX. Previous material extrusion processes (i.e. fused deposition modelling (FDM)) optimisation workflow would often correlate the preestablished filament information (i.e. filament size and melting temperature) with the printing parameters (i.e. layer height, extrusion temperature) ¹². Other material extrusion printing (i.e. direct ink writing (DIW)) optimisation workflow often carefully tune the ink rheological properties, and empirically link the extruded filament sizes with the printing parameters ^{121,124}. Similar approach was undertaken in this study to design the standard process optimisation workflow for the REX system, with additional further considerations being made for the impact of in-situ mixing and reaction characteristics upon the process parameter. One key design feature that need to be achieved is to avoid the static mixer nozzle clogging from the fast crosslink network build up within the mixer before the filament leaves the end of the nozzle. However, the in-situ reaction within the filament should afford stronger cross-linking network, as reaction continues, after the filaments has been deposited onto the print platform. Optimised reaction/crosslinking kinetic together with rheological properties of the feedstocks and ink, provide a combination that would lead to a double reinforcing effect to assist layer stacking and filament fidelity.

Therefore, the step 1 and 2 of the proposed workflows essentially identified the optimum extrusion flowrate and can served the aforementioned needs to leverage the in-situ mixing and reaction.

The experimentation demonstrated that a flowrate of $Q_f=1$ ml/min presented the largest deviation to the pre-set values (Figure 4- 9). This was proposed to explain why the lowest mixing intensity was achieved at this flowrate, and consequently led to slower reaction.

Filaments printed at this flowrate exhibited higher sagging tendency, and the printing quality eventually deteriorated.

The higher temperature of in the printed filaments at flowrate Q_f =3 ml/min , potentially could reduce the viscosity (i.e. reduce density at higher temperatures) and storage modulus of the both the "first" filament layers and the next layer printed on the top of this first layer ⁹¹. This would result in relatively poorer filament fidelity of both the first and upper layer and exacerbate the reduction in printing quality. Therefore, optimum flowrate was defined to be Q_f =2 ml/min this was utilised for the remainder of the study.

The layer height was optimised at 1 mm to accommodate the extruded filament, and to mitigate the potential for the formation of gelled lumps near the nozzle tips caused when the layer height was kept too low (Figure 4- 14). Such gelled lumps can form due to the imbalanced flowrate at the top and bottom side of the filaments and become indistinguishable once the layer height can accommodate this differential flowrate.

4.2.3 Porous structure

A highly porous morphology was shown to exist at the microscale in the cross-sections of printed PU woodpile structure filaments. The exothermic reaction is believed to be the main cause of the voids in the cross-section. There is the side reaction between free isocyanate group and water which forms CO₂, along the main reaction to form PU ⁴². Furthermore, when one layer was printed, it is proposed that only intra-layer reaction occurs, whereas when subsequent layers are stacked onto the previous ones, both the intra-layer and inter-layer reactions progressed. These synergetic effect of reactions on the same plane and across the planes would speed up the overall reactions in the system, partly due to the insulating effect of the top layer reducing loss of exotherm temperature to the surroundings. Thus, a higher exotherm is achieved. Consequently, these exothermic reactions advanced at greater speed at the mid-layers (i.e., the second and third layer for a four-layer woodpile print), as heat dissipation from the mid-layers were more challenging compared with the top layer which exposed to the ambient environment. As the result, there were more voids seen in the mid-layers. In contrast, the single layer filament was produced with no voids at the cross-section, owing to the better heat dissipation. Furthermore, PMDI Mn340 formulation with no catalyst showed dense crosssection in the four-layer woodpile prints. This was attributed to the slower reaction and less heat was generated during the reaction.

Thus, during processing, these bubbles were potentially captured and grown around the filler nanoparticles which it was proposed acted as nucleation centres. The combined effect of these bubbles in the inks and printing at ambient environment without enclosed inert gas shielding led to the porous cross-section in the prints at such fast kinetics.

4.3 Conclusion

In this chapter, a standard workflow has been established for printability analysis and process optimisation for any PU formulations fabricated via the REX system. PMDI Mn340 formulation was screened out and successfully printed with good reproducibility following on the proposed guidance.

To highlight the fundamental difference between REX and other material extrusion 3D printing technologies, specific considerations of the in-situ mixing, and reaction were considered: (1) transitional ink rheology is the key characterisation tools in the printability analysis step, as it offers great insight on how fast the cross-linking network develops. (2) In the printing optimisation step, the optimum flowrate is the key parameter to evaluate, to identify the favourable mixing intensity to afford the printing fidelity. To pursue the fast reaction kinetics of PU, there is a trade-off in the printing quality at the micro-scale. The fast exothermic reaction could lead to micro-voids in the cross-section.

CHAPTER Five

5 Investigation the Effects of Feed Rheology on the Three
Types of Mixing Modes and Printed Polyurethane
Properties

In this chapter, cross-linked thermoset PU formulations were investigated, formed by contacting a polymeric isocyanate (PMDI Mn340) with feedstocks containing multiple hydroxyl functional groups that exhibit different rheological properties. The aim is to reveal the significance of these properties on the mixing, reaction kinetics and the thermo-mechanical properties of final PU printed from a REX process. To achieve this, three mixing modes were designed by including into the separate feeds varying levels of fumed silica (FS) particles to act as rheology modifiers. Rheological properties, such as the viscosity ratio and elasticity ratio between two feeds, were investigated to assess their impacts on the level/type of mixing achieved in the REX processes during filament production and the influence this had on the properties of the printed parts.

5.1 Results

In REX 3D printing, the mixing efficiency and reaction kinetics are highly synergistic. Furthermore, both are greatly influenced by the rheology of the two feeds. Thus, it was initially demonstrated that three mixing modes (designated as MM1, MM2 and MM3) were obtained when the two feeds exhibit different feed rheological properties. These mixing modes were achieved when processing the following feeds through the REX static mixer. The isocyanate (NCO) feed composed of a polymeric isocyanate and three different levels of FS particles (5 wt.% - MM1, 2.5 wt.% = MM2 and 1 wt.% = MM3) with a composite multi-ol feed containing a polymeric diol soft segment, a low molecular weight diol (1,4 butanediol - 1,4BD), 5 wt.%

FS and a polymerisation catalyst (1 wt.%). Figure 5- 1 shows the type of final flow regime that was exhibited by the different mixing modes.

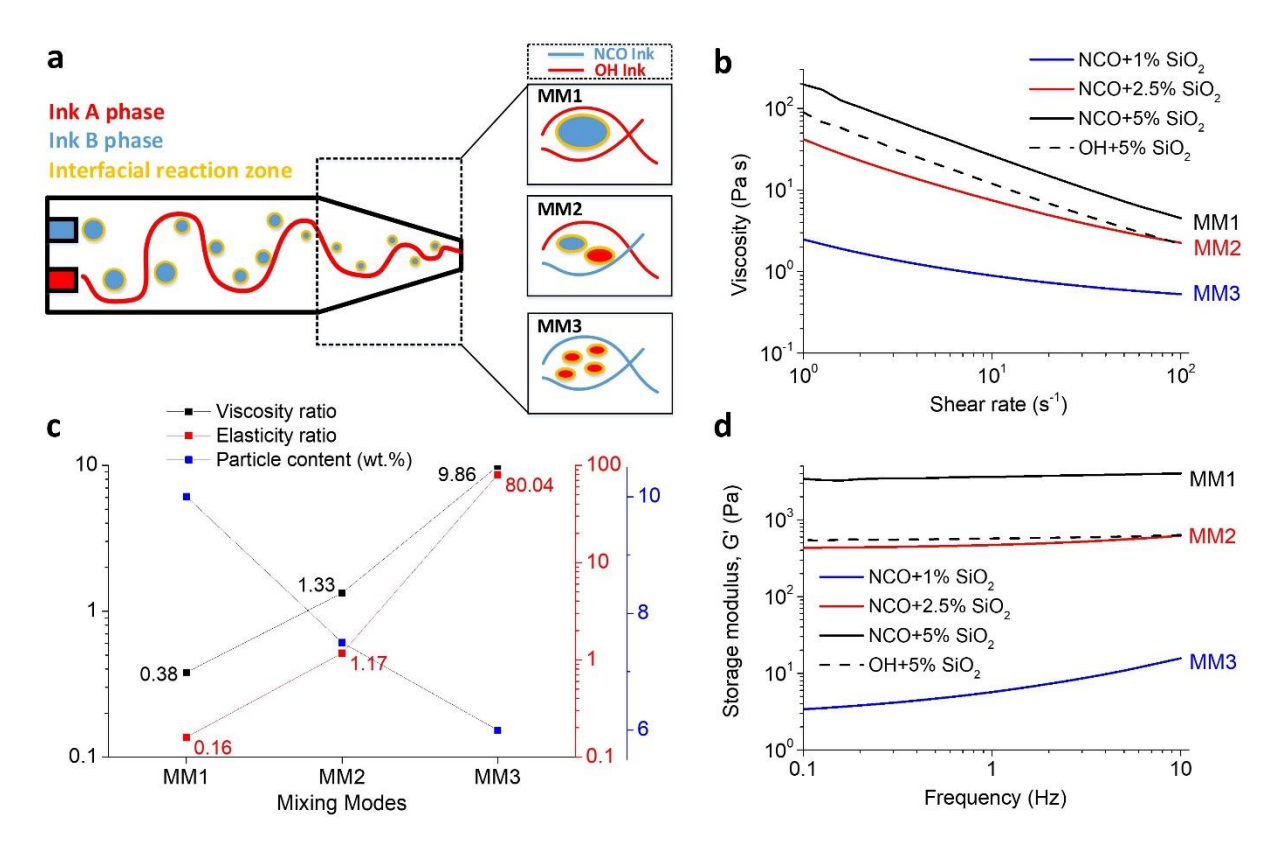


Figure 5- 1. Rheological comparisons between MM1, MM2 and MM 3. a) A schematic of mixing process in the static mixer for all mixing modes. b) A plot of viscosity as a function of shear rate for all the mixing modes. c) A plot of the viscosity ratio (OH: NCO), elasticity ratio (OH: NCO) and particle content loadings that result in the three mixing modes. d) A plot of G' as a function of frequency for all mixing modes.

Mixing morphology of viscoelastic fluids have been well studied before, it was shown that one of following morphologies will form: matrix/droplet¹²⁵, matrix/fibre ¹²⁶, co-continuous ¹²⁷. When viscoelastic fluids mixed through a static mixer, matrix/droplet morphology, also noted as dispersed/continuous phase would formed ^{128,129}. It suggested that when the two viscoelastic feeds got in contact in REX static mixer, an interfacial reaction zone would likely be generated between two phases (Figure 5- 1a), typical of the interfacial polymerisation found in PU chemistry ^{52,55,57}. It has been proposed that the formation of the interfacial zone is heavily influenced by the viscosity ratio, elasticity of the polymer ¹³⁰. Therefore, the viscosity ratio and

elasticity of the polymer would effectively determine the reaction rate, as these will also define any diffusion limitation within the viscous PU materials oligomers.

Based on the feed rheological properties, for this study, feed formulations were designed by adding various levels of FPs to generate the desired viscosities from both feeds, such that they would deliver these three mixing modes with distinct interfacial mixing profiles. The formulation for MM1 comprised NCO+5% SiO₂ and OH+5% SiO₂, where both the viscosity and G' of the NCO ink was higher than that of the OH ink. Also, the viscosity of NCO feed was the highest among the three MMs (Figure 5- 1b and 1d). The MM2 feed consisted of NCO+2.5% SiO₂ and OH+5% SiO₂, such that similar rheological properties were presented from both the NCO and OH feeds. Meanwhile, the MM3 feed were NCO+1% SiO₂ and OH+5% SiO₂. Thus, the OH feed displayed a dominant viscosity and storage modulus of over NCO feed. The difference between the two feeds' viscosity and elasticity was the greatest among the MMs.

Thus, the feed rheological properties are key indicators which define whether (a) the desired mixing mode that will be achieved and (b) the product feeds can be self-supportive when deposited onto the print bed ¹²⁰. Hence, the effect adding FS particles had upon the rheological properties of both the isocyanate and polyol feeds was examined and the data comparing the change in viscosity as a function of shear rate and change in dynamic moduli as a function of frequency are shown in Figure 5- 2.

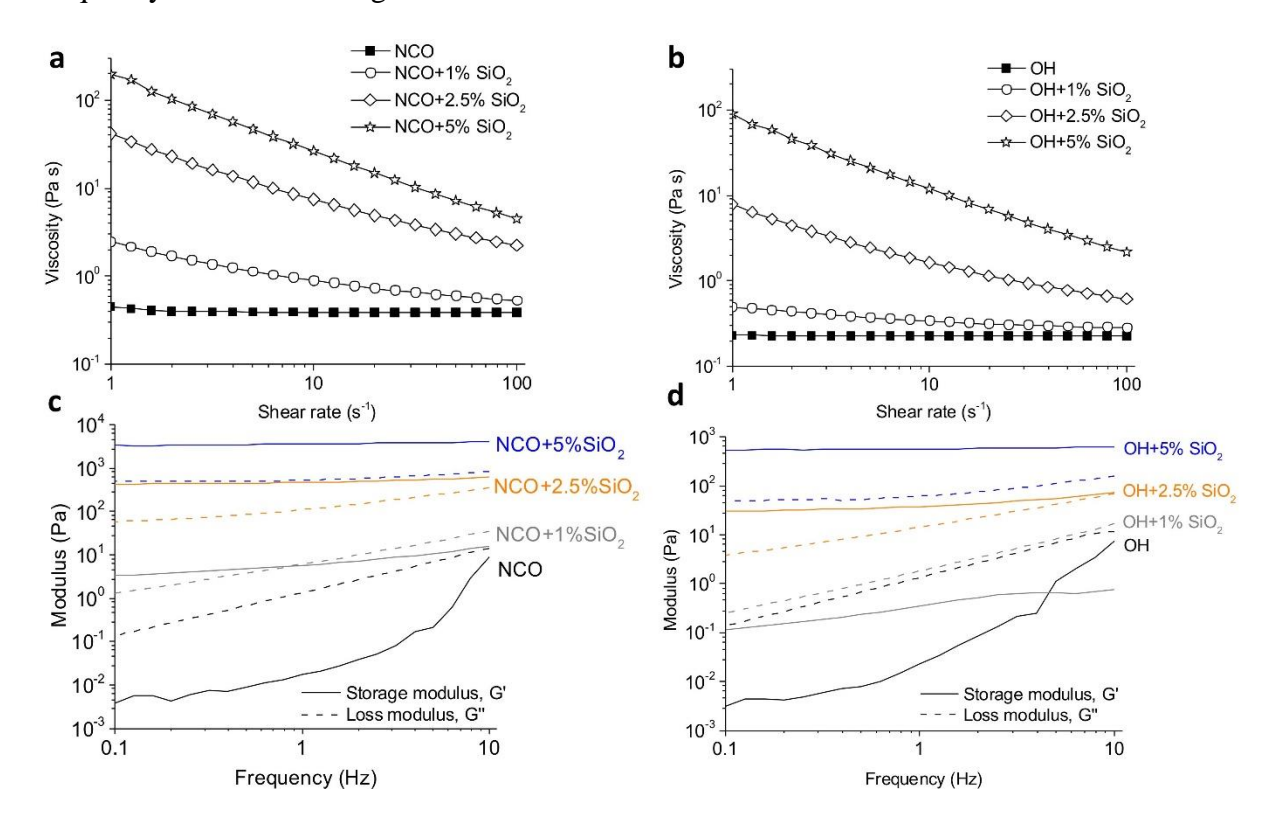


Figure 5- 2. Rheological properties of the feeds. Viscosity as a function of shear rate for a) NCO feeds, b) OH feeds. Storage modulus and loss modulus as a function of frequency c) NCO feeds, d) OH feeds

The data showed that shear-thinning behaviour was observed with the feed mixtures that had received additions of FS. By comparison, the neat reagents (i.e. isocyanate and polyol only) exhibited an apparent viscosity that were independent of shear rate. Furthermore, it was noted that the higher the FS content, the greater the viscosity the NCO and OH feeds exhibited (Figure 5- 2a and 2b). Furthermore, both the storage modulus (G') and loss modulus (G'') increased with the addition of silica particles (Figure 5- 2c and 2d).

Both reagents displayed viscous liquid behaviour, with frequency-independent loss modulus being observed to be larger than the storage modulus. In the case of the NCO feed, upon addition of 1% FS, a "crossover" in the G' and G" values were exhibited (i.e. G' began to exhibit larger modulus values) at 1 Hz, where such a crossover is referred to as the gel point. In this case, the gel point to have occurred when the feed starts to exhibit viscoelastic solidlike behaviour, giving it the ability to sustain structural integrity upon deposition. Furthermore, as the loading of FS was further increased, G' was noted to dominate over G" throughout the full range of frequencies tested. These results indicate that both NCO+5% FS and NCO+2.5% FS showed more elastic behaviour. As a plateau was reached in the storage modulus data of both the NCO+5% FS and NCO+2.5% FS samples, this indicated a solid-like ink behaviour. For the polyol feed material, OH+1% FS still presented as a viscous liquid, with lower G' than G" at all frequencies. Meanwhile, like isocyanate feed, OH+5% FS and OH+2.5% FS both exhibited like elastic solid behaviour. The G' values of samples with OH+5% FS loading was significantly higher than that of both the samples with lower silica particle loadings and the neat reagents. Thus it was concluded that both the NCO and OH feeds with higher FS loadings were characterised by the superior viscoelastic and gel-like properties, which is essential in preventing the distortion during printing process ¹⁵.

The effect of introducing FS into the feeds on the yield stress was also investigated, see Figure 5-3a and 3b.

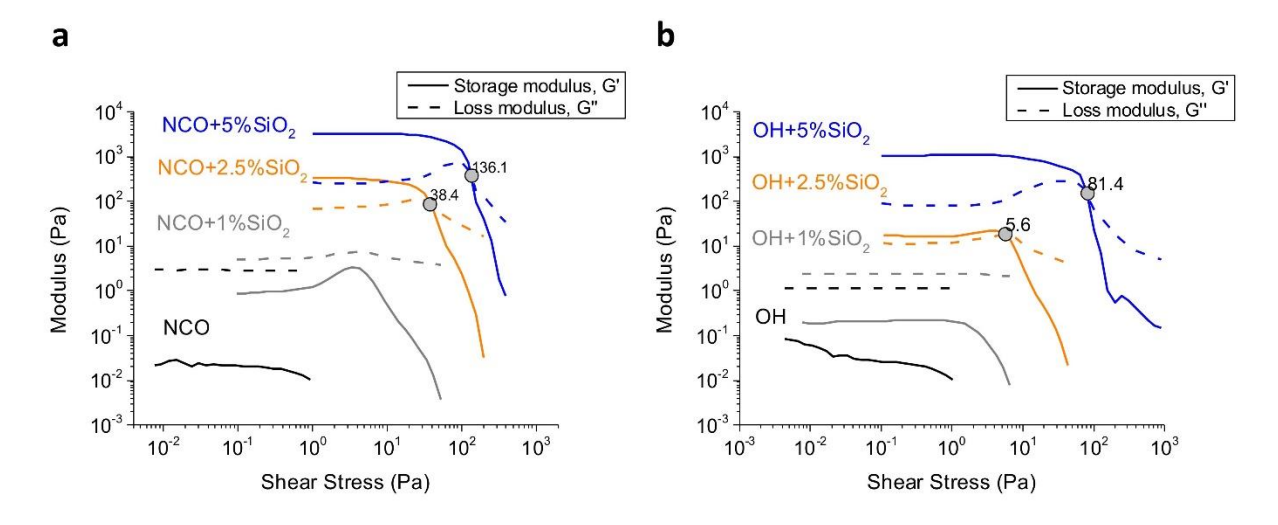


Figure 5-3. Oscillatory rheology data of investigated feeds. a) Isocyanates feeds and b) Polyol feeds.

This data showed that, for both the neat feeds without FS loading and those with 1% FS loading, both NCO and OH feeds presented as viscous liquids, with G" demonstrated to be higher than G' regardless of the shear stress applied. By comparison, for the feeds with 2.5% and 5% FS, the NCO and OH feeds exhibited elastic solid behaviour, when subjected to low shear stress. Additionally, the G' and G" data exhibited cross-over points as stress increased. After the cross-over point, they, started to behave like a viscous liquid i.e., higher G" than G'. Furthermore, it was observed that higher yield stresses were exhibited by the NCO feeds when compared to the OH ink with same level of FS loading. This was attributed to better interaction/wetting between the FS particles with the NCO matrix materials (Table 5- 1)

Table 5-1. Yield stress of the inks obtained from oscillatory rheology test.

Inks	Yield Stress (Pa)
NCO+5% SiO ₂	136.1
NCO+2.5% SiO ₂	38.4
OH+5% SiO ₂	81.4
OH+2.5% SiO ₂	5.6

The literature also documents that the reaction kinetics will be influenced by the mixing mode achieved, the kinetics of three MM systems were therefore monitored and compared as shown in Figure 5-4.

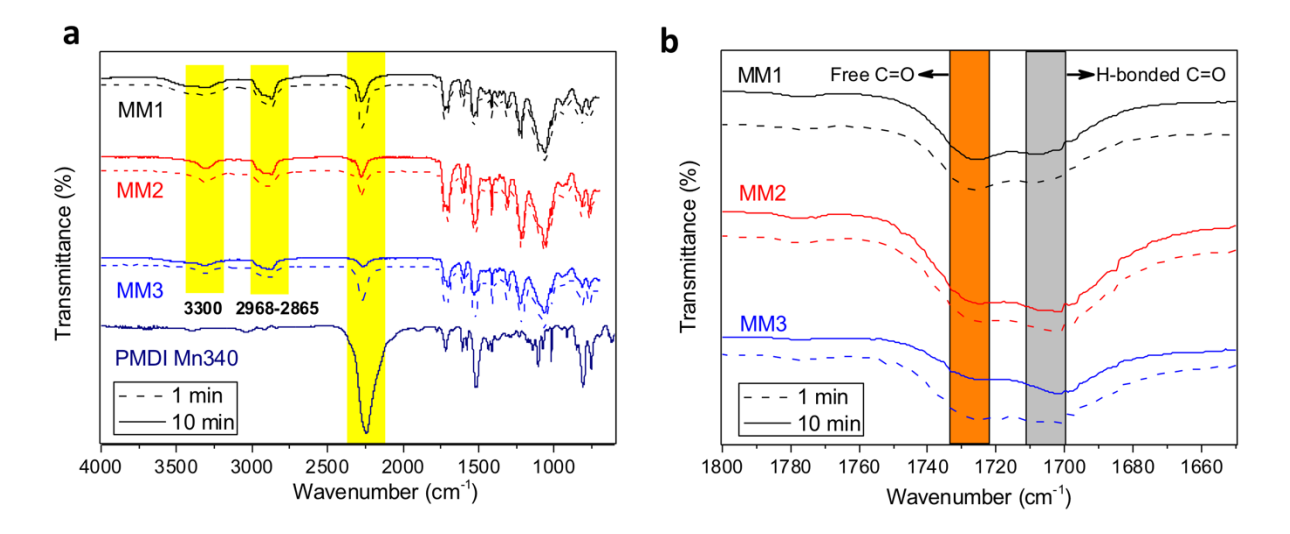


Figure 5- 4. FT-IR spectra of samples after printing at 1 min (dash line) and 10 min (solid line) from three mixing modes, schematic of hydrogen bonds within the PU structure. a) FT-IR spectra of PMDI M_n340, PU samples printed from MM1, MM2 and MM3. Amplified spectra of b) Free and hydrogen bonded carbonyl peaks (C=O).

The FTIR data confirmed that significant cure levels were achieved within the first 10 minutes of processing. As the PU reaction progressed from 1 to 10 minutes, significant reductions in the characteristic FTIR peaks for the isocyanate group (~2250 cm⁻¹) were observed for all samples (Figure 5- 4a). In all three mixing modes, a stretching hydrogen bonded N-H group (~3300 cm⁻¹) was observed ^{50,107,117}, whilst the C-H peak ~2865-2968 cm⁻¹ remained unaltered throughout the reaction. Within this time region the FTIR peaks were attributed to free and hydrogen bonded urethane carbonyl peak (C=O, ~1725 cm⁻¹ and ~1701 cm⁻¹ ^{117,131}. A more intense H-bonded C=O peak in contrast to free C=O peak was displayed in MM3 (Figure 5-4b).

Additionally, the NCO peak for MM3 was noted to be smaller than those of MM1 and MM2 at 10 min, potentially indicating higher reaction conversion and this faster reaction kinetics exhibited for MM3 (Figure 5-5).

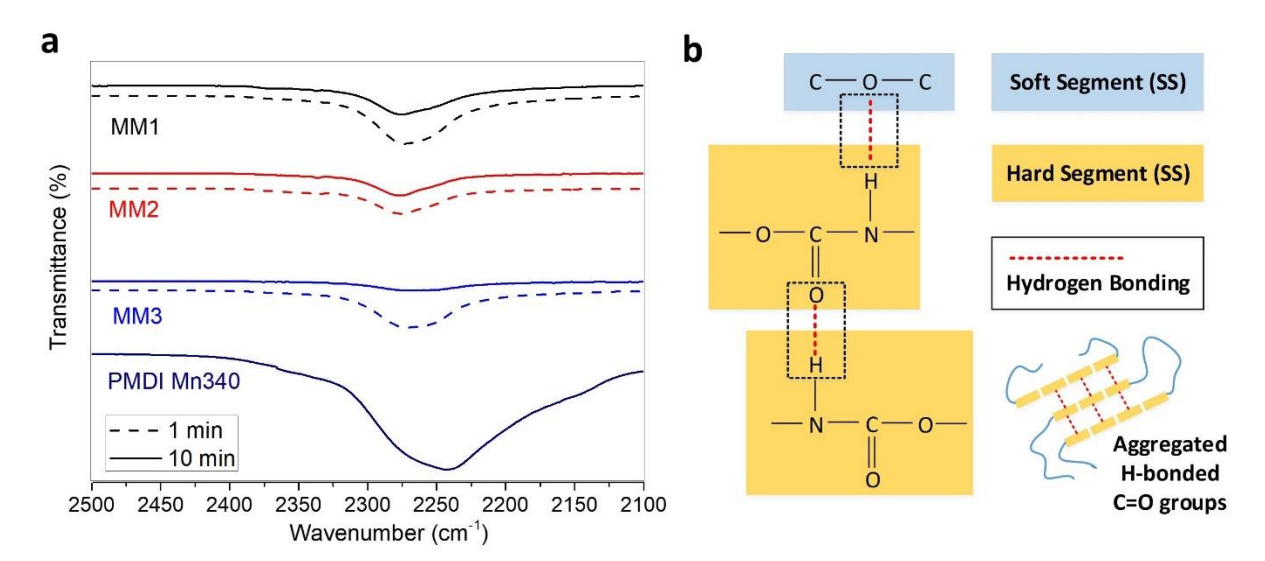


Figure 5- 5. FT-IR spectra of PMDI M_n340 , PU samples printed from MM1, MM2 and MM3. a) Amplified spectra of Isocyanate peak (-NCO). b) Schematic of hard segment, soft segment and hydrogen bond within the printed PU structure and aggregated hydrogen bonded urethane carbonyl group (C=O).

 $Table \ 5-\ 2. \ Reaction \ conversion \ of \ polyure thane \ samples \ printed \ utilising \ MM1, MM2 \ and \ MM3 \ at \ 1 \ min \ and \ 10 \ min.$

Time	Reaction Conversion			
(min)	(%)			
	MM1 MM2 MM3			
1	80 84 83			
10	84	87	93	

The thermal decomposition properties of printed PUs were analysed and compared. This data presented in Figure 5- 6.

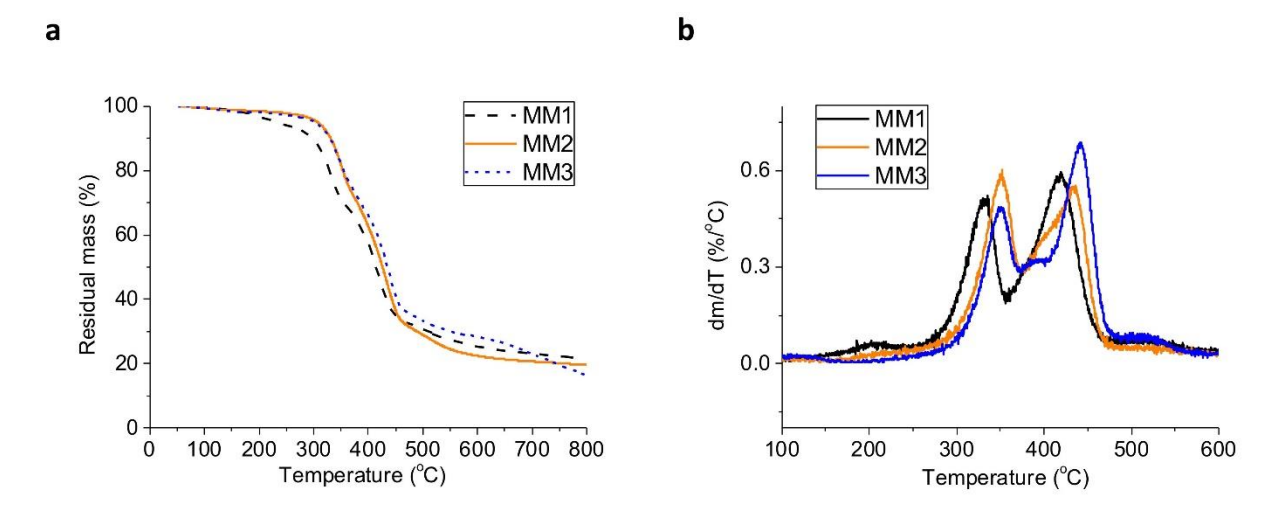


Figure 5- 6. a) TGA mass loss and b) differential thermogravimetric (DTG) analysis thermograms of PU samples printed from three mixing modes.

The TGA thermograms (Figure 5- 6a) for all three samples were very similar, with the exception that the MM1 exhibited an additional lower temperature decomposition step commencing at 200 °C. This was attributed to impurities introduced on the surface of silica particles ^{131,132}. This conclusion was supported by the observation that the size of this weight loss increased in MM1 as more silica particles were introduced. Meanwhile, two pronounced peaks (DTG (I)_{max} and DTG(II)_{max}) were observed in (Figure 5- 6b), indicating the potential that microphase-separation had occurred in all three mixing modes printing. DTG (I)_{max} was at 340-370 °C and DTG (II)_{max} located within 430-450 °C which corresponded to the decomposition of the urethane bond in the hard segment and ether bond in the soft segment respectively ^{58,119,133}.

Both DTG (I)_{max} and DTG(II)_{max} again showed graduation in the data with greater similarity between MM2 and MM3 (Table 5- 3), suggested that the thermal stability of printed is influenced by the type of mixing modes.

Table 5- 3.Thermal properties of PU samples printed from MM1, MM2 and MM3. $T_{5\%}$: Temperature at 5% weight loss obtained from TGA mass loss thermogram. DTG (I)_{max} and DTG(II)_{max}: lower and higher peak temperature in the DTG theromogram, respectively.

Mixing Modes	T _{5%} (°C)	DTG (I) _{max} (°C)	DTG (II) _{max} (°C)
MM1	252.3	344.9	431.8
MM2	294.7	362.0	442.3
MM3	319.2	368.3	450.6

The DSC analysis for the PU printed samples also showed a trend in the data from MM1 to MM3 with the T_g 's define to the 51.0 °C (MM1), 73.0 °C (MM2) and 80.5 °C (MM3), whilst no melting endotherm was detected, indicating the printed samples are cross-linked (Figure 5-7).

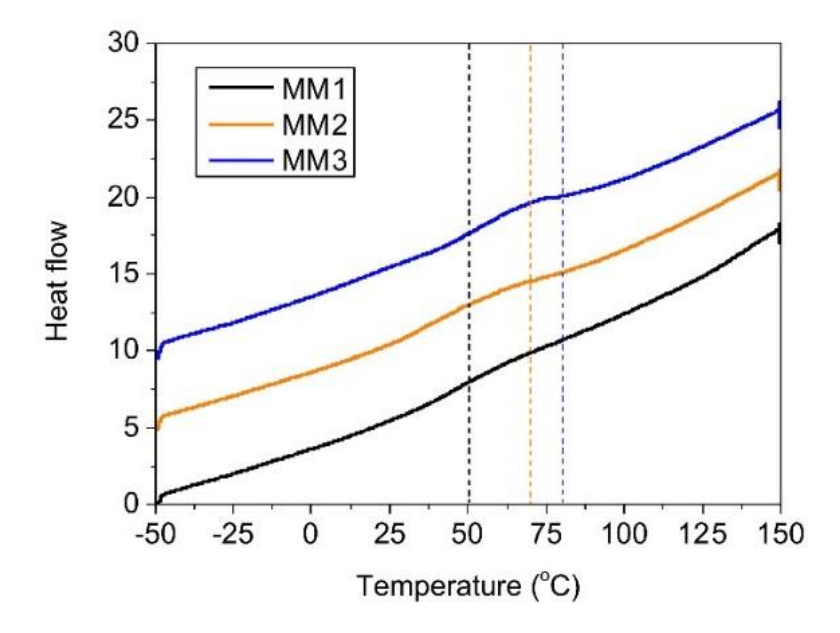


Figure 5-7. DSC curves of PU samples printed from three mixing modes.

Meanwhile, typical reaction exotherms recorded for the three MMs are shown in Figure 5-8.

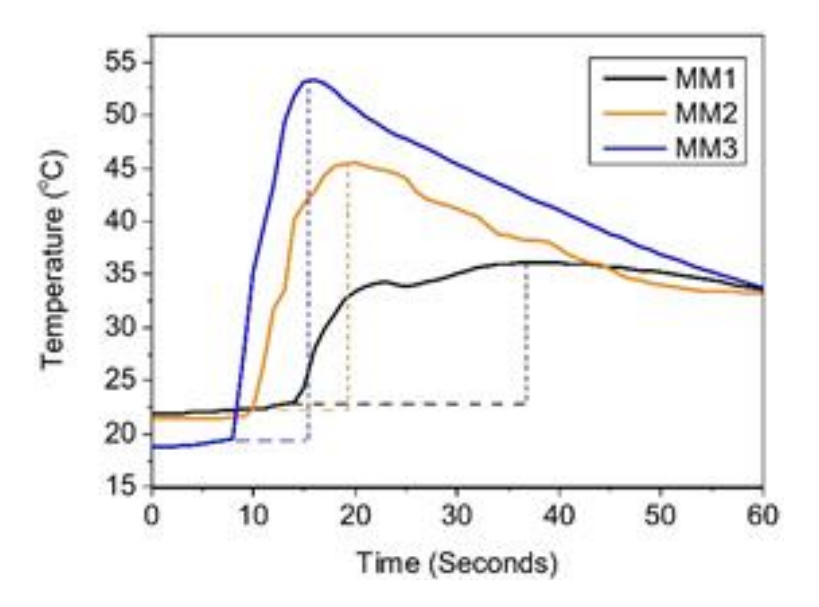


Figure 5-8. Reaction exotherm for PU samples printed from MMs.

The temperature in the printed samples rose rapidly due to the exothermic PU reaction ¹²³. The time where the exothermic reactions started was 14 s, 10 s and 8 seconds for MM1, MM2 and MM3 respectively (Table 5- 4), with MM3 reaching the highest peak temperature. This was ascribed to the highest reaction kinetics in MM3, suggesting that there had been more intimate mixing of the reagents with this mode. The rate of reaction exotherm ($\Delta T/\Delta t$) for MM3 is 1.8 times and 7 times higher than the value of MM1 and MM3, respectively.

Table 5- 4. Reaction exotherm for PU samples printed from MMs. T_1 and T_2 are the sample temperature at t_1 and t_2 respectively, whereas t_1 and t_2 are the starting point when the temperature increased and the time when peak temperature was reached, respectively. The dotted line defined the range between t_1 and t_2 .

	T_1	T ₂	t ₁	t_2	$(\Delta T/\Delta t)$
	(°C)	(°C)	(s)	(s)	(°C/s)
MM1	22.99	36.07	14	37	0.6
MM2	22.41	45.52	10	20	2.3
MM3	19.47	53.38	8	16	4.2

The mechanical properties of three MMs were assessed and variation of the storage modulus and $\tan\delta$ as a function of temperature were presented in Figure 5-9.

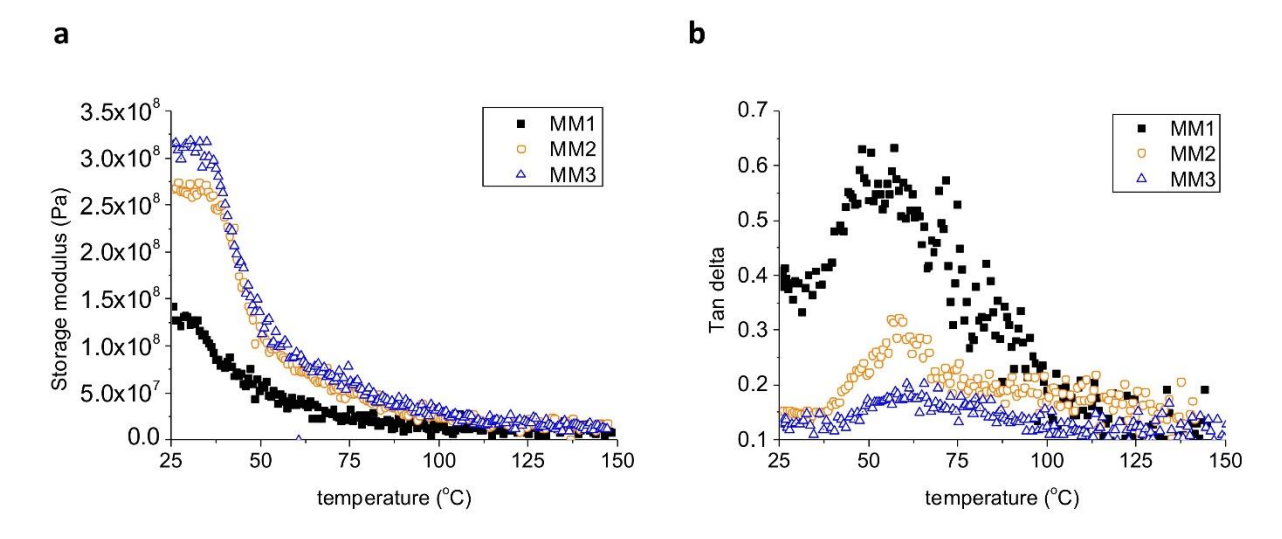


Figure 5-9. DMA temperature scan of PU samples from three mixing modes. a) Storage modulus. b) Tan delta.

The storage modulus of PU from MM3 (314.0 MPa) was higher than that of MM2 (266.8 MPa) and MM1 (142 MPa) at 25 °C, suggesting the stiffest PU was obtained from MM3 (Figure 5-9a), this supported the earlier conclusion that there was greater levels of crosslinking / cure in this samples. All three samples showed single $\tan\delta$ peaks, the temperature at which this occurs corresponds to the T_g^{25} (Figure 5-9b). The $\tan\delta$ temperature increased from MM1 to MM3 which was the same trend observed in the DSC estimation of T_g . Furthermore, the MM3 $\tan\delta$ value was the lowest with the trend increasing through MM2 to MM1. This observation suggested that higher degree of molecular motion exhibited in MM1, and more energy can be absorbed and dissipated for the MM1 sample, again suggesting that there is less cross-linking in this sample.

The printability of the formulation was demonstrated by printing woodpile structures, which essentially are 3D periodic structures showing "gap spanning" features (Figure 5- 10a) ^{120–122}. The spanning feature in between the second the third layer was shown in the front view of the printed sample (Figure 5- 10b)

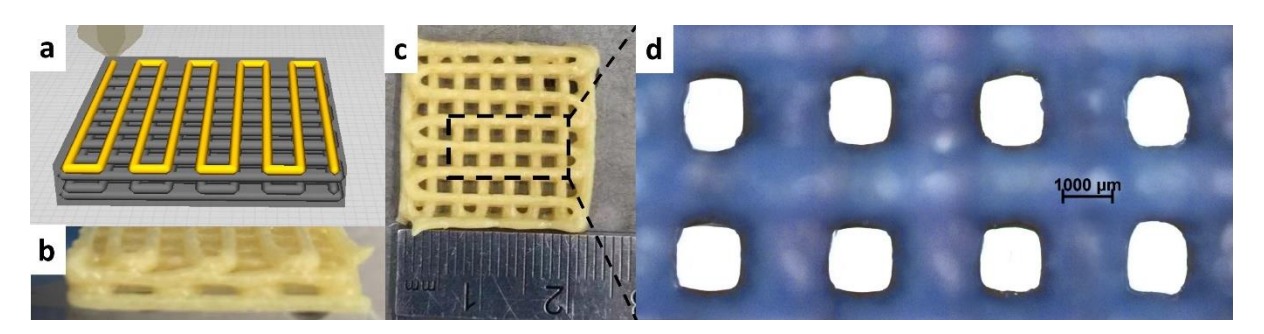


Figure 5- 10. Woodpile feature blocks printed using investigated PU formulation MM1. a) Design pattern. b) front-view and c) Top-view of the printed structure. d) microscopic images of the printed structure.

The printed woodpile structure showed both the structural integrity of the printed formulation as the overhang on the top of second layer was free-standing (Figure 5- 10b), and high fidelity to the CAD designs (Figure 5- 10a, 8c and 8d).

Furthermore, the spatial resolution of the print was characterised based on the block feature size (Figure 5- 11 and Figure 5- 12), where good consistency i.e. < 6% variance observed in all measurements when compared with the model pre-set value see (Table 5- 5 and Table 5- 6). Overall, the block features showed that the print was of good quality and exhibited good reproducibility, where the resolution of the print was predominantly governed by the static mixer nozzle size (ID=1mm).

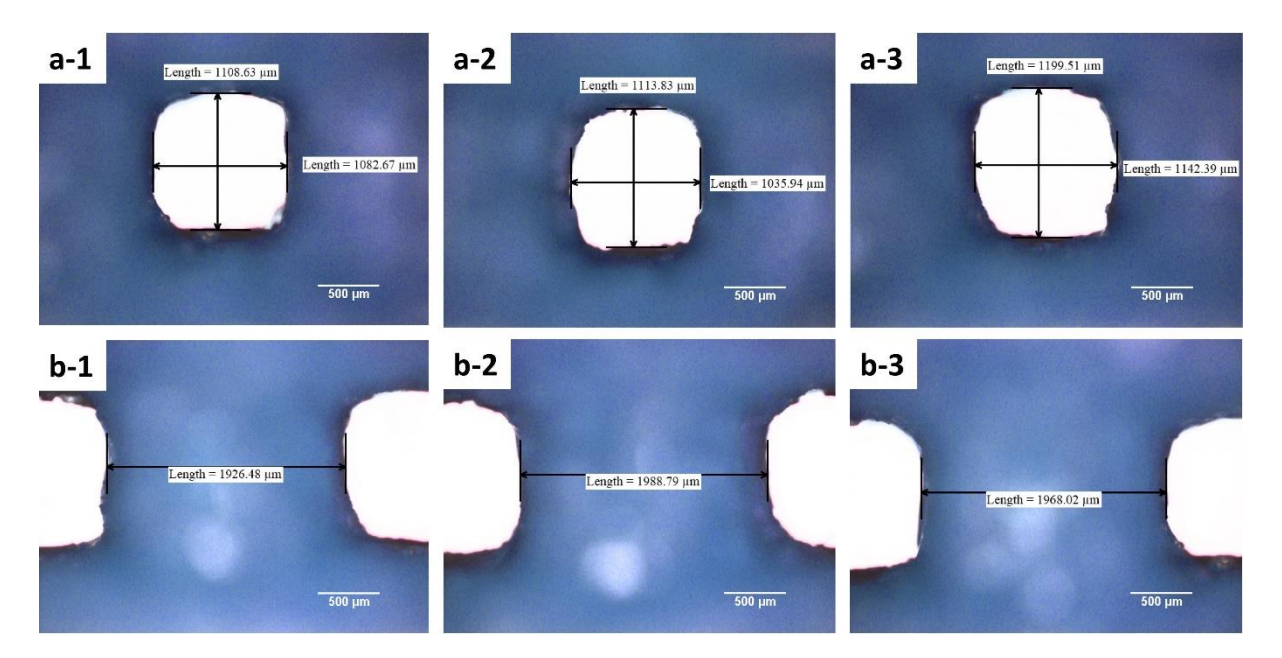


Figure 5- 11.Woodpile feature block size measurements. a-1, a-2, a-3: three separate measurements of W_{b1} and W_{b2} . b-1, b-2 and b-3: three separate measurements of W_L . (W_{b1} and W_{b2} : the width of the block; W_L : Line width; D_I : Infill distance).

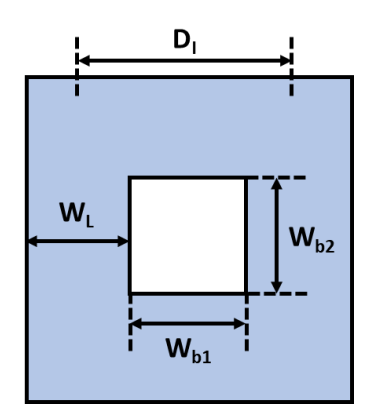


Figure 5- 12. Schematic of block feature (W_{b1} and W_{b2} = the width of the block; W_L - Line width; D_I = Infill distance, i.e. the travel distance between in-plane adjacent filaments).

Table 5-5. Block feature size measurements.

Feature block size	1st Measurement (mm)	2nd Measurement (mm)	3rd Measurement (mm)	Average (mm)
$\overline{D_{_{\rm I}}}$	3.034	3.101	3.167	3.101±0.054
$\overline{\mathbf{W}_{_{\mathrm{L}}}}$	1.926	1.988	1.968	1.961±0.026
W _{b1}	1.108	1.113	1.199	1.14±0.042
W_{b2}	1.082	1.035	1.142	1.086±0.044

Table 5- 6. The woodpile feature block calculated percentage deviation of the feature.

Feature block size	1st Measurement	2nd Measurement	3rd Measurement
D _I Deviation ⁱ	1.13%	3.37%	5.57%
W _L Deviation ii	-1.77%	1.39%	0.37%
W _{b1} Deviation iii	-2.81%	-2.37%	5.18%
W_{b2} Deviation iV	-0.40%	-4.73%	5.12%

i. D_I Deviation=100 x $(D_I-D_{I_set})/D_{I_set}$ (Note: $D_{I_set}=3$ mm)

5.2 Discussion

The effect of the addition of FS on the rheology properties of the feeds was the delivery of a change from Newtonian to Shear thinning behaviour. This was attributed to the formation of an inter-particle percolation network by the FS particles within the polymer matrix ^{15,39,118}, which was created by interaction between the polar groups on the FS particle surface ¹⁰². This conclusion was supported by the observation of an increase in viscosity of both NCO and OH feeds when FS particles were incorporated, which would be expected if such a network was formed. Furthermore, the fact that the feeds exhibited shear thinning behavior was proposed to result from the disassociation of the percolated network when the applied shear forces was increased, such as in an extrusion process. Consequently, feeds can be readily extruded onto

ii. W_L Deviation=100 x (W_L- W_{L_average})/ W_{L_average}

iii. W_{b1} Deviation=100 x (W_{b1}- W_{b1_average})/ W_{b1_average}

iv. W_{b2} Deviation=100 x (W_{b2}- W_{b2_average})/ W_{b2_average}

the print bed through the nozzle, and quickly reform the viscoelasticity to retain its shape. Thus, it is highly desirable to introduce FS as an formulation additive, as the resulting shear thinning feeds allow for easy processing in material extrusion 3D printing without the need of excessive force ^{15,27}.

The observed transition from viscous liquid to viscoelastic solid through the incorporation of FS, was also attributed to the FS particles forming a network within in the polymer matrix. When compared with neat polymer, the FS filled polymer matrix was then better able to store and dissipate energy when stress is applied, resulting in higher dynamic modulus (G' and G'') values. The substantial increase in yield stress in the case of 5% FS loading was considered to be favourable for extrusion 3D printing, as it should result in the printed structure retaining its fidelity when undergoing multi-layer stacking. Thus, it was proposed that the rheology behaviour of feeds with high G' and yield stress, could help printed structures to retain their shape upon extrusion and support the subsequent layer built on top ¹⁰⁴.

The key differences between the three mixing modes were demonstrated in Figure 5-1, which compares both the viscosity and elasticity ratios (G' ratio) between the OH and NCO feeds for the different mixing modes. Clear ascending trends were observed for both ratios when going from MM1 to MM3. The elasticity ratio for MM3 (80.04) being four orders of magnitude higher than that of MM1 (0.06), whilst the viscosity ratio increase was a single order of magnitude by comparison. The greater the difference in the two parameters then the more likely the system is to favour deformation of dispersed domains into smaller drops (Figure 5- 1a) ⁵⁷. This will result in a larger interfacial reaction zone between the two phases, hence beneficial for mitigating the diffusion limitation incurred by the interface. In the mixing modes achieved in this study, MM1 is believed to be hindered most by the diffusion limitation with the smallest

interfacial reaction zone among the three MMs. This was attributed to the fact that the MM1 feeds presented the highest viscosity and elasticity values. It also had the lowest viscosity: elasticity ratio (OH:NCO), both of which combine to produce the largest dispersed domains of the three modes. Furthermore, in PU chemistry, given the fast reaction kinetics, viscosity quickly builds up with the formation of oligomers, which hinder the reaction speed. The reaction becomes diffusion limited once oligomers form [29–31].

Introducing FS to modify the rheological behaviour of the feeds was shown to be beneficial, as it altered feed behaviour from the Newtonian to shear-thinning and highly viscoelastic feeds with sufficient yield stress to minimise the shape distortion during the layer stacking. The feeds in MM1 showed highest yield stress for the NCO feeds, which would normally be considered as the more ideal situation for extrusion 3D printing process ^{24,27}. Nevertheless, the MM1 product material, even with highest level of total FS loading (10%), fell behind MM2 (7.5%) and MM3 (6%) in terms of the printed PU thermos-mechanical properties. In contrast, MM3's NCO feed showed viscoelastic liquid behaviour (G'< G'') with no apparent yield stress, but it was still successfully printed on REX and lead to best product material properties from the three MMs. Thus, the filler loading needs to be optimised to deliver a feed with adequate rheological properties for extrusion printing. However, the feeds rheology must also minimise any hindrance to achieving a high degree of cross-linking network.

The viscosity and elasticity ratios between OH and NCO feeds have also been shown to be of significance for successful REX 3D printing. The results in this study demonstrated that a disparity in rheological properties between two feeds, heavily impacts on the mixing regime and so the reaction kinetics achieved in the static mixer. Thus MM3, with the greatest differences in the rheological properties between the NCO and OH feed, resulted in printing /

printed material performance that surpassed the other two MMs, with respect to thermal decomposition temperature, glass transition temperature, reaction exotherm and mechanical properties.

In this study, the thermal stability of PUs was shown to principally be associated with the crosslinking density within the structure. This hypothesis has also reported in the literature, where the mobility of soft segment was reduced due to chemical crosslink in the hard segment, and, as a result, the thermal stability of the polymer was improved ⁵⁸, ⁴⁹. This dominance of the crosslinking explains the ascending order of DTG (I)_{max} from MM1 to MM3. As the level of exotherm indicated that the highest level of cure / cross-linking was presented in MM3 samples. This is in accordance to the fact, the MM3 was concluded to be the least affected by diffusion limitations among the three MMs.

The T_g of the PU is predominantly affected by the mobility of the polymer chains. Higher T_g will be shown when the polymer chain has more freedom to move. As more urethane bonds were formed in the structure, the free rotation of the long chain polyol will be restricted. The more cross-linked structures will therefore be linked with increasing T_g^{49} , which is in the case of MM3 which has been proposed to contain the highest level of cross-linking. Thus again suggesting that the fastest reaction kinetics in MM3 could be beneficial for REX printing, in contrast to the other MMs, since higher level of crosslinking was achieved at a shorter time. The stronger cross-linking network formed in MM3 was also to improve the structure integrity whilst printing. The mechanical results from the DMA analysis are also in line with the fact there are more agglomerated hydrogen bonded hard segments presented in MM3, leading to stronger crosslinking network. This can reduce the free movement of polymers chains, with an increasing T_g and deliver better mechanical properties.

5.3 Conclusion

This study highlighted the significant impact from rheology properties of the dual feeds, on the reaction kinetics, mixing efficiencies and printed PU properties, via printing three mixing modes with distinct ink rheological properties.

MM3 with the greater differences in the viscosity ratio and elasticity ratio between the two feeds, outperformed the MM1 and MM2: (1) It demonstrated faster reaction kinetics and greater reaction exotherm; (2) It contained stronger crosslinking network (evidencing from aggregated H-bonded hard segment in the PU structure, higher thermal decomposition temperatures and Tg) and (3) improved mechanical properties (G'=314.0 MPa for MM3) in contrast to (G'=266.8 MPa and 142 MPa for MM2 and MM1 respectively). The enhancement in material properties is owing to the fact, MM3 is least affected by diffusion limitation.

To sum up, this chapter shows the REX printed materials properties can be tuned on-demand by adjusting the ink rheology properties. Ink rheology shall be optimised to find the best combination of MMs, with prominent printing performance.

CHAPTER SIX

6 Investigation the Reinforcing Effect from Amine-based Functional Silica Nanoparticles on the Printed Polyurethane Crosslink Network

Following Chapter 5, the effect of dual feed rheology on the REX printing has been revealed. To further explore the effect of filler on the REX process, reactive functional silica nanoparticles (FSPs) were incorporated in reinforcing polyurethane system printed via REX. Two types of amine based FSPs were synthesised to show their potential as reactive fillers which could enhance polyurethane material properties through a hybrid reinforcing effect combining both physical and covalent crosslink network.

The different crosslinked network is illustrated in Figure 6- 1. Both the amine FSPs (SiO₂-NH₂ and SiO₂-NH₂/CH₃) and the commercial fumed silica (SiO₂-PDMS) parties were then incorporated into 3D printing PU composites via REX. The effect of different functional groups on the dispersion of particles in matrix, feed rheology properties and thermo-mechanical properties of printed PU are described and the concept of utilising FSPs as reactive fillers to strengthen AM nanocomposites was demonstrated.

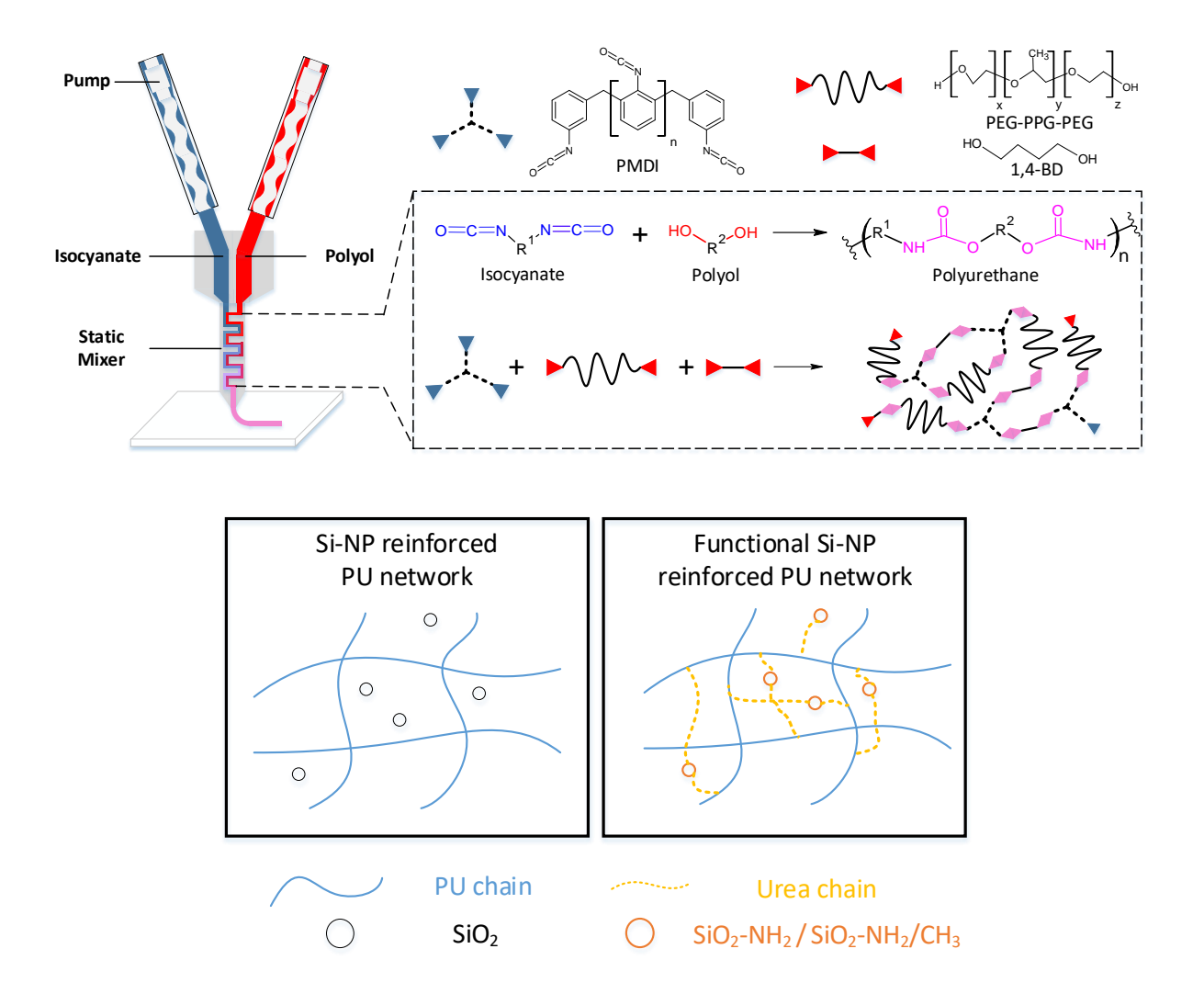


Figure 6- 1. Schematic diagram of how isocyanate and polyol were processed using REX 3D printing to form PU. The chemical structure of isocyanates and polyol used in the study and general PU reaction scheme are presented. The covalent bonding formed between the FSP and the PU network is illustrated.

6.1 Results

Particle Functionalisation: All functionalized silica nanoparticles (FSP) used in this study (except for the commercially available SiO₂-PDMS) were synthesised using a method reported by Stober *et al.* ¹¹¹. Tetraethyl orthosilicate was used to produce the core particles and the corresponding functional group containing orthosilicates were used as silane coupling agents to form the FSPs. Two types of FSPs were synthesised including amine only FSP (SiO₂-NH₂) and three FSP variants containing a mixture of amine and alkyl functional groups (SiO₂-NH₂/CH₃-01, 02 and 03). The three variants of amine/alkyl FSPs were produced by varying the ratio between amino and propyl silane coupling agents during the coupling process, with the aim to define how differences in amine functional group loadings on the particle surface would impact the ink rheology properties. The molar ratio of amine to propyl silane coupling agents used were 1:1, 2:1 and 1:2 for SiO₂-NH₂/CH₃-01, SiO₂-NH₂/CH₃-02 and SiO₂-NH₂/CH₃-03, respectively.

The introduction of amine and alkyl groups onto the surface of bare silica nanoparticles was confirmed by TGA (Figure 6- 2a), FT-IR (Figure 6- 2b) and further quantified by elemental analysis.

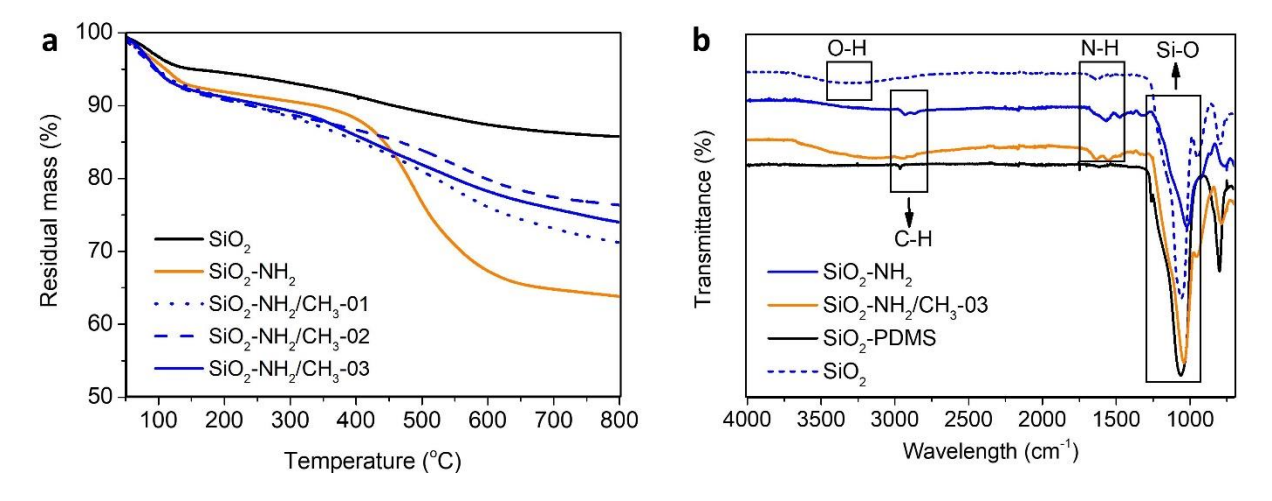


Figure 6- 2. Particle characterisations. a) TGA thermograms and b) FT-IR spectra of silica particles (SiO₂, SiO₂-NH₂ and three variants of SiO₂-NH₂/CH₃).

TGA analysis showed that there were two decomposition stages exhibited. An initial weight loss was observed in all particles below 200 °C, which was attributed to the release of surface absorbed water and solvents ^{25,135}. The synthesised FSPs data contained higher weight loss at this stage when compared to the commercial SiO₂. Meanwhile, the weight loss at higher temperature (>200 °C) was ascribed to the elimination of organo-functional groups bound onto the surface ²⁹. The observation that the weight loss on the single functional group SiO₂-NH₂ was more well-defined was attributed to the fact that only one functional group was present. On average the total weight loses (>200 °C) were 27.1 wt. % for SiO₂-NH₂ and 15.34 wt. % for SiO₂-NH₂/CH₃ which compared to 8.18 wt. % for the commercial SiO₂ (Table 6- 1). These differences indicate that the functional groups have been grafted successfully onto the surfaces of the synthesised silica particle.

Table 6-1. Weight loss data of SiO₂, SiO₂-NH₂ and SiO₂-NH₂/CH₃ obtained from TGA.

	Weight loss (<200°C, wt. %)	Weight loss (200-400°C, wt. %)	Weight loss (400-700°C, wt. %)
SiO ₂	5.00	3.25	4.93
SiO ₂ -NH ₂	7.46	3.70	23.40
SiO ₂ -NH ₂ /CH ₃ -01	8.02	5.90	12.09
SiO ₂ -NH ₂ /CH ₃ -02	8.34	4.12	9.25
SiO ₂ -NH ₂ /CH ₃ -03	8.30	5.26	10.08

The surface chemistry of silica particles was studied using FT-IR spectroscopy (Figure 6- 2b, Figure 6- 3 and Figure 6- 4). The spectra thus obtained exhibited strong absorbance bands at ~1100 cm⁻¹, which corresponds to the Si-O-Si stretching²⁵, demonstrating the formation of the silica core. The absorption at 3400 cm⁻¹ was attributed to the surface located hydroxyl groups (-OH).

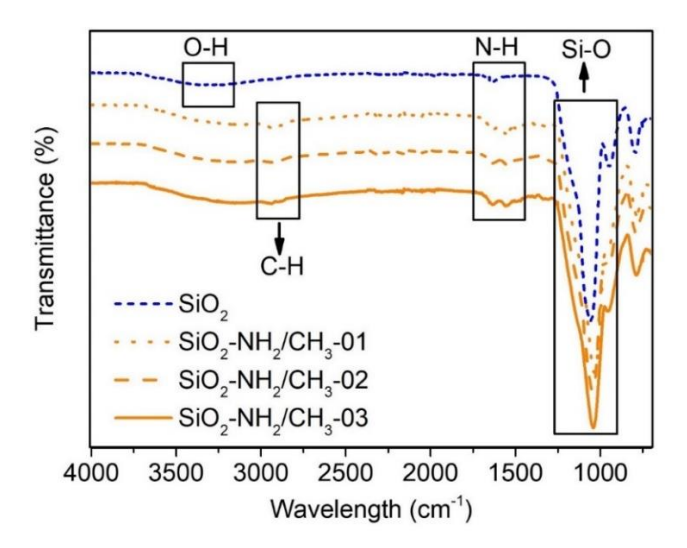


Figure 6-3. Full FT-IR spectra of SiO₂ and synthesised SiO₂-NH₂/CH₃ (01, 02 and 03).

Most notably, there were new vibration bands also evident in the spectra of the FSPs that were not present in the spectra of the commercially sourced SiO₂-PDMS sample (Figure 6- 4b and Figure 6- 4d). A weak C-H stretching absorption at ~2970 cm⁻¹ ^{25,136} in the spectra for all FSP (Figure 6- 4a and Figure 6- 4c). Additionally, another weak absorption band at ~1600 cm⁻¹ was associated with N-H bending were exhibited in the spectra of all the FSP. Thus, the presence of these stretching bands (C-H and N-H) indicate that the amine and alkyl groups have been grafted successfully onto the particle surface.

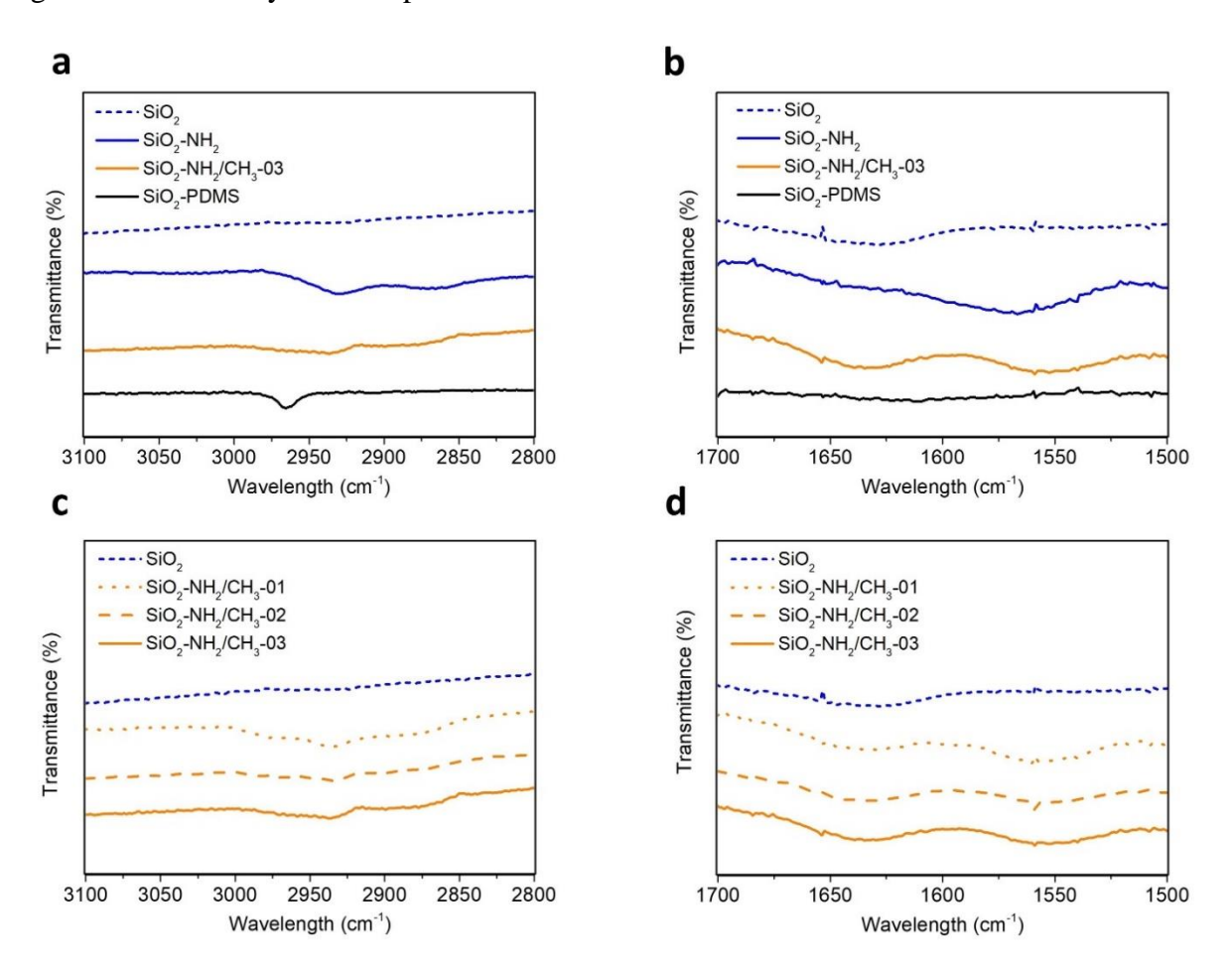


Figure 6- 4. FT-IR spectra of particles (SiO₂, SiO₂-NH₂ and SiO₂-NH₂/CH₃), a) N-H and b) C-H region of SiO₂ vs SiO₂-NH₂/CH₃-01 vs SiO₂-NH₂/CH₃-02 vs SiO₂-NH₂/CH₃-02 vs SiO₂-NH₂/CH₃-03.

The chemical composition of functional groups on the SiO₂-NH₂/CH₃ was quantitatively investigated by elemental analysis and this data is summarised in Table 6- 2. Briefly, the weight percent of carbon, hydrogen and nitrogen were determined experimentally for each sample. These percentages were then attributed to mol% by stoichiometric calculation based on the nitrogen content. Accordingly, the amine: propyl ratio was determined to be 1:1.19, 2.41:1 and 1:2.1 for SiO₂-NH₂/CH₃-01, SiO₂-NH₂/CH₃-02 and SiO₂-NH₂/CH₃-03, respectively. Again, the elemental analysis results provided further proof that the functional groups have been grafted onto SiO₂ particles.

Table 6-2. Summary of the results of the elementary analysis of SiO₂-NH₂/CH₃ particles.

	SiO ₂ -NH ₂ /CH ₃ -01	SiO ₂ -NH ₂ /CH ₃ -02	SiO ₂ -NH ₂ /CH ₃ -03
Amine (mmol.g-1)	2.89	2.27	2.52
$Propyl \; (mmol.g^{\text{-}1})$	2.42	0.94	1.20
Amine:Propyl	1:1.19	2.41:1	1:2.1

Particle and Particle-Filled Feed Composite Morphology: The effect of particle surface functionality on the particle dispersion was investigated via both the TEM and optical microscopy of the composite feeds, i.e., the isocyanates and diol reagents after inclusion of the particles and high shear mixing. The TEM images (see Figure 6- 5) revealed strong agglomeration for feeds containing the SiO₂-NH₂ particles. This suggested that the SiO₂-NH₂ particles have higher tendency to aggregate and form clusters even in the absence of any polymeric matrix.

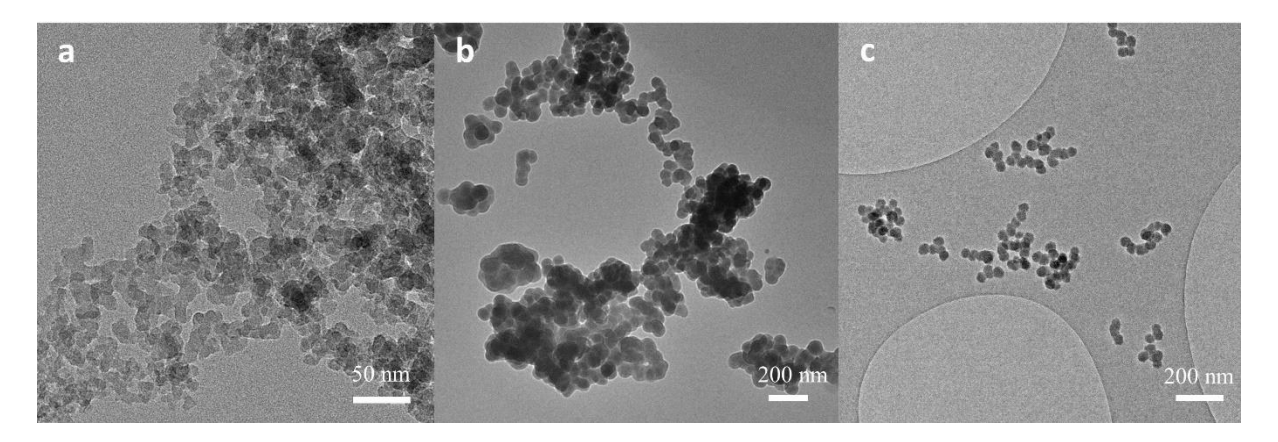


Figure 6-5. TEM images of the different silica nanoparticles. a) SiO₂-PDMS, b) SiO₂-NH₂ and c) SiO₂-NH₂/CH₃-03.

The optical microscopy images (Figure 6- 6) confirmed that SiO₂-NH₂ exhibited poor dispersion of particles, which resulted in a higher optical contrast between the polymer matrix and the particles aggregates.

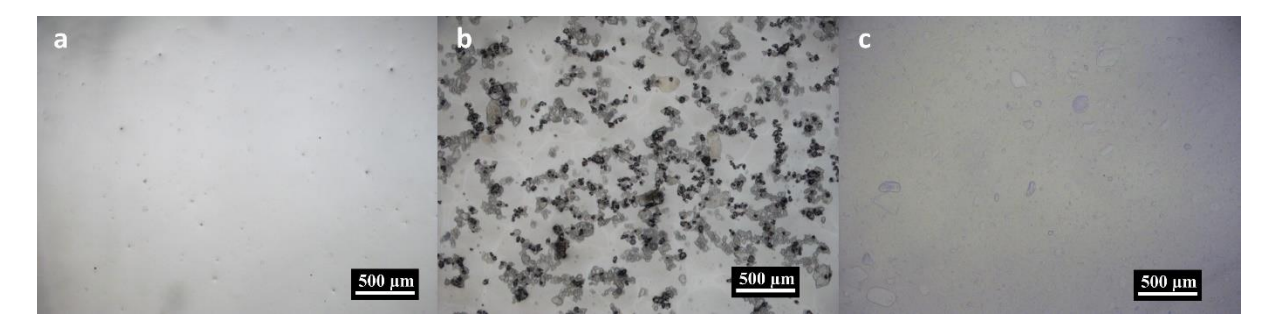


Figure 6- 6. Optical Microscopy images of OH feeds with different silica nanoparticles. a) SiO₂-PDMS, b) SiO₂-NH₂ and c) SiO₂-NH₂/CH₃-03.

Meanwhile, the feeds containing particles with PDMS and mixed –NH₂/alkyl functional groups exhibited better dispersion in the OH matrix and so the individual particles were consequently less distinguishable within the polymer network.

Of the three variants of amine/alkyl FSPs, the SiO₂-NH₂/CH₃-03 particles exhibited the least aggregation and were well dispersed in the OH feeds (Figure 6- 7 and Figure 6- 8).

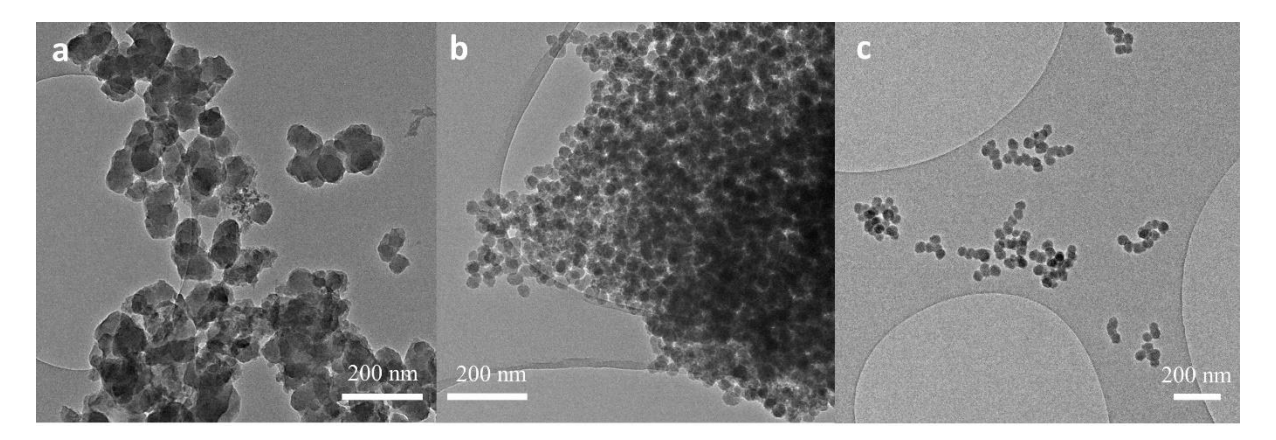


Figure 6-7. TEM images of different amine/alkyl FSPs. a) SiO₂-NH₂/CH₃-01. b) SiO₂-NH₂/CH₃-02. c) SiO₂-NH₂/CH₃-03.

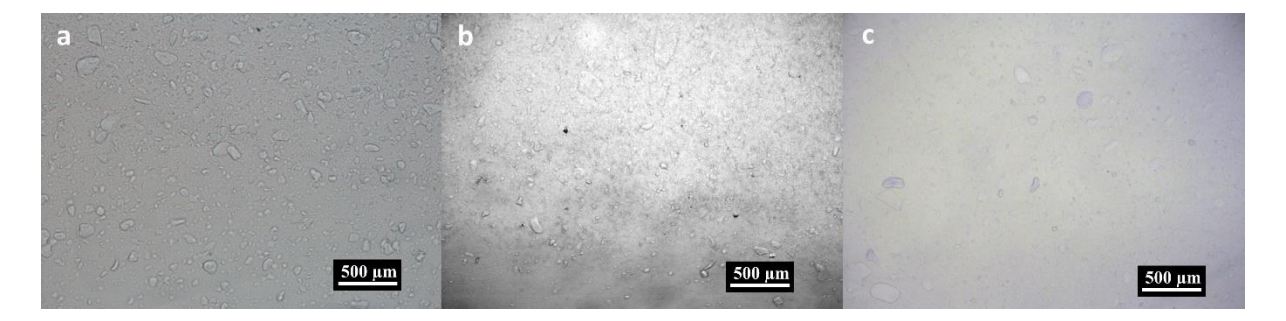


Figure 6- 8. Microscopic images of OH inks using different amine/alkyl FSPs. a) SiO_2 -NH₂/CH₃-01. b) SiO_2 -NH₂/CH₃-02. c) SiO_2 -NH₂/CH₃-03.

Rheological Properties: The effect that adding both synthesised FSPs and commercial silica particles had on the rheological properties of polyol feeds was also examined. The results detailing the comparison of the changes in (a) viscosity as a function of shear rate and (b) dynamic moduli as a function of frequency are shown in Figure 6-9.

shear-thinning behaviour was observed for all ink mixtures containing the silica particles, whilst the polyol sample without inclusion of silica nanoparticles exhibited an apparent viscosity that was independent of shear rate. The OH ink with SiO₂-PDMS exhibited the highest viscosity, when compared to those with FSP incorporated. Furthermore, the -OH feeds with alkyl groups FSP's (SiO₂-NH₂/CH₃-O3) showed higher viscosity compared to feeds containing FSP with only amine groups (SiO₂-NH₂) grafted onto the surface (Figure 6- 9a).

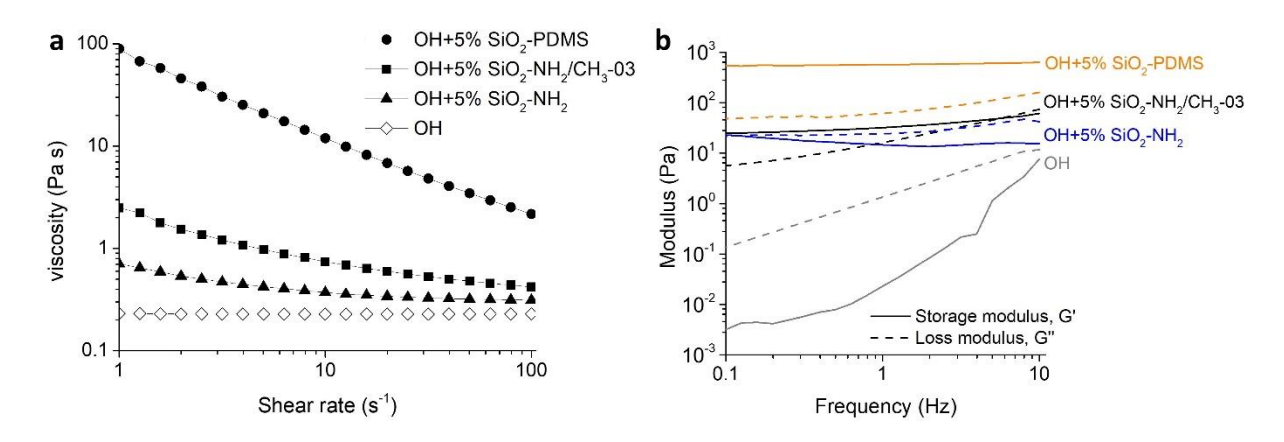


Figure 6- 9. Rheological properties of the OH feeds with three different silica particles (SiO₂-PDMS, SiO₂-NH₂ and SiO₂-NH₂/CH₃-03). a) Viscosity as a function of shear rate, b) Storage modulus and loss modulus as a function of frequency

The viscoelastic profiles of feeds are shown in Figure 6- 9b. Both the polyol feeds without particles and feeds containing SiO₂-NH₂ displayed viscous liquid behaviour, with the frequency-independent loss modulus (G'') being observed to be larger than the storage modulus (G'). When particles were added into the neat -OH feeds, both the G' and G'' of feeds increased. Interestingly, -OH feeds with SiO₂-NH₂/CH₃-O3 exhibited higher G' than G'' except at the frequency over 7 Hz, where a crossover such that G'' became greater than G' occurred.

Thus, the OH feeds with SiO₂-NH₂/CH₃-03 showed a more elastic behaviour than the feeds with SiO₂-NH₂. When loaded with SiO₂-PDMS, the G' of the ink was noted to dominate over G" throughout the full range of frequencies tested for OH feeds. These results indicate OH feeds with SiO₂-PDMS demonstrated a solid-like behaviour.

In Chapter 5, it was proposed that three different mixing modes (MM) of the feeds could be achieved in the REX system, based on the relative ink rheological properties of both the NCO and OH feeds. This report detailed that these different MM types were achieved by introducing varying level of commercial PDMS functionalised silica particles into the -OH and -NCO feed feeds, to control their relative viscosities. The final product properties delivered from the materials produced from the REX system were shown to be highly dependent upon the specific MM achieved within a specific formulation. Furthermore, the MM in which the viscosity of the -OH ink was greater than that of the NCO feed was shown to lead to the best product qualities.

Thus, in this study it was fundamentally important to gauge any influence that the surface functionality of the synthesized FSPs had upon the MMs achieved in the REX system. The data in Figure 6- 10 and Table 6- 3 defined that both formulations containing FSPs (SiO₂-NH₂ and SiO₂-NH₂/CH₃-03) exhibited MM2 profile, in contrast to the more favourable MM3 profile afforded by the formulation with SiO₂-PDMS. Of the FSP formulations, the SiO₂-NH₂/CH₃-03 presented higher viscosity and storage modulus ratio than formulation with SiO₂-NH₂, thus its mixing mode was becoming more MM3 like.

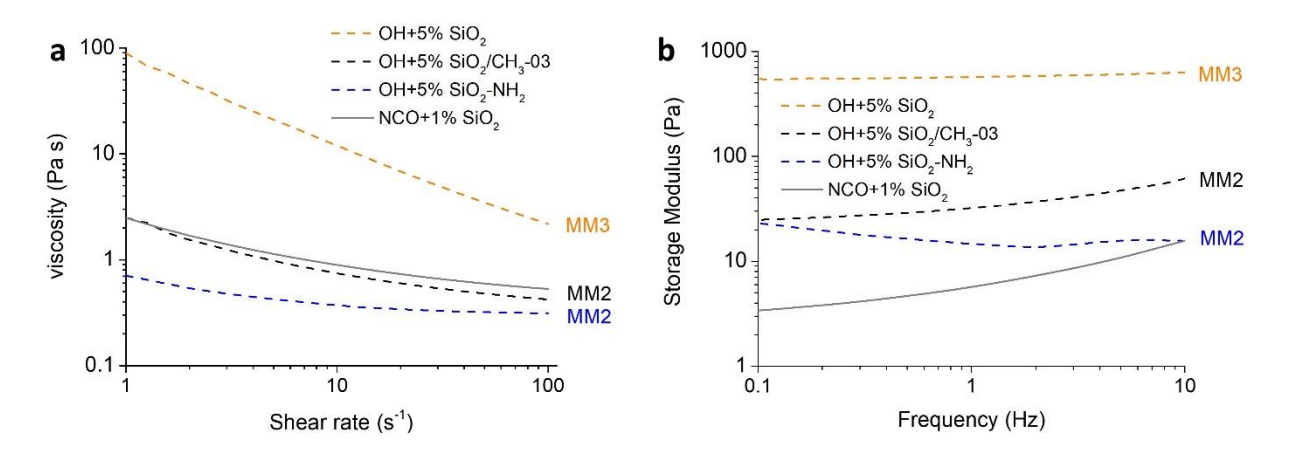


Figure 6- 10. Rheological comparisons between three investigated formulations in terms of mixing modes (MMs). a) A plot of viscosity as a function of shear rate for all formulations. b) A plot of G' as a function of frequency for all mixing modes.

Table 6-3. Viscosity ratio (OH: NCO) and storage modulus ratio (OH:NCO) comparison between the three investigated formulations.

Formulations	SiO ₂ -PDMS	SiO ₂ -NH ₂	SiO ₂ -NH ₂ /CH ₃ -03
Viscosity ratio	9.86	0.46	0.82
Storage modulus Ratio	80.04	1.87	5.06

Meanwhile, amongst the series of FSP with alkyl groups, the viscosity of OH feeds followed the order: $SiO_2-NH_2/CH_3-02 < SiO_2-NH_2/CH_3-01 < SiO_2-NH_2/CH_3-03$ (Figure 6- 11a), defining that as the alkyl group content increased so the viscosity increased, which reflected the great level of dispersion achieved as the $-CH_3$ content increases.

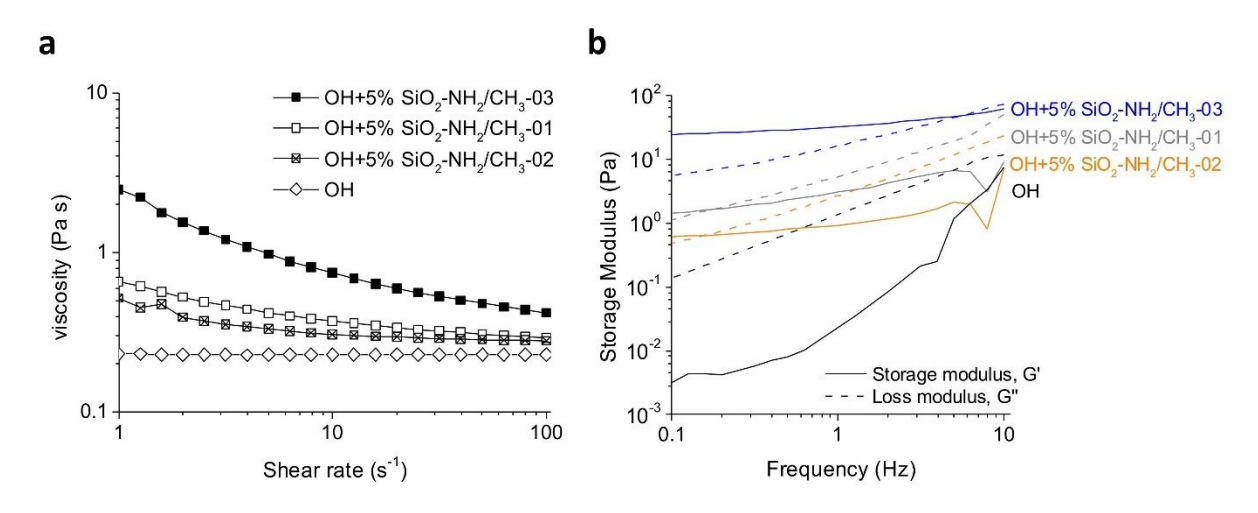


Figure 6- 11. Rheological properties of the OH feeds with functional silica particles (three versions of SiO₂-NH₂/CH₃).

a) Viscosity as a function of shear rate. b) Storage modulus and loss modulus as a function of frequency.

Furthermore, within the FSP with alkyl groups, feeds with SiO₂-NH₂/CH₃-03 demonstrated more elastic gel-like behaviour when compared to feeds with SiO₂-NH₂/CH₃-01 and SiO₂-NH₂/CH₃-02 (Figure 6- 11b), i.e. it is the FSP ink that is nearest that of MM3 mixing mode behaviour. Hence, SiO₂-NH₂/CH₃-03 was used in subsequent printing and comparison with SiO₂-NH₂/CH₃ ink studies.

The effect on the yield stress of incorporation of the silica particles into the feeds was investigated and this data is shown in Figure 6- 12.

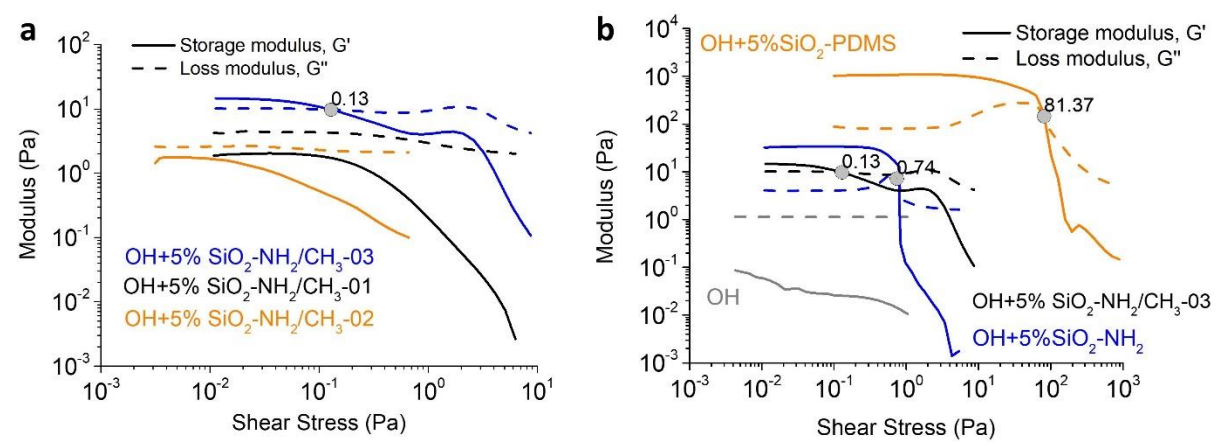


Figure 6- 12. Oscillatory rheology data of -OH feeds. a) OH feeds with FSP (three version of SiO_2-NH_2/CH_3), b) -OH feeds with three different silica particles (SiO_2-PDMS , SiO_2-NH_2 and SiO_2-NH_2/CH_3-03).

The feeds without particles, 5% FSP (SiO₂-NH₂/CH₃-01 and SiO₂-NH₂/CH₃-02) loading presented as viscous liquids, with higher G'' than G', regardless of the shear stress applied. Feeds with 5% FSP (SiO₂-NH₂/CH₃-03 and SiO₂-NH₂) and 5% SiO₂-PDMS incorporated, exhibited elastic solid behaviour, when subjected to low shear stress. Additionally, the G' and G'' data exhibited cross-over points as the stress increased. After this cross-over point, these feeds, started to behave like a viscous liquid, i.e., higher G'' than G'. Furthermore, it was observed that yield stresses exhibited by the OH feeds with 5% SiO₂-PDMS were over 100 and 600 times higher those with 5% SiO₂-NH₂/CH₃-03, respectively (Table 6-4).

Table 6-4. Yield stress of the inks obtained from oscillatory rheology test.

Ink	Yield Stress (Pa)
OH+5% SiO ₂ -PDMS	81.37
OH+5% SiO ₂ +NH ₂	0.74
OH+5% SiO ₂ +NH ₂ /CH ₃ -03	0.13

Reaction Kinetics: The reaction kinetics of PU filaments printed using formulations with different particles were monitored and compared via FTIR spectroscopic analysis and this data is shown in Figure 6- 13.

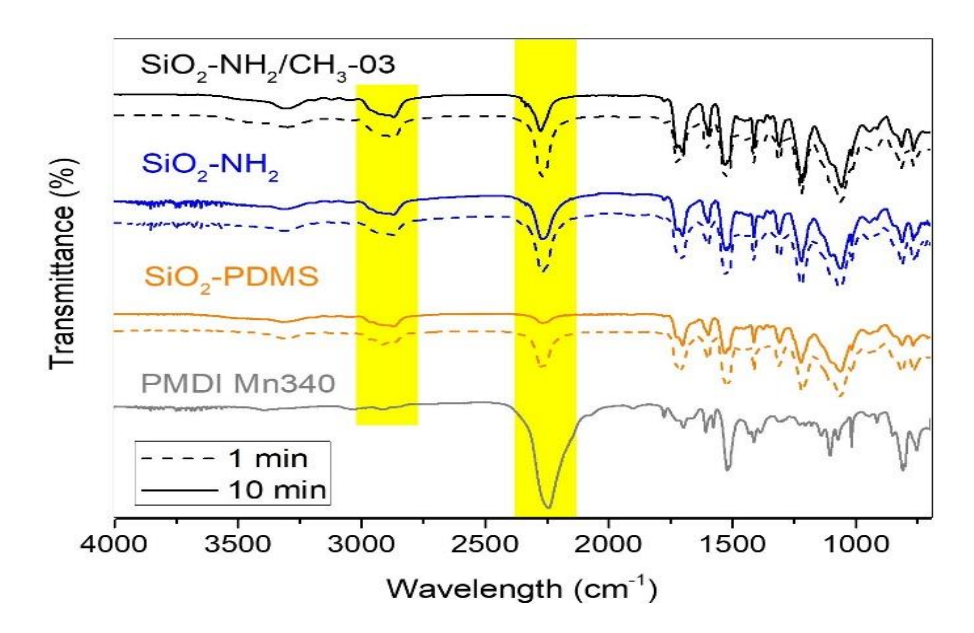


Figure 6- 13. FTIR spectra of PMDI Mn340, PU samples using three different silica particles (SiO2-PDMS, SiO2-NH2 and SiO2-NH2/CH3-03) after printing at 1 minute (dash line) and 10 minutes (solid line).

As the PU network formation progressed, a reduction of the peak at ~2250 cm⁻¹ was observed, which was attributed to the isocyanate stretch (-NCO) (Figure 6- 13), it was evident in all PUs printed using three different silica particles at the start of the reaction ^{107,116,117}.

As the reaction progressed from 1 to 10 minutes, the intensity of -NCO absorbance band reduced. The reaction kinetics for all formulations were shown to be similar (Table 6-5), based on the calculation described in Methodology using the data summarised in Table 6-6.

Table 6- 5. Reaction conversion of PU samples using three different silica particles (SiO₂-PDMS, SiO₂-NH₂ and SiO₂-NH₂/CH₃-03) at 1 minute and 10 minutes.

Time	Reaction Conversion			
(min)	SiO ₂ -PDMS	SiO ₂ -NH ₂	SiO ₂ -NH ₂ /CH ₃ -03	
1	85%	82%	83%	
10	95%	85%	89%	

Table 6- 6. Peak data obtained from Perkin Elmer Spectrum for isocyanate and reference peak at different reaction times.

	Time (min)	$A_{NCO(t)}$	A _{CH(t)}
PMDI Mn340	0	77.97	4.94
SiO ₂ -PDMS	1	11.73	4.94
	10	3.27	4.59
SiO ₂ -NH ₂	1	25.06	10.37
	10	21.10	10.31
SiO ₂ -NH ₂ /CH ₃ -03	1	19.42	8.53
	10	12.09	8.53

Other absorption bands were attributed in the following way; (a) ~3300 cm⁻¹ - stretching of a hydrogen bonded N-H group, ^{50,107,117} 2865 - 2968 cm⁻¹ - symmetrical and non-symmetrical stretching of C-H group ^{117,119}, which remained unaltered throughout the reaction, and (c) 1725 cm⁻¹ and 1701 cm⁻¹ – "free" and hydrogen bonded carbonyl peak, respectively (Figure 6- 14a) ^{117,131}

This latter region has been employed in the investigation of the structure property relationship in synthetic PUs by revealing the degree of hydrogen bonding evident in the material ^{117,137,138}. More intense hydrogen bonded C=O absorbances than "free" C=O bands were displayed in all samples printed from SiO₂-PDMS (Figure 6- 14b), SiO₂-NH₂ (Figure 6- 14c) and SiO₂-NH₂/CH₃-O3 (Figure 6- 14d). This difference was more pronounced in samples printed from SiO₂-PDMS, in comparison with the samples printed using the other two FSPs where increased hydrogen bonding was anticipated to improve the stiffness of the PU, as the result of agglomeration of hard segments ^{139–141}.

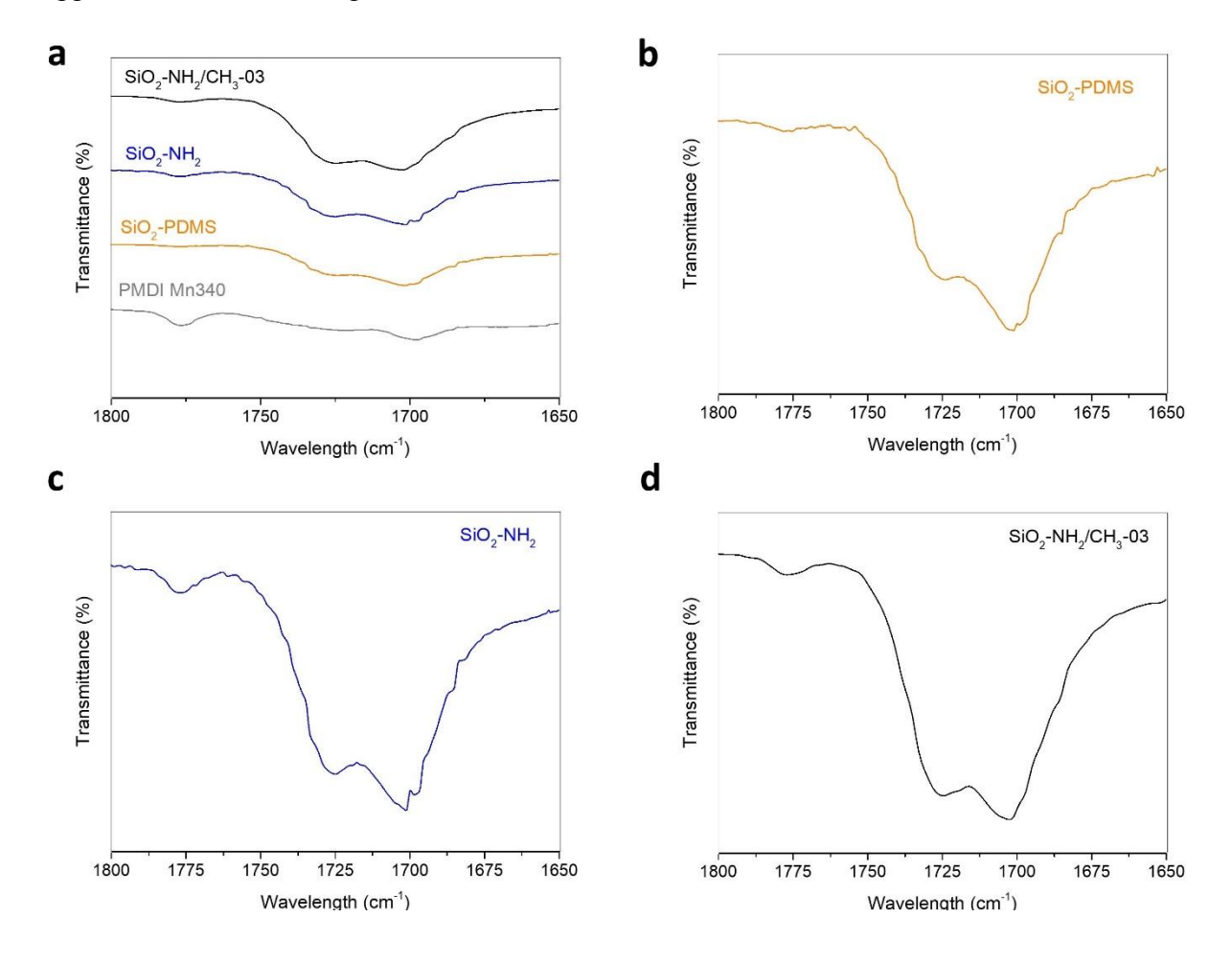


Figure 6- 14. FT-IR spectrum of PMDI Mn340 and polyurethane samples printed from formulations with (SiO₂-PDMS, SiO₂-NH₂ and SiO₂-NH₂/CH₃). a) C=O carbonyl region. Amplified C=O region for samples printed from b) SiO₂-PDMS. c) SiO₂-NH₂. d) SiO₂-NH₂/CH₃.

With the FSP containing materials, a more pronounced hydrogen bonded N-H stretching peak was presented for the SiO₂-NH₂/CH₃-03 formulation, when compared to the other two FSP formulations (Figure 6- 15a). Additionally, an amide III band (C-N stretching and N-H bending) was presented in all samples at 1223 cm⁻¹ (Figure 6- 15b) ¹⁴², indicating a N-H in the hydrogen bonded state and formation of a urethane-urea network ^{138,142}.

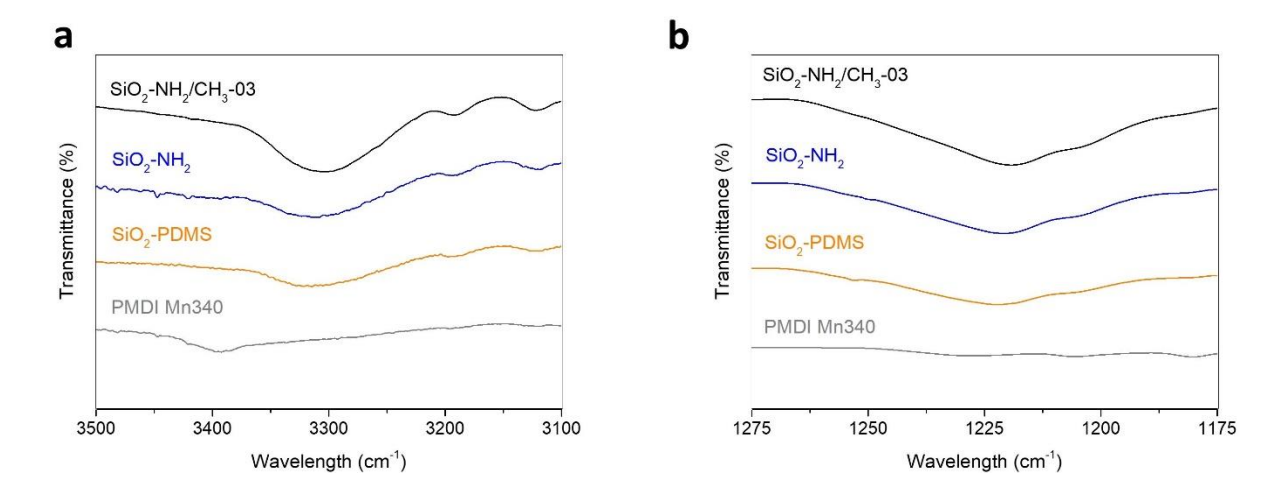


Figure 6- 15. FT-IR spectrum of PMDI Mn340 and polyurethane samples printed from formulations with (SiO₂-PDMS, SiO₂-NH₂and SiO₂-NH₂/CH₃). a) H-bonded N-H stretching. b) Amide III peak (C-N stretching and N-H bending).

Thermal Properties: The thermal properties of printed PUs were analysed and comparison between the three formulations is presented in Figure 6- 16.

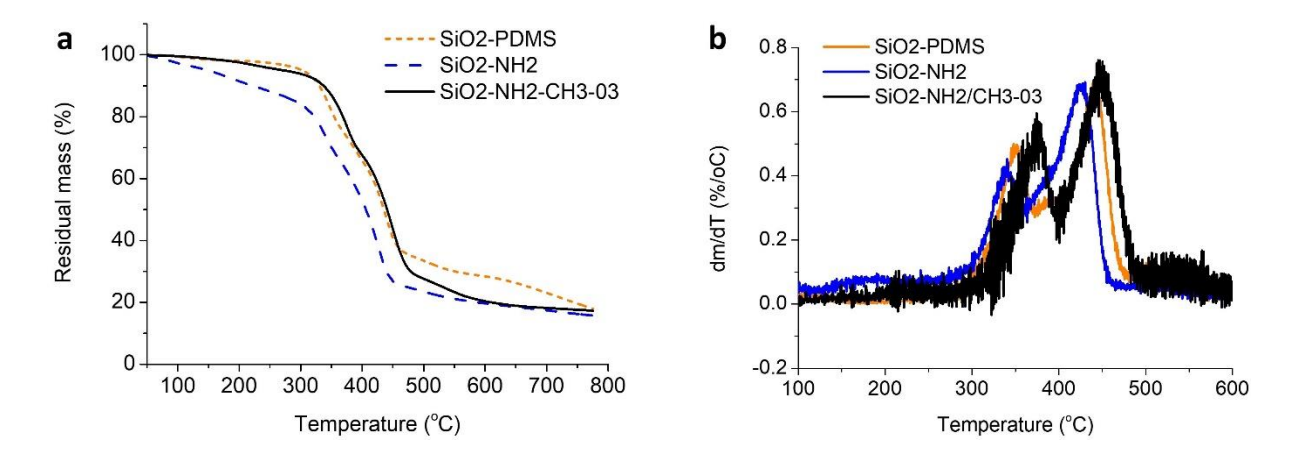


Figure 6- 16. a) TGA curves and b) differential thermogravimetric (DTG) analysis curves of PU samples printed using three different silica particles (SiO₂-PDMS, SiO₂-NH₂ and SiO₂-NH₂/CH₃-03).

Table 6-7. DTG analysis curves of PU samples printed using three different silica particles (SiO₂-PDMS, SiO₂-NH₂ and SiO₂-NH₂/CH₃-03). T_{5%}: Temperature at 5% weight loss obtained from TGA graph. DTG (I)max and DTG (II)max: lower and higher peak temperature in the DTG curve, respectively

Samples	T _{5%} (°C)	DTG $(I)_{max}$ (°C)	DTG (II)max (°C)
SiO ₂ -PDMS	302.2	351.5	442.5
SiO_2 -NH ₂ /CH ₃ -03	271.7	374.4	450.3
SiO ₂ -NH ₂	148.5	340.8	430.2

The onset temperatures of thermal decomposition ($T_{5\%}$) for the samples followed the order SiO_2 -NH₂ < SiO_2 -NH₂/CH₃-03 = SiO_2 -PDMS, with the latter two samples presented very similar data. Substantial weight loss starting from 100 °C was observed in the SiO_2 -NH₂ sample only, and was attributed to material associated via hydrogen bonding to the surface of silica particles as a result of the high amine group density 131,132 . All samples exhibited two pronounced peaks (DTG (I)_{max} and DTG (I)_{max}) (Figure 6- 16b), indicating microphase-separation development in the case of all PU samples. DTG (I)_{max} was at 340 - 375 °C and DTG (I)_{max} located within 430 - 450 °C. These peaks were corresponding to the decomposition

of the urethane bond in the hard segment and ether bond in the soft segment respectively 58,119,133 . Both DTG (I)_{max} and DTG (II)_{max} follows the same order from SiO₂-NH₂ < SiO₂-PDMS = SiO₂-NH₂/CH₃-03. Again, SiO₂-PDMS and SiO₂-NH₂/CH₃-03 displayed very similar profiles.

Meanwhile, comparison of glass transition temperatures for PU materials printed from three formulations (Figure 6- 17) showed that higher glass transition temperatures (T_g) exhibited by the samples printed from SiO₂-PDMS (80.5 °C) and SiO₂-NH₂/CH₃-03 (74.8 °C) when compared to the samples with SiO₂-NH₂ (53.7 °C).

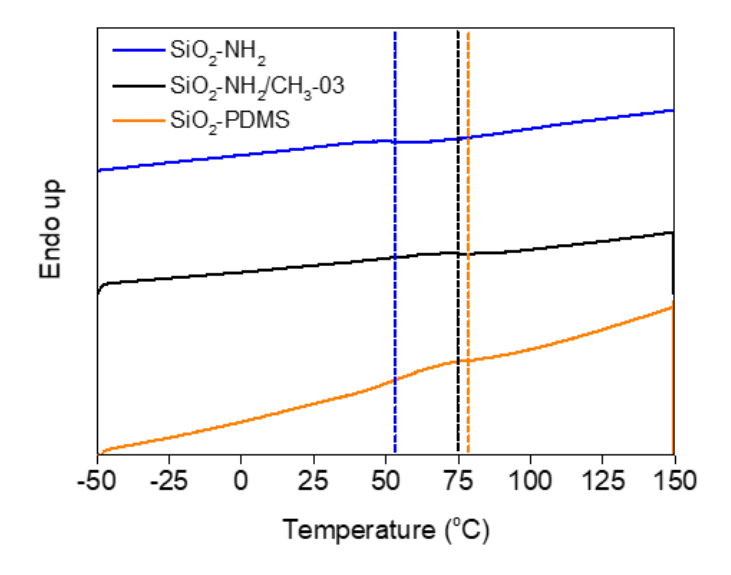


Figure 6- 17. DSC curves of PU samples printed using three different silica particles (SiO_2 -PDMS, SiO_2 -NH₂ and SiO_2 -NH₂/CH₃-03).

Mechanical Properties: The mechanical properties of three formulations were analysed, and the observed variation of the storage modulus is presented in Figure 6- 18.

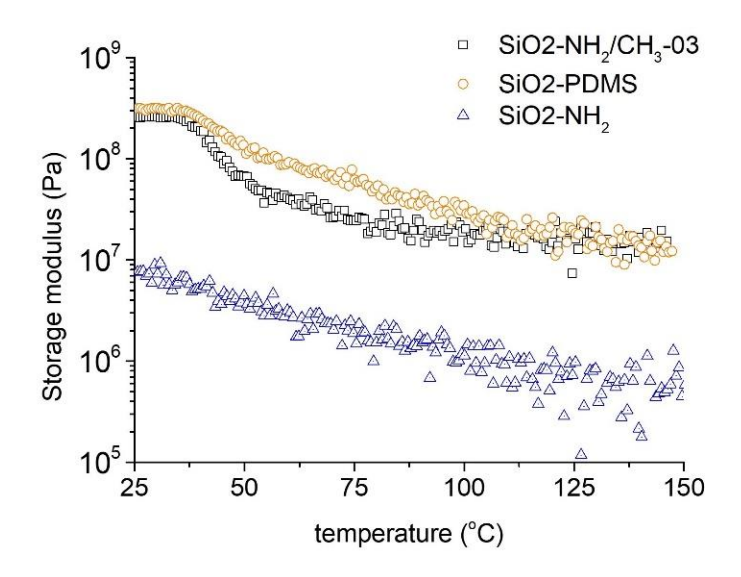


Figure 6- 18. DMA temperature scan of PU samples using three different silica particles (SiO_2 -PDMS, SiO_2 -NH₂ and SiO_2 -NH₂/CH₃-03).

The storage modulus of PU from SiO₂-PDMS (314.0 MPa) was again higher but very similar to than that of samples with SiO₂-NH₂/CH₃-03 (258.0 MPa) and both were significantly higher than that of the SiO₂-NH₂ (7.6 MPa) included PU's at 25 °C. This suggested that the stiffest PU's were obtained using SiO₂-PDMS and SiO₂-NH₂/CH₃-03. This substantial difference in storage modulus was also noted to persist when samples were heated from 25 °C to 150 °C.

Single filament printing profile:

The single filament printing profile characterised data collected via optical microscopy, showed that the width of the printing single filament for formulations with SiO₂-NH₂ was 97% and 25% larger than the width of filament from formation with SiO₂-PDMS and SiO₂-NH₂/CH₃-O₃, respectively (Figure 6- 19).

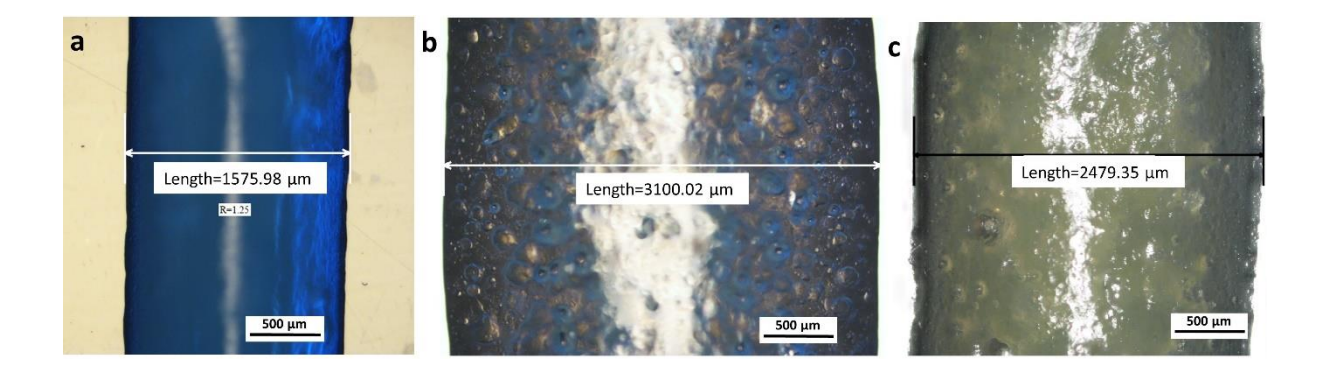


Figure 6-19. Single filament profile under microscope. a) SiO₂-PDMS, b) SiO₂-NH₂ and c) SiO₂-NH₂/CH₃-03.

6.2 Discussion

Effects of functional groups on dispersion and ink rheology: The agglomeration of the 100% SiO₂-NH₂ was ascribed to the bridging between the amino-functionalising agents (APTES) on adjacent silica nanoparticles ¹⁴³. There were several reactions that were proposed to occur when APTES was added into the bare silica particles during particle functionalisation. This commences with hydrolysis, which is followed by a competition between grafting onto the particle surface and homo-condensation ¹⁴⁴. Thus, as APTES contains three ethoxy groups, when the ratio between APTES/bare silica particles exceeds a limit, it is highly likely that some of the APTES will form an organic network via homo-condensation. Once this network structure becomes significant it can connect the silica particles via "bridging" the void between them so resulting in aggregation. Furthermore, owing to the SiO₂-NH₂ networks hydrophilic nature (-NH₂ and –OH on the particle surface), it will be inherently more susceptible to bridging aggregation when mixing with non-polar polyol matrix, when compared with the alkyl containing silica nanoparticles which are more hydrophobic in nature ³⁶.

The variations in the nanoparticle/matrix interaction resulted in the rheological property differences in the mixed polyol inks. The highest level of viscosity, dynamic moduli and yield stress was exhibited in polyol inks containing the SiO₂-PDMS particles and was attributed to good dispersion, wetting of the particles in the matrix resulting in minimum agglomeration resulting in MM3 mixing being achieved. Meanwhile, the rheology properties of the inks with SiO₂-NH₂/CH₃-03 were more akin to that of the SiO₂-PDMS when compared to inks with SiO₂-NH₂/CH₃-01 and SiO₂-NH₂/CH₃-02, whilst having exhibited MM2 type behaviour. This ranking was ascribed to the increasing hydrophobic nature of the particles as greater alkyl groups contents were applied ³⁷. It was also proposed that the alkyl groups from the silane agent (PTES) also served as a spacer between silica particles, i.e., imparting some steric stabilisation,

to mitigate the interaction between nanoparticles and hence the agglomeration during preparation. Overall, this data demonstrated that achieving the correct level of dispersion and particle; matrix interaction could deliver the materials properties from an MM2 system that matched those exhibited by materials from the optimum MM3 type mixing.

Effects of reactive fillers on the printing performances: The introduction of three types of silica nanoparticles into the ink, successfully tuned the ink rheology to deliver the shear-thinning, gel-like properties, which are critical for material extrusion process. From the rheological characterisation, inks with SiO₂-PDMS were found to exhibit superior viscoelastic properties and yield stress than the inks with SiO₂-NH₂ and SiO₂-NH₂/CH₃-O₃, thus were less susceptible to distortion during extrusion printing process. Hence, the printed filament would be more likely to sustain its shape upon deposition onto the substrate.

Thus, the initial hypothesis was that the introduction of amine groups onto the surface of the particles would enhance the PU material properties through the urea bonding. However, the formulations with the SiO₂-NH₂ particles significantly under-performed relative to those containing commercial (SiO₂-PDMS) particles, both in terms of reaction kinetics and thermomechanical properties. This was attributed to the agglomeration of SiO₂-NH₂ particles, i.e. when the agglomeration hindered the reaction between matrix reagents and particle functional groups by blocking the reaction path between the isocyanate and amine groups. As a result, formulations with SiO₂-NH₂ subsequently contained a weaker cross-linking network in the final structure. Hence, PU printed articles using SiO₂-NH₂, exhibited lower thermal stability, glass transition temperature and storage modulus.

Meanwhile FSP's containing a mix of surface amine and alkyl groups (SiO₂-NH₂/CH₃-03), were shown to improve the dispersion of the particles within the matrix because the inclusion of alkyl groups significantly reduced the particle agglomeration. However, the inks with SiO₂-NH₂/CH₃-03 were found to exhibit lower viscosity, storage modulus, yield stress and poorer particle dispersion when compared to inks featuring SiO₂-PDMS. This observation was linked to the observation that the formulations with SiO₂-NH₂/CH₃-03 adopted the less favourable

MM2 profile, in comparison with the MM3 profile exhibited in formulation with SiO₂-PDMS. The latter has been shown in prior studies to be the mixing mode that resulted in the best materials properties from the extrudate. Thus, it was concluded that the presence of functional groups did have an influence of the REX processing because of the presence of inter-particle interactions within the feeds. Consequently, it was predicted that the samples printed using SiO₂-NH₂/CH₃-O₃ would present inferior material properties to the samples using SiO₂-PDMS.

However, comparable material properties (i.e., thermal stability, mechanical properties) were demonstrated by the samples produced using both SiO₂-NH₂/CH₃-03 and SiO₂-PDMS. Furthermore, samples using SiO₂-NH₂/CH₃-03 exhibited additional cross-linking between the hard segments. This observation suggested a stronger/more dense cross-linking network had been formed due to the self-assembly of the hard segments *via* the presence of both covalent urea bonding and hydrogen bonding. Thus together, the inclusion of both alkyl and amine groups onto the particles resulted in both improved particle dispersion (diluting amine number and including steric stabilisation), and a considerable improvement in material properties for a FSP composite material (stemming from covalent particles-matrix bonding being established). This marked property enhancement was attributed to the hybrid-reinforcing effect of using FSP as reactive filler providing a stronger intramolecular network. The use of a reactive filler was found to overcome issues related to the type of mixing mode that was achieved. Thus, it was demonstrated that a dual network offered by alkyl/amine FSP, successfully improved the crosslinking network in the polyurethane composite structure, consequently leading to property reinforcement when produced by additive manufacturing techniques.

6.3 Conclusion

In this chapter, amine functionalised FSPs have been successfully used to serve as reactive fillers to reinforce PU nanocomposite printed via REX. Furthermore, it has been shown that optimising the functionality on the particles can have significant beneficial influence upon the feed ink processability and final composite material properties. To achieve this, amine, and mixed amine / alkyl FSPs (SiO₂-NH₂and SiO₂-NH₂/CH₃ 01 to 03 respectively) were synthesised and the resultant processability and final composite material properties obtain from REX processing compared to the results from non-reactive (i.e., "inert") commercial silica particle (SiO₂-PDMS). The inclusion of alkyl groups on the particle surface at a specific ratio, i.e., sample SiO₂-NH₂/CH₃ -03 with an amine: alkyl ratio of 1:2, was demonstrated to produce a reinforced PU composite which significantly outperformed the amine only (i.e., SiO₂-NH₂) composites. It exhibited (1) faster reaction kinetics due to a good dispersion of particles within the ink, (2) more covalent and H-bonded hard segments and as a result (3) higher thermal stability and mechanical properties (e.g., a 34-fold increase in G' at 25 °C). Furthermore, the PU composite with SiO₂-NH₂/CH₃ -03 presented comparable printing performance to the completely "inert" SiO2-PDMS reinforced samples. These results demonstrated that both the mixing mode achieved during processing and the degree of covalent matrix: particle bonding can beneficially influent the final device properties. Additionally, these results demonstrated that good particle/matrix interactions can overcome composite performance issues related to mixing mode issues related to the ink viscosities. Thus, this study has shown that the concept of introducing dual-network particle reinforcing filler to strengthen the matrix materials, opens a new route for developing advanced nanoparticle reinforcement composite systems.

CHAPTER SEVEN

7 Conclusion and Future Work

7.1 Conclusion

This work presents a systematic study of processing of polyurethane (PU) via the reactive extrusion 3D printing process (REX). It filled the knowledge gap on how we assess the feasibility of processing fast curing PU formulations via REX. It started by establishing a standard workflow for printability screening for different PU formulations. With the workflow, PMDI Mn340 was selected among the other PU formulations, due to the faster reaction kinetics. It is the second group of "ideal REX formulations" capitalising the faster reaction kinetics, instead of the superior rheological properties and remains the focus for this study. It expands the processing window (i.e., lowering the rheology property requirements for feed materials) for material extrusion processes, which opens opportunities to explore other formulations.

In this workflow, transitional ink rheology was demonstrated as the key characterisation for printability screening, to identify the speed of the cross-linking network development. The proposed workflow for process optimisation demonstrated the capability of printing PU structures with good fidelity and dimensional accuracy, despite the porous micro-voids in the cross-section caused by the fast exothermic PU reaction.

To pursue a deeper insight into the effect of feed rheology on the printed PU functionalities, the focus was placed in understanding the effect of non-reactive rheology filler in the system (specifically on mixing, reaction, and printed product qualities). It uncovered the crucial but unknown relationship between the rheology, mixing and reaction in the REX system. Three mixing modes were designed and printed in such a way, with same dual feed materials but

distinctive rheological properties. The mixing mode (MM3) with the most distinctive rheological differences (i.e., viscosity ratio and elasticity ratio) between the two feeds, showed the faster reaction kinetics, stronger cross-linking network, superior mechanical properties in contrast to the other two mixing modes. Thus, future study when exploring other formulations (besides PU) need to tune the feed rheology, to afford the desirable mixing modes between dual feeds, and consequently achieved the tuned on-demand printed material functionalities.

A further exploration of the filler types used in PU processing via REX continued and use amine based functional filler as reinforcing agent sparked a great interest. To our knowledge, this is the first study to introduce the FSPs as a reactive filler into PU system using an AM processing methodology to reinforce the PU nanocomposite material properties. Through careful design of both functional groups loadings and surface functional group type/density, the resultant novel FSP reinforced PU system showed comparable printing performance to a system using commercial silica particles. Furthermore, the resultant PU polymer was shown to have clear influence on the material property exhibited by the final printed material. The interaction between the filler and matrix resulting in improvements from using the reactive filler, as it was shown to overcome issues related to the mixing mode behaviour exhibited by the specific combination of inks used.

7.2 Future Work

This study has established a framework can be applied for the future studies on REX, especially for fast-curing PU formulations and prepared a baseline on achieving the tunable PU printing qualities through tailoring the feed filler types (both non-reactive/reactive filler). However, there are still other area can be explored:

7.2.1 Functional Parts with Fully Dense Structure

Porous structure could be beneficial as elastomeric foaming applications. However, due to the fast reaction kinetics and rapid exothermic reaction, full dense cross-section of the printed PU was challenging to achieve in the current REX set-up, as outlined in Chapter 4. There are three ways to approach this in the future. One could be incorporating moisture scavenger in the formulation, to reduce the side reaction between water and isocyanate. The other approach could be designing an inert gas shielding around the REX dosing unit, to mitigate the side reaction between isocyanate and the environmental moisture. Lastly, the PU formulations could be tailored further to afford a much faster and favourable reaction between the isocyanate and polyol than the side reaction between isocyanate and water.

7.2.2 Expanded Feed Processing Windows for Material Extrusion (Lower Rheology Feed Formulations)

This fundamental study of feed rheology is crucial if more sophisticated designs are printed via REX in the future. Free-form structure without the need of support can be produced via REX using feeds with low filler contents (feed yield stress lower than 100 Pa), which expands the feed processing windows previously reported where good printing results can be attained with feed yield stress values over 300 Pa ²⁷. The unparalleled feature of the REX enables the exploration of more feed formulations previously unattainable from other material extrusion AM processes.

In additional, thermoset polyurethane and polyurethane-urea formulations were explored in this study. Due to the versatility of PU applications, other functional PU products (e.g., thermoplastic PU elastomer) remained to be explored via REX system. Also, silica particles with higher reactive functional group loadings or different morphology could also be incorporated to the matrix, and enable better functionality produced via REX system.

7.2.3 Parts with Functional Gradient Properties

Parts with functional gradient properties have gained huge interest as it opens a new era to fabricate a structure with different functionality (e.g., rigid on one end and soft on another end). It is envisioned that following the guidance on the ink rheology properties, a much wider range of chemistries can be printed using REX to produce functional gradient materials (FGMs) by selectively tuning the mixing ratio between the feeds, in replicating the heterogeneous functionalities and anisotropic properties exhibited in the biological materials (FGX). For REX system, the unique mixing capabilities enables more explorations can be done in this regard. Non-reactive feed materials with different properties (e.g., rheology) can be mixed at different ratio during the printing process to create the functional gradient products.

7.2.4 Scale-Up REX Printer

REX essentially offers the new route in synthesising reactive formulations with tunable material properties distributed spatially and potentially in scale. Based on this study of the fast-curing PU formulation, it can be envisioned there could be opportunity in scaling up the REX process for the manufacturing industry, where PU foams were widely used as insulation panel in the building. REX process can be quickly adapted to the on-going development of 3D printing house, selectively printing the insulation on-demand. This could further add-on the benefits such as the short development time and lower material/labour cost compared to conventional housing manufacturing. To achieve this, the mixing apparatus between the dual feed could be envisioned to adapted onto an industry robot arm and moving gantry.

7.2.5 Expanding the Applications of FSPs to Other AM Processes

Thus, future investigation of the application of functional nanoparticle as reinforcement filler in AM will need to investigate the balance and level of functional groups loading for specific composites, to ensure the system exhibits maximum processability and materials properties via the particle-matrix interactions. Additionally, the optimum balance between mixing mode and crosslink density will need to be identified to obtain the best reinforcing performance. This, because the final materials properties are a synergistic effect between the additional bonding offered by the functional groups and the particle dispersion defined by the feed rheology and so mixing mode that the systems adopt. To maximise the benefit of the FSP concept, the inclusion of other surface groups, both functional and "inert" (i.e., not reactive) to both improve the FSP dispersion and establish covalent links with other matrix chemistries merit further study. Finally, there is potential for the application of FSPs beyond the REX system and to transfer their use into other 3D printing technologies to improve the properties of AM polymer composites devices.

8 References

- 1. Fenn DR, Olson KG, Rock RM, Kutchko C, Donaldson SF, Sun H, et al. Methods for reactive three-dimensional printing by extrusion. 2016.
- 2. Akindoyo JO, Beg MDH, Ghazali S, Islam MR, Jeyaratnam N, Yuvaraj AR. Polyurethane types, synthesis and applications a review. RSC Adv [Internet]. 2016;6(115):114453–82. Available from: http://xlink.rsc.org/?DOI=C6RA14525F
- 3. Engels HW, Pirkl HG, Albers R, Albach RW, Krause J, Hoffmann A, et al. Polyurethanes: Versatile materials and sustainable problem solvers for today's challenges. Angew Chemie Int Ed. 2013;52(36):9422–41.
- 4. Zhang L, Zhang M, Hu L, Zhou Y. Synthesis of rigid polyurethane foams with castor oil-based flame retardant polyols. Ind Crops Prod [Internet]. 2014;52:380–8. Available from: http://dx.doi.org/10.1016/j.indcrop.2013.10.043
- Gite V V., Mahulikar PP, Hundiwale DG. Preparation and properties of polyurethane coatings based on acrylic polyols and trimer of isophorone diisocyanate. Prog Org Coatings [Internet].
 2010;68(4):307–12. Available from: http://dx.doi.org/10.1016/j.porgcoat.2010.03.008
- 6. Sheikhy H, Shahidzadeh M, Ramezanzadeh B, Noroozi F. Studying the effects of chain extenders chemical structures on the adhesion and mechanical properties of a polyurethane adhesive. J Ind Eng Chem [Internet]. 2013;19(6):1949–55. Available from: http://dx.doi.org/10.1016/j.jiec.2013.03.008
- 7. Salimi S, Wu Y, Barreiros MIE, Natfji AA, Khaled S, Wildman R, et al. A 3D printed drug delivery implant formed from a dynamic supramolecular polyurethane formulation. Polym Chem [Internet]. 2020;11(20):3453–64. Available from: http://xlink.rsc.org/?DOI=D0PY00068J
- 8. Ligon SC, Liska R, Stampfl J, Gurr M, Mülhaupt R. Polymers for 3D Printing and Customized Additive Manufacturing. Chem Rev. 2017;117(15):10212–90.
- 9. Sinh LH, Harri K, Marjo L, Minna M, Luong ND, Jürgen W, et al. Novel photo-curable polyurethane resin for stereolithography. RSC Adv. 2016;6(56):50706–9.

- 10. Yuan S, Shen F, Bai J, Chua CK, Wei J, Zhou K. 3D soft auxetic lattice structures fabricated by selective laser sintering: TPU powder evaluation and process optimization. Mater Des [Internet]. 2017;120:317–27. Available from: http://dx.doi.org/10.1016/j.matdes.2017.01.098
- 11. Bates SRG, Farrow IR, Trask RS. Compressive behaviour of 3D printed thermoplastic polyurethane honeycombs with graded densities. Mater Des [Internet]. 2019;162:130–42. Available from: https://doi.org/10.1016/j.matdes.2018.11.019
- 12. Bates SRG, Farrow IR, Trask RS. 3D printed polyurethane honeycombs for repeated tailored energy absorption. Mater Des [Internet]. 2016;112:172–83. Available from: http://dx.doi.org/10.1016/j.matdes.2016.08.062
- 13. Kröber P, Delaney JT, Perelaer J, Schubert US. Reactive inkjet printing of polyurethanes. J Mater Chem. 2009;19(29):5234–8.
- 14. Ren L, Song Z, Liu H, Han Q, Zhao C, Derby B, et al. 3D printing of materials with spatially non-linearly varying properties. Mater Des. 2018;156:470–9.
- 15. Kokkinis D, Schaffner M, Studart AR. Multimaterial magnetically assisted 3D printing of composite materials. Nat Commun. 2015;6.
- 16. Kokkinis D, Bouville F, Studart AR. 3D Printing of Materials with Tunable Failure via Bioinspired Mechanical Gradients. Adv Mater [Internet]. 2018 May;30(19):1705808. Available from: http://doi.wiley.com/10.1002/adma.201705808
- 17. Walker S, Daalkhaijav U, Thrush D, Branyan C, Yirmibesoglu OD, Olson G, et al. Zero-Support 3D Printing of Thermoset Silicone Via Simultaneous Control of Both Reaction Kinetics and Transient Rheology. 3D Print Addit Manuf [Internet]. 2019;3dp.2018.0117. Available from: https://www.liebertpub.com/doi/10.1089/3dp.2018.0117
- 18. Yirmibesoglu OD, Morrow J, Walker S, Gosrich W, Canizares R, Kim H, et al. Direct 3D printing of silicone elastomer soft robots and their performance comparison with molded counterparts. 2018 IEEE Int Conf Soft Robot RoboSoft 2018. 2018;295–302.
- 19. Müller M, Huynh QU, Uhlmann E, Wagner MH. Study of inkjet printing as additive manufacturing process for gradient polyurethane material. Prod Eng. 2014;8(1–2):25–32.
- 20. Sturgess C, Tuck CJ, Ashcroft IA, Wildman RD. 3D reactive inkjet printing of

- polydimethylsiloxane. J Mater Chem C [Internet]. 2017;5(37):9733–45. Available from: http://dx.doi.org/10.1039/C7TC02412F
- 21. de Gans B-J, Duineveld PC, Schubert US. Inkjet Printing of Polymers: State of the Art and Future Developments. Adv Mater [Internet]. 2004;16(3):203–13. Available from: http://doi.wiley.com/10.1002/adma.200300385
- 22. Rios O, Carter W, Post B, Lloyd P, Fenn D, Kutchko C, et al. 3D printing via ambient reactive extrusion. Mater Today Commun [Internet]. 2018;15(March):333–6. Available from: https://doi.org/10.1016/j.mtcomm.2018.02.031
- 23. Ren L, Song Z, Liu H, Han Q, Zhao C, Derby B, et al. 3D printing of materials with spatially non-linearly varying properties. Mater Des [Internet]. 2018;156:470–9. Available from: https://doi.org/10.1016/j.matdes.2018.07.012
- 24. Compton BG, Lewis JA. 3D-printing of lightweight cellular composites. Adv Mater. 2014;26(34):5930–5.
- 25. Guo Q, Zhu P, Li G, Wen J, Wang T, Lu D (Daniel), et al. Study on the effects of interfacial interaction on the rheological and thermal performance of silica nanoparticles reinforced epoxy nanocomposites. Compos Part B Eng [Internet]. 2017;116:388–97. Available from: http://dx.doi.org/10.1016/j.compositesb.2016.10.081
- 26. Navidfar A, Sancak A, Yildirim KB, Trabzon L. A Study on Polyurethane Hybrid Nanocomposite Foams Reinforced with Multiwalled Carbon Nanotubes and Silica Nanoparticles. Polym Plast Technol Eng [Internet]. 2018;57(14):1463–73. Available from: https://doi.org/10.1080/03602559.2017.1410834
- 27. Hmeidat NS, Kemp JW, Compton BG. High-strength epoxy nanocomposites for 3D printing.
 Compos Sci Technol [Internet]. 2018;160:9–20. Available from:
 https://doi.org/10.1016/j.compscitech.2018.03.008
- 28. Ji X, Hampsey JE, Hu Q, He J, Yang Z, Lu Y. Mesoporous Silica-Reinforced Polymer Nanocomposites. 2003;(28):3656–62.
- 29. Chen Y, Zhou S, Yang H, Wu L. Structure and properties of polyurethane/nanosilica composites. J Appl Polym Sci. 2005;95(5):1032–9.

- Rahman IA, Padavettan V. Synthesis of Silica nanoparticles by Sol-Gel: Size-dependent properties, surface modification, and applications in silica-polymer nanocompositesa review. J Nanomater. 2012;2012.
- 31. Liu H, Mo J. Study on nanosilica reinforced stereolithography resin. J Reinf Plast Compos. 2010;29(6):909–20.
- 32. Weng Z, Zhou Y, Lin W, Senthil T, Wu L. Structure-property relationship of nano enhanced stereolithography resin for desktop SLA 3D printer. Compos Part A Appl Sci Manuf. 2016;88:234–42.
- Dizon JRC, Chen Q, Valino AD, Advincula RC. Thermo-mechanical and swelling properties of three-dimensional-printed poly (ethylene glycol) diacrylate/silica nanocomposites. MRS Commun. 2019;9(1):209–17.
- 34. Chunze Y, Yusheng S, Jinsong Y, Jinhui L. A nanosilica/nylon-12 composite powder for selective laser sintering. J Reinf Plast Compos. 2009;28(23):2889–902.
- 35. Chen Q, Cao PF, Advincula RC. Mechanically Robust, Ultraelastic Hierarchical Foam with Tunable Properties via 3D Printing. Adv Funct Mater. 2018;28(21):1–9.
- 36. Hassanajili S, Sajedi MT. Fumed silica/polyurethane nanocomposites: effect of silica concentration and its surface modification on rheology and mechanical properties. Iran Polym J (English Ed. 2016;25(8):697–710.
- 37. Shirono H, Amano Y, Kawaguchi M, Kato T. Characteristics of alkyltrimethoxysilane-treated fumed silicas and rheological behavior of fumed silica suspensions in an epoxy resin. J Colloid Interface Sci. 2001;239(2):555–62.
- 38. Behniafar H, Nazemi MK. Effect of amine-functionalized silica nanoparticles on thermal and mechanical behaviors of DGEBA/IPD epoxy networks. Polym Bull. 2017;74(9):3739–49.
- 39. Wichmann MHG, Cascione M, Fiedler B, Quaresimin M, Schulte K. Influence of surface treatment on mechanical behaviour of fumed silica/epoxy resin nanocomposites. Compos Interfaces. 2006;13(8–9):699–715.
- 40. Bayer Material Science AG. The Chemistry of Polyurethane Coatings. 2005;31.
- 41. Chattopadhyay DK, Raju KVSN. Structural engineering of polyurethane coatings for high

- performance applications. Prog Polym Sci. 2007;32(3):352–418.
- 42. Król P. Synthesis methods, chemical structures and phase structures of linear polyurethanes. Properties and applications of linear polyurethanes in polyurethane elastomers, copolymers and ionomers. Prog Mater Sci. 2007;52(6):915–1015.
- 43. Delebecq E, Pascault JP, Boutevin B, Ganachaud F. On the versatility of urethane/urea bonds:

 Reversibility, blocked isocyanate, and non-isocyanate polyurethane. Chem Rev.

 2013;113(1):80–118.
- 44. de Avila Bockorny G, Forte MMC, Stamboroski S, Noeske M, Keil A, Cavalcanti WL. Modifying a thermoplastic polyurethane for improving the bonding performance in an adhesive technical process. Appl Adhes Sci. 2016;4(1).
- 45. Desai S, Thakore IM, Sarawade BD, Devi S. Structure-property relationship in polyurethane elastomers containing starch as a crosslinker. Polym Eng Sci. 2000;40(5):1200–10.
- 46. Chu B, Gao T, Li Y, Wang J, Desper CR, Byrne CA. Microphase Separation Kinetics in Segmented Polyurethanes: Effects of Soft Segment Length and Structure. Macromolecules. 1992;25(21):5724–9.
- 47. Chattopadhyay DK, Sreedhar B, Raju KVSN. Effect of chain extender on phase mixing and coating properties of polyurethane ureas. Ind Eng Chem Res. 2005;44(6):1772–9.
- 48. Yu TL, Lin TL, Tsai YM, Liu WJ. Morphology of pôlyurethanes with triol monomer crosslinked on hard segments. J Polym Sci Part B Polym Phys. 1999;37(18):2673–81.
- 49. Petrović ZS, Javni I, Divjaković V. Structure and physical properties of segmented polyurethane elastomers containing chemical crosslinks in the hard segment. J Polym Sci Part B Polym Phys. 1998;36(2):221–35.
- 50. Tan C, Tirri T, Wilen C-E. Investigation on the Influence of Chain Extenders on the Performance of One-Component Moisture-Curable Polyurethane Adhesives. Polymers (Basel). 2017;9(12):184.
- 51. Barikani M, Ebrahimi MV, Mohaghegh SMS. Influence of diisocyanate structure on the synthesis and properties of ionic polyurethane dispersions. Polym Plast Technol Eng. 2007;46(11):1087–92.

- 52. Pearson RG, Williams EL. Interfacial polymerization of an isocyanate and a diol. J Polym Sci
 Polym Chem Ed [Internet]. 1985 Jan;23(1):9–18. Available from:
 https://doi.org/10.1002/pol.1985.170230102
- 53. Fields SD, Thomas EL, Ottino JM. Visualization of interfacial urethane polymerizations by means of a new microstage reactor. Polymer (Guildf). 1986;27(9):1423–32.
- 54. Wickert PD, Ranz WE, Macosko CW. Small scale mixing phenomena during reaction injection moulding. Polymer (Guildf). 1987;28(7):1105–10.
- 55. Machuga SC, Midje HL, Peanasky JS, Macosko CW, Ranz WE. Microdispersive interfacial mixing in fast polymerizations. AIChE J. 1988;34(7):1057–64.
- 56. Kolodziej P, Macosko CW, Ranz WE. The influence of impingement mixing on striation thickness distribution and properties in fast polyurethane polymerization. Polym Eng Sci. 1982;22(6):388–92.
- 57. Verhoeven VWA, Padsalgikar AD, Ganzeveld KJ, Janssen LPBM. The reactive extrusion of thermoplastic polyurethane and the effect of the depolymerization reaction. Vol. 21, International Polymer Processing. 2006. 295–308 p.
- 58. Król P, Pilch-Pitera B. Phase structure and thermal stability of crosslinked polyurethane elastomers based on well-defined prepolymers. J Appl Polym Sci [Internet]. 2007 May 5;104(3):1464–74. Available from: http://doi.wiley.com/10.1002/app.25011
- 59. Lan PN, Corneillie S, Schacht E, Davies M, Shard A. Synthesis and characterization of segmented polyurethanes based on amphiphilic polyether diols. Biomaterials. 1996;17(23):2273–80.
- 60. Deckard C. METHOD AND APPARATUS FOR PRODUCING PARTS BY SELECTIVE SNTERNG. 1986;(19). Available from: https://patents.google.com/patent/US4863538
- 61. Li Z, Wang Z, Gan X, Fu D, Fei G, Xia H. Selective Laser Sintering 3D Printing: A Way to Construct 3D Electrically Conductive Segregated Network in Polymer Matrix. Macromol Mater Eng. 2017;302(11):1–10.
- 62. Verbelen L, Dadbakhsh S, Van den Eynde M, Strobbe D, Kruth JP, Goderis B, et al. Analysis of the material properties involved in laser sintering of thermoplastic polyurethane. Addit Manuf

- [Internet]. 2017;15:12–9. Available from: http://dx.doi.org/10.1016/j.addma.2017.03.001
- 63. Melchels FPW, Feijen J, Grijpma DW. A review on stereolithography and its applications in biomedical engineering. Biomaterials [Internet]. 2010;31(24):6121–30. Available from: http://dx.doi.org/10.1016/j.biomaterials.2010.04.050
- 64. Vasquez M, Haworth B, Hopkinson N. Methods for quantifying the stable sintering region in laser sintered polyamide-12. Polym Eng Sci [Internet]. 2013 Jun;53(6):1230–40. Available from: https://onlinelibrary.wiley.com/doi/10.1002/pen.23386
- 65. Yuan S, Bai J, Chua CK, Wei J, Zhou K. Material evaluation and process optimization of CNT-coated polymer powders for selective laser sintering. Polymers (Basel). 2016;8(10).
- 66. Gan X, Wang J, Wang Z, Zheng Z, Lavorgna M, Ronca A, et al. Simultaneous realization of conductive segregation network microstructure and minimal surface porous macrostructure by SLS 3D printing. Mater Des [Internet]. 2019;178:107874. Available from: https://doi.org/10.1016/j.matdes.2019.107874
- 67. Ronca A, Rollo G, Cerruti P, Fei G, Gan X, Buonocore GG, et al. Selective laser sintering fabricated thermoplastic polyurethane/graphene cellular structures with tailorable properties and high strain sensitivity. Appl Sci. 2019;9(5):1–15.
- 68. Schmid M, Amado A, Wegener K. Materials perspective of polymers for additive manufacturing with selective laser sintering. J Mater Res. 2014;29(17):1824–32.
- 69. Awasthi P, Banerjee SS. Fused deposition modeling of thermoplastic elastomeric materials: Challenges and opportunities. Addit Manuf [Internet]. 2021;46(May):102177. Available from: https://doi.org/10.1016/j.addma.2021.102177
- 70. Kim G, Barocio E, Pipes RB, Sterkenburg R. 3D printed thermoplastic polyurethane bladder for manufacturing of fiber reinforced composites. Addit Manuf [Internet]. 2019;29(June):100809.
 Available from: https://doi.org/10.1016/j.addma.2019.100809
- 71. Lin X, Coates P, Hebda M, Wang R, Lu Y, Zhang L. Experimental analysis of the tensile property of FFF-printed elastomers. Polym Test [Internet]. 2020;90(May):106687. Available from: https://doi.org/10.1016/j.polymertesting.2020.106687
- 72. Christ JF, Aliheidari N, Ameli A, Pötschke P. 3D printed highly elastic strain sensors of

- multiwalled carbon nanotube/thermoplastic polyurethane nanocomposites. Mater Des. 2017;131:394–401.
- 73. Peng S, Li Y, Wu L, Zhong J, Weng Z, Zheng L, et al. 3D Printing Mechanically Robust and Transparent Polyurethane Elastomers for Stretchable Electronic Sensors. ACS Appl Mater Interfaces. 2020;12(5):6479–88.
- 74. Patel DK, Sakhaei AH, Layani M, Zhang B, Ge Q, Magdassi S. Highly Stretchable and UV Curable Elastomers for Digital Light Processing Based 3D Printing. Adv Mater. 2017;29(15):1–7.
- 75. Schüller-Ravoo S, Feijen J, Grijpma DW. Preparation of flexible and elastic poly(trimethylene carbonate) structures by stereolithography. Macromol Biosci. 2011;11(12):1662–71.
- 76. He Y, Tuck CJ, Prina E, Kilsby S, Christie SDR, Edmondson S, et al. A new photocrosslinkable polycaprolactone-based ink for three-dimensional inkjet printing. J Biomed Mater Res Part B Appl Biomater. 2017;105(6):1645–57.
- 77. Clark EA, Alexander MR, Irvine DJ, Roberts CJ, Wallace MJ, Sharpe S, et al. 3D printing of tablets using inkjet with UV photoinitiation. Int J Pharm [Internet]. 2017;529(1–2):523–30. Available from: http://dx.doi.org/10.1016/j.ijpharm.2017.06.085
- 78. Cummins G, Desmulliez MPY. Inkjet printing of conductive materials: a review. Circuit World [Internet]. 2012;38(4):193–213. Available from: http://www.emeraldinsight.com/doi/10.1108/03056121211280413
- 79. Sturgess C. Fully Reactive 3D Inkjet Printing of Polydimethylsiloxane and Polyurethane By Craig Sturgess A doctoral thesis submitted in partial fulfilment of the requirements for the award of doctor of philosophy of Nottingham. 2017;(June).
- 80. Ohnesorge W V. Die Bildung von Tropfen an Düsen und die Auflösung flüssiger Strahlen.

 ZAMM J Appl Math Mech / Zeitschrift für Angew Math und Mech [Internet]. 1936;16(6):355–

 8. Available from: https://onlinelibrary.wiley.com/doi/10.1002/zamm.19360160611
- 81. Derby B. Inkjet printing of functional and structural materials: Fluid property requirements, feature stability, and resolution. Annu Rev Mater Res. 2010;40:395–414.
- 82. Schuster F, Hirth T, Weber A. Reactive inkjet printing of polyethylene glycol and isocyanate

- based inks to create porous polyurethane structures. J Appl Polym Sci. 2019;136(3):1–8.
- 83. Teo MY, Kee S, RaviChandran N, Stuart L, Aw KC, Stringer J. Enabling Free-Standing 3D Hydrogel Microstructures with Microreactive Inkjet Printing. ACS Appl Mater Interfaces. 2020;12(1):1832–9.
- 84. Śliwiak M, Bui R, Brook MA, Selvaganapathy PR. 3D printing of highly reactive silicones using inkjet type droplet ejection and free space droplet merging and reaction. Addit Manuf. 2021;46(February).
- 85. Zawadzki M, Zawada K, Kowalczyk S, Plichta A, Jaczewski J, Zabielski T. 3D reactive inkjet printing of aliphatic polyureas using in-air coalescence technique. RSC Adv. 2022;12(6):3406–15.
- 86. Lindahl J, Hassen AA, Romberg S, Hedger B, Peter Hedger PH, Walch M, et al. Large-scale additive manufacturing with reactive polymers. CAMX 2018 Compos Adv Mater Expo. 2018;
- 87. Uitz O, Koirala P, Tehrani M, Seepersad CC. Fast, low-energy additive manufacturing of isotropic parts via reactive extrusion. Addit Manuf [Internet]. 2021;41(March):101919.

 Available from: https://doi.org/10.1016/j.addma.2021.101919
- 88. Bakarich SE, Gorkin R, Gately R, Naficy S, in het Panhuis M, Spinks GM. 3D printing of tough hydrogel composites with spatially varying materials properties. Addit Manuf [Internet]. 2017;14:24–30. Available from: http://dx.doi.org/10.1016/j.addma.2016.12.003
- 89. Tang D, Hao L, Li Y, Li Z, Dadbakhsh S. Dual gradient direct ink writing for formation of kaolinite ceramic functionally graded materials. J Alloys Compd [Internet]. 2020 Jan;814:152275. Available from: https://linkinghub.elsevier.com/retrieve/pii/S0925838819335212
- 90. Ober TJ, Foresti D, Lewis JA. Active mixing of complex fluids at the microscale. Proc Natl Acad Sci [Internet]. 2015;112(40):12293–8. Available from: http://www.pnas.org/lookup/doi/10.1073/pnas.1509224112
- 91. Romberg SK, Hershey CJ, Lindahl JM, Carter W, Compton BG, Kunc V. Large-scale additive manufacturing of highly exothermic reactive polymer systems. Int SAMPE Tech Conf. 2019;2019-May.

- 92. Cora Leibig; Daniel Gilbert. Manufacture of three dimensional objects from thermosets [Internet]. 2017. Available from: https://patents.google.com/patent/US11065816B2/en?q=chromatic+3d&oq=chromatic+3d#pat entCitations
- 93. Subramanian AS, Peng E, Lau WC, Goh DCW, Pramono S, Sriramulu D, et al. Morphological Effects of Various Silica Nanostructures on the Mechanical Properties of Printed Parts in Digital Light Projection 3D Printing. ACS Appl Nano Mater. 2021;4(5):4522–31.
- 94. Street DP, Mah AH, Patterson S, Pickel DL, Bergman JA, Stein GE, et al. Interfacial interactions in PMMA/silica nanocomposites enhance the performance of parts created by Fused Filament Fabrication. Polymer (Guildf) [Internet]. 2018;157(September):87–94. Available from: https://doi.org/10.1016/j.polymer.2018.10.004
- 95. Street DP, Mah AH, Ledford WK, Patterson S, Bergman JA, Lokitz BS, et al. Tailoring Interfacial Interactions via Polymer-Grafted Nanoparticles Improves Performance of Parts Created by 3D Printing. ACS Appl Polym Mater. 2020;2(3):1312–24.
- 96. Hmeidat NS, Pack RC, Talley SJ, Moore RB, Compton BG. Mechanical anisotropy in polymer composites produced by material extrusion additive manufacturing. Addit Manuf [Internet]. 2020;34(December 2019):101385. Available from: https://doi.org/10.1016/j.addma.2020.101385
- 97. Romberg SK, Islam MA, Hershey CJ, DeVinney M, Duty CE, Kunc V, et al. Linking thermoset ink rheology to the stability of 3D-printed structures. Addit Manuf [Internet]. 2020;37(October 2020):101621. Available from: https://doi.org/10.1016/j.addma.2020.101621
- 98. Kuang X, Chen K, Dunn CK, Wu J, Li VCF, Qi HJ. 3D Printing of Highly Stretchable, Shape-Memory, and Self-Healing Elastomer toward Novel 4D Printing. ACS Appl Mater Interfaces. 2018;10(8):7381–8.
- 99. Rostami M, Ranjbar Z, Mohseni M. Investigating the interfacial interaction of different aminosilane treated nano silicas with a polyurethane coating. Appl Surf Sci [Internet]. 2010;257(3):899–904. Available from: http://dx.doi.org/10.1016/j.apsusc.2010.07.087
- 100. Metcalf RL. Isocyanates, organic. Ullmann's Encycl Ind Chem. 2000;264–322.

- 101. Alexandridis P, Alan Hatton T. Poly(ethylene oxide)poly(propylene oxide)poly(ethylene oxide) block copolymer surfactants in aqueous solutions and at interfaces: thermodynamics, structure, dynamics, and modeling. Colloids Surfaces A Physicochem Eng Asp. 1995;96(1–2):1–46.
- 102. Maisel JW, Wason SK. Rheology of precipitated silica in epdxies. Polym Plast Technol Eng. 1982;19(2):227–42.
- 103. Mansour G, Tzetzis D. Nanomechanical Characterization of Hybrid Multiwall Carbon Nanotube and Fumed Silica Epoxy Nanocomposites. Polym Plast Technol Eng. 2013;52(10):1054–62.
- 104. Romberg SK, Islam M, Hershey CJ, DeVinney M, Duty CE, Kunc V, et al. Linking thermoset ink rheology to the stability of 3D-printed structures. Addit Manuf [Internet]. 2020 Oct;101621.
 Available from: https://doi.org/10.1016/j.addma.2020.101621
- 105. Niyogi S, Sarkar S, Adhikari B. Catalytic activity of DBTDL in polyurethane formation. In: Indian Journal of Chemical Technology [Internet]. InTech; 2002. p. 330–3. Available from: http://nopr.niscair.res.in/handle/123456789/18904
- 106. Silva AL, Bordado JC. Recent developments in polyurethane catalysis: Catalytic mechanisms review. Catal Rev Sci Eng. 2004;46(1):31–51.
- 107. Wang P, Auhl D, Uhlmann E, Gerlitzky G, Wagner MH. Rheological and Mechanical Gradient Properties of Polyurethane Elastomers for 3D-Printing with Reactive Additives. Appl Rheol. 2020;29(1):162–72.
- 108. Matsoukas T, Gulari E. Dynamics of growth of silica particles from ammonia-catalyzed hydrolysis of tetra-ethyl-orthosilicate. J Colloid Interface Sci. 1988;124(1):252–61.
- 109. Van Blaaderen A, Van Geest J, Vrij A. Monodisperse colloidal silica spheres from tetraalkoxysilanes: Particle formation and growth mechanism. J Colloid Interface Sci. 1992;154(2):481–501.
- 110. Rahman IA, Vejayakumaran P, Sipaut CS, Ismail J, Bakar MA, Adnan R, et al. An optimized sol-gel synthesis of stable primary equivalent silica particles. Colloids Surfaces A Physicochem Eng Asp. 2007;294(1–3):102–10.
- 111. Stöber W, Fink A, Bohn E. Controlled growth of monodisperse silica spheres in the micron size range. J Colloid Interface Sci [Internet]. 1968 Jan;26(1):62–9. Available from:

- https://www.jstage.jst.go.jp/article/jpts/29/1/29_jpts-2016-866/_article
- 112. An Y, Chen M, Xue Q, Liu W. Preparation and self-assembly of carboxylic acid-functionalized silica. J Colloid Interface Sci. 2007;311(2):507–13.
- 113. Preghenella M, Pegoretti A, Migliaresi C. Thermo-mechanical characterization of fumed silica-epoxy nanocomposites. Polymer (Guildf). 2005;46(26):12065–72.
- 114. Altaf K, Ashcroft IA, Hague R. Investigation of the effect of relative humidity on polymers by depth sensing indentation. J Mater Sci. 2011;46(23):7551–7.
- 115. M'Barki A, Bocquet L, Stevenson A. Linking Rheology and Printability for Dense and Strong Ceramics by Direct Ink Writing. Sci Rep. 2017;7(1):1–10.
- 116. Xu J, Cheng L, Zhang Z, Zhang L, Xiong C, Huang W, et al. Highly exfoliated montmorillonite clay reinforced thermoplastic polyurethane elastomer: in situ preparation and efficient strengthening. RSC Adv [Internet]. 2019;9(15):8184–96. Available from: http://xlink.rsc.org/?DOI=C8RA10121C
- 117. Behera PK, Usha KM, Guchhait PK, Jehnichen D, Das A, Voit B, et al. A novel ionomeric polyurethane elastomer based on ionic liquid as crosslinker. RSC Adv. 2016;6(101):99404–13.
- 118. Courtial EJ, Perrinet C, Colly A, Mariot D, Frances JM, Fulchiron R, et al. Silicone rheological behavior modification for 3D printing: Evaluation of yield stress impact on printed object properties. Addit Manuf [Internet]. 2019;28(February):50–7. Available from: https://doi.org/10.1016/j.addma.2019.04.006
- 119. Trovati G, Sanches EA, Neto SC, Mascarenhas YP, Chierice GO. Characterization of polyurethane resins by FTIR, TGA, and XRD. J Appl Polym Sci [Internet]. 2010 Jan 5;115(1):263–8. Available from: http://doi.wiley.com/10.1002/app.31096
- 120. Lewis JA. Direct-write assembly of ceramics from colloidal inks. Curr Opin Solid State Mater Sci. 2002;6(3):245–50.
- 121. Lewis JA. Direct ink writing of 3D functional materials. Adv Funct Mater. 2006;16(17):2193–204.
- 122. Wang L, Zhang S, Wang Q, Chen J, Jiang W, Chen RT. Fabrication of three-dimensional (3D) woodpile structure photonic crystal with layer by layer e-beam lithography. Appl Phys A Mater

- Sci Process. 2009;95(2):329–34.
- 123. Verhoeven VWA, Padsalgikar AD, Ganzeveld KJ, Janssen LPBM. A kinetic investigation of polyurethane polymerization for reactive extrusion purposes. J Appl Polym Sci. 2006;101(1):370–82.
- 124. Lei D, Yang Y, Liu Z, Chen S, Song B, Shen A, et al. A general strategy of 3D printing thermosets for diverse applications. Mater Horizons. 2019;6(2):394–404.
- 125. Wu S. Formation of dispersed phase in incompatible polymer blends: Interfacial and rheological effects. Polym Eng Sci. 1987;27(5):335–43.
- 126. Gonzalez-Nunez R, Favis BD, Carreau PJ, Lavallée C. Factors influencing the formation of elongated morphologies in immiscible polymer blends during melt processing. Polym Eng Sci. 1993;33(13):851–9.
- 127. Miles IS, Zurek A. Preparation, structure, and properties of two-phase co-continuous polymer blends. Polym Eng Sci. 1988;28(12):796–805.
- 128. Vanoene H. Modes of dispersion of viscoelastic fluids in flow. J Colloid Interface Sci. 1972;40(3):448–67.
- 129. Cardinaels R, Moldenaers P. Morphology development in immiscible polymer blends. Polym Morphol Princ Charact Process. 2016;40:348–73.
- 130. Ghodgaonkar PG, Sundararaj U. Prediction of dispersed phase drop diameter in polymer blends:

 The effect of elasticity. Polym Eng Sci. 1996;36(12):1656–65.
- 131. Pattanayak A, Jana SC. Thermoplastic polyurethane nanocomposites of reactive silicate clays: Effects of soft segments on properties. Polymer (Guildf). 2005;46(14):5183–93.
- 132. Chen Y, Zhou S, Yang H, Wu L. Structure and properties of polyurethane/nanosilica composites. J Appl Polym Sci. 2005;95(5):1032–9.
- 133. Pedrazzoli D, Manas-Zloczower I. Understanding phase separation and morphology in thermoplastic polyurethanes nanocomposites. Polym (United Kingdom) [Internet]. 2016;90:256–63. Available from: http://dx.doi.org/10.1016/j.polymer.2016.03.022
- 134. Al-Moameri H, Ghoreishi R, Suppes G. Impact of inter- and intra-molecular movements on thermoset polymerization reactions. Chem Eng Sci [Internet]. 2017;161:14–23. Available from:

- http://dx.doi.org/10.1016/j.ces.2016.12.007
- 135. Kunc F, Balhara V, Sun Y, Daroszewska M, Jakubek ZJ, Hill M, et al. Quantification of surface functional groups on silica nanoparticles: Comparison of thermogravimetric analysis and quantitative NMR. Analyst. 2019;144(18):5589–99.
- 136. Liu S, Eijkelenkamp R, Duvigneau J, Vancso GJ. Silica-Assisted Nucleation of Polymer Foam Cells with Nanoscopic Dimensions: Impact of Particle Size, Line Tension, and Surface Functionality. ACS Appl Mater Interfaces. 2017;9(43):37929–40.
- 137. Lee HS, Wang YK, MacKnight WJ, Hsu SL. Spectroscopic analysis of phase-separation kinetics in model polyurethanes. Macromolecules [Internet]. 1988 Jan;21(1):270–3. Available from: https://pubs.acs.org/doi/abs/10.1021/ma00179a055
- 138. Zhang S, Ren Z, He S, Zhu Y, Zhu C. FTIR spectroscopic characterization of polyurethane-urea model hard segments (PUUMHS) based on three diamine chain extenders. Spectrochim Acta Part A Mol Biomol Spectrosc. 2007;66(1):188–93.
- 139. Salimi S, Hart LR, Feula A, Hermida-Merino D, Touré ABR, Kabova EA, et al. Property enhancement of healable supramolecular polyurethanes. Eur Polym J [Internet]. 2019;118(February):88–96. Available from: https://doi.org/10.1016/j.eurpolymj.2019.05.042
- 140. Hermida-Merino D, O'Driscoll B, Hart LR, Harris PJ, Colquhoun HM, Slark AT, et al. Enhancement of microphase ordering and mechanical properties of supramolecular hydrogen-bonded polyurethane networks. Polym Chem. 2018;9(24):3406–14.
- 141. Woodward PJ, Merino DH, Greenland BW, Hamley IW, Light Z, Slark AT, et al. Hydrogen bonded supramolecular elastomers: Correlating hydrogen bonding strength with morphology and rheology. Macromolecules. 2010;43(5):2512–7.
- 142. Zhang C, Ren Z, Yin Z, Qian H, Ma D. Amide II and amide III bands in polyurethane model soft and hard segments. Polym Bull. 2008;60(1):97–101.
- 143. Pham KN, Fullston D, Sagoe-Crentsil K. Surface charge modification of nano-sized silica colloid. Aust J Chem. 2007;60(9):662–6.
- 144. Posthumus W, Magusin PCMM, Brokken-Zijp JCM, Tinnemans AHA, Van Der Linde R. Surface modification of oxidic nanoparticles using 3- methacryloxypropyltrimethoxysilane. J

Colloid Interface Sci. 2004;269(1):109–16.